To the Graduate Council:

I am submitting herewith a dissertation written by James Wilson McCamy entitiled "Growth of Epitaxial ZnS, ZnSe, and $ZnSe_{1-x}S_x$ Alloy Thin Films, Multilayers and Superlattices by Pulsed-Laser Ablation." I have examined the final copy of this dissertation for form and content and recommend that it be accepted in partial fulfillment of the requirements for the degree of Doctor of Philosophy, with a major in Metallurgical Engineering.

Douglas H. Lowndes, Major Professor

We have read this dissertation
and recommend it acceptance:

Accepted for the Council:

Associate Vice Chancellor
and Dean of The Graduate School

Growth of Epitaxial ZnS, ZnSe, and $ZnSe_{1-x}S_x$ Alloy Thin Films, Multilayers and Superlattices by Pulsed-Laser Ablation

A Dissertation

Presented for the

Doctor of Philosophy

Degree

The University of Tennessee, Knoxville

James Wilson McCamy

December, 1993

DEDICATION

This dissertation is dedicated to Ann

my wife and best friend

ACKNOWLEDGMENTS

I would like to thank first, my major professor, friend and mentor, Doug Lowndes for his support and stimulating insights and conversations. I am especially grateful for his ability to provide guidance when necessary and his willingness to let me pursue my own avenues of interest when needed.

I would like to thank various members of the Oak Ridge National Laboratory for their help and acknowledge their many contributions to this work. Jay Jellison performed the ellipsometric measurements and analyzed the resulting data. The ion probe experiments were performed with the help of Dave Geohegan. Special thanks go to Dave for letting me use his spectrometer for the room temperature photoluminescence experiments. John Budai performed the the 4-circle x-ray diffraction measurements. Many thanks go to Brian Chakoumakos for letting me used his x-ray diffractometer. The Rutherford backscattering spectrometry measurements were obtained with the help of Ray Zuhr and Steve Withrow. The secondary ion mass-spectrometry data were obtained by Tom Rosseel. The help of Pam Flemming, Frank Rau, Barbara Shoopman, Jim Shoopman, and Phil Herrell is gratefully acknowledged.

Help with the transmission electron microscopy investigation was provided by Mukund Godbole and X. Zhang of The University of Tennessee. The cryogenic photoluminescence spectra were obtained by Dr. Irving Herman and Mr. S. Kim. Their help is gratefully acknowledged.

This research was sponsored by the Division of Materials Sciences, U.S. Department of Energy under Contract No. DE-AC05-84OR21400 with Martin Marietta Energy Systems. A portion of the work published herein was performed in the Laboratory Graduate Participation Program under contract number DE-AC05-76OR00033 between the U.S. Department of Energy and Oak Ridge Associated Universities. Many thanks go to Kathy Ketner of ORAU for her help.

Finally, I wish to thank my parents for their guidance and inspiration. Most of all, I thank my wife, Ann. She has provided unceasing support and encouragement throughout this work.

ABSTRACT

Pulsed KrF (248 nm) laser ablation of polycrystalline ZnS and ZnSe targets was used to grow high quality, fully epitaxial ZnS and ZnSe thin films on GaAs (001), GaAs(111). Lower quality single crystal films resulted when ZnS was grown on GaP(001), while polycrystalline films resulted when ZnS was grown on Si(001) and Ge(001). The optimal growth temperature was determined from the rocking curve FWHM of the (004) x-ray diffraction (XRD) peak. For ZnS the optimal growth temperature was found to be $T_g = 325°C$; while the optimal temperature for PLA-growth of ZnSe it was $T_g = 300°C$.

For the films grown on GaAs, XRD showed that the in-plane film and GaAs [100] and [010] axes were aligned (i.e., true three-dimensional epitaxy). For ZnS grown on GaAs(111), XRD showed that the in-plane directions of the ZnS were aligned in two types of domains with respect to the underlying GaAs substrate. This is consistent with a zinc blende structure with a large degree of hexagonal stacking. The XRD pattern from the ZnSe film grown on GaAs(111) also indicated that the in-plane directions of the ZnSe might have been aligned in two types of domains with respect to the GaAs substrate.

Stacking faults were found to be the dominant defects present in the ZnS films. The stacking fault density was determined to have an upper bound of $\rho_{sf} \sim 2.5 \times 10^{10}$ cm·cm^{-3}. This stacking fault density is less than that in ZnS films grown by conventional techniques (e.g., MOCVD). Furthermore, the widths of the rocking curves of the PLA-grown ZnS films were less than for MBE-grown ZnS films of comparable thickness. Misfit dislocations were found to be the dominant defects present in the ZnSe films. The rocking curve width from the ZnSe(004) reflection, for a 225 nm thick film grown at the optimal T_g, implied a misfit dislocation density within the film of $\rho_d = 1.6 \times 10^{14}$ cm^{-3}.

The band structures of the ZnS and ZnSe films grown on GaAs(001) were investigated by inspecting the dielectric function (ε_1, ε_2). For ZnS and ZnSe, ε_2 approached zero below the bandedge indicating that both the PLA-grown ZnS and ZnSe films were of high optical quality. The E_o and

$E_0+\Delta_0$ transitions (Γ-point) also were clearly seen in the dielectric function spectrum of ZnS, while the E_1 and $E_1+\Delta_1$ transitions (L-point) were not seen because they occur above the upper limit of investigation. The E_0, $E_0+\Delta_0$, E_1, and $E_1+\Delta_1$ transitions all were seen clearly in the dielectric function spectrum of the ZnSe films.

Photoluminescence measurements of the ZnS and ZnSe films on GaAs(001) showed donor- and acceptor-bound excitonic emissions. Both films also showed free excitonic emissions. In the ZnSe film this free exciton peak was split into the heavy- and light-hole components because of the strain present in the film.

A multitarget holder was installed that allowed *in situ* selection of either a ZnS or a ZnSe target. By alternately ablating each target, strained layer superlattices of the form $(ZnSe)_m$-$(ZnS)_n$ were grown. The $\theta/2\theta$ XRD pattern from a sample having 65 periods of compositional modulation showed several orders of superlattice satellite peaks. The SLS compositional modulation period, determined from the separation of adjacent superlattice peaks, was L = 4.8 nm. This period compared well (only 4% difference) with the desired value.

A new technique that utilized ablation of ZnSe into a low-pressure H_2S gas ambient was developed to permit fabrication of $ZnSe_{1-x}S_x$ alloy films. The variation of sulfur content (x) with H_2S partial pressure was found to follow the relation $x = A[P(H_2S)]^B$, with $B \sim \frac{1}{2}$. The ability to grow films having predetermined compositions was evaluated by using this relation to determine the H_2S partial pressure needed to grow an (001)-oriented alloy film having x = 0.075; the resulting sulfur content for this film was x = 0.06. Room temperature photoluminescence of the (001) $ZnSe_{1-x}S_x$ films showed that the bandgap increased with increasing sulfur content; this behavior is consistent with sulfur entering the lattice on the selenium sites. To evaluate this spatial control over film composition, a $ZnSe_{1-x}S_x$ multilayered epitaxial structure was fabricated that simultaneously incorporated both continuously graded and successive abrupt, periodic compositional changes.

This same technique also was applied to incorporate doping elements into semiconductor films by growing ZnS films in low pressure HCl

ambients. Room temperature photoluminescence of a ZnS:Cl film grown in a 0.1% (~ 2 μTorr) HCl ambient showed a broad emission between 2 and 3 eV. This emission is due to transitions through deep levels associated with Cl complexes, and demonstrates that Cl was incorporated into the ZnS.

For both ZnS and ZnSe, a growth rate anisotrophy was observed for growth on the (001) and (111) surfaces. The difference in growth rates is due to differences in desorption rates on these surfaces. This difference in the rates is due to the difference in: (i) the site densities of the two surfaces, and (ii) the activation energies of the desorption rate constant.

Growth of the $ZnSe_{1-x}S_x$ alloys in ambients with and without He buffer gas showed that the alloy-formation mechanism depends only on the H_2S partial pressure and not the total ambient pressure. It also was found that the alloy composition is controlled by the dissociation of H_2S.

To assist in identifying the rate-limiting step, $ZnSe_{1-x}S_x$ films were grown in a $P(H_2S)$ = 22 mTorr ambient at various T_g. For the (001)-oriented alloys, the sulfur content was found to increase with increasing temperature, while the (111)-oriented alloys showed a constant sulfur content at all T_g. The slope of the line for the (001)-oriented alloy data gave an activation energy of 0.23 eV. It is shown that these data are consistent with the rate-limiting step being the replacement of the selenium with sulfur by adsorption.

PREFACE

This work was undertaken to evaluate the PLA process for the growth of wide-bandgap II-VI materials. This involved examining the structural, electrical, and optical properties of PLA-grown materials and evaluating the results in the context of the other existing technologies (i.e., MBE, CVD). To perform an objective evaluation requires a thorough knowledge of wide-bandgap II-VI material properties so that the quality of the PLA grown films can be established. In addition, both the operational advantages and disadvantages of other growth methods, and the quality of the films grown by those techniques, must be known. This, then, is the purpose behind the review found in chapters 2-4 of this work. This review was written with the expectation that the reader has a background in one or more of the review sections, but not in all. To the extent that this is true, those sections that the reader is familiar with may be passed over with little loss of continuity.

TABLE OF CONTENTS

LIST OF TABLES

LIST OF FIGURES

CHAPTER 1

INTRODUCTION

The properties of wide bandgap II-VI materials like ZnS and ZnSe have been investigated since the early 1900's, when the semiconducting materials were discovered. With the invention of the transistor in the 1950's, the focus of semiconductor research became centered on the silicon and germanium systems. With the development of chemical vapor deposition (CVD) and molecular beam epitaxy (MBE) technologies in the 1960's and 1970's, the focus of research in the semiconductor field shifted to III-V materials. The application of these technologies to the growth of II-VI materials has lagged the III-V work by about a decade. Recently, however, a blue solid-state laser multilayer structure was fabricated from the ZnSe-ZnCdSe system using MBE (Haase, 1991). It was primarily because of this development that interest has increased to the point that entire symposia at international conferences have been devoted to the growth and analysis of the wide-bandgap II-VI materials.

The development of the pulsed-laser ablation technology began at about the same time as that of MBE. However, although MBE has moved into production facilities, the PLA process has remained in the laboratory. However, PLA as an alternative deposition process became popular during the mid 1980's when PLA was (very) successfully used to grow thin, stoichiometric, epitaxial films of the high temperature (HT_c) superconducting oxides, and this technique is now the process of choice for growth of these materials. While it appears that PLA may move into production lines for the growth of these HT_c materials (e.g., Conductus, Inc., American Superconductor, Inc.), it has not been recognized as a competitive process for the growth of semiconductors.

For a new semiconductor growth process to be considered competitive with MBE and CVD, it must be demonstrated that the films are of high structural, electrical, electronic and optical quality. Further, the control of this process must be such that the films have uniform thickness across large (wafer size) areas and it must be possible to grow multilayered and

superlattice structures. Additionally, it must be possible to dope films with this technique. Finally, though not a necessary condition for competitiveness, it certainly is desirable to be able to fabricate structures which have a compositional or doped modulated structure.

This work was undertaken to evaluate the PLA process for the growth of wide-bandgap II-VI materials based on these criteria and in the context of the other existing technologies (i.e., MBE, CVD). To perform an objective evaluation requires a thorough knowledge of wide-bandgap II-VI material properties so that the quality of the PLA grown films can be established. In addition, both the operational advantages and disadvantages of other growth methods, and the quality of the films grown by those techniques, must be known. This, then, is the purpose behind the review found in chapters 2-4 of this work. Conventional PLA film-growth also is reviewed in chapters 5 and 6. The remaining chapters describe the advances in wide-bandgap II-VI growth that resulted from this work and examine the PLA growth process in the light of the criteria listed above.

CHAPTER 2

MATERIALS PROPERTIES

Physical Properties

Like other II-VI materials, the principal crystalline forms of ZnS and ZnSe are the zinc blende (cubic, T_d^2–$F\bar{4}3m$ space group) and the wurtzite (hexagonal, C_{6v}^4–$P6_3mc$ space group) structures. The zinc blende structure is most easily thought of as two interpenetrating fcc sublattices, one having Zn atoms and the other S (or Se) atoms. In the same manner, wurtzite can be described as two interpenetrating close-packed hexagonal sublattices. For both structures, the absence of a center of symmetry gives rise to many interesting and potential useful electrical and optical properties. In both ZnS and ZnSe, wurtzite is the stable phase at high growth temperatures (i.e., $T_g \geq$ ~1000°C), with zinc blende being the stable structure at lower temperatures (e.g., $T_g <$ ~500°C). Because of this low-temperature stability, and since most semiconductor substrates (i.e., GaAs) also possess the cubic structure, the zinc blende form is the desired structure and low-temperature growth methods are important.

As shown in Figure 2-1, both phases consist of the cation (Zn) atoms surrounded tetrahedrally by the anion (chalcogen) atoms. The similarity of the two structures is such that it is necessary to look at third-nearest neighbors before any significant difference is found. For ZnS and ZnSe, in fact, the only structural difference between the cubic and hexagonal phases is the stacking order. This stacking consists of alternating layers of cations and anions along the close-packed direction (the <111> axis for zinc blende, the c-axis for wurtzite). The stacking order is aAbBaAbB... for wurtzite and aAbBcCaAbBcC... for zinc blende (where a, b, c and A, B, C represent the three possible orientations separated by 120° rotations for the cation and anion layers, respectively). The stacking fault (SF) energy is simply the difference in energy between the two structures (e.g., aAbBaAbB $\rightarrow$ aAbB$\downarrow$cCaAbB where the vertical arrow represents the SF). The SF energies for ZnS and ZnSe are quite small (Table 2-1), and they are easily

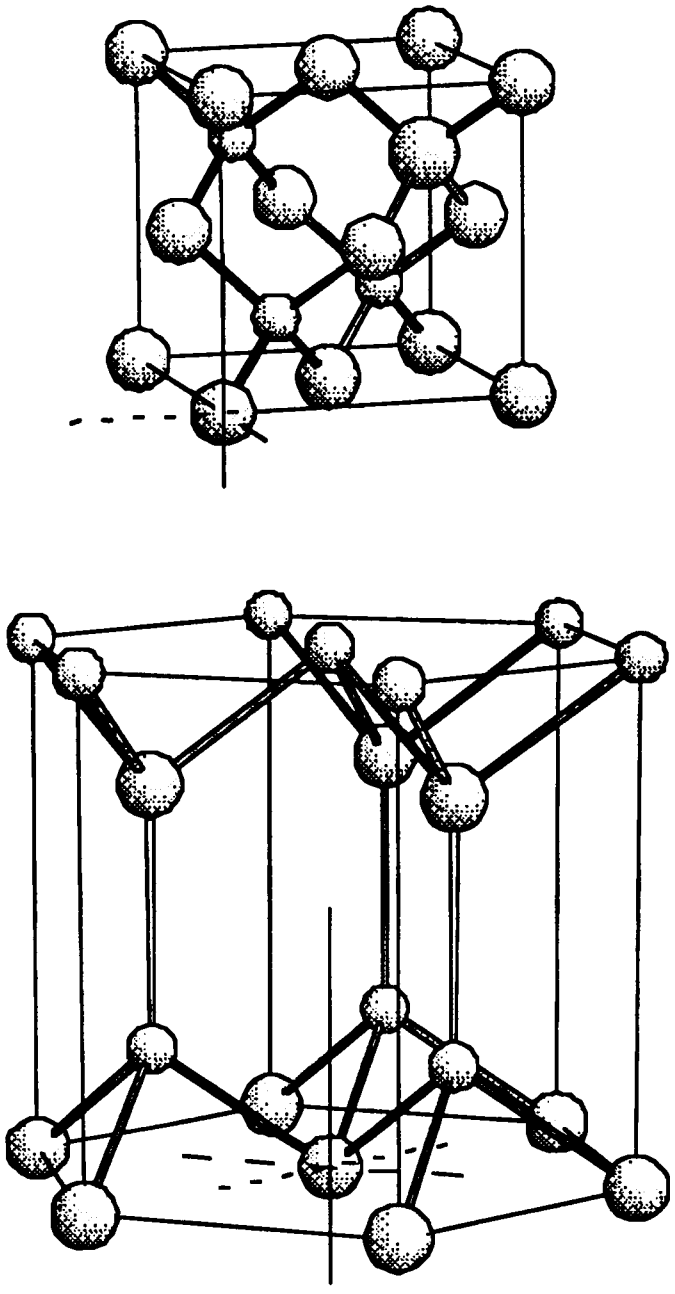

Figure 2-1 Zinc blende (top) and wurtzite (bottom) structures.

Table 2-1
Physical Properties of Various Semiconductors
(References in brackets)

Property	Si	Ge	GaAs	GaP	ZnS (zb)	ZnSe (zb)
Lattice Constant (nm)	0.543072	0.565754	0.565315	0.54505	0.54093	0.56676
C_{11} (x 10^{12}) (dyne·cm^{-2})	1.657[a]	1.289[a]	1.181[a]	1.412[a]	1.040[a]	0.810[a]
C_{12} (x 10^{12}) (dyne·cm^{-2})	0.639[a]	0.483[a]	0.532[a]	0.625[a]	0.650[a]	0.488[a]
C_{44} (x 10^{12}) (dyne·cm^{-2})	0.796[a]	0.671[a]	0.592[a]	0.705[a]	0.462[a]	0.441[a]
<100> Poisson's Ratio	0.28	0.27	0.31	0.31	0.38	0.38
Stacking Fault Energy (mJ·m^{-2})	58 ±6 [b]	75 ±10 [b]	55 ±5 [c]	41 ±4 [c]	5.4 ±1.8 [d]	12.6 ±0.4 [d]
Expansion Coefficient (α x 10^6 K^{-1})	3.1	6.0	5.7	5.3	6.5	6.8

[a] Muramatsu, S., Kitamura, M., *J. Appl. Phys.*, **73**, 4270 (1993)

[b] Denteneer, P.J.H., van Haeringen, W., *J. Phys. C: Solid State Phys.*, **20**, L883 (1987)

[c] Takeuch, S., Suzuki, K., Maeda, K., *Phil. Mag. A*, **50**, 171 (1984)

[d] Tairov, Y.M., Tsvetkov, V.F., Growth of Polytypic Crystals in *Growth and Defect Structures*, H.C. Freyhardt, ed, Springer Varlag, New York, 1984

formed under suitable growth conditions or by slip on the close-packed planes. In cubic material the SF may be thought of as a layer of material in the hexagonal position bounded on one or both sides by layers of material with cubic stacking. Thus, it is often customary to quantify the number of these defects by the degree of anisotropy α_{sf}, which is defined as the relative fractional content of the hexagonal material (Fedrov, 1992). Twinning occurs when two SF are oriented such that a stacking sequence of the form aAbBcCaA↓cCbBaA...aAcCbB↓cCaAbBcC, results.

Because the formation of polytypes and other defect complexes related to the cubic-hexagonal transformation is especially prevalent at higher growth temperatures, low growth temperatures are preferred. However, due to the small SF energies, stacking faults and twins are found even in cubic material grown at low temperatures (T_g < ~300°C). Further, these defects are especially prevalent in heteroepitaxial films because of the strain caused by lattice constant mismatch and by differences in thermal expansion coefficients between the film and substrate. The concentration of these defects can be greatly reduced by using an appropriately matched substrate or a buffer layer to minimize the strain.

Electronic Properties

The strong interest in ZnS and ZnSe stems from their wide, direct bandgaps (3.70 eV and 2.715 eV at 300 K, respectively). The energy-band structures for zinc blende ZnS and ZnSe, calculated using a self-consistent tight-binding model (Bertho, 1991), are reproduced in Figure 2-2. Pertinent room temperature electronic properties for ZnS and ZnSe are compared with those of other semiconductors in Table 2-2.

Although the bonding in ZnS and ZnSe involves some hybridization of the s- and p-orbitals of both the anions and cations, these compounds are still highly ionic due to the large localization of electronic charge about the chalcogen atoms. The relevant atomic orbitals for the constituent atoms are the 4s- and 4p-orbitals for both Zn and Se, and the 3s- and 3p-orbitals for S. These result in the bottom of the conduction band (CB) being s-like and the top of the valence band (VB) being p-like. At $k = 0$ in

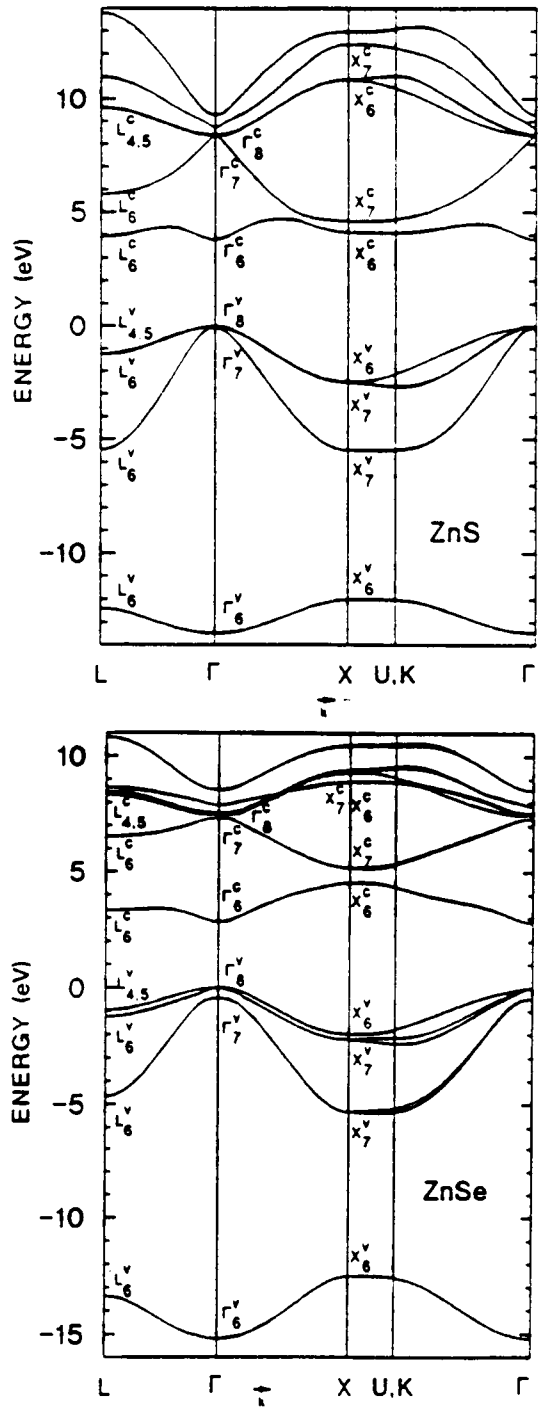

Figure 2-2 Electronic band structure for ZnS (top) and ZnSe (bottom) having the zinc blende structure. Reproduced from Bertho et al. (1991).

Table 2-2
Electronic Properties of Various Semiconductors

Property	Si	Ge	GaAs	GaP	ZnS (zb)	ZnSe (zb)
Bandgap E_g (eV)	1.12 (I)	0.67 (I)	1.42 (D)	2.26 (D)	3.70 (D)	2.71 (D)
Dielectric Constants ($\varepsilon_{static}/\varepsilon_{opt}$)	11.9 11.9	16.0 16.0	13.1 11.1	11.0 9.1	8.6 5.2	8.3 5.9
Electron Mobility ($cm^2 \cdot V^{-1} \cdot s^{-1}$)	1450	3900	8500	110	165	540
Hole Mobility ($cm^2 \cdot V^{-1} \cdot s^{-1}$)	450	1900	400	75	5	30
Effective Electron Mass (m_e)	0.58	0.35	0.067	0.35	0.34	0.16
Effective Hole Mass (m_{hh}/m_{lh})	0.52 0.16	0.34 0.043	0.62 0.087	0.86 0.14	1.76 0.23	1.44 0.23
Spin-Orbit Splitting (meV)	N/A	N/A	350	800	64	430

the T_d^2 structure without spin, the s-like CB behaves like the Γ_1 group, and the p-like VB as the Γ_4 group. When spin is included (zero field), the symmetry of the CB transforms as $\Gamma_1^c \rightarrow \Gamma_6^c$, and splitting of the upper VB occurs such that $\Gamma_4^v \rightarrow \Gamma_7^v + \Gamma_8^v$ (Reynolds, 1981). The result (Figure 2-2) is that the CB minimum is a single $S_{1/2}$ band (Γ_6^c, J=1/2), while the VB maximum consists of a fourfold degenerate $P_{3/2}$ band (Γ_8^v, $J = 3/2$, $m_j = \pm 3/2$, $m_j = \pm 1/2$) and a lower-energy, twofold degenerate $P_{1/2}$ band (Γ_7^v, $J = 1/2$, $m_j = \pm 1/2$). The energy difference between the VB maximum (Γ_8^v) and the CB (Γ_6^c) is the direct bandgap energy, E_g, while the difference between the Γ_8^v and Γ_7^v valence subbands (VSB) is the spin-orbit splitting energy, Δ_{so}.

Optical Properties

The optical properties of ZnS and ZnSe are determined by the interaction between the photons and the crystalline electronic energy levels. The dielectric response of the material is given by the complex dielectric constant $\varepsilon = \varepsilon_1 + i\varepsilon_2$, where ε_1 and ε_2 represent the dispersive and dissipative contributions, respectively. Since the electronic band structure spans a range of energies, the measurement of the dielectric function over a wide range of wavelengths is one of the most direct methods of obtaining information about the electronic energy band structure. This measurement is also a powerful tool for determining the quality of a particular sample and thereby evaluating the method by which it was grown.

Figure 2-3 shows the high resolution dielectric function spectrum for ZnSe (Adachi, 1991). This spectrum is dominated by direct interband transitions at the Γ (E_0) and L (E_1) critical points in the Brillouin zone in the range 1-6 eV. Because of the large spin-orbit splitting energy in ZnSe, the transition from the lower VSB at the Γ point ($E_0 + \Delta_0$) is observed as a separate peak. Although the splitting of the VSB at the L point is also large (Δ_1 ~300 meV), at room temperature the strength and dispersion of the E_1 transition is such that the $E_1 + \Delta_1$ transition appears as a shoulder on the

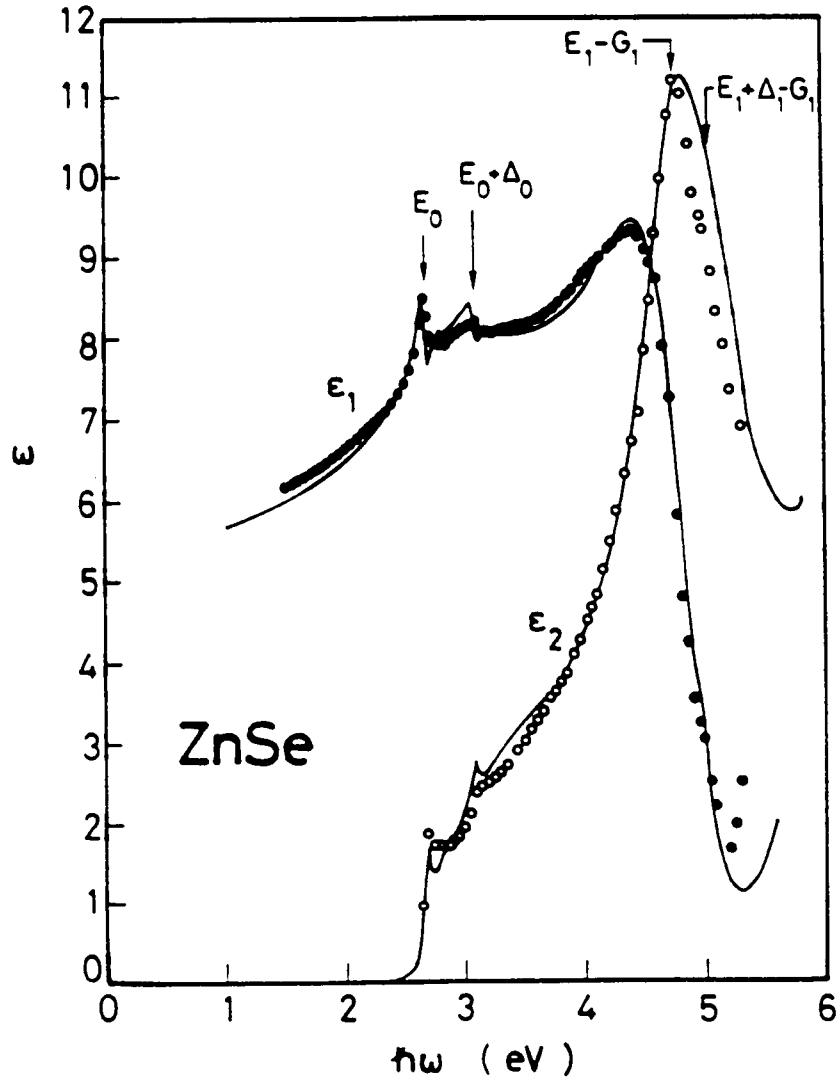

Figure 2-3 Dielectric function spectrum for ZnSe. Reproduced from Adachi and Taguchi (1991).

side of the E_1 peak. The E_0 and $E_0 + \Delta_0$ interband transitions are 3-D M_0 (i.e., direct band-edge exciton) type, while the E_1 and $E_1 + \Delta_1$ are believed to be 3-D M_1 (i.e., saddle-point exciton) type (Adachi, 1991).

No high resolution dielectric function data are available for ZnS to date. However, because the band structures of ZnSe and ZnS are similar, it is expected that the interband transitions are of the M_0 and M_1 type as well. Thus, it is anticipated that the dielectric function spectrum of ZnS is similar to that for ZnSe. However, the Δ_0 and Δ_1 splitting energies are small, and these splittings are expected to appear as broadening of the E_0 and E_1 peaks.

Characteristic of semiconductors, both ZnS and ZnSe are transparent ($\varepsilon_2 \sim 0$) below their bandgaps. Because of their large bandgaps, these materials are transparent to a broader range of wavelengths than most semiconductors, making them better suited for use in such optical applications as anti-reflection coatings, waveguides (Yokogawa, 1988), and for second-harmonic generation (Saitoh, 1991).

Electronic Properties of Defects

The wide direct bandgaps of ZnS and ZnSe allow doping with impurities (i.e., Tb) which form radiative deep centers in the visible part of the spectrum. The doping properties and optical transitions associated with these centers are not affected greatly by the other deep levels caused by extended defects such as stacking faults or dislocations, or by point defects. Thus, the emission from these deep doping levels is highly efficient. As a result, these doped materials have found wide use as phosphors in cathode ray tubes and colored electroluminescent panels (Kukimoto, 1992). However, because structural defects form deep centers that can release or trap carriers, their presence is of great concern when considering the intrinsic near-bandedge (NBE) optical transitions. The decay times of nonradiative transitions associated with these centers range from $\sim 10^{-8}$ s for the M-center (Talas, 1991) to $\sim 10^{-10}$ s for Hall-Shockley-Read centers (Zheng, 1992). Although a number of BE and NBE radiative transitions are possible (i.e., band-to-band recombination), the dominant mechanism of

NBE emission in n-ZnSe at room temperature is the recombination of an electron on a shallow donor with a free hole in the VB (Zheng, 1990). However, for even moderate (i.e., 10^{16}-10^{17} cm^{-3}) free-electron concentrations, the decay time of this emission is estimated to be two orders of magnitude longer than for the nonradiative processes (Talas, 1991). Conversely, defects which act as trapping centers remove free carriers from the recombination process preventing the desired NBE emission. Thus, the presence of defects greatly reduces the efficiency of NBE optical transitions.

Point defects are perhaps the most commonly observed defects in the wide bandgap II-VI materials. This group of defects consists of vacant lattice sites, atoms occupying interstitial positions, and substitutional impurities. Because the zinc blende structure does not have a center of symmetry, this last case also includes antisite defects where an atom of one sublattice is substituted onto the opposite sublattice (i.e., S_{Zn}, Se_{Zn}, and Zn_x). Further, since the sublattices are not equivalent, a particular defect (i.e., a vacancy) on one sublattice is not equivalent to the same defect on the other sublattice. In ZnS and ZnSe, the chalcogen vacancy (V_x) has a highly localized, unpaired electron symmetrically distributed over the four nearest Zn neighbors; while the zinc vacancy (V_{Zn}) results in a hole being highly localized in a p-orbital of a neighboring chalcogen atom. Because of this, the V_x has donor-like properties, and the V_{Zn} has acceptor-like properties. Although isolated vacancies are relatively immobile at room temperature, at slightly higher temperatures (i.e., ~100°C), vacancy diffusion occurs that results in the formation of vacancy-impurity pair complexes (Watkins, 1977). Since the reaction of the mobile vacancy with impurities of opposite carrier type is energetically favored, the complexes formed will be donor-acceptor pairs (DAP). Because of the ubiquitous nature of the V_{Zn}, the more common DAP are those associated with the V_{Zn}. Although no specific luminescence emission has been observed that can be attributed to isolated vacancies, electron paramagnetic resonance (EPR) and optically detected magnetic resonance (ODMR) examination of isolated V_{Zn} centers in ZnSe show absorption bands at 1.1, 1.4 and 2.65 eV (Jeon, 1986). However, Jahn-Teller relaxation, due to localization of the

hole following photoexcitation, causes the level at 2.65 eV to rise by ~0.7 eV. The well known 'self-activated' luminescence band has been identified as emission from an electron recombining with a hole located at this lower level, e.g., ~2.0 eV (Watkins, 1977). Since the origin of this electron can be the donor of the DAP or an isolated donor (Brandt, 1976), the V_{Zn} can compensate both its associated donor, and others as well. In the same way, DAP formed due to V_x can compensate the acceptors in p-doped material. In addition, V_x also can react to form three-member defect complexes (i.e., V_{Se}-Zn-N_{Se}). These complexes are thought to compensate the acceptors in N-doped ZnSe, causing the active acceptor concentration (N_A - N_D) to saturate (Hauksson, 1992). This problem is enhanced for Zn_i (e.g., Zn interstitials) in p-type material, since this defect can act as a double donor (Jansen, 1989).

The slip system in ZnS and ZnSe is $(a_o/2)$ {111} $\langle 1\bar{1}0 \rangle$, as a result, the line defects that form (i.e., threading or misfit dislocations) are of the 60° type. As illustrated in Figure 2-4, dislocations with edge components are created by adding or removing an extra half-plane of atoms. In both ZnS and ZnSe the mobile dislocations are on the chalcogen glide set (Osip'yan, 1986), and the zinc vacancies at the dislocation core result in a line of large negative charges. The application of stress results in movement of the dislocations; the motion of the charges associated with the dislocations causes current flow and alters the electrical transport properties. Conversely, carrier injection or application of an electric field exerts a force on the dislocations and alters the mechanical properties (electroplastic and photoplastic effects). Like isolated vacancies, the line of vacancies along the core also results in the formation of defect levels in the midgap region of the electronic structure. Luminescence studies in ZnSe (Myhajlenko, 1984) indicate that the Y_o (~2.60 eV) and S (~2.52 eV) band emissions are caused by dislocations. It is observed that these locations are consistent with the measured positions of the isolated V_{Zn} before and after Jahn-Teller relaxation; thus, it may be inferred that only a portion of the holes associated with the V_{Zn} line defect are localized. Myhajlenko also found that quenching of the D^o-X excitonic transition correlated with the

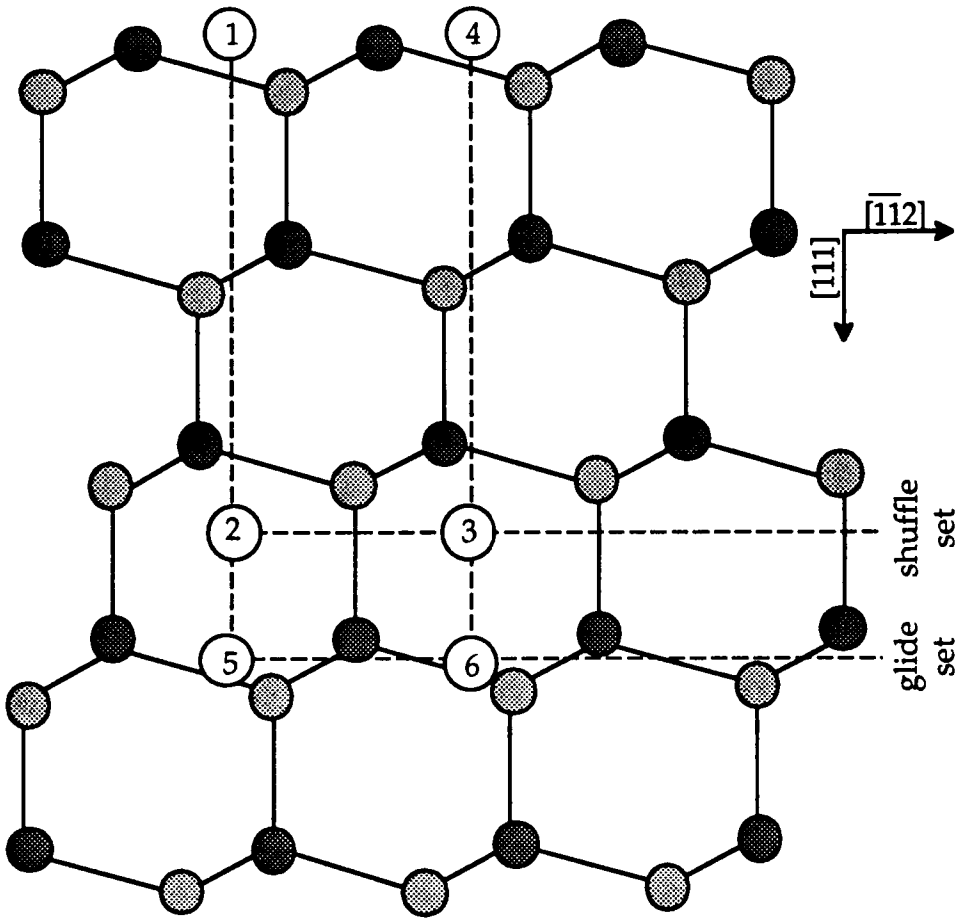

Figure 2-4 Zinc blende structure projected onto the $(1\bar{1}0)$ plane showing the formation of dislocations. A glide dislocation is formed by adding or removing material along 1-5, 5-6 and 6-4 and then connecting the vertical surfaces along 1-5 and 6-4. The shuffle set dislocation is formed by cutting along 1-2, 2-3 and 3-4 and then joining the surfaces.

presence of the Y_o line emission. Thus, both the electrical and electronic properties in ZnS and ZnSe are degraded when these defects are present.

When a SF defect is introduced into the lattice, the change in stacking order alters the local symmetry ($T_d^2 \rightarrow C_{3v}$) and the resulting anisotropic crystal field splits the upper VSB ($\Gamma_8^v \rightarrow \Gamma_9^v + \Gamma_7^v$). The magnitude of this splitting is determined by the crystal field parameter Δ_{cr} (Fedrov, 1992). For ZnSe Δ_{cr} is ~70 meV and ~55 meV for ZnS. Thus, the presence of SF results in shallow levels near the VB that can result in the formation of DAP which compensate the donors in n-type material (i.e., native defect self-compensation). These acceptor-like levels are confined to the plane of the SF resulting in polarization of the defect dipoles, and a corresponding influence on the electron-hole recombination. Further, SF are bounded by a set of ⟨112⟩ Shockley partial dislocations. Because of their edge component, these partial dislocations have vacancies associated with them which, as discussed previously, also adversely affect the electronic properties of these materials.

Aspects of Defect Formation

In all the cases discussed above, defects can compensate the carriers introduced by doping. Both SF and threading dislocation concentrations are strongly dependent on such exogenous factors as the film growth mode. If 3-D (island) growth occurs, the coalescence of the islands having different orientations may result in the formation of SF. It also has been found that when the initial growth mode is 3-D, the density of threading dislocations (i.e., 60° type) is about one order of magnitude greater than when the initial growth is layer-by-layer (Guha, 1992). The formation of misfit dislocations (also 60° type) is related primarily to the strain field present in the film. The magnitude and direction of the strain field is determined by the differences in the thermal expansion coefficients and lattice constants of the film and the underlying substrate (see Chapter 3). By manipulating the growth conditions and the lattice constants of the film, buffer layer and substrate, the tensorial properties of these fields can be 'engineered' and the defect concentration controlled (Hua, 1992).

On the other hand, it has long been argued that the self-compensation effect is due to endogenous properties such as the concentration of intrinsic point defects (Mandel, 1964; Jensan, 1989). However, Laks et al. have investigated the process of defect generation using a pseudoatomic tight-binding, mixed-basis-set model that incorporated the Zn 3d-states (Laks, 1992; van de Walle, 1992). Using this model, it was found that the native defect concentration in stoichiometric ZnSe (both n- and p-type) was less than 10^5 cm^{-3} at room temperature, and less than 10^{13} cm^{-3} at 300°C. For typical doping levels (~10^{17} cm^{-3} carriers), these equilibrium concentrations of compensating defects are too small to explain either the observed self-compensation at these carrier levels or the saturation effect seen at higher doping concentrations. Researchers in this field generally assume that stoichiometry is achieved during growth. While it is accepted that even small deviations (i.e., $\{[N_{Zn}] - [N_X]\}/\{[N_{Zn}] + [N_X]\} < 10^{-5}$) result in the formation of large numbers of defects, it is argued that this cannot explain the inability to easily p-dope ZnSe (Laks, 1991). These studies also assume equilibrium conditions and bulk materials; not considered, however, are the effects of growth kinetics, surface energies, preferred site incorporation, and/or relative adsorption-desorption rates on the formation and incorporation of these defects during growth.

Donor Acceptor Pair (DAP) Emission

This emission process consists of three steps: excitation, relaxation, and recombination. Since each donor and acceptor have specific levels to which they are excited and from which they recombine, an ideal way to identify which impurities are present would be to observe the emission spectra and identify the DAP from their emissions. Much of the research in the past thirty years has been directed toward this end, and tables of these emission levels from individual acceptors and donors, as well as from DAP complexes, have been published in a number of review articles (see for example, Nelkowski, 1982; Gutowski, 1990). In general, however, the photon energy from DAP recombination is:

$$E_{DAP} = E_g - (E_A + E_D) + \frac{e^2}{\varepsilon R_{DA}} \qquad 2.01$$

Here E_g is the bandgap energy, E_D and E_A are the binding energies of the donor and acceptor, and the final term is the Coulomb energy of the ionized D-A pair (Baru, 1976). Unfortunately, since the recombination energy depends on the donor and acceptor energies relative to the conduction and valence bands, and not their absolute values, it is not possible to assign a specific emission peak to a particular DAP. In addition, the hole located on a particular acceptor may recombine not only with the electron associated with the donor in that defect pair, but also with an electron from an isolated donor (Brandt, 1976). Because of the r^{-1} dependence of the Coulomb term in Equation 2.01, the peak location and dispersion of the transition energy are determined not only by the relative energy levels of the DAP, but also by the density and distribution of the donors as well.

Excitonic Properties and Emission

The excitons in ZnS and ZnSe are Wannier-Mott excitons. The Hamiltonian to describe them can be written as $\mathcal{H} = \mathcal{H}_0 + U_c$, where U_c describes the Coulomb interaction between the electron and hole. Within the effective mass approximation, ignoring short-range terms (i.e., exchange integrals), and assuming parabolic bands with no splitting, the associated eigenvalues of the Schrödinger equation are a series of hydrogenic-like states. The lowest of these states (n = 1) is the excitonic binding energy (E_b). At a temperature of 4 K, this energy is 36 meV in ZnS and 19 meV in ZnSe (Nelkowski, 1982); at room temperature, the corresponding E_b are 43 meV and 14 meV, respectively (Taguchi, 1992). Using the data in Table 2-2, the corresponding Bohr radii (at 4 K) are calculated to be ~2.3 nm in ZnS and ~4.6 nm in ZnSe.

The e-h pair that makes up the exciton can be generated by either bandedge-to-bandedge or defect-bandedge transitions, with the dominant process being determined by the energy of the exciting photon and the

density of defect states. The final excitonic state for an interband transition lies just below (above) the CB (VB); the minimum photon energy needed to form this exciton is the energy required to excite the electron to the n = 1 state and is given by (Böer, 1990)

$$E_x = E_g - E_b + E_K \qquad 2.02$$

Here E_x is the energy of the absorbed photon, the bandgap energy (E_g) is measured from the top of the appropriate VSB to the bottom of the CB, and E_K is the kinetic energy due to the center of mass motion of the exciton. Since the only contribution to the momentum of the exciton in a direct gap semiconductor is that of the photon, this last term is negligible for the exciton generation process.

In a perfect crystal at 0 K, the absorption peak would be sharp; however, in a real crystal at a temperature above 0 K, the excitonic absorption line is broadened. This lifetime broadening consists of two parts and, as a first-order perturbation, may be written (Nurmikko, 1992)

$$\Gamma(T) = \Gamma_{inh} + \Gamma_{LO}\left[e^{E_{LO}/kT} - 1 \right]^{-1} \qquad 2.03$$

Here, Γ_{inh} is the linewidth of inhomogeneous broadening (i.e., lattice disorder) and the second term is the linewidth due to homogeneous broadening (i.e., phonon effects in the perfect crystal). Γ_{LO} represents the strength of the exciton-LO phonon coupling and E_{LO} is the phonon energy. In ZnS the phonon energy is ~45 meV at 77 K, while for ZnSe it is ~32 meV at 80 K (Nelkowski, 1982). The interpretation of this temperature dependent line broadening and finite lifetime of the bound exciton state is that since E_{LO} is larger than E_b, every collision between an exciton and a phonon ionizes the exciton, releasing a free e-h pair with substantial energy. At higher temperatures, the large phonon density increases the collision frequency, reducing the exciton lifetime. At room temperature, the absorption of a photon creates an exciton that almost immediately

collides with a phonon, producing a free e-h pair. Indeed, the exciton lifetime in III-V semiconductors is on the order of 10^{-12} s at room temperature (Schmitt-Rank, 1989).

Because of variations in composition (particularly in alloys and solid solutions), the distribution of the exciton ground state energy has a spatial component as well. Since the Wannier-Mott exciton formed by an interband transition is mobile (e.g., a free exciton or FE), it can move to a local minimum (e.g., $E(x_1,y_1,z_1, n = 1) < E(x_0,y_0,z_0,n = 1)$) within the ground state. The excess energy appears as kinetic energy which is lost to the lattice through phonon interaction. The consequence is that excitons tend to be trapped in this local minimum before decaying (Wilkinson, 1992). Thus, in addition to inhomogeneous broadening, the excitonic emission peak is shifted toward an energy less than the E_x of Equation 2.02. Because of the interference of lifetime-broadened resonance (Harris, 1989), it is believed that this displacement of the emission distribution results in gain which is responsible for the laser action in the Zn(Cd)Se/ZnSe structures (Nurmikko, 1992; Ding, 1992). However, the temperature dependent exciton lifetime (equation [2.03]) restricts this excitonic driven laser action to low temperatures.

A bound exciton (BE) is one formed by a defect-band transition or a FE that binds to a defect; in either case the BE is an extrinsic property of the material. The defect centers can be either donors or acceptors; further, these centers can be either neutral (D^0, A^0) or ionized (D^+, A^-). Due to the exciton-defect binding energy, the energies of both the absorbed and emitted photons of the BE are always less than those associated with the FE; and, because of the ionization energy, the neutral bound exciton energies are less than those associated with ionized centers. Since the BE complex is associated with a single donor or acceptor, the photon energy should be precisely determined. However, the BE energy also depends on the strain present in the sample. In addition, impurity atoms can be present in defect complexes as well as by simple substitutional incorporation (Gutowski, 1990). Thus, like DAP spectra, the BE spectra can provide clues as to which impurities are present, but cannot provide conclusive identification of those impurities. On the other hand, the ratio of the intensity of the FE to

BE emissions, as well as of the BE to deep-level emissions, has been used to describe the overall purity of ZnSe samples (Gutowski, 1990).

The inhomogeneous linewidth (Γ_{inh}, Equation 2-3) is caused by lattice disorder and compositional fluctuations. As discussed above, SF are a primary cause of disorder in these materials. The relation between the broadening and the SF fraction (α_{sf}) can be estimated using a one-dimensional model (Fedrov, 1992; Maslov, 1992)

$$\Gamma_1 = \left[1.69 \left[\frac{dE_g}{d\alpha_{sf}} \right]^2 \frac{M \alpha_{sf} (1-\alpha_{sf})}{\hbar S} \right]^{\frac{2}{3}} \qquad 2.04$$

Here, M is the translational exciton mass and S is the number of close-packed layers per unit length along the close-packed direction. Since for a given material both of these are approximately constant, Equation 2.04 can be rewritten as

$$\Gamma_1 = \kappa [\alpha_{sf} (1-\alpha_{sf})]^{\frac{2}{3}} \qquad 2.05$$

Using the data for ZnS from Figure 2 of Maslov (1992), κ is determined to be ~12 meV at a temperature of 4.2 K. It is easily seen then from Equation 2.05, that little broadening occurs for a small number of SF in pure materials (e.g., α_{sf} = 1%, results in Γ_1 only ~0.5 meV).

Properties of $ZnSe_{1-x}S_x$ Alloys and Solid Solutions

The $ZnSe_{1-x}S_x$ ternary alloy has many advantages over the binary compounds because the bandgap and lattice parameter can be determined by controlling the composition. In particular, by lattice matching the film to the underlying substrate, the film can be grown with little or no strain. This decrease in strain reduces the density of misfit dislocations and the corresponding defect complexes. Assuming Vegard's law holds so that $a(ZnSe_{1-x}S_x) = xa(ZnS) + (1-x)a(ZnSe)$, then at room temperature a sulfur

content (x) of 0.056 is required for lattice matching to GaAs, while at 300°C, a sulfur content of 0.063 is required. Analysis of the strain splitting of the free exciton emissions from alloy films grown by MBE on GaAs (001) showed that there is zero strain in the film for x = 0.055 (Matsumura, 1989). Further, high resolution transmission electron microscopy (HRTEM) of a $ZnS_{0.06}ZnSe_{0.94}$ film grown on GaAs (001) by metalorganic chemical vapor deposition (MOCVD) showed that the film-substrate interface was completely epitaxial with no stacking faults or misfit dislocations, indicating lattice matching for x = 0.06 (Williams, 1984).

The compositional dependence of the bandgap in a semiconductor alloy AB_xC_{1-x} is described with an empirical bowing parameter b

$$E_g(x) = xE_{AB} + (1-x)E_{AC} - bx(1-x) \qquad 2.06$$

Here E_{AB} corresponds to the bandgap of ZnS and E_{AC} to that of ZnSe. For the ZnSSe alloy the bowing parameter b = 0.41 at 77 K and 0.63 at 300 K (Mach, 1982). The $E_o + \Delta_o$ transition energy is also observed to depend on the alloy composition. For this transition, b = 0.596 at 300 K. On the other hand the spin-orbit splitting was found to have only a weak, negative dependence on x, resulting in a bowing parameter of -0.067 (Ebina, 1974). The full form of the spin-orbit splitting is

$$\Delta_o(x) = 0.436 - 0.261x - 0.067x^2 \quad eV \qquad 2.07$$

The non-zero values for these bowing parameters originates mainly in the nonlinear variation of CB position (relative to the vacuum level) as the composition is changed. The VB position varies linearly with composition for $x > \sim 0.15$, and deviates only slightly from this linear relation for $x < 0.15$ (Bertho, 1993).

Electronic Properties of p-type Dopants

Not shown in Figure 2-2 is the Zn 3d-band, which lies 9.0 eV below the VB maximum in ZnS, and 9.2 eV below in ZnSe. (In most band structure calculations these orbitals are not included because they are assumed to be chemically inert core states.) This band, positioned between the two lowest VB (Γ_7^v and Γ_6^v) and having the same symmetry representation, couples with the anion p-states (Wei, 1988). With no impurities present, this p-d interaction contributes to the observed bandedge structure. When the d-states are included this mixing raises (lowers) the energy level of the antibonding (bonding) state relative to the level formed through s-p interaction alone. Thus, when an impurity atom (with d-states) is added, new levels are introduced near the bandedge. The position of this level is (to lowest order) inversely proportional to the energy difference between the anion p- and cation d-orbitals (Dow, 1985). Since the energy level of donors (acceptors) should be less than ~3$\mathcal{k}$T from the CB (VB) edge if they are to be highly ionized, this p-d mixing can play a significant role in the doping behavior of impurities.

The general technique for doping a compound semiconductor is to add impurities that, for n-type doping, lie to the right of the anion in the periodic table, or to the left of the cation for p-type doping. However, the addition of Cu (group IB) as a p-type dopant results in the formation of insulating deep levels (~1.2 eV above the VB maximum in ZnS and ~0.75 eV above in ZnSe). The deep position of these levels is due to the energy separation between the Cu^{2+} 3d- and anion p-orbitals being less than that between the Zn^{2+} 3d- and anion p-orbitals. This smaller energy difference results in the p-d mixing raising the antibonding states to energies above the VB maximum, resulting in the observed deep acceptor levels (Wei, 1988).

To avoid the formation of these levels, elements without d-orbitals must be used for p-type doping. (This deleterious effect of transition metal impurities is generally true for III-V, II-VI, and elemental semiconductors.) Group IA elements (e.g., Li and Na) substituted onto the Zn site have been used with some success for p-doping both ZnS and ZnSe (Mitsuishi, 1990;

Kawazu, 1989; Yahata, 1990; Yamada, 1990). However, group I impurities also act as donors if introduced onto the interstitial site (Isshiki, 1988; Hingerl, 1991). Because of its small radius, Li is highly mobile and easily enters the lattice as an interstitial. On the other hand, Na is easily substituted onto the Zn lattice site during photo-assisted metalorganic chemical vapor (MOCVD) growth of ZnS (Ohno, 1991). However, its binding energy of 160 meV in ZnS (Kawazu, 1989) is too deep (> 6 $\mathcal{k}$T at room temperature) to consider it an acceptable doping candidate.

Another technique for p-doping is to substitute an impurity that lies to the left of the anion onto the chalcogen site. While it has been suggested that co-doping ZnSe:Li films with either As or P can suppress the diffusion of Li (Kukimoto, 1991a), these two elements also can produce deep levels in ZnSe (Van de Walle, 1992). Nitrogen is a suitable p-dopant because its binding energy is ~74 meV in ZnSe (Yang, 1992), and it forms shallow acceptor levels in both ZnS and ZnSe thin films. Two readily available potential sources of N are N_2 and NH_3. While NH_3 has used during MOCVD growth (Yoshikawa, 1988; Kawazu, 1989), both N_2 and NH_3 neutrals have low sticking coefficients (Ohkawa, 1991). Recently the N_2 radical has become the dopant precursor of choice during growth of p-ZnSe and p-$ZnSe_{1-x}S_x$ by MBE (Ohkawa, 1992; Haase, 1991; Jeon, 1992). The reason for this is that the N_2 radical has a much higher sticking coefficient than the neutral; this has resulted in the incorporation of N up to 10^{19} cm^{-3} in ZnSe thin films, and in acceptor concentrations up to 8×10^{18} cm^{-3} (i.e., dopant activation ~80%). The N_2 radicals were generated using N_2 in a RF plasma; optical emission spectra of this plasma showed only N_2 molecules (both ground and excited states) present. An *ab inito* study of the incorporation of N_2 radicals onto $(Zn_mSe_n)H_6$ cluster surfaces showed that a path with an energy minimum exists only for the $^3\Sigma_u^+$ excited state species incorporated onto a Zn-terminated surface (Nakao, 1992). No energy minimum was found for the $^1\Sigma_g^+$ ground state as it approached a Zn- surface, nor was one found for any N_2 radical approaching a Se-terminated surface. Because the plasma requires moderate-vacuum conditions (P < 10 mTorr), this method of generating N_2 radicals cannot be used during MOCVD growth. However, since the excited state lies only

~6.2 eV above the ground state, other energy sources (e.g., the ArF excimer line, $\lambda = 193$ nm, $\hbar\nu = 6.4$ eV) can be used to increase N dopant atom incorporation in films grown in higher pressure systems (Kawakyu, 1988). The largest reported net acceptor concentration using N as the dopant is ~8×10^{18} cm^{-3} (Yang, 1992). At this level the carrier concentration saturates and the additional N atoms are not incorporated as acceptors. It has been found that there is significant residual compressive strain in these films. Further, it was found that point defects were generated and that the defect density increased with increased N incorporation (Petruzzello, 1993). It is possible that these defects compensate the acceptors and result in the saturation effect observed.

Electronic Properties of n-type Dopants

For n-type material, group IIIB impurities (i.e., Al) substituted onto the Zn site have been used with some success (Yasuda, 1986; Stutius 1982). While Al-doped ZnS thin films are highly conductive (~10^{-3} Ω·cm for an Al concentration of 5×10^{19} cm^{-3}), SA centers are formed in films having Al concentrations as low 1×10^{18} cm^{-3} (Kitagawa, 1989). The emissions associated with these centers are observed at ~1.5 eV and ~1.8 eV in ZnSe (Kitagawa, 1989), and at ~2.6 eV in ZnS (Yamaga, 1988). They are caused by V_{Zn}-D defect complexes. The V_{Zn} concentration can be reduced by increasing the Zn flux (J_{Zn}); however, this increases competition with the Al atoms for the Zn site, reducing the ability to control the doping level (Kamata, 1988).

The group VIIB elements, which (ideally) are substituted onto the chalcogen site, permit growth under high J_{Zn} conditions, resulting in few or no V_{Zn}. Within this group, Cl is the best choice for doping since there can be no p-d interaction to form deep levels. In addition, the doping level is more easily controlled when Cl is used (Kamata, 1988), than when Al is used, for example. Indeed, using standard techniques (i.e., constant J_{Cl}, which results in uniform doping throughout the sample), the carrier concentration is proportional to the concentration of incorporated Cl. However, at doping levels greater than ~10^{19} cm^{-3} the carrier concentration

saturates, and eventually begins to decrease. Zhu showed, that, by using a planar-doping technique, that this saturation effect can be overcome in MBE-grown ZnSe (Zhu, 1992). Zhu's procedure involved incorporating the Cl into ZnSe layers that were separated by pure ZnSe spacer layers. The thickness of the ZnSe:Cl layers was determined by controlling the length of time the dopant was introduced into the system. The resulting carrier concentration of a film having 40 periods of 1.2 nm ZnSe:Cl / 7.8 nm ZnSe grown using this technique was 3×10^{20} cm^{-3}. This very high carrier concentration indicates that this method of modulation doping is a technique that perhaps can be applied more broadly. Electrical measurements (van der Pauw) taken in the temperature range 30 to 300 K showed that there was no significant change in either the concentration or mobility of the carriers. Moreover, photoluminescence (PL) measurements of this sample showed a marked decrease in SA center emission and a corresponding increase in the NBE emission, as compared to uniformly Cl doped ZnSe samples.

CHAPTER 3

THIN FILMS AND SUPERLATTICES

Strain Accommodation and Dislocations

Because of lattice constant and thermal expansion mismatch, strain is always present in heteroepitaxial layers grown at elevated temperatures. If the strain (ε) is defined to be positive for compression, the strain field caused by biaxial stress parallel to a [001]-oriented film-substrate interface is

$$\varepsilon = -\varepsilon_{xx} = -\varepsilon_{yy} \qquad 3.01a$$

$$\varepsilon_{zz} = \frac{2C_{12}}{C_{11}}\varepsilon \qquad 3.01b$$

$$\varepsilon_{xy} = \varepsilon_{yz} = \varepsilon_{xz} = 0 \qquad 3.01c$$

Here x and y are orthogonal directions parallel to the interface, z is the growth direction normal to the interface (i.e., z $\|$ [001]), and C_{ij} is the appropriate component of the elastic stiffness tensor. For a coherent film grown on a thick, rigid substrate, (i.e., may be treated as semi-infinite and inelastic), the in-plane strain at a growth temperature T_g, caused by the lattice mismatch and thermal expansion mismatch between the film (f) and the substrate (s) can be written

$$\varepsilon_{xx} = \varepsilon_{||}(T_g) = \varepsilon_{epi} + \varepsilon_{therm} = \frac{a_f - a_s}{a_f} + (\alpha_f - \alpha_s)(T_g - T_0) \qquad 3.02$$

Here a_i is the lattice constant, α_i is the thermal expansion coefficient and T_0 is the reference temperature for the lattice constants (i.e., 300 K for values in Table 2-1). For a typical growth temperature of ~300° C, the in-plane (ε_{xx}) strain for ZnSe on GaAs is 2.9×10^{-3}; for ZnS on GaAs and GaP, this strain is -44.9×10^{-3} and -7.3×10^{-3} respectively.

The energy associated with the elastic in-plane strain field is proportional to the square of the strain, to a geometric factor (B) determined by the substrate orientation and growth direction, and to the thickness (L) of the film (Matthews, 1975)

$$E_\varepsilon = \varepsilon_{||}^2(T)\, BL \qquad 3.03$$

The strain can be accommodated, and the strain energy reduced, by the presence of dislocations in the film which reduce the misfit (Ball, 1983). The film thickness at which the accommodation occurs is known as the critical thickness (L_c). This thickness was first calculated by minimizing the sum of the interfacial energy and the strain energy of the film (for a review see van der Merwe, 1972). In this approach it was assumed that the misfit dislocations were generated from threading dislocations present during growth (i.e., without nucleation.) The nucleation of misfit dislocations was explicitly considered by Matthews and Blakeslee (1974) who set the driving force from the strain equal to that of the line tension of a dislocation, and by People and Bean (1985, 1986) who set the "areal energy density" of a screw dislocation equal to the strain energy density. Although the choice of the screw-type dislocation as a misfit dislocation is not correct because the observed misfit dislocations in diamond and zinc blende semiconductors are 60° type, the predicted L_c agreed well with experimental data for Ge_xSi_{1-x} alloys grown on Si. Fukuda et al. (1990) have used the energy balance approach and applied it to the 60° type dislocation. They assume that these dislocations nucleate at the surface atomic steps, and expand to the interface by glide processes. Using this approach, the relation between the critical thickness of the film and the strain in the film is

$$L_c = \frac{b\,(8 - 5\upsilon)}{8\pi\varepsilon\,(\upsilon + 1)} \ln\left(\sqrt{\frac{6}{4}}\frac{\beta L_c}{b}\right) \qquad 3.04$$

Here, b is the length of the Burger's vector, υ is Poisson's ratio, and β is the dislocation core parameter. For ZnSe on GaAs at 350° C ($\varepsilon = 3.25 \times 10^{-3}$), the predicted L_c is 170 nm. This value is in excellent agreement with the experimental data for MBE ZnSe on GaAs (350° C), for which the L_c was found to be 160 nm (Olego, 1988). However, a L_c as large as 510 nm has been reported for ZnSe on GaAs by atomic layer epitaxy (ALE) at 400° C, (Koukitu, 1990). As discussed below, this increase is perhaps due to the difference in growth techniques and the associated initial growth modes.

For ZnS, if we assume that for tensile strain, $\varepsilon = |\varepsilon_{\parallel}|$ in Equation 3.04, then, L_c is 64 nm for growth on GaP substrates and, at most, 7 nm for GaAs substrates. This last value is probably high, and, based on data for Si grown on GaAs ($\varepsilon = -41.7 \times 10^{-3}$), is more likely closer to 1-2 nm (Zalm, 1985).

While these models predict the L_c with some degree of success, none seems to describe adequately the resulting strain accommodation. Often, it is assumed that the strain is fully relaxed in layers thicker than L_c, but, Mohammed et al. (1987) have demonstrated that this is not the case. Measurements of the strain by the photoluminescence, TEM, and x-ray diffraction techniques, showed that, although relaxation of the strain in ZnSe layers on GaAs begins when the film thickness reaches ~L_c, it is not complete until L = ~850 nm.

Dislocation Type and Initial Growth Modes

Planar transmission electron microscopy of undoped ZnSe films grown by MBE on GaAs (001) showed irregular arrays of misfit dislocations (Petruzzello, 1988, 1993). For 180 nm thick films, these arrays were predominantly (~95%) 60° type and the remainder were Lomer edge type with the Burger's vectors in the plane of the interface. The reported density of the misfit dislocations was ~10^9 cm^{-2} (this corresponds to ~5×10^{13} cm^{-3} for an 180 nm thick film). While no misfit dislocations were seen in films thinner than this (L = 50 nm and 87 nm), stacking faults, bounded by partial dislocations were seen. The SF density in these films was ~10^9 cm^{-2}; SF were also observed, but at a lower density, in the 180 nm thick film as well. Cross-sectional high resolution TEM of ZnSe grown by

MOCVD on GaAs (001), showed no misfit dislocations (Cockayne, 1985). The film thicknesses were in the range L = 600-4000 nm, and, in all cases, the predominant defects observed, both near the interface and in the bulk layer, were SF. Further, the SF density (both at the interface and in the bulk) for all the films was in the range of 4-8 x 10^{11} cm^{-2}. This is perhaps due to the fact that while the SF energy in ZnSe is small, few of the misfit dislocations will dissociate in a compressive field. When the samples are prepared for cross-sectional viewing, the compressive strain is relaxed and the misfit dislocations can easily dissociate into partials and the associated SF. However, one also notes that the two techniques used to grown these samples were significantly different, and that the dislocation type and density is quite sensitive to the initial growth mode. Guha et al. (1992, 1993) have shown that, for 2-D growth of ZnSe (L = 200-270 nm) on GaAs by MBE, the defects are predominantly (~70%) 30° Shockley partials, and trailed by SF; while, for 3-D growth, the defects are found to be mostly of the perfect 60° type. It is possible then, that growth of the Petruzzello samples (MBE) proceeded in the 3-D mode, while those of Cockayne (MOCVD) proceeded in the 2-D mode and would explain the differences in the type of dislocations observed. Since the islands present in 3-D growth act as nucleation sites for misfit dislocations, these results are also consistent with the increase of the L_c to 510 nm for films grown by ALE (2-D growth).

For undoped ZnS grown on GaAs (001) by MOCVD, cross-sectional high resolution TEM showed only SF and twinning (Williams, 1984; Cockyane, 1985); the SF density was observed to be ~10^{11} cm^{-2}. Since the strain in this system is tensile and very large, and the SF energy of ZnS small (Table 2-1), this result is not unexpected. In contrast, Kawakami et al. (1987) observed (by plan-view TEM) only misfit (Frank) dislocations in MOCVD ZnS films grown on GaAs (001). On the other hand, twins and SF were observed in ZnS films grown on GaAs (111) substrates. For the Kawakami samples, the reactants were dimethylzinc (DMZn) and hydrogen sulfide (H_2S). Williams and Cockyane used DMZn and either H_2S, thiophene (C_4H_4S), or tetrahydothiophend (C_4H_4S) in their work, with little difference in the corresponding SF densities. The only

significant difference in the reported growth parameters, was the use of He as a carrier gas by Kawakami and H_2 by Williams and Cockyane. It has since been shown that, for metalorganic MBE (MOMBE) growth of ZnSe on GaAs, the presence of H_2 results in 2-D growth (Kawakami, 1990). Thus, it is possible that the samples grown with He as the carrier gas proceeded in the 3-D mode, while those with H_2 as the carrier gas proceeded in the 2-D mode; and that the difference in growth modes is responsible for the differences in the type of dislocations observed.

Thus, in both ZnS and ZnSe, the dislocation type and density is understood to depend strongly on the mechanism by which these dislocations are formed, and that this mechanism depends on the initial growth mode. Where the growth mode is 3-D, the dislocations nucleate at island coalescence boundaries that are formed during growth. In contrast, for 2-D growth the dislocations are believed to be formed as a direct consequence of the misfit. The nucleation sites in this case are either the free surface (half-loop formation) or the interface (full-loop formation). Thus, the conditions under which 2-D growth is initiated are of crucial importance. For MBE growth on thermally treated GaAs substrates, 2-D growth was initiated when an As-stabilized GaAs substrate was exposed to Zn flux for ~1 minute; on the other hand, 3-D growth was initiated when a Ga-stabilized substrate was exposed to Se flux for ~1 minute (Guha, 1993). For MOMBE growth, it has been found that 2-D nucleation and growth is initiated if the surface of the GaAs can be sulfur-passivated, and that this is easily achieved by pretreating the substrate in an ammonium sulfide ($(NH_4)_2S_x$) solution (Wu, 1990). It has also been reported that this treatment reduces the surface state density (Kawakami, 1991)

Strain Effects on the Electronic Structure

The difference between the in-plane strain and that parallel to the growth direction (Equations 3.01a and 3.01b, respectively) results in tetragonal distortion which lowers the lattice symmetry from T_d to D_{2d}. Although the $S_{1/2}$ conduction band (CB) is unaffected by this symmetry change, the $P_{3/2}$ valance band (VB) splits into $m_j = \pm 1/2$ (light-hole) and

$m_j = \pm 3/2$ (heavy-hole) subbands. In addition, the hydostatic component of the strain shifts the center of gravity of both the $P_{1/2}$ and $P_{3/2}$ VB. Thus, within the effective mass ($\mathbf{k} \cdot \mathbf{p}$) framework, the complete Hamiltonian to describe the VB may be written as $\mathcal{H}_V = \mathcal{H}_{\mathbf{kp}} + \mathcal{H}_{so} + \mathcal{H}_\varepsilon$, where $\mathcal{H}_{so}$ is used to describe the spin-orbit splitting (Chapter 2), $\mathcal{H}_\varepsilon$ describes the strain effects, and $\mathcal{H}_{\mathbf{kp}}$ describes the unperturbed VB (People, 1990). In the nomenclature of Pikus and Bir (1960), the energy shifts due to strain are

$$\Delta E_{HH} = \Delta E(J=\tfrac{3}{2}, m_j=\pm\tfrac{3}{2}) = \left[-2a\frac{C_{11}-C_{12}}{C_{11}} + b\frac{C_{11}+2C_{12}}{C_{11}} \right]\varepsilon \qquad 3.05a$$

$$\Delta E_{LH} = \Delta E(J=\tfrac{3}{2}, m_j=\pm\tfrac{1}{2}) = \left[-2a\frac{C_{11}-C_{12}}{C_{11}} - b\frac{C_{11}+2C_{12}}{C_{11}} \right]\varepsilon \qquad 3.05b$$

$$\Delta E_{E+\Delta_0} = \Delta E(J=\tfrac{1}{2}, m_j=\pm\tfrac{1}{2}) = \left[-2a\frac{C_{11}-C_{12}}{C_{11}} \right]\varepsilon \qquad 3.05c$$

In Equation 3.05, the HH, LH and $E + \Delta_0$ subscripts correspond to the heavy-hole, light-hole and the spin-orbit subbands respectively; a is the hydrostatic deformation potential and describes the center of gravity shift, and b is the shear deformation potential. It is seen that the hydrostatic component of an in-plane compressive (tensile) strain causes the VB shift to be away from (toward) the CB, while biaxial strain pushes the light-hole subband to a position below (above) the heavy-hole subband. For ZnSe the hydrostatic and shear deformation potentials are -5.4 eV and -1.2 eV respectively; for ZnS, these potentials are -4.0 eV and -0.7 eV (Blacha, 1984). Thus, the VB shifts (eV) for ZnSe (Equations 3.06a, 3.06b, 3.06c) and ZnS (Equations 3.06d, 3.06e, 3.06f) are calculated to be

$$\Delta E_{HH} = 1.642\,\varepsilon \qquad 3.06a$$

$$\Delta E_{LH} = 6.436\,\varepsilon \qquad 3.06b$$

$$\Delta E_{E+\Delta_0} = 4.289\,\varepsilon \qquad 3.06c$$

$$\Delta E_{HH} = 1.433\,\varepsilon \qquad 3.06d$$

$$\Delta E_{LH} = 4.581\,\varepsilon \qquad 3.06e$$

$$\Delta E_{E+\Delta_0} = 3.007\,\varepsilon \qquad 3.06f$$

Superlattice Structures

A superlattice (SL) is a structure that consists of alternating thin layers of two materials and is periodic along the dimension normal to the plane of those layers. For semiconductor materials, the periodicity of the compositional modulation results in a periodic oscillation of the bandgaps along the SL direction, and, consequently, a superlattice potential. In addition, if the layers are coherently strained, the strain periodicity contributes to this superlattice potential as well. If the width of the SL layers is less than the electron mean free path, then the superlattice potential modifies the band structure of the constituent materials, resulting in new electronic properties.

A strained layer superlattice (SLS) is one in which the constituent layers are coherently strained; thus, the in-plane lattice parameter is the same for all layers. For the free-standing SLS (i.e., not strained coherently with the underlying substrate) with constituents α and β, the effective in-plane lattice constant is

$$a_{\parallel} = \frac{a_\alpha G_\alpha L_\alpha + a_\beta G_\beta L_\beta}{G_\alpha L_\alpha + G_\beta L_\beta}\,, \qquad 3.07$$

where a_i is the lattice constant, L_i is the thickness of each constituent layer, and the shear modulus (G_i) for the i^{th} constituent is given by

$$G_i = 2(C^i_{11} + C^i_{12})\left(1 - \frac{C^i_{12}}{C^i_{11}}\right) \qquad 3.08$$

In practice, a SLS is not free-standing, but is strained by the lattice mismatch between itself and the substrate. In this situation, the components of the strain tensor are determined by applying Equations 3.01 and 3.02 to each constituent layer, and the critical thickness of the SLS as a whole can be calculated from Equations 3.02 and 3.04 with the $a_{\parallel}$ determined from Equation 3.08 used in place of a_f. In addition, the perpendicular lattice constant for the i^{th} constituent layer is found from

$$a_{\perp}^{i} = a_{o}^{i}\,(1 + \varepsilon_{zz}^{i}) = a_{o}^{i}\left(1 + \frac{2\,C_{12}}{C_{11}}\right)\left(-\varepsilon_{xx}^{i}\right) \qquad 3.09$$

Where a_o is the bulk lattice parameter for that constituent and the in-plane strain is determined from the misfit between the substrate and that layer.

Parameters for ZnS-ZnSe SLS Construction

The primary purpose for fabricating SLS structures in wide bandgap II-VI systems is either to confine the excitons and serve as a structure for lasing, or to provide a structure for an optical waveguide for second-harmonic generation (SHG). For lasing, the ZnSe, with its smaller energy gap is the well, with ZnS acting as the barrier layer. The optoelectronic requirements and the structural parameters (i.e., L_c) determine the SLS layer widths necessary for device construction; a growth process must be able to fabricate the SLS within these constraints to be considered viable.

In the III-V semiconductors, lasing occurs due to the gain caused by the population inversion of an e-h plasma. In the wide bandgap II-VI materials, lasing is believed to occur due to gain related to the interference of lifetime-broadened resonance in the absorption and in the emission accompanying recombination of the excitons (Nurmikko, 1992; Ding, 1992). However, at high temperatures (i.e., ~20°C), this process is prevented by the short exciton lifetimes (see Equation 2.03 and discussion following). The exciton lifetime can be increased by increasing the binding energy (E_b) such that it is greater than the energy of the LO-phonon (E_{LO}). In ZnS and ZnSe, the E_{LO} values are ~36 meV and ~32 meV respectively; while, for 3-D

excitons, the E_b are ~36 meV and ~19 meV respectively (Nelkowski, 1982). It has been shown that if the excitons are confined such that they behave in a 2-D manner, then the binding energy is four times larger than in the 3-D case (Chemla, 1988). Thus, if the width of the active layer in the SLS is less than the diameter of the exciton (~4.6 nm in ZnS and ~9.2 nm in ZnSe) then the E_b is increased, and the desired population inversion can occur. Indeed, for a ZnS(2.5 nm)-ZnSe(5.0 nm) SLS, the binding energy has been found to be ~160 meV (Adachi, 1991). If the layer widths are such that the electron and hole wavefunctions overlap, then the exciton lifetime also will be reduced. However, no evidence of this has been reported in II-VI semiconductors.

Defining L' as a relative thickness parameter (e.g., $L' = L_{ZnS} / L_{ZnSe}$), the in-plane lattice constant (in Å) is calculated to be

$$a_{||} = \frac{9.754\times10^{12}L' + 8.201\times10^{12}}{1.803\times10^{12}L' + 1.447\times10^{12}} \qquad 3.10$$

Figure 3-1 shows the relation between the L_c and L' calculated from Equations 3.10 and 3.04 for a ZnS-ZnSe SLS on a thick (e.g.., unstrained, $a_{||} = a_o$) ZnSe buffer layer and on a GaAs substrate (or buffer layer having a lattice constant equal to GaAs). These calculations were made assuming that the difference between the thermal expansion coefficients for the SLS and underlying layer is negligible. The range of interest for L' is determined by the critical thickness of the constituent layers, the layer thickness required for exciton confinement, and the unit cell size of the materials (assuming that unit cell control of the growth is possible). For the ZnS-ZnSe system, this range of interest is $12 > L' \geq 1/17$. Lattice matching to a GaAs substrate requires a L' ~1/21; thus, it is not possible to lattice match a ZnS-ZnSe SLS to a GaAs substrate. More realistically, for L' = 0.5, the critical thickness is ~36.5 nm on a GaAs substrate, and ~31 nm on a ZnSe buffer layer. This corresponds to less than 4 periods in a SLS with a period of $(ZnS)_{\sim6}$-$(ZnSe)_{\sim12}$.

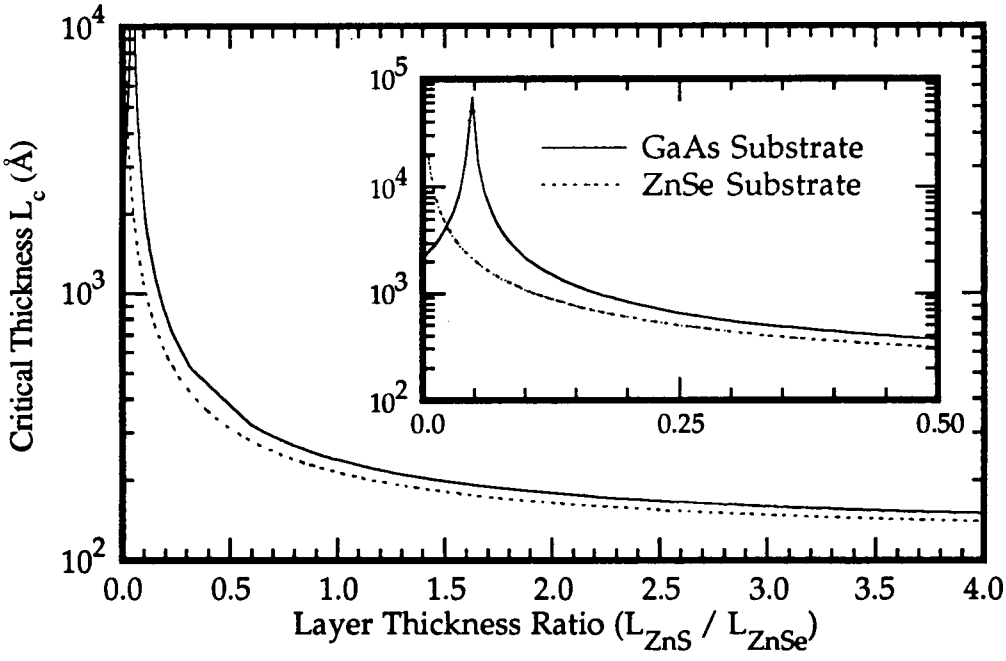

Figure 3-1 The relation between the critical thickness and layer thickness ratio for a ZnS-ZnSe SLS on a thick ZnSe buffer layer and on a GaAs substrate.

Parameters for $ZnSe_{1-x}S_x$-ZnSe SLS Construction

The critical thickness of the SLS can be increased if the ZnS cladding layers are replaced by $ZnSe_{1-x}S_x$ ternary alloy layers. However, it is desirable that the bandgap energy of the cladding layer material be about 300 meV higher than that of the active layer (Okuyama, 1992). This criterion is met for $x \geq 0.46$. The L_c for this alloy ($x = 0.46$) is ~30 nm when coherently strained with GaAs; thus, the range of interest for L" (L_{ZnSeS}/L_{ZnSe}) is $53 > L'' \geq 1/16$. Figure 3-2 shows the relation between the L_c and L" calculated for a $ZnSe_{0.54}S_{0.46}$-ZnSe SLS on a GaAs substrate. These calculations were made assuming a negligible difference between the thermal expansion coefficients for the SLS and underlying layer, and that the elastic constants scale linearly with composition. Lattice matching with GaAs occurs for $L'' = 1/8$; for $L'' = 0.5$, the L_c is ~110 nm, which is approximately 11 periods of $(ZnSe_{0.54}S_{0.46})_{\sim 6}$-$(ZnSe)_{\sim 12}$.

Other Criteria for SLS Construction

In a perfect SLS, there are no dislocations, interfaces are atomically sharp, and there is no compositional interdiffusion or disorder. As discussed above, the presence (or lack thereof) of dislocations is determined by the growth mode and by the thickness of the layers. The perfection of the interface also is determined by the growth mode, which affects the resulting smoothness of the surface and by interdiffusion.

In reality, of course, the growth surfaces and interfaces are not perfect, but have thickness fluctuations. In SLS, there are two types of thickness fluctuations. One is a variation in the layer-to-layer thickness; the other is a thickness fluctuation along a particular interface between two layers. The more obvious result of the layer-to-layer variation is that there will be different confinement energies (E_{con}) in layers of different thickness. In an infinitely deep well, the difference in E_{con} varies as L^{-3}, assuming that ΔL is independent of L (Weisbuch, 1981). Thus, the concern for the construction of SLS is the magnitude of these thickness fluctuations. For example, a change of only one unit cell (UC) in the interface of a 6 x 12 structure (i.e.,

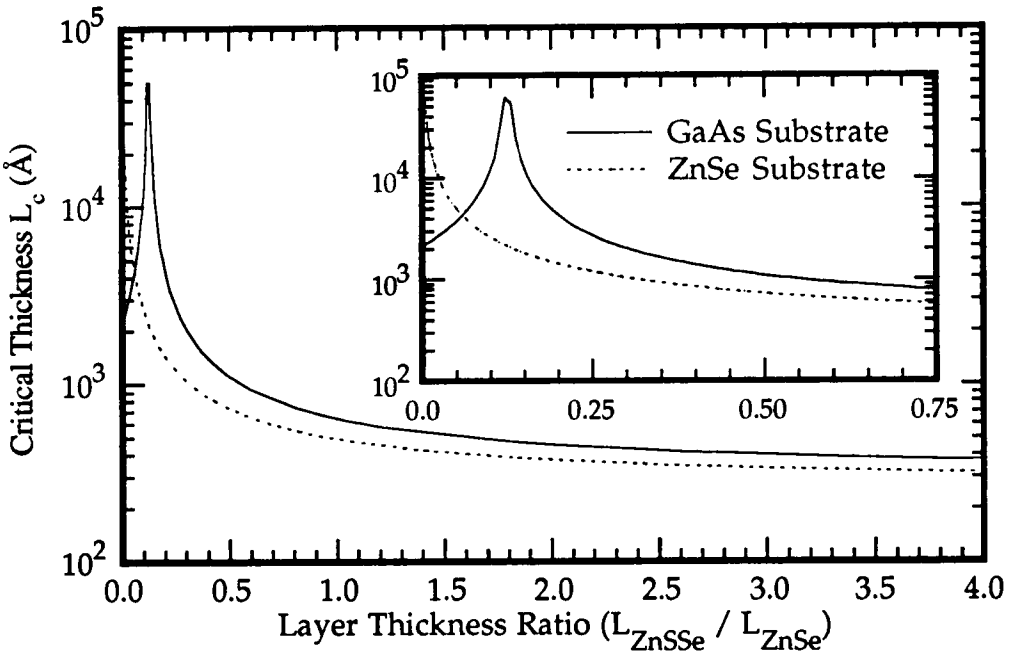

Figure 3-2 The relation between the critical thickness and layer thickness ratio for a $ZnSe_{0.54}S_{0.46}$-ZnSe SLS on a thick ZnSe buffer layer and on a GaAs substrate.

6 UC by 12 UC in each period) is a difference 8% in the well (ZnSe) layer thickness which corresponds to an ~22% change in the E_{con}. In the case of interface fluctuations, the primary concern is both the magnitude and distribution of these thickness variations. If the lateral width of these fluctuations is small on the scale of the exciton radius, each exciton will span several "islands", and the electron and hole confinement energies will be diminished due to the averaging of the thickness over the exciton wavefunction. The resulting variation in the energy of the exciton can be taken as the sum of the fluctuations in the electron and hole confinement energies (Weisbuch, 1981), with a corresponding shift and/or broadening in the exciton absorption and emission.

This "islanding" on the interface depends on the interfacial energy between the two materials. Therefore, the degree of interfacial fluctuation depends on the properties of the materials chosen for the heterostructure and the interaction between those materials. In addition, the interface morphology is determined by the growth mode. The mode of growth depends on several competing processes, including absorption, desorption, surface diffusion (mobility) and nucleation of 2-D or 3-D clusters. A common feature of all epitaxial growth techniques that produce smooth surfaces is the presence of high lateral surface mobility of the constituent atoms (Gossard, 1988). Because of this mobility, the atoms can migrate to lower regions on the growth surface, where there are more energetically favored bonding sites and where the atoms can form progressively smoother surfaces. In general, the kinetic energy (E_K) of these mobile atoms is supplied by the E_K of the incident atoms and the thermal energy of the substrate. Increasing the growth temperature is of limited benefit since high substrate temperatures result in increased diffusion across the interface and, thus, destruction of the sharp interface (Parbrook, 1992). Thus, for growth of a particular heterostructure at low substrate temperatures, the best way to control the interfacial morphology is by manipulating the E_K of the incident atoms. The minimum E_K needed is determined by the mobility required, while the maximum E_K is determined by the damage threshold of the film and substrate materials.

CHAPTER 4

STANDARD THIN FILM GROWTH TECHNIQUES

The three techniques most often used to grow ZnS, ZnSe and $ZnSe_{1-x}S_x$ thin films and superlattices are physical vapor transport (PVT), metalorganic chemical vapor deposition (MOCVD), and molecular beam epitaxy (MBE). Each technique is capable of producing high quality, single crystalline, epitaxial thin films on a variety of substrates, and each has a number of advantages as well as disadvantages. The order of review chosen is not only chronological, but also corresponds to increasing complexity, cost, and film quality.

Physical Vapor Transport (PVT)

Typically, PVT growth is carried out by placing solid ZnX (where X is S or Se) in a high temperature furnace, where it decomposes. A carrier gas, either H_2 or an inert gas (i.e., Ar) is passed over the ZnX and carries the Zn and X constituents to a heated substrate, where the reverse reaction occurs. In the presence of H_2, the group VI constituent reacts to form the group VI hydride (H_2X) which is transported to the substrate. These reactions are given by 4.01 for the inert gas carrier and 4.02 for the H_2 carrier (Lilley, 1978).

$$ZnX \leftrightarrows Zn + \tfrac{1}{2}X_2 \leftrightarrows ZnX \qquad 4.01$$

$$ZnX + H_2 \leftrightarrows Zn + H_2X \leftrightarrows ZnX + H_2 \qquad 4.02$$

Here, the leftmost side of the reaction occurs in the furnace, the rightmost side occurs at the substrate, and the middle takes place within the flowing carrier gas flow. These reactions require high growth temperatures of 500-900°C; defect complexes, which may act as carrier trapping centers, are formed at these temperatures. Further, the surface morphology of films

grown at these temperatures is poor. Although the morphology can be improved by adding indium (In) to the carrier gas (Fuke, 1986), the growth temperatures are still high (T > ~600°C). In addition, In is an n-type dopant; thus, this method cannot be used to fabricate p-n junctions. Recently Muranoi et al. (1990a) showed that p-type dopants can be incorporated into ZnSe films grown from elemental Zn and Se using H_2 (without In) as the carrier gas. They also showed that proper design of the reactor chamber can result in lower growth temperatures (Muranoi, 1990b). Although the electrical properties of these films were good, scanning electron microscopy (SEM) revealed that the surface morphology was still very poor. More recently, atmospheric pressure atomic layer epitaxy (ALE) has been used to grow both ZnSe (Koukitu, 1990) and ZnS (Koukitu, 1992) from metallic Zn and the group VI hydrides. X-ray diffraction (XRD) analysis showed that for a 500 nm thick ZnS film grown on GaP at 400°C, the full width at half maximum (FWHM) was ~300 arcsec, indicating that films grown at moderate temperatures by this method are of high crystalline quality. However, no information regarding the surface morphology was presented. Only one instance of ZnS-ZnSe superlattice growth by PVT has been reported (Kuwabara, 1985); the lack of success in fabricating superlattices by this method is perhaps due to diffusion across the interface, which occurs at high growth temperatures, and to the generally poor surface morphology. In addition, the self-activated defects in ZnSe films can only be avoided by using growth temperatures less than 400°C (Irvine, 1987).

Metalorganic Chemical Vapor Deposition (MOCVD)

Metalorganic precursors have been used to grow ZnS, ZnSe and $ZnSe_{1-x}S_x$ films at lower temperatures than PVT by the MOCVD technique (Stutius, 1982; Wright, 1989). As shown in Equations 4.03 and 4.04, this method proceeds via the reaction of a zinc alkyl (e.g., dimethyl- or diethylzinc) and either the chalcogen hydride (H_2X) or the chalcogen alkyl (e.g., dimethylsulfur or dimethylselenide).

$$R_2Zn + H_2X \leftrightarrows ZnX + 2R + H_2 \qquad 4.03$$

$$R_2Zn + R_2X + H_2 \leftrightarrows ZnX + 4R \qquad 4.04$$

Here R represents the alkyl group (e.g., usually ethyl or methyl). Experience to date with pyrolytic MOCVD (Kukimoto, 1991) shows that the principal problems with this approach are either premature reactions in systems using the chalcogen hydride or the high temperatures needed to promote the alkyl-alkyl reaction. The premature reaction can be suppressed by carrying out the hydride growth at low pressures (Stutius, 1981), and the temperature of the alkyl-alkyl reaction can be reduced by photoassisted growth (Fujita, 1988). In either case, the presence of an alkyl in the reaction poses an inherent problem of carbon incorporation in the film, which may result in film polycrystallinity and formation of carbon defect complexes (Giapis, 1990). Films produced by this method, however, are generally of high quality. Alkyl-alkyl sources and a growth temperature of 515°C recently were used to grow ZnSe-$ZnS_{0.18}Se_{0.82}$ superlattices having 50 Å layer thicknesses (Kuroda, 1992). Transmission electron microscopy (TEM) analysis of these structures showed abrupt heterointerfaces. Photocurrent spectra clearly showed the light-hole (LH) and heavy-hole (HH) free exciton (FE) peaks, and photoluminescence measurements showed the predicted blue shift of the HH peak as the well width was decreased.

However, as discussed in Chapter 2, the pressures used in MOCVD (~0.3 Torr) make p-type doping impossible with the N_2 radical plasma ($P \leq 10$ mTorr) technique. Other p-type dopants such as Li and Na have been tried. But, Li also can act as a donor if incorporated as an interstitial, while the binding energy of Na is too large for efficient doping (Isshiki, 1988; Hingerl, 1991). Thus, while high quality $ZnSe_{1-x}S_x$-ZnSe structures are easily grown and exhibit laser action when photopumped (Suemune, 1990; Dabbicco, 1992), there have been no reports of electrically driven lasing (p-n junction injection) in MOCVD-grown structures. To date, the

only reports of electrically driven lasing or of light emitting diode emission used MBE-grown material (Haase, 1991; Jeon, 1991; Ren, 1991).

Molecular Beam Epitaxy (MBE)

For those who can afford it, MBE is the technique of choice to grow ZnSe and $ZnSe_{1-x}S_x$ alloys at this time. In MBE growth, the molecular beams of the constituent species are generated from Knudson effusion cells. The evaporation crucibles in these cells usually have an internal diameter of 1-2 cm, and a length of 5-10 cm (Herman, 1986). For growth of III-V materials, these crucibles are generally made from either graphite or boron nitride (BN). However, ZnS and ZnSe films grown using BN crucibles have high resistivity (Yao, 1981); therefore, graphite crucibles are used exclusively for the growth of these materials. Thus, carbon (from graphite) can be unintentionally incorporated into the films using this technique. When the ZnX compound is used as the source material, the partial pressures of the gaseous species are controlled by the equilibrium constant for the reaction

$$2ZnX \leftrightarrows 2Zn + X_2 \qquad 4.05$$

The evaporated material passes through an orifice above the crucible into an ultrahigh vacuum (UHV) environment, generating the molecular beam. For the i^{th} component, the beam flux (J_i) at the substrate is given by (Yao, 1985)

$$J_i = 1.12\times10^{22}\, A\, P_i \left[\ell^4 MW_i\, T\right]^{-1/2} \cos(\theta) \qquad 4.06$$

Here, A is the area of the orifice (cm^2), P_i and MW_i are the partial pressure and molecular weight of the component, ℓ is the source-substrate distance (cm), T is the cell temperature (K) and θ is the angle between the substrate normal and the direction along the beam axis. A growth rate of ~1 $\mu m \cdot hr^{-1}$ requires Zn and chalcogen fluxes of $\sim 6 \times 10^{14}$ $cm^{-2} \cdot s^{-1}$. To obtain these

fluxes for ZnS and ZnSe, cell temperatures of 880°C and 830°C, respectively, are required (Yao, 1985). Because of the thermodynamic equilibrium within the cell, independent control of the constituent fluxes is not possible when a compound source is used. However, independent control is easily achieved by using Knudson cells with elemental sources (i.e., Zn and X). In this case, the partial pressures of the gaseous species are controlled by the equilibrium constants for the reactions given by

$$Zn(s) \leftrightarrows Zn(g) \qquad 4.07a$$

$$X(s) \leftrightarrows a_1X(g) + a_2X_2(g) + \ldots a_nX_n(g) \qquad 4.07b$$

As shown in Equation 4.07b, the vapor over the group II elements is composed of monoatomic molecules, with S_8 being the principal species above the S cell. The Se vapor contains, in descending order of concentration, Se_5, Se_2, Se_6, Se_7, Se_3 and Se_8 (Yao, 1985). For a growth rate of ~1.5 $\mu m \cdot hr^{-1}$, cell temperatures of 250°C and 350°C are needed for the Se and Zn cells (Yao, 1985). However, while growth of ZnS is possible using elemental S (Tomomura, 1990), its high vapor pressure make it unsuited for use in conventional Knudson cells (Konagai, 1992).

The ZnSe MBE growth process does not take place under thermal equilibrium, but is controlled by the kinetics of the adsorption, chemisorption, desorption and sublimation processes (Zhu, 1989, 1990). Although no comparable studies for the growth of ZnS have been reported, the similarity of the materials suggests that the same mechanisms control its growth process as well. This nonequilibrium growth under UHV conditions permits 2-D growth at initial growth temperatures as low as 250°C for ZnSe (Gaines, 1992) and 260°C for ZnS (Tomomura, 1990), with beam pressure ratios of $P_{Se}/P_{Zn} = 2$ and $P_S/P_{Zn} = 5$, respectively. Growth kinetics are affected (and possibly controlled) by the flux and kinetic energy (E_K) of the beams. (These two parameters are determined by the relation in 4.06.) For a given cell, they are not independent and the E_K of the beam cannot be changed without a corresponding change in the flux. The low temperatures required for evaporation of the elemental sources implies a

low E_K for the associated beams; this is perhaps the reason for the short surface diffusion length observed for Se (Λ~4.0 nm) on a ZnSe film during growth using elemental sources (Gaines, 1992).

$ZnSe_{1-x}S_x$ alloy thin films also have been grown by MBE using Zn, Se and ZnS as source materials (Matsumura, 1985). Using separate sources in this manner requires precise control of the relative fluxes (e.g., J_{Zn}/J_S, J_{Zn}/J_{Se}, and J_S/J_{Se}) for growth of the $ZnSe_{1-x}S_x$ alloy. Since the absolute flux from a particular cell is dependent on the temperature of that cell, and because the crucibles have a significant thermal mass (for temperature stability), growth of a superlattice containing alternating layers having two different alloy compositions is not trivial. Indeed, the only reports of superlattice growth by this technique are those for ZnSe-$ZnSe_{1-x}S_x$ structures with the ZnSSe alloy having a fixed composition (Shahzad, 1988, 1990). To date there have been no reports of $ZnSe_{1-x}S_x$-$ZnSe_{1-y}S_y$ structures grown by MBE.

CHAPTER 5

PULSED-LASER ABLATION: MECHANISMS

Pulsed-laser ablation (PLA) is conceptually quite simple, and the deposition of inorganic materials by this technique began to be studied shortly after the development of the pulsed ruby laser (Smith, 1965). By 1970, a full compliment of III-V semiconductor (GaP, GaAs, GaSb, and InAs) and II-VI semiconductor (ZnO, ZnS, ZnSe, ZnTe, CdS, CdSe, and CdTe) thin films had been grown (Ban, 1970). A pulsed ruby laser was used in this work, operating in the non-Q-switched mode, and capable of delivering 2.2 J output energy in a 500 μs pulse. Although the films were uniform and had the same composition as the target material (e.g., congruent evaporation), they also were polycrystalline and were not suited for electronic devices. A number of researchers also investigated the use of a CW laser (e.g., CO_2) as a heating source, but found that the thermal evaporation flux produced using the CW laser was not congruent (Ban, 1970).

The flexibility of the PLA technique was demonstrated as early as 1976 when multiple targets were used to grow superlattices (Gaponov, 1980 and references therein). However, PLA film growth did not become popular until the mid 1980's when it was (very) successfully used to grow thin, stoichiometric, epitaxial films of the high temperature superconducting (HT_c) oxides. Today, it is the technique of choice for deposition of the HT_c materials, as well as a wide range of other ceramic insulators, and is currently being evaluated by a number of groups for the growth of semiconductors.

PLA Process Description

As shown in Figure 5-1, the PLA system consists of one or more targets and a substrate heater mounted inside a vacuum chamber. Typically, the target and heater are rotated independently about the axes normal to their surfaces. The pulsed laser beam passes through a window

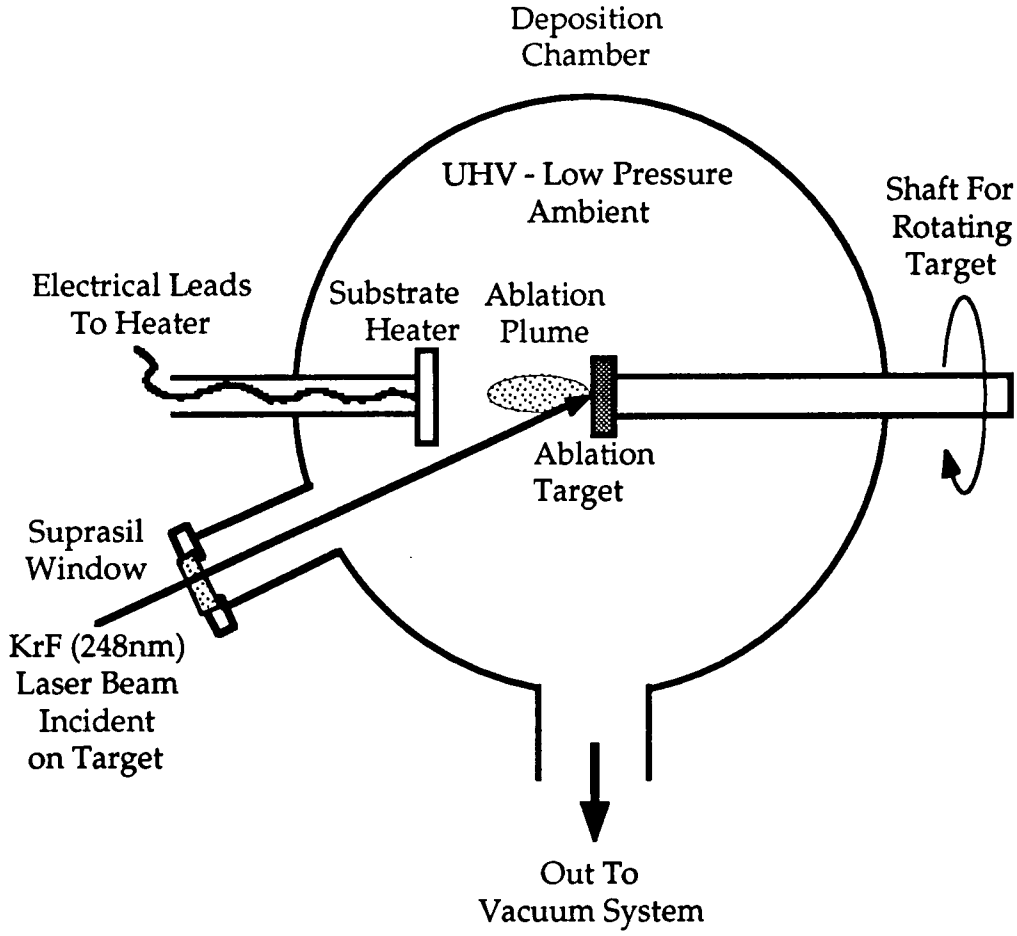

Figure 5-1 Schematic of the PLA process. Laser beam enters chamber from the left and strikes the target. Material is ablated from the target and is transported (plume) across the chamber to the substrates mounted on the heater.

and strikes the target. A lens, placed between the laser and the window, is used to focus the beam onto the target in order to control the laser energy density (E_ℓ) at the target surface. Above a critical E_ℓ the focused beam produces a high-velocity plasma directed normally away from the target surface. Upon reaching the substrate, this vapor condenses and forms a film. The film quality depends on a number of parameters including the growth temperature (T_g), the distance between the target and the substrate (D_{st}), E_ℓ, and the pressure and composition of the atmosphere present within the chamber (i.e., ~200 mTorr O_2 for the growth of $YBa_2Cu_3O_7$).

One feature of PLA is that all of these parameters can be controlled, though they are somewhat interdependent. This control is one advantage of the process since, for example, the last three parameters can be used to modify the composition and momentum of the ablated species before they strike the substrate. Unlike MBE, the range of ambient pressures within which PLA can be used is from UHV up to 1 Torr. This wide range of ambient gas density provides an easy way to control the E_K of the ablated species. Further, by manipulating the laser E_ℓ, the flux (and E_K) of the ablated material can be controlled with submonolayer precision. The low end of the range of useable E_ℓ is determined by the threshold E_ℓ required for plasma formation and congruent transfer of material. The upper end is limited by the optics used to focus the beam, or by the need to avoid target boiling that may result in "splashing" liquid drops of material. For oxide ceramics this range is from 1-6 $J \cdot cm^{-2}$, for metals from 5-10 $J \cdot cm^{-2}$, but for semiconductors appears to be somewhat lower, from ~0.1-0.2 $J \cdot cm^{-2}$ to perhaps several $J \cdot cm^{-2}$.

As implied above, there are two distinct E_ℓ regimes, defined by the composition of the beam of ablated material. The first regime is where the E_ℓ is only sufficient for thermal evaporation of the solid. When very little material is evaporated (i.e., < ~½ monolayer) no collisions occur in the vapor, and the behavior of the vapor leaving the surface is thermal (Kelly, 1988). For this effusive behavior, the flux from the surface is proportional to $\cos(\theta)$, where θ is measured from the target normal. For compound materials, this regime is marked by nonstoichiometric transport due to the differences in the vapor pressures of the constituent species. The second,

or ablation regime is marked by plasma formation as the material is heated further by absorption of the latter part of the laser pulse, resulting in ionization and plasma formation. This plasma contains electrons, as well as ground- and excited-state atoms and ions. The threshold E_ℓ (E_{th}) marks the beginning of the ablation regime and is the E_ℓ above which congruent transfer of material takes place (see Lowndes, 1993). The expansion of this high-pressure and high-temperature plasma away from the target surface is responsible for the directionality of the beam of ablated material.

Mechanisms for Ablation of Compound Semiconductors

For solid compounds, the successive processes that occur during ablation are lattice heating by the laser pulse, bond breaking, desorption (or ejection) of material from the target surface, further absorption of laser energy by atoms or molecules above the surface (resulting in plasma formation) and expansion of this material into the ambient. The understanding of the first three processes for ablation of compound semiconductors is incomplete at this time. However, a number of possible mechanisms have been proposed. The ablation of CdTe using photons having an energy less than the band gap appears to proceed by a multiphoton process (Cheung, 1992). Since multiphoton processes are very inefficient, a single photon process is clearly preferred.

Ablation of GaAs, GaP, GaN and CdS using photons with energies larger than the band gap is a single photon process and proceeds via the reaction (Ichige, 1988)

$$MX \xrightarrow{\hbar\nu} M + a_1X + a_2X_2 + \ldots a_nX_n \qquad 5.01$$

For these semiconductors, the extent of dimerization, trimerization, etc. of the nonmetallic component was found to depend somewhat on the fluence (i.e., E_ℓ). For CdS (E_g = 2.42 eV) irradiated with a N_2 laser ($\hbar\nu$ = 3.68 eV), the S monomer and dimer both were observed for E_ℓ as low as ~70 mJ·cm^{-2}, whereas the S_3 and S_4 species were not seen until E_ℓ = 133 mJ·cm^{-2} and E_ℓ = 147 mJ·cm^{-2}, respectively. Desorption of the Cd

monomer was observed to begin at E_ℓ = 133 mJ·cm^{-2}; however no dimers, trimers, etc. of this metallic component were observed at any fluence. For all E_ℓ, the principal nonmetallic species from CdS, GaP and GaN was the X_2 dimer molecule, but, for GaAs, the As monomer was the main anionic component. For GaAs, the ratio of dimer-to-monomer yields was found to be 0.5; this ratio was 2.0 for GaP, 4.0 for CdS and > 10 for GaN. The yield ratios would be expected to correlate with dimer bond strength, if dimer formation occurred in the vapor; however, this is not the case. For GaP, the formation of dimers was found to begin at a specific E_{th} and the dimer yield increased in a nonlinear manner with E_ℓ. Thus, the reaction (Equation 5.01) is clearly a non-equilibrium one, since, for an equilibrium thermal process, the relation between the yield and E_ℓ is expected to be linear and pass through the origin (E_{th} = 0). As shown in Figure 5-2, the E_{th} for semiconductors is found to correlate well with the Philip's ionicity (f_P). The f_P of ZnS and ZnSe is ~0.7; thus, the E_{th} for these materials is expected to be ~15 mJ·cm^{-2}. Further, it was observed that the mean energy (E_m) of the dimers from CdS and GaP increased rapidly for E_ℓ above the E_{th}, while the E_m of the As monomer from GaAs remained constant for E_ℓ above the E_{th} (Namiki, 1987). Finally, although the E_m for all the anionic species was in the thermal range, the distribution of the desorption flux of the S_2 dimer (from CdS) with respect to the polar angle (Namiki, 1986) showed significant deviation from that expected for collision-free thermal desorption.

Based on these observations, Namiki et al. (1987) postulated that the relationship between E_{th} and f_P shown in Figure 5-2 is associated with the stability of the tetrahedral structure. They noted that, if the bond breaking were due to local electronic excitation at the surface, the E_m of the dimers should be greater than 1 eV; they concluded that bond breaking must occur by a bulk phase transition. They proposed that this transition is induced by a dimerization interaction occurring in the dense e-h plasma that forms when the semiconductor is irradiated with photons having energies greater than the band gap. The electrons in this plasma reduce the bond charge, while the free holes induce the dimerization interaction between nearest neighbors on the nonmetallic sublattice; both of these actions

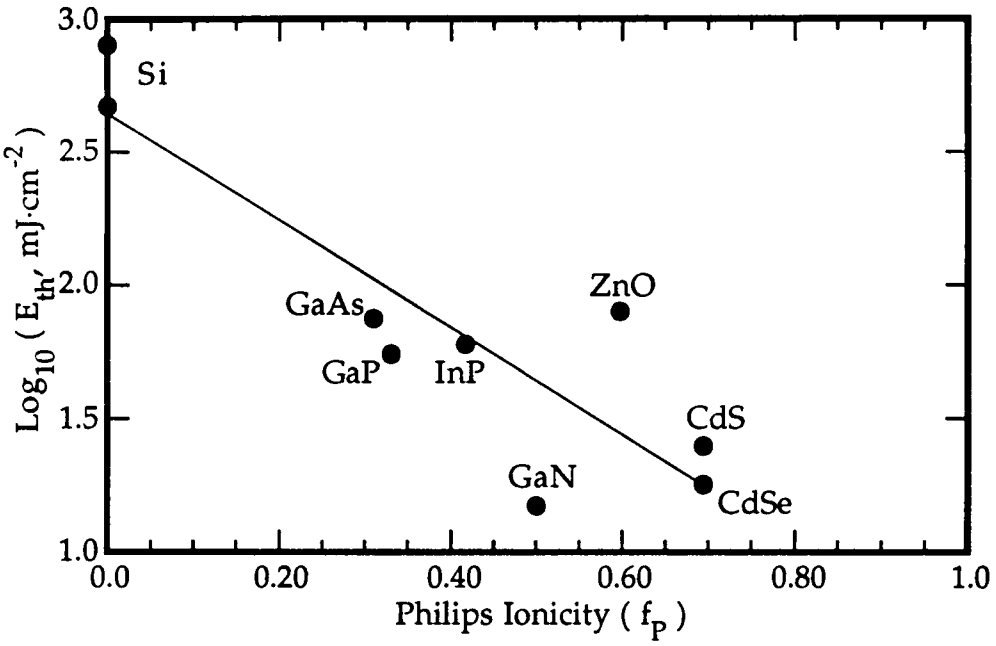

Figure 5-2 Threshold energy for ablation plotted against the Philip's ionicity for different semiconductors.

increase f_P. When f_P reaches a critical value (0.785), the tetrahedral structure becomes unstable. A first order phase transition occurs and it is during this phase transition that formation of dimers occurs. Finally, they speculated that the final phase is a liquid and that the desorption from this liquid proceeds via a thermal process.

The data of Namiki et al. also can be explained using the ablation model of Simpson and Williams (1991). This model was developed based on observations of the ion yield from ZnSe ablated using an ArF excimer laser ($\hbar\nu$ = 6.43 eV). Measurements of the ion yields were made by placing a stainless-steel collector in front of the target and measuring the current flow under various bias voltages. The first current flow was seen at E_ℓ = 90 mJ·cm^{-2}, which is substantially greater than predicted by the data in Figure 5-2. At this threshold, a single peak in the time-of-flight (TOF) ion trace was seen. As E_ℓ was increased an abrupt increase in ion yield, and the appearance of a second peak in the TOF trace, was seen at 210 mJ·cm^{-2}. This second peak appeared at about 2 μs longer delay time than the first peak at a target-collector distance of 2 cm. This longer delay time in the TOF spectrum indicates that the ions making up this second peak were ejected at a lower effective desorption temperature than those forming the first peak. Simpson and Williams concluded that the first peak observed was due to a thermal process, and second component was formed from another, more efficient process. They proposed that the second component is the result of the creation of sufficient e-h pairs at the material surface to result in the collapse of the covalent bonding, followed by rapid vaporization at a lattice temperature lower than the melting point. In this model, Simpson and Williams assumed disintegration of the surface layer occurred when ~35% of the lattice bonds were broken. Their calculations indicated that, at the E_ℓ = 210 mJ·cm^{-2} threshold, this occurred within the first 5 ns of the pulse. A final result from this work was the observation of the deposition of dustlike particulates when the collector was negatively biased. When the collector was positively biased, however, a specular deposit was seen. Thus, it was shown that it is possible to select various plume components for deposition by imposing a biasing potential on the plume.

The primary differences between the models proposed by Simpson and by Namiki is the localization of the electronic excitation and whether the disintegration of the lattice occurs via a thermal or electronic process. Namiki proposed that the bond breaking must be due to a bulk interaction and that the desorption was a thermal process. On the other hand, Simpson notes that the optical absorption of ZnSe is quite high at this wavelength and that the laser is efficiently coupled to the solid in the near-surface region. Further, a number of transitions are available (i.e., X, Δ and Σ edges) which result in photocarriers that have excess kinetic energies in the range 0.1-1.0 eV. Simpson proposed that it is these photocarriers, localized near the surface, which constitute the e-h plasma and cause the bond breaking. Although this is a local electronic excitation at the surface, since the E_K of the carriers is less than 1 eV, the vaporized material also would have an E_m less than 1 eV as observed by Namiki.

The E_ℓ ranges in the studies of Simpson and Namiki overlap only slightly and it is likely that separate mechanisms were being observed in the two different E_ℓ ranges. In the region of lower E_ℓ, the ablation mechanism is dominated by a non-equilibrium thermal desorption process, while in the upper region it is dominated by a non-equilibrium nonthermal desorption process. This two-mechanism model agrees with the observation that the velocity distribution of Zn neutrals, ejected during laser irradiation of ZnS, is well fit by a Maxwell-Boltzmann (MB) function for $E_\ell = \leq 80$ mJ·cm^{-2} (Arlinghaus, 1989) while for dimer desorption, deviation of the velocity distribution from the Maxwellian is observed for E_ℓ = 50-250 mJ·cm^{-2} (Namiki, 1987). Arlinghaus found that the temperatures determined from the MB fits and the yield of Zn neutrals both scaled linearly with the inverse of the target temperature and the inverse of E_ℓ. These observations indicate that an equilibrium thermal process is responsible for desorption of the Zn species from ZnS for $E_\ell = \leq 60$ mJ·cm^{-2}. Above $E_\ell = \sim 60$ mJ·cm^{-2}, however, both the temperature and yield increasingly deviated from the linear relation as E_ℓ was increased. Likewise, the deviation from MB behavior seen by Namiki was small at E_ℓ = 50 mJ·cm^{-2}, increased as the E_ℓ was increased from 50-125 mJ·cm^{-2}, and remained constant at larger E_ℓ. Therefore, it appears that for both ZnSe and

ZnS the transition of the ablation mechanism from a purely thermal desorption process to a nonthermal one occurs in the range E_ℓ = 50-125 mJ·cm^{-2}.

As E_ℓ is increased into this nonthermal ablation regime, plasma formation occurs in the vaporized species above the target surface and is usually easily visible. The laser beam interacts with this plasma, and if the density of free electrons is high enough, the beam is fully absorbed in the plasma via the inverse Bremmstrahlung process. When this occurs, the target is shielded from the rest of the laser pulse. Although this has been studied for the PLA of HT_c oxides, no detailed investigations of the plasma-formation process have been reported for the ablation of compound semiconductors.

While the models of Simpson and Namiki provide arguments to describe the observed data, there are several fundamental problems with the data and with the assumptions made in the models. Examination of the negative species TOF by Simpson (1991) showed a wide distribution of velocities, suggesting that a flux of particles having an equivalently wide mass range was present. Although this is consistent with polymerization of the anionic species, Simpson's model is based entirely on the behavior of the Zn ions and polymerization of the anions is not considered. Further, the bond-breaking mechanism used to explain the appearance of the second peak occurs on a ps timescale. This timescale is not consistent with the μs delay seen in the TOF data. On the other hand, the dimer yields reported by Namiki were measured using a quadrupole mass spectrometer (QMS). In the QMS, it is implicitly assumed that each species has a single charge (e.g., X^{1+}) and determination of a particular species depends only on the mass of that species. This ignores the possibility that multiply charged species (e.g., X^{2+}) may be present. Since the charges are quantized, dimer and trimer species with multiply charges exhibit the same response as the monomer species assumed to be present (e.g., X_2^{2+} gives the same response as X_1^{1+}). It is also possible that the ionization source potential of the QMS acts in a manner similar to the biasing of the collector in the work of Simson, and that a number of desorbed species were not examined. Finally, while the mechanisms proposed by both Namiki and Simpson can

explain the high translational energy (E_T) of the species desorbing along the surface normal, they explain neither the angular dependence of the flux and E_T nor the non-Maxwellian velocity distribution of the ablated species.

Ablation Plume Distribution During Expansion

Kelly and Dreyfus (1988b) observed that the temperatures (determined from the TOF data of Namiki) for species desorbed along the axis normal to the target surface and those measured at oblique polar angles ($\theta = 60°$) differed by a factor of as much as 4.5. Further, they noted (from the same data) that the flux distribution was consistent with an angular distribution approaching $\cos(\theta)$ at low fluences (i.e., near E_{th}), while at higher fluences ($E_\ell = 250$ mJ·cm^{-2}) the distribution was close to $\cos^4(\theta)$. A number of different ablation studies have shown similar non-equilibrium angular distributions, which suggests a common mechanism for the non-Maxwellian velocity and angular distributions (NoorBatcha, 1988). In investigating this effect, Kelley and Dreyfus (1988a) showed that when transport of the vapor species from the surface is not collision-free, a Maxwellian distribution of the velocities is valid only for the initially emitted particles at the target surface (e.g., $x = 0$). Moreover, Monte Carlo simulations of rapid desorption of D_2 from W (NoorBatcha, 1987), and of NO from an LiF surface (NoorBatcha, 1988) showed that the simulated angular dependence of the flux and temperature agreed with the experimental data only when collisions were considered in the calculations. Additional information is gained by calculating the Knudson number ($\mathcal{K}_0$), which is the ratio of the species mean free path to the diameter of the source (in this case, the laser spot). For an effusive (i.e., thermal) source $\mathcal{K}_0 >> 1$, indicating the vaporized species are initially in free molecular flow and undergo no velocity-changing collisions. However, for laser vaporization, $\mathcal{K}_0 << 1$, which is also the case for a supersonic molecular-beam source. In this regime, the expanding material can be treated as a continuum fluid undergoing adiabatic expansion (Saenger, 1991). Thus, the rapid desorption process that occurs in laser ablation is similar to a supersonic expansion in which collisions of the particles

convert the random thermal (Maxwellian) motion of the ejected species into directed motion along the surface normal (NoorBatcha, 1988). The result is that the ablated flux is forward peaked, and scales as $\cos^n(\theta)$. When only the collisions in the Knudson layer are considered, Kelley (1989) has shown $n = 4$. However, for S_2 desorption from CdS (Namiki, 1986), the angular dependence scales as $\cos^{25}(\theta)$. Kelly (1988b, 1989) showed that this behavior ($n >> 4$) is due to numerous collisions resulting from desorption of as little as ~½ monolayer, and resulting in the formation of a Knudson layer. An initially unsteady adiabatic expansion then evolves into a free expansion of the vaporized species.

CHAPTER 6

PULSED-LASER ABLATION:THIN FILM GROWTH

Plume Expansion and Film Uniformity

One potential advantage of PLA is that there is less waste of rare or expensive source materials because the beam is strongly forward-directed due to the $\cos^n(\theta)$ distribution (Lowndes, 1993). However, a stationary point-like focus of the laser beam onto the target surface results in nonuniform films. A related problem is that of texturing and coning of the target surface (Dubowski, 1988). This occurs when the laser beam strikes the same area repeatedly and from the same direction. This change in surface morphology results in a decrease in ablation flux, a tilt in the direction of maximum flux away from the target normal (usually toward the direction of the laser beam), and an increase in the number of large particles ejected (Lowndes, 1993).

Several techniques, all of which rely on modifying the ablation geometry, have been developed to exploit this forward peaking in order to deposit large-area uniform films and to reduce coning. Lowndes et al. (1990), brought the laser beam to a line focus on the target using a cylindrical lens, and then translated the lens in a direction perpendicular to the line. This moved the focussed spot across the target and "painted" the substrate with the ablation plume (Figure 6-1, top). The relative orientation and position of the target surface with respect to the incident laser beam was changed by rotating the target. This reduced the formation of cones and their effect on the plume. However, this rotation does not affect the deposition geometry, relative to the substrate. Using this "painting" technique, Norton et al. (1989) were able to grow large area (~5 cm x ~2.5 cm) HT_c films. Control of the film uniformity was such that single-unit-cell layers and superlattices were easily grown (Norton, 1991). Ideally, the area of film uniformity is determined by the length of the focussed spot and the size of the target. From a practical standpoint however, the length of the vertically line-focussed spot is limited by the

laser beam height and the benefit of the larger area of uniform deposition must be weighed against the increased capital cost. Further, large targets of expensive materials can result in high operating costs which may make the process uneconomical.

Dietsch et al. (1993) made use of the fact that the ablation flux is greatest along the axis normal to the target surface and that the surface normal of a cylinder spans 360°. By focussing the laser beam onto the side of a cylindrical target and moving the target perpendicular to the beam direction, the plume axis was made to scan across the substrate surface (Figure 6-1, middle). To achieve better uniformity, horizontal motion of the substrate also was incorporated. Using this system, thin C and Ni films and C-Ni multilayers were grown. Coverage of 6.0 cm diameter Si substrates was achieved with 68.6 nm thick C films having thickness deviations of ~1%, as determined by ellipsometric measurements. Transmission electron microscopy (TEM) showed that the interface roughness of a 20 period Ni(2.5 nm)-C(3.25 nm) multilayer was less than 0.2 nm, and that the standard deviation of the Ni layer thickness was ~0.1 nm. Although a spot focus was used in this work, a line focus could be used to increase the width of the uniform-thickness area. Once again this will depend on the laser beam height and on target size and cost.

Another geometry, utilizing precessional motion of the target axis, is shown in Figure 6-1 (bottom). Here the target is tilted such that the target normal, and consequently the plume, sweeps out a conical volume as the target is rotated. By adjusting the angle of the target and the target-to-substrate distance, the area of uniform film deposition can be controlled. One difficulty with this technique is the target tilt adjustment, combined with the target rotation. Further, the operating window (e.g., optimal energy density) must be such that the Knudson layer strongly controls the plume expansion. It has been found (McCamy, this work) that for ablation of ZnS at low energy densities, small target tilt angles (i.e., $< \sim 10°$) are insufficient to result in significant "sweeping" of the plume and thus, do not yield good thickness uniformity. At this time, no other attempts to use this geometry have been reported.

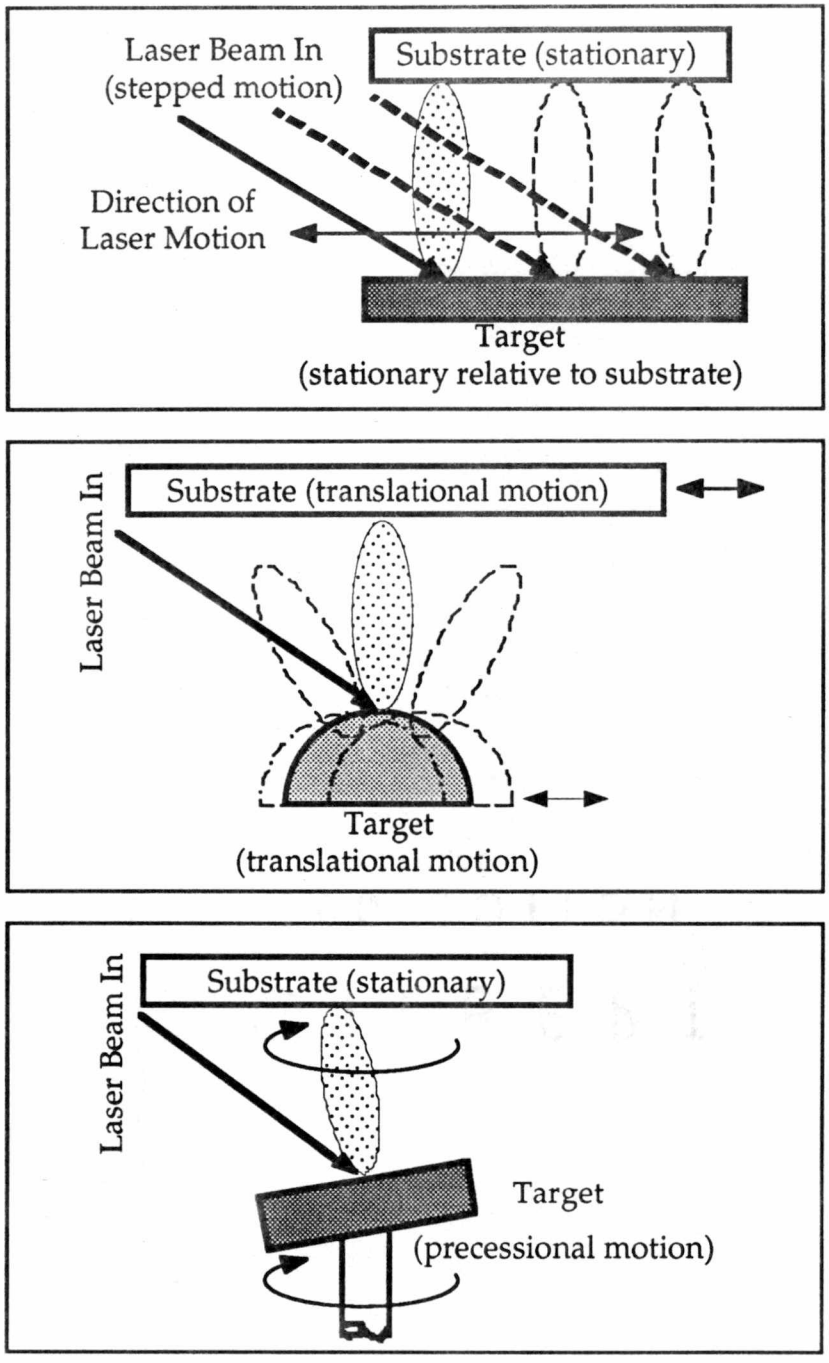

Figure 6-1 Various PLA deposition geometries. PLA deposition geometry of Lowndes et al., (top), Dietsch et al., (middle) and tilted target, precessional axis geometry (bottom). See text for discussion of each.

A third technique is based on an offset geometry that was originally described by Dubkov (1982) and has since been developed independently by several other groups (McCamy, 1992, Lowndes, 1993 and references therein). In this instance, the laser spot is offset from the rotational centerline of the substrate and moves (relative to the substrate) in a circle relative to the substrate centerline. (The target is also rotated about its centerline to reduce texturing of the target surface, but this does not affect the deposition geometry.) The relative motion of the plume and substrate is realized either by rotating the substrate heater about its centerline and thereby scanning the plume over it (McCamy, 1992), or by using an external rotating mirror to scan the laser beam in a circular path on the target surface (Lowndes, 1993). To maintain equivalent geometries, the center of the beam scan also must be the centerline of the substrate. Figure 6-2 shows this geometry, where the laser spot (S) is offset from the centerline by a distance ρ. Since the laser is pulsed, there will be a discrete set of laser spots (S_i) whose angular separation is $2\pi i/N$, where N is the number of laser pulses per revolution and $i = 1,2...N$. Dubkov (1982) showed that if $N \geq 6$, this set of discrete points is equivalent to an annular ring source. For an annular source, the thickness (L) at a fixed point (P) on the substrate can be written (see Appendix 1)

$$L = 2\left(\int_0^{\pi}\left[J_0\{1+\frac{R^2+\rho^2}{D^2}-\frac{2R\rho}{D^2}\cos(\phi)\}^{-n/2}\right]d\phi\right) \qquad 6.01$$

Here, n is the coefficient describing the angular distribution of the plume (i.e., $\cos^n(\theta)$) and J_0 is the flux from a single laser pulse. Figure 6-3 shows the thickness profile ($x = 0$) of a film calculated using Equation 6.01, with $n = 10$, $D = 5$, for various offsets, ρ. It illustrates that, for fixed D and n, the thickness profile depends on the radius of the annular ring (laser spot offset). For a given flux distribution, there is an optimal D/ρ ratio that depends only on the coefficient n (see Appendix 1). For $6 \leq n \leq 26$, the relation between the distribution coefficient and the optimal ratio is described by Equation 6.02.

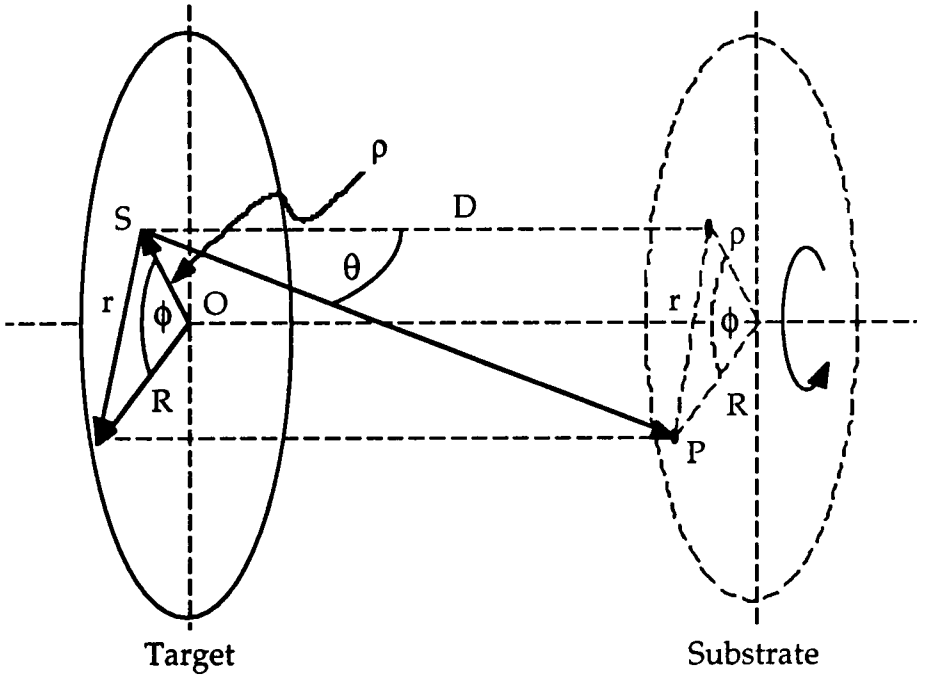

Figure 6-2 Offset-source ablation geometry. The laser beam strikes target at S; ρ is the offset distance from the target centerline axis normal, D is the distance between target and substrate, and θ is the angle between the normal at B and the displacement vector $\vec{SP}$. Equivalent relations are shown on the substrate surface.

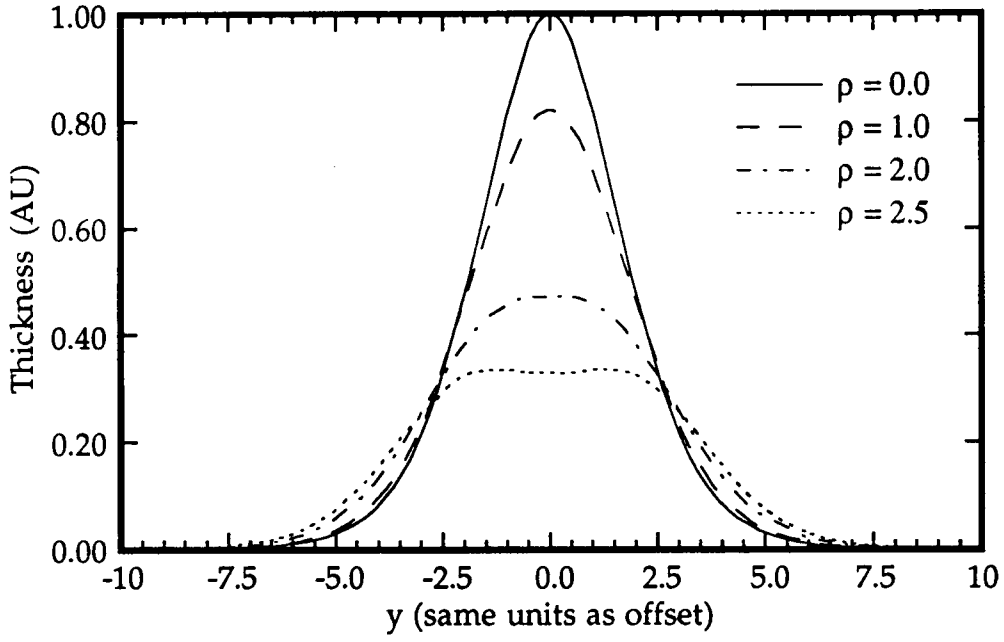

Figure 6-3 Thickness profiles for n = 10, target-substrate separation fixed at D = 5, and various offset distances (ρ) from the rotational centerline.

$$\left(\frac{D}{\rho}\right)_{opt} = 0.658\, n^{0.51} \qquad 6.02$$

Using this relation, the optimal offset for a given target-substrate separation can be determined. As an example, for n = 10, the optimal ratio is $(D/\rho)_{opt} = 2.13$. Using these values, Figure 6-4 illustrates that the area of uniformity spans a diameter only slightly less than 2ρ and, thus scales with D^2. Since the only limitations on D are the chamber size or attenuation of the plume by collisions with ambient gas, scaleup using this geometry is simple and inexpensive, relative to the cost of a larger laser. A further advantage is that a full disk of source material is not required to deposit large-area uniform-thickness films, since only an annular area is irradiated. Thus, the amount of source material (and the associated operating cost) is greatly reduced.

As noted earlier, a tightly focussed beam will result in coning. This effect can be neutralized if the beam direction is reversed (relative to the target surface) before it strikes the target again. This occurs automatically if the beam is scanned around the target and the target is simultaneously rotated so that the target has moved 180° before the laser strikes the same point on the target (Lowndes, 1993). Another method of doing this is to offset the target rotational centerline from that of the substrate heater by an appropriate distance, and then use a line focus that is centered on the rotational axis of the target. Finally, if the line focus has significant width, the target need not be offset and the geometry in Figure 6-2 can still be used. In this case, the irradiated region is struck by the laser beam from several directions and the coning effect is reduced (though not necessarily eliminated). If the line focus is used, the optimal ratio, $(D/\rho)_{opt}$, can be determined empirically.

The calculated profiles in Figure 6-4 have been normalized and, for a given number of shots, the actual thickness of course decreases as D is increased. Depending on the ablation characteristics of the material being deposited, this too can be an advantage. If the single-shot flux is too great at the desired energy density and a particular D, this rate can be decreased by

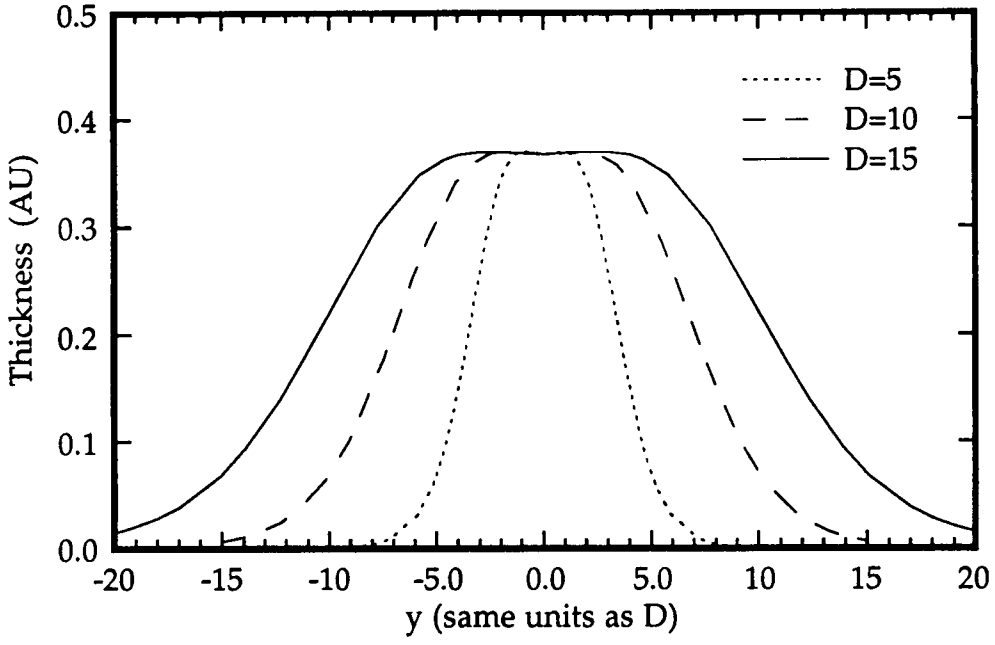

Figure 6-4 Thickness profile for n = 10, $D/\rho = (D/\rho)_{opt} = 2.125$ for various target-substrate separations (D).

increasing D. Since the ablated material transport and film growth occurs on a short time scale (<< ms), the laser repetition rate can be increased to raise and optimize the overall deposition rate. This ability to reduce the single-shot deposition rate by simply increasing D also permits control of the layer thickness with submonolayer and sub-unit cell precision. It also may be a method of controlling the initial film-growth mode.

Film Growth Modes During PLA

The mode of film growth depends on a number of competing processes, including absorption, desorption, surface diffusion (mobility) and nucleation of 2-D or 3-D clusters. For 2-D growth, high lateral surface mobility of the constituent atoms is required so that the deposited atoms can migrate to regions which have more energetically favored bonding sites, allowing progressively smoother surfaces to form. Since this process depends not only on the mobility of the incident species, but also on the time available for migration and the amount of material which must be redistributed, the deposition rate is inherently a factor determining the growth mode.

For most growth techniques (Chapter 4), the processes of adsorption, desorption, diffusion, and nucleation occur concurrently with the deposition of material. Further, for most techniques, the deposition rate is such that a supersaturated condition is maintained at the growth surface at all times. This is not the case for PLA growth. PLA deposition involves short periods of very high supersaturations, separated by long time intervals with no deposition flux. For example, a high but still typical deposition rate for PLA is on the order of ~1 unit cell per laser shot (an average growth rate of ~2 $\mu m \cdot hr^{-1}$ for a 1 Hz laser pulse rate). Based on the negative and positive ion TOF data for ablation of ZnSe in the nonthermal ablation regime (i.e., E_ℓ > ~100 $mJ \cdot cm^{-2}$; Simpson, 1991), the time scale for the arrival of material at the surface is 5-25 μs, which corresponds to a deposition flux in the range J ~ 10^{19}-10^{20} $cm^{-1} \cdot s^{-1}$. Further, the translational kinetic energy, determined from a Maxwell-Boltzmann fit to this same

data, is $E_K \sim 5$ eV. The pressure at the surface due to this impinging material can be estimated from

$$P = J[2\pi m k T]^{1/2} \quad , \qquad 6.03$$

where m is the mass of the impinging atoms (in this case taken to be Zn), and k is Boltzmann's constant. From this, the pressure during the deposition pulse is in the range P ~ 1-10 Torr. The time interval separating each pulse is ~10^5 times larger than the deposition interval, and it is during this period that the diffusion and desorption processes occur. For comparison, the standard growth rate for MBE is ~1 $\mu m \cdot hr^{-1}$, which corresponds to a flux of $J \sim 5 \times 10^{14}$ $cm^{-1} \cdot s^{-1}$. MBE beams are thermal (i.e., $E_K \sim 0.05$ eV), and the estimated pressure is $P \sim 10^{-6}$ Torr. Although 2-D MBE growth of ZnSe and ZnS is observed (Gaines, 1992; Tomomura, 1990), it is not immediately obvious that 2-D PLA growth can occur under conditions of ~1 unit cell deposited per laser pulse. However, the relatively large E_K (i.e., > 1 eV) would be expected to promote increased surface diffusion (i.e., higher mobility). In addition, if the desorption energies of the film constituents are significantly different, the relative long time interval between deposition periods should result in preferential desorption of one constituent and preferential coverage by the other constituent. As a consequence, if the deposition rate is reduced to ~ 1 monolayer or less per laser pulse, then the growth mechanism should be similar to that of 2-D MBE, which is dependent on the absorption and sublimation processes (Zhu, 1990).

The only reports of the growth mode during PLA of compound semiconductors were by Dubowski et al. (1989, 1990). In the earlier work, reflection high-energy electron diffraction (RHEED) measurements, carried out during Nd:YAG laser ($E_\ell \leq$ ~90 $mJ \cdot cm^{-2}$, 1 kHz) growth of CdTe on GaAs, showed elongated streaks which indicated 2-D growth. However, for several reasons, the 'ablation' mechanism appears to be thermal (i.e., a desorptive process), and the deposition conditions were not far removed from those for MBE growth. First, the photon energy of the laser

(E = 1.17 eV) is less than the bandgap (E_g = 1.56 eV) of CdTe. Second, the energy density used was less than the reported threshold for CdTe irradiated at this wavelength (E_{th} = ~2 J·cm^{-2}; Dubowski, 1988), and, for E_ℓ < ~100 mJ·cm^{-2}, very few electrons or ions are produced (Dubowski, 1986). Finally, under these conditions the deposition rate was ~ 0.002 nm per laser pulse which corresponds to a flux of J ~ 10^{16} cm^{-2}·s^{-1}. Assuming a thermal E_K for the vaporized species, the resulting pressure is P ~ 10^{-5} torr. All of these conditions point to a thermal-type deposition. In the more recent work, Dubowski et al. also reported streaky RHEED patterns during the growth of $Cd_{1-x}Mn_xTe$ using Nd:YAG and XeCl lasers (Dubowski, 1990). While the photon energy of the XeCl laser (4.03 eV) was greater than the bandgap of the $Cd_{0.93}Mn_{0.07}Te$ target, the energy density was not reported and the deposition rate was still small (~ 0.004 nm per laser pulse). Thus, while these reports are encouraging, they do not present conclusive evidence of 2-D growth in the pure PLA deposition regime.

Alloying PLA II-VI Films

Two different methods have been reported for PLA growth semiconductor thin films having ternary alloy composition. The first and most obvious method involves growth from a target having the same (or approximately the same) composition as the desired film. Dubowski (1990) used this technique to grow $Cd_{1-x}Mn_xTe$ thin films and CdTe-$Cd_{1-x}Mn_xTe$ superlattice structures on InSb and $Cd_{0.955}Zn_{0.045}Te$ substrates. A series of samples, grown from a $Cd_{0.93}Mn_{0.07}Te$ target at temperatures in the range T_g = 200-240°C, showed that the Cd content increased from x = 0.096 to x = 0.114 as the temperature was increased. The alloy films grown by this method were epitaxial and of high crystalline quality, as indicated by the (004) x-ray rocking curve (FWHM = 45 arcsec) from a 1 μm thick $Cd_{0.89}Mn_{0.11}Te$ film on the $Cd_{0.955}Zn_{0.045}Te$ substrate.

This method also was used by Aydinli and Compaan (1993) to grow ternary thin films of $Cd_{1-x}Zn_xTe$ and $ZnSe_xTe_{1-x}$ on GaAs substrates These films were grown using a frequency doubled Nd:YAG laser, the energy densities used were in the range E_ℓ = 2.0-2.5 J·cm^{-2}, and the growth

temperature was $T_g = 300°C$. Analysis of $Cd_{1-x}Zn_xTe$ films grown from targets with x = 0.85, 0.72, 0.60, 0.35 and 0.10, showed that the resulting film compositions were x = 0.80, 0.63, 0.51, 0.26 and 0.08 respectively, while analysis of $ZnSe_xTe_{1-x}$ films grown from targets with x = 0.25, 0.50 and 0.75, showed that the resulting film compositions were x = 0.29, 0.57 and 0.85 respectively.

These results show that the primary difficulties with this method are the difference between the film and target compositions, and the temperature dependence of this difference. At this time, neither an explanation nor a solution has been reported for either of these. Another difficulty with this technique is that it is not possible to grade continuously the film composition. Continuous grading is desired in order to construct novel devices by bandgap engineering, i.e., by grading or modulating the semiconductor energy bandgap.

The second technique for growing II-VI semiconductor alloy thin films was developed by Cheung (1987) and was used to grow $Hg_{1-x}Cd_xTe$ films on CdTe substrates at a $T_g = 180°C$. This method involved ablating a CdTe target with a Q-switched Nd:YAG laser in the presence of constant-fluence Te and Hg beams from Knudson cells. By varying the laser repetition rate, the Cd content in the films could be controlled in a continuous manner. The control was such that films were grown with smoothly graded or abruptly modulated, predesigned composition profiles. Indeed, this technique was used to fabricate films containing sawtooth superlattices and other nonrectangular quantum wells, as well as a single film having a sinusoidal structure, a rectangular barrier, and two linear ramps with different heights (Cheung, 1988). While this technique works well to control Cd content in an otherwise conventional $Hg_{1-x}Cd_xTe$ MBE growth system, it does not appear well suited for growing $ZnSe_{1-x}S_x$ alloys. It is not known whether the Knudson cell(s) will work properly given the high vapor pressure of the more volatile chalcogen elements. Furthermore, the advantage of PLA is its flexibility in quickly changing targets. The large thermal mass of the Knudson cells clearly reduces this advantage and their presence increases the capital cost enormously.

CHAPTER 7

EXPERIMENTAL EQUIPMENT AND FILM ANALYSIS TECHNIQUES

All equipment and facilities discussed were designed by the author. The chamber was fabricated by MDC Vacuum Products Corporation, Hayward, CA. The substrate heater and target holders were fabricated at the Oak Ridge National Laboratory, Oak Ridge, TN. The drawings included in this chapter are intended to convey the design and function of the equipment only. While the scale is indicated on each diagram, they should not be considered precise engineering drawings.

Although the main topics of this chapter are the equipment and film analysis techniques used in this work, a number of experimental results are included as well. This was done to maintain continuity and, in some cases, to provide the rationale for various procedures and equipment designs. Several of the analytic methods are not discussed in detail because they are well known (e.g., x-ray diffractometry), while less well known techniques are treated more fully (e.g., *in situ* thickness measurements, spectral ellipsometry, and Rutherford backscattering spectrometry).

Deposition System and Experiments: Design Criteria

Because there were no reports of previous attempts to grow epitaxial ZnS and ZnSe thin films by pulsed-laser ablation, the deposition system was designed to allow various deposition geometries to be used. Two key variables considered during the design process to maintain flexibility were the substrate-target separation distance and the orientation of the substrate and target (i.e., vertical or horizontal). Since the preferred geometry was not known, an excessive number of excimer and probe laser ports also were incorporated. Since the necessary ambient (i.e., vacuum, inert gas, etc.) was not known, the vacuum and gas supply systems were designed to permit control at ambient pressures from 10^{-7} Torr up to several Torr. Finally, the optical system used to focus the pulsed excimer laser beam was designed to provide a broad range of laser fluences at the target surface.

The experiments conducted were designed to evaluate the pulsed-laser ablation (PLA) process for the growth of wide bandgap II-VI thin films, in comparison with more established techniques (see Chapter 4). The suitability of PLA for epitaxial ZnS and ZnSe thin film growth was evaluated quantitatively by determining the structural, optical and electronic properties of the films and comparing them with literature values for those grown by other techniques, primarily MBE and MOCVD. PLA's capability to grow uniform thin films, as well as epitaxial multilayers and strained layer superlattices, also was evaluated. Finally, a new technique for growing alloyed and doped films, by controlling the partial pressure of an ambient gas in the chamber during growth was discovered and investigated.

Deposition Chamber

The thin film samples were grown in a 14" diameter spherical stainless steel deposition chamber. The horizontal cross-section of this chamber is shown in Figure 7-1. The interior of the chamber was electro-chemically polished by the manufacturer to provide a smooth, non-porous surface and to remove any organic residue remaining from the fabrication process.

A series of six large (main) and sixteen small (probe) ports allowed probe and excimer laser access into the chamber. Their sizes and access allocations are given in Table 7-1. To permit *in-situ* reflectivity monitoring of film thickness during growth, the centerline of each probe port was set at a 25° angle from the nearest main port and passed through the center of the chamber. Eight ports were set in the horizontal plane, and eight were set in the vertical plane, that passed through the front and rear main ports. The position and orientation, relative to the corresponding plane, was the same for both set of ports.

Windows mounted on o-ring seals were used to transmit the excimer and probe laser beams while maintaining vacuum/ambient gas conditions within the chamber. The windows for the probe laser and viewports were made of fused silica (90% transmission to $\lambda \sim 300$ nm), while those for the excimer laser were made from Suprasil II (90% transmission to

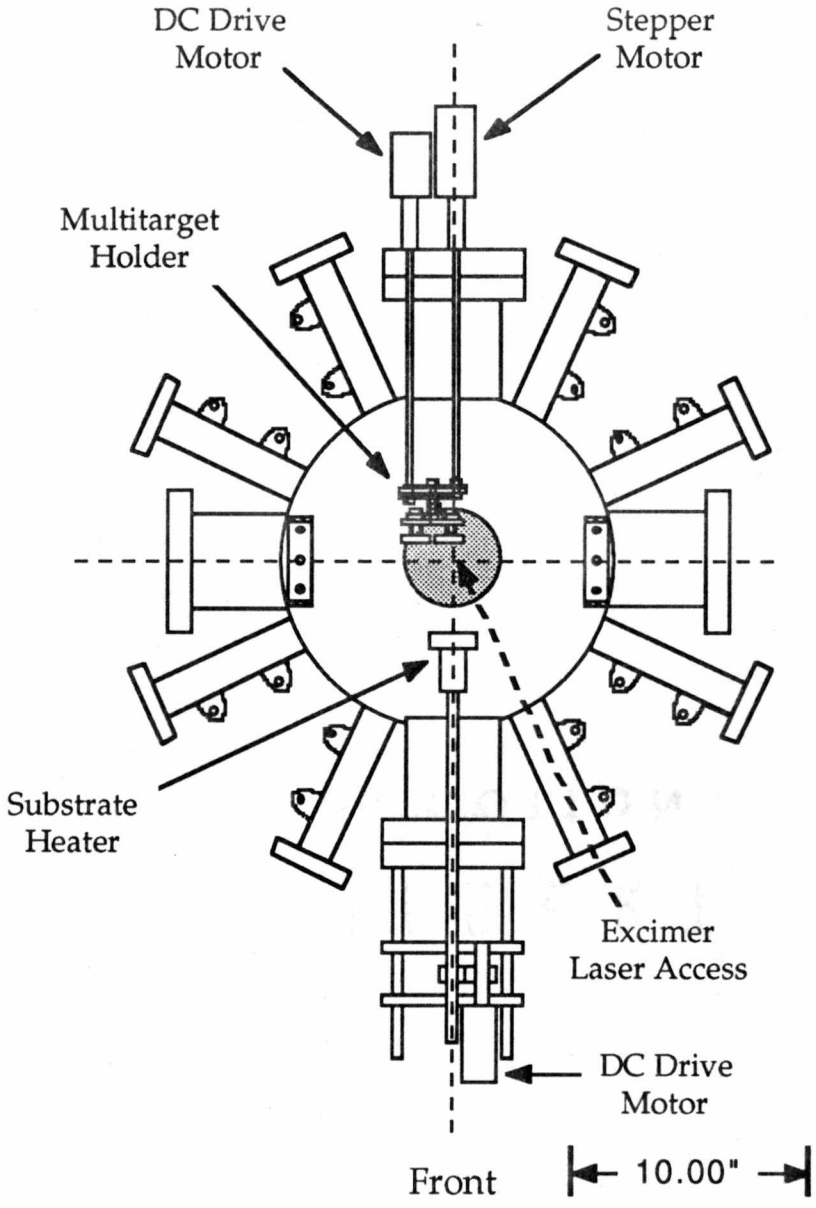

Figure 7-1 Horizontal cross-section of the pulsed-laser ablation deposition chamber and location of the substrate heater and multitarget holder.

Table 7-1
Port Allocations for II-VI Pulsed-Laser Ablation Chamber

Port and Location	Allocation
Main, Front	Substrate Heater
Main, Rear	Multitarget Holder
Main, Bottom	Single Target Holder and UHP N_2 Inlet
Main, Top	Viewport and Excimer Laser Access for Bottom Target
Main, Left (facing chamber front)	Shutter
Main, Right (facing chamber front)	To Vacuum System Through Turbomolecular Pump and Flow-Control Valve
Probe, Front-Right	Excimer Laser Access
Probe, Rear (all)	HeNe Laser Probe Access
Probe, Left-Rear	Gas Inlet (from gas manifold)
Probe, all others	Viewports or Blanked Off

Port Sizes and Connections

Main 4.01" OD x 3.810" ID x 5.25", connected through a 6" rotatable Conflat™ flange

Probe 1.51" OD x 1.375" ID x 12.00" 3-3/8", connected through a non-rotatable Conflat™ flange.

to $\lambda < \sim 190$ nm). Thin films of ablated material were unintentionally deposited on these windows during growth. Although the region struck by the excimer laser beam on the Suprasil II window appeared free of this deposition, this window was cleaned between deposition runs in an ultrasonic bath containing a 1:3 mixture of concentrated HCl and distilled, deionized H_2O. In addition, after ~10 cleaning treatments, this window was refurbished by polishing with 1 μm optical polishing compound.

Target Holders

Two different target holders were designed and constructed. The first held only one target and was used during the growth of the ZnS and ZnSe films. The second target holder was capable of holding up to three targets and was used during the growth of ZnS-ZnSe multilayers and alloys. In both cases the targets were rotated during growth to reduce coning of the target surface. Although several mounting orientations were possible, in all experiments the target holder was mounted on the rear flange and the substrate heater assembly was mounted on the front flange, such that the rotational centerlines of the ablation target and heater were coincident. The positions of both target holders along the front-rear centerline could be adjusted to aid alignment of the laser beam on the target surface.

The unique feature of the single target holder was the ability to tilt the target under vacuum conditions. This was done so that, by oscillating the target during growth, the plume could be made to "paint" the substrate surface in order to grow uniform films. Figure 7-2 shows that tilting of the target was achieved by mounting a bearing race onto the front plate of a Newport vacuum-compatible optical mount. The rod holding the 1.00" ID Zn target mount was passed through this bearing race and connected to a rotational drive shaft with a vacuum compatible U-joint. The drive shaft was driven by a DC motor attached to a UHV rotational feedthrough mounted on the rear flange. A second shaft was connected to a similar feedthrough. The rotational motion of this second shaft was converted to linear motion via a screw assembly at the corner of the support plate (Figure 7-2). As a result the target face could be tilted by ±10° from the

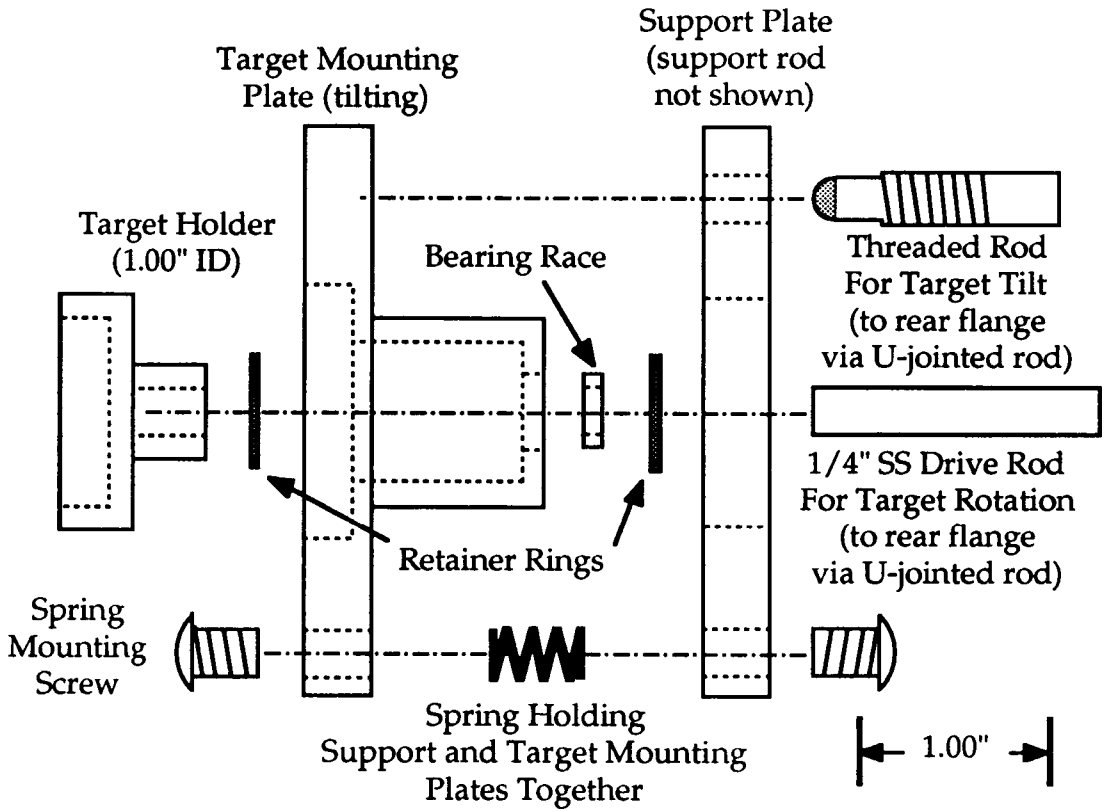

Figure 7-2 Single target holder for II-VI pulsed laser ablation chamber. Mounting plate assembly constructed from modified optical mount, Newport model number MM-2A-VC.

rotational centerline while rotation was maintained. When the multitarget holder was installed, this single-target holder was moved to the main port on the bottom of the chamber, and the laser beam was directed through the top port to ablate dopant-atom targets.

The multitarget holder design is shown in Figure 7-3; it allows *in vacuo* target selection and rotation. The holder was supported from the rear flange by three stainless steel rods (not shown in Figure 7-3). Three 1.00" diameter Zn target mounts were connected to spur gears by rods mounted in bearings in the front plate. To reduce contamination due to the redeposition of ablated material, a thin aluminum plate covered the two targets which were not in use. A stepper motor (mounted on the rear flange and connected using a rotary UHV feedthrough) was used to rotate the front plate; it ensured precise and repeatable positioning of the targets. The rotation of the separate targets (during growth) was driven (through an UHV feedthrough) by a DC motor mounted on the rear flange. The rotary motion of this motor was coupled to the target spur gears through an idler gear. This design allowed the motions associated with target selection and rotation to take place independently and without interference.

Targets

The ablation targets used in this work were solid, polycrystalline ZnS (99.999+% purity, 99+% density) and ZnSe (99.999+% purity, 99+% density) that were purchased from Angstrom Sciences (Pittsburgh, PA). Both were 2.54 cm diameter x 0.318 cm thick and each target face was finished with a smooth, fine-ground surface finish. The ZnS and ZnSe compounds were grown using the $Zn+H_2S$ and $Zn+H_2Se$ reactions. As a result, both targets were carbon-free. Impurities present in these targets were quantitatively determined by the vendor using inductively coupled plasma (ICP) analysis. The results of these analyses are presented in Tables 7-2 and 7-3. The major impurities in the ZnS and ZnSe were Ca (0.09 ppm, 0.25 ppm respectively), Cd (0.07 ppm, 0.09 ppm) and Cu (0.45 ppm, 0.08 ppm). As is discussed in Chapter 2, Cu is a source of electronic defect levels in both ZnS and ZnSe.

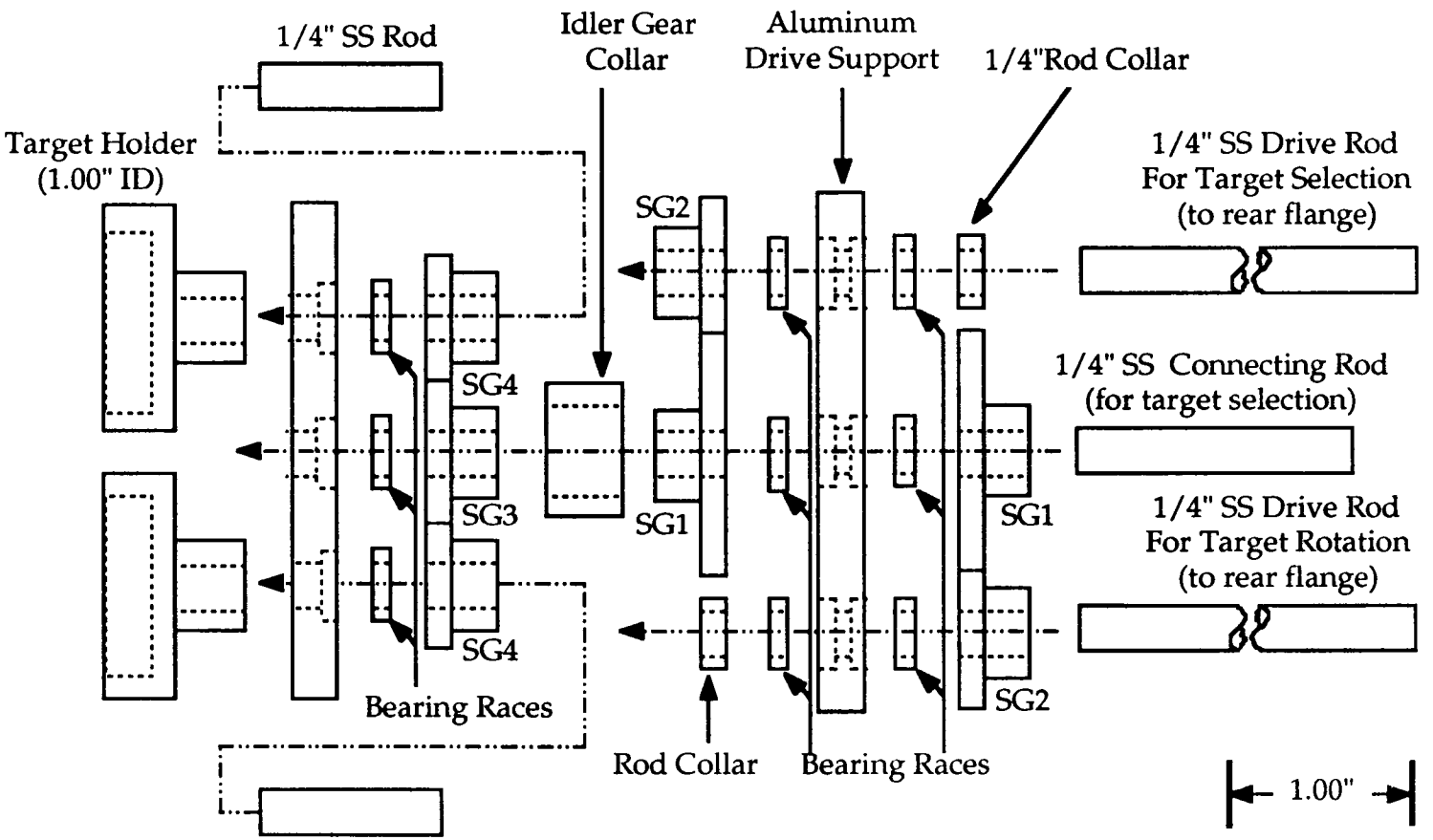

Figure 7-3 Multitarget Holder, target drive is via spur gears (SG), where

SG1: 48 pitch, 1.500" PD SG2: 48 pitch, 1.000" PD

SG3: 48 pitch, 0.833" PD SG4: 48 pitch, 0.666" PD

Table 7-2

Actual Chemical Analysis for the ZnSe Ablation Target

(< indicates concentration was less than instrumental resolution)

Element	Concentration (ppm)	Element	Concentration (ppm)
Ag	< 0.02	Na	< 0.02
Al	< 0.02	Nb	< 0.04
As	< 0.2	Nd	< 0.05
Au	< 0.08	Ni	< 0.02
B	< 0.02	Os	< 0.2
Ba	0.003	P	< 0.02
Be	< 0.02	Pb	< 0.02
Bi	< 0.2	Pd	< 0.02
Ca	0.09	Pr	< 0.06
Cd	0.07	Pt	< 0.2
Ce	< 0.3	Rb	< 0.2
Co	< 0.02	S	
Cr	< 0.02	Sb	< 0.5
Cs	< 2	Sc	< 0.004
Cu	0.45	Se	< 0.5
Fe	< 0.02	Si	< 0.04
Ga	< 0.03	Sm	< 0.04
Gd	< 0.07	Sn	< 0.02
Ge	< 0.05	Sr	< 0.003
Hg	< 0.2	Ta	< 0.1
In	< 0.04	Tb	< 0.06
K	< 0.02	Te	< 0.5
Li	< 0.02	Ti	< 0.02
Mg	< 0.002	Tl	< 0.03
Mn	< 0.02	W	< 0.2
Mo	< 0.04	Y	< 0.02
Ir	< 0.2	Zr	< 0.04

Table 7-3

Actual Chemical Analysis for the ZnSe Ablation Target

(< indicates concentration was less than instrumental resolution)

Element	Concentration (ppm)	Element	Concentration (ppm)
Ag	< 0.02	Na	< 0.02
Al	< 0.02	Nb	< 0.04
As	< 0.02	Nd	< 0.05
Au	< 0.08	Ni	< 0.02
B	< 0.02	Os	< 0.2
Ba	< 0.003	P	< 0.02
Be	< 0.02	Pb	< 0.02
Bi	< 0.2	Pd	< 0.02
Ca	0.25	Pr	< 0.06
Cd	0.09	Pt	< 0.2
Ce	< 0.3	Rb	< 0.2
Co	< 0.02	S	< 5
Cr	< 0.02	Sb	< 0.5
Cs	< 2	Sc	< 0.004
Cu	0.08	Se	
Fe	< 0.02	Si	0.04
Ga	< 0.03	Sm	< 0.04
Gd	< 0.07	Sn	< 0.02
Ge	< 0.05	Sr	< 0.003
Hg	< 0.2	Ta	< 0.1
In	< 0.04	Tb	< 0.06
K	< 0.02	Te	< 0.5
Li	< 0.02	Ti	< 0.02
Mg	0.006	Tl	< 0.03
Mn	< 0.02	W	< 0.2
Mo	< 0.04	Y	< 0.02
Ir	< 0.2	Zr	< 0.04

However, for impurity concentrations this small, no published data were found in which the number of defect levels was quantitatively related to the impurity concentration.

Substrate Heater Assembly

Figure 7-4 shows the substrate heater assembly. This assembly consisted of a modified Tayco (Long Beach, CA) spiral heater brazed onto a metal-to-glass seal (for electrical isolation of the heater face), which then was welded onto a hollow 1/2" diameter shaft. The heater face was 2.00" diameter and fabricated from 316 stainless steel. To ensure uniform temperature across the heater face, the heater wire was wound in two spiral layers and brazed onto the back of the heater face plate. The maximum design temperature of this heater was 1000°C. The temperature of the heater face was measured using a chromel-alumel (Cr-Al) thermocouple in contact with the (back) center of the heater plate.

Following construction, the heater was calibrated by attaching nine 7 mm x 7 mm Si squares onto the heater face and directly measuring their temperatures using an IRCON™ pyrometer. For consistency, the method for attaching these Si samples was the same as that used to attach the other substrates. In addition, these squares were similar in size to the substrates used later. In the temperature range T = 400-700°C, the average measured Si temperatures were consistently larger than those measured by the thermocouple. The maximum observed deviation between a single Si sample and the TC was 9°C at 450°C, while the average error increased monotonically from 0.6% at 400°C to 1.0% at 700°C. Because the magnitude of the average errors was small, the temperatures reported in this work are those measured by the thermocouple.

The heater assembly rotation was driven by a DC motor connected through two spur gears. The heater assembly typically was rotated at 4.8 revolutions per minute. The electrical connections to the heater were isolated from the chamber by passing the power and thermocouple leads down the center of the rotating shaft. Electrical power was supplied to the heater by a programmable, 1000 W Hewlett-Packard DC power supply. Contact to the heater leads was maintained during rotation via a split-ring

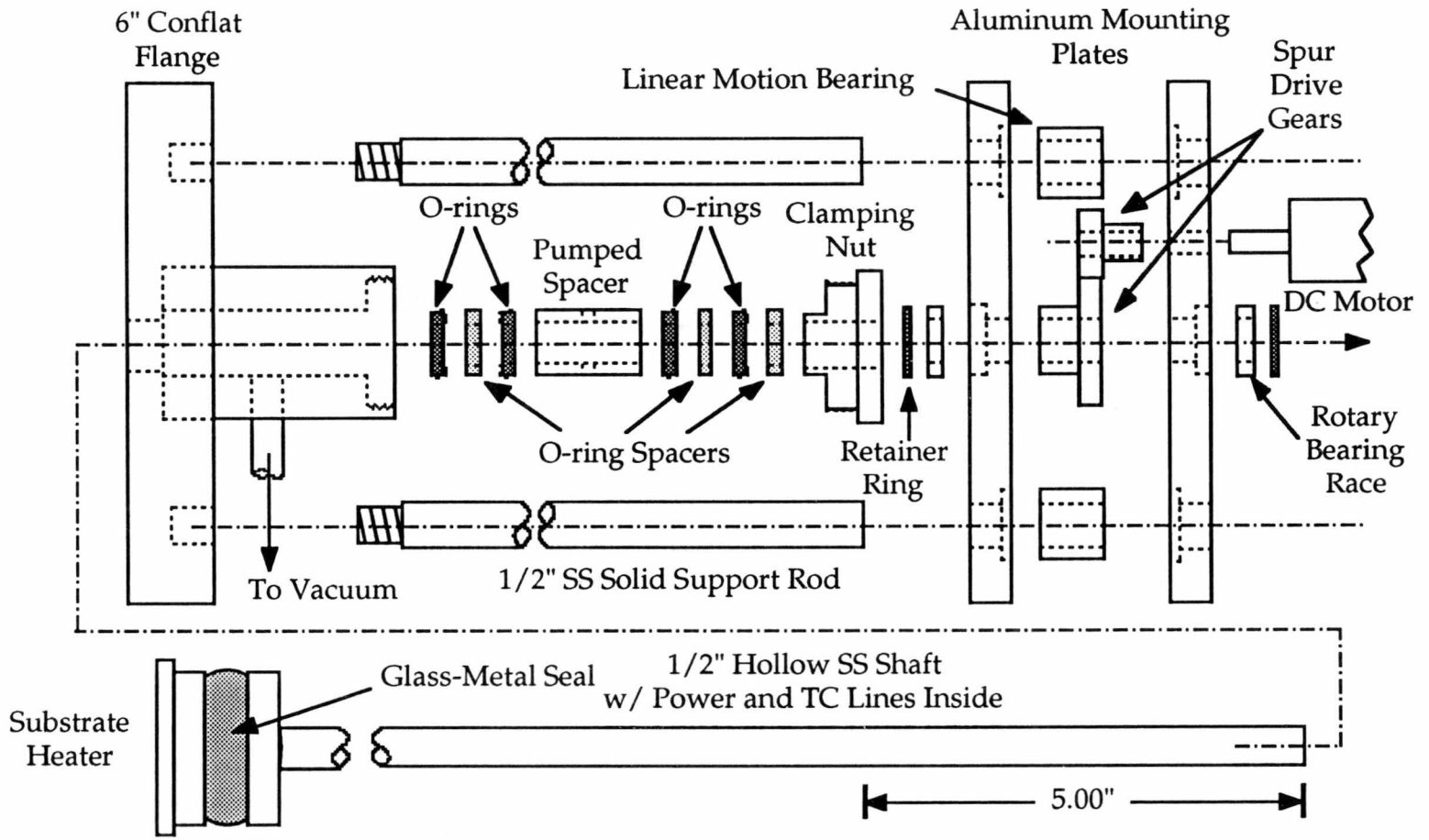

Figure 7-4 Rotating substrate heater for II-VI pulsed-laser ablation deposition chamber.

assembly fitted with spring loaded graphite bushings. A Barber-Coleman temperature controller was used to regulate the power supply; the thermocouple feedback connection to the temperature controller was maintained during rotation using an Omega thermocouple slip-ring assembly mounted axially on the end of the heater shaft. The drive motor and bushing assembly was mounted on two plates supported by four stainless steel rods attached to the front flange. These rods passed through linear motion bearings attached to the mounting plates. This design allowed the position of heater face (and consequently, the substrate-target separation) to be easily and precisely adjusted.

Systematic evaluation of the film-thickness uniformity provided by the offset-rotation deposition geometry required accuracy in both rotational and linear motions of the heater. To permit both motions while still maintaining the integrity of the vacuum, a Wilson seal was incorporated into the heater assembly design. This seal was made by passing the shaft through two sets of o-rings (Figure 7-4). These were separated by a spacer section which was connected to the low vacuum system (typically ~10^{-2} Torr during growth), so that any air leaking past the outside o-ring set would be evacuated before reaching the chamber interior.

Vacuum System

Evacuation of the deposition chamber was accomplished by an Alcatel two-stage, rotary vane pump (roughing pump) with at a free air displacement of 7.5 $\ell \cdot s^{-1}$ and an ultimate pressure of 4×10^{-4} Torr. A base pressure (without bake out) of 2×10^{-7} Torr was achieved using a Balzers TPU-170 turbomolecular pump. Both pumps were prepared for corrosive service (halogen gases, etc.). The roughing pump was operated at a constant speed, while the speed of the turbomolecular pump could be controlled using an electronic drive unit.

Ambient Gas Pressure and Composition Control

The composition of the deposition ambient was controlled using the gas manifold system shown in Figure 7-5. Three 10 sccm Vacuum General

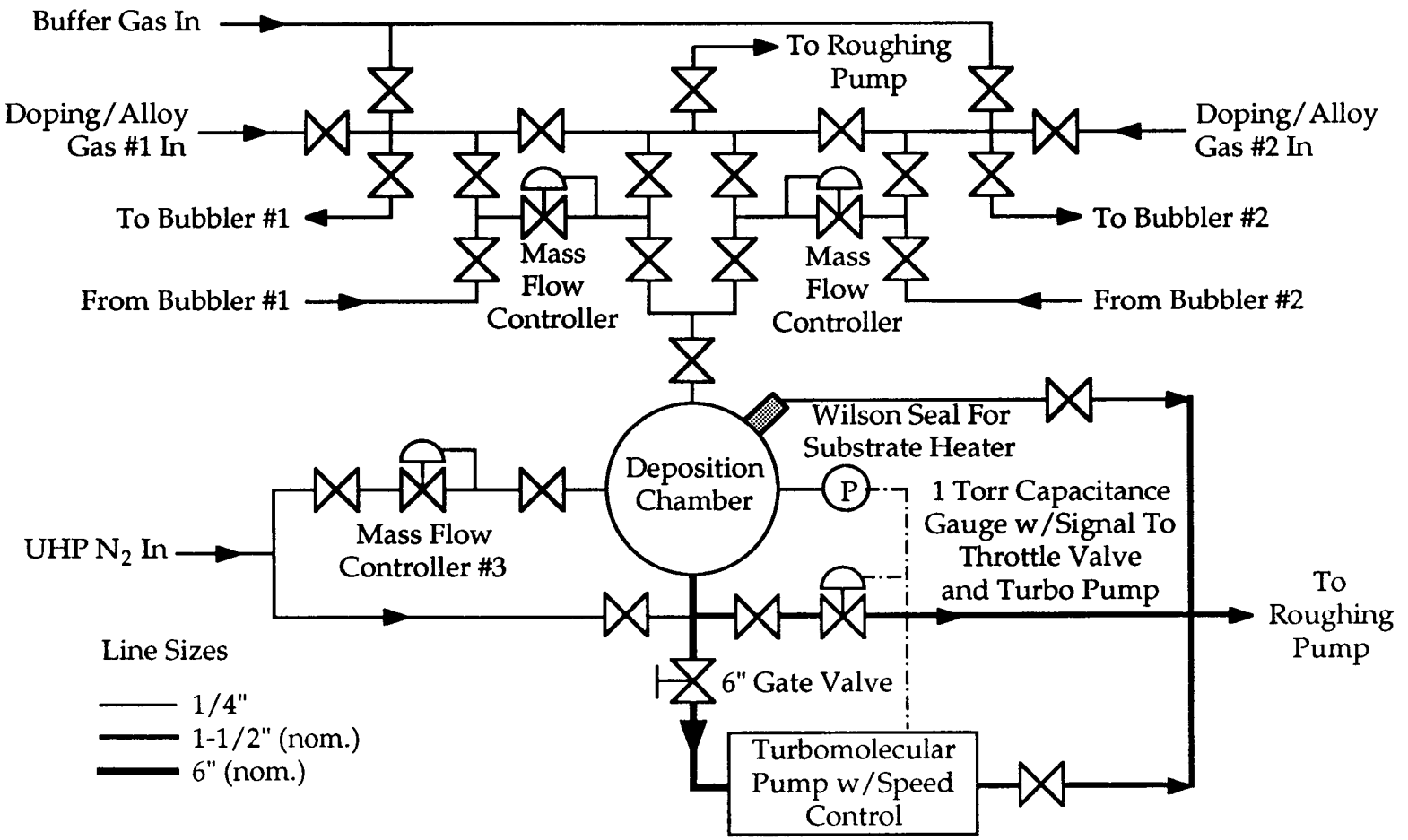

Figure 7-5 Schematic of the gas flow and vacuum system for the II-VI PLA deposition system.

mass flow controllers (MFCs) were used to regulate the gas flowrate(s) into the chamber. The advertised accuracy of these MFCs was ±2% of flow; however, stable operation was found to be difficult below ~0.3 sccm. Typically, the flowrate was stabilized by flowing the gas into the low-vacuum side of the vacuum system. Once stable flow had been established, the gas flow was quickly switched into the chamber. The ambient pressure then was regulated by controlling the flowrate out of the chamber. For pressures < ~2×10^{-3} Torr, this was done by directing the flow through the turbomolecular pump and controlling the pump speed. For pressures > 2×10^{-3} Torr, the flow was directed through an MKS variable-impedance throttle valve. In both cases, the pressure feedback signal to the controllers was provided by an MKS high accuracy (0.12% of absolute reading) 1 Torr capacitance pressure gauge. Using this system, the ambient pressure was controlled easily in the range P = 10^{-4} - 10^{-1} Torr.

As many as three different gases could be introduced into the chamber simultaneously. However, the buffer gas in all experiments was ultrahigh purity (UHP) He. The concentration of the alloying and doping gases was controlled by regulating the ambient pressure and the relative (alloy:buffer or doping:buffer) gas flowrates. Without adding any buffer gas, the range of partial pressures of the alloying or doping gas was P = 10^{-4} - 10^{-1} Torr. Dilution of the alloying or doping gas, by adding buffer gas to the flow allowed the lower end of this range to be extended. Thus, the full range of alloying and doping gas partial pressures was P = 10^{-5} - 10^{-1} Torr.

Following every run, all gas flow was stopped and the chamber was isolated from the vacuum system. UHP N_2 then was used to purge the chamber and equalize the chamber and atmospheric pressures. Whenever the chamber was opened, a continuous flow of UHP N_2 was used to reduce contamination of the chamber interior.

Excimer Laser and Beam-Handling Optics

A model 2640 Questek excimer laser was used to ablate the target materials. A KrF (λ = 248 nm) gas mixture and stable resonator optics were used. In this mixture, He (not Ne) was used as the buffer gas, consequently, the laser pulse width (FWHM) was ~35 ns. The output beam energy was

typically in the range 0.4-0.6 J per laser pulse depending on the condition of the gas mixture and the electrode voltage. The desired beam energy could be programmed by the operator; the beam energy then was monitored internally and the electrode voltage adjusted automatically to maintain the desired energy.

The beam path between the laser and the ablation targets is shown schematically in Figure 7-6. A beam block (not shown in Figure 7-6) was located between the laser and the turning prism. The turning prism was offset horizontally such that only a portion of the laser beam struck the prism and was directed vertically. The remainder of the beam traveled unimpeded past the prism. During most experiments the vertical beam was blocked between the prism and aperture #2. This beam block was removed only during experiments involving ablation of the solid doping target.

The energy passing through aperture #1 was measured using a Scientec energy meter placed between the aperture and the laser access window. Typically this energy was in the range 0.08-0.13 J. All the optical components were made from UV-grade fused silica (transmissivity = 90% at 248 nm), thus, the energy striking the target surface was reduced 10% for every component in the beam path. The energy density (E_ℓ) at the target surface was controlled by varying the beam area striking the target surface with a focusing lens; this area typically was in the range 0.10-0.35 cm^2. Because this cylindrical lens was oriented with its curved cross-section vertical, only the width of the beam changed with lens-target separation. This had the advantage that E_ℓ varied linearly with the lens position. Thus, an E_ℓ in the range E_ℓ = 0.2-1.0 $J \cdot cm^{-2}$ could easily be selected. The lower end of this range could be extended by placing tilted quartz plates in the beam path. Each every plate reflected ~10% of the energy out of the beam, so the lower end of this range was limited only by the number of plates available. The lowest energy density investigated was E_ℓ = 0.1 $J \cdot cm^{-2}$. By moving the target holder to the limit of its travel and careful conditioning the laser and its gas mixture, the upper end of the E_ℓ range could be extended to 1.5 $J \cdot cm^{-2}$.

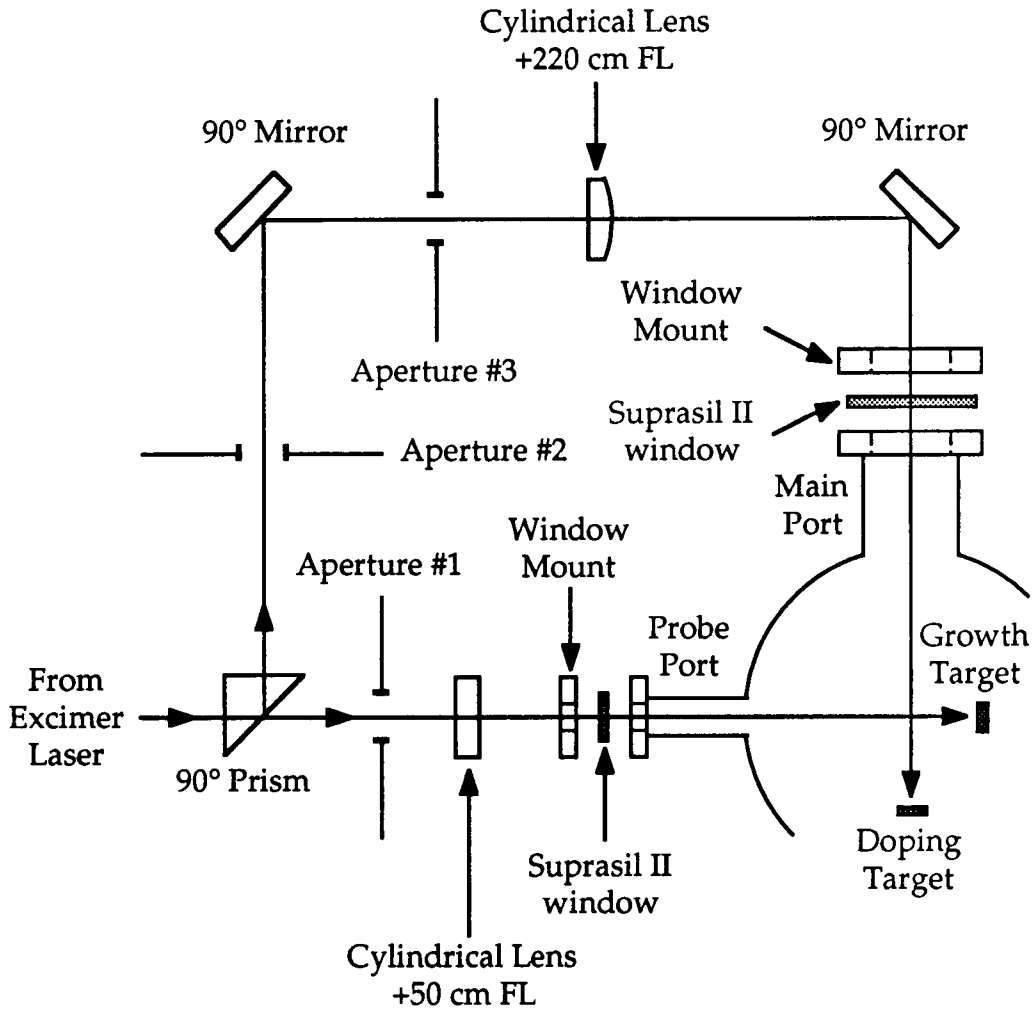

Figure 7-6 Excimer laser beam path between the laser and the ablation targets

Distribution of Ablated Material

Because the aperture profile was rectangular, the area struck by the focused beam also was rectangular. As a result, it was expected that the plume distribution would not be of the $\cos^n(\theta)$ form. To investigate the actual distribution, a ZnS film was grown on a Si substrate at 200°C. The substrate position was fixed (i.e., non-rotating) and the substrate-target separation was 5.7 cm. The film was grown with a total of 1200 laser pulses incident on a 0.358 cm x 0.752 cm area of the target, with $E_\ell = 0.33$ J·cm^{-2}. Visual observation of the "color fringes" (caused by the thickness variation) indicated that the distribution was elliptical with respect to θ. Rutherford backscattering spectrometry (RBS) was used to determine the thickness profile along the major and minor axes of the film. This profile was well fit ($\chi^2 < 0.05$) by an elliptical contour function and is presented in this form in Figure 7-7.

Deposition Geometry

Two different geometries were investigated to evaluate the deposition of uniform films by PLA. The first geometry utilized the tilting feature of the single target holder. Observations by the author indicated that, during the PLA growth of $YBa_2Cu_3O_{7-x}$, using $E_\ell \sim 3$ J·cm^{-2}, the ablation flux is greatest along the axis normal to the target surface even when the target was tilted. It was expected that, by oscillating the target during growth, the plume could be made to "paint" the substrate surface and be used to grow uniform films. With the single target holder it was possible to tilt the target normal by as much as ±10° out of the horizontal plane. However, when a ZnS target was irradiated with an $E_\ell = 0.25$-0.35 J·cm^{-2}, and the target tilted, the ablation plume was observed to remain in the horizontal plane. A possible reason for this difference in plume behavior is that the energy densities used were quite different, and it is likely that two different ablation regimes were being observed during the two experiments (YBCO and ZnS). In addition, the laser beam was incident on the target face in the

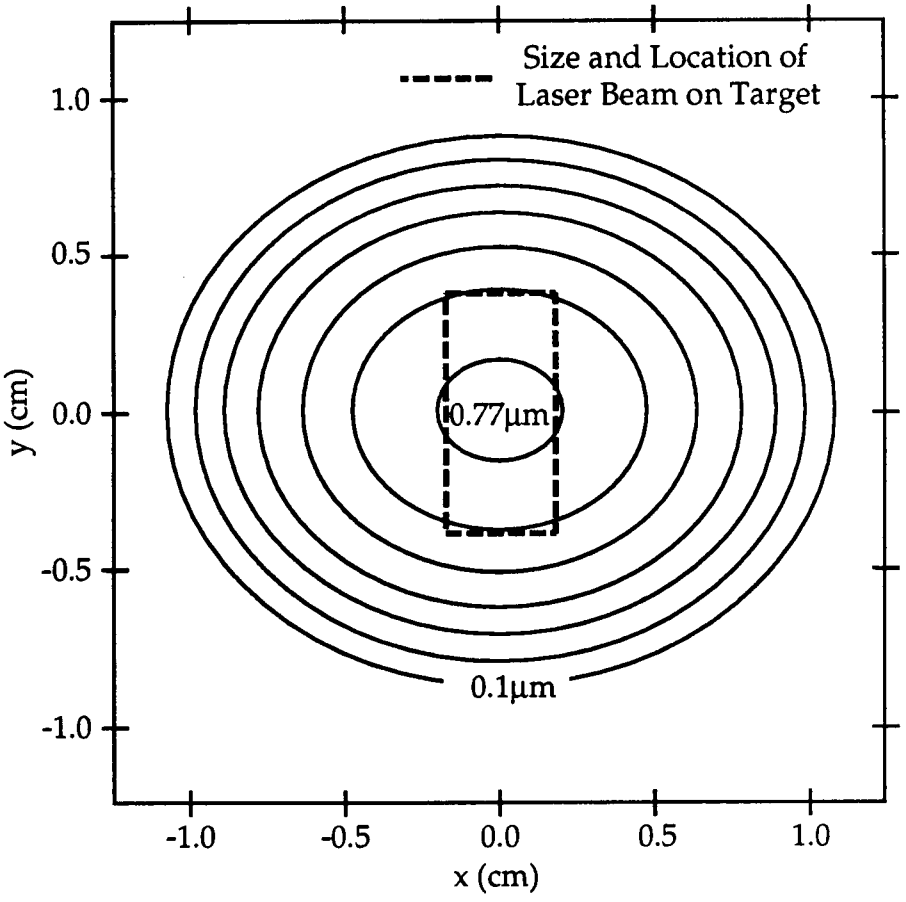

Figure 7-7 Deposition thickness contours for ZnS grown on Si substrate, non-rotating substrate, target-substrate distance of 5.7 cm. For comparison, the target area and relative location (with respect to the deposited film) are also shown in this figure.

horizontal plane. Thus, it appears that when the target normal is tilted out of the plane of incidence in this ablation regime and when using a large angle of incidence (25° from the target normal), the near surface expansion effects play a smaller role than does the orientation of the incident laser beam. It is possible that if a higher energy density were used during the ablation of ZnS, these expansion effects could be increased and plume "steered" by the tilting. Finally, the effect of the tilt might be more pronounced if the direction of tilt remained within the horizontal plane. However, this approach to film uniformity was abandoned when the tilting mechanism design was found to be unsuitable for multitarget use. As a result, neither the higher E_ℓ nor the horizontal tilt was investigated.

The second deposition geometry investigated was the offset-rotation geometry discussed in Chapter 6. To evaluate the effect of varying the radial offset distance while keeping the substrate-target distance fixed, it was necessary to change the position of the focused laser beam on the target. To accomplish this, the cylindrical lens was oriented such that the beam was brought to a vertical line focus. Thus, the beam could be translated horizontally across the target face simply by moving the lens in the horizontal direction. Since the height of the beam striking the target during this investigation was equal to the height of the aperture opening (0.75 cm), the maximum horizontal offset was ±1 cm from the center of the 2.54 cm ablation target. The height of the beam was 1.5 cm when it exited the laser; as a result, the beam could be translated vertically up to ±0.25 cm by moving the aperture vertically. Finally, because of the long focal length of the lens and the near-normal incidence (~25°) of the beam on the target, these translations had no significant effect on the E_ℓ. This geometry was used in all experiments, except those during which the tilt geometry was evaluated.

In Situ Growth Rate Monitoring

For any growth technique, one variable of interest is the growth rate. Although an average growth rate can be determined *ex situ* from the final film thickness, the controlled growth of multilayers and superlattices undertaken in this work required an *in situ* continuous determination of

the growth rate. Since optical methods are simple and inexpensive, the reflectance technique was used to monitor continuously the sample thickness during all experiments.

This method involves probing the thin film during growth with a low-power CW laser beam and measuring the reflectance, R. Figure 7-8 shows the geometry used. The total reflectance is the average of the s- and p-polarized reflectances (R_s, R_p); each of these is the product of its respective reflectance amplitude (r_s, r_p) and its complex conjugate. As the thickness increases, the interference between the light reflected from the ambient-film and the film-substrate interfaces changes in a periodic manner. This results in modulation of the reflectance amplitudes and, consequently, a measurable modulation of R. For the geometry shown in Figure 7-8, the reflectance amplitude can be calculated from

$$r_p = \frac{[\rho_p]_{1,2} + [\rho_p]_{2,3} e^{-\delta}}{1 + [\rho_p]_{1,2}[\rho_p]_{2,3} e^{-\delta}} \qquad 7.01a$$

$$r_s = \frac{[\rho_s]_{1,2} + [\rho_s]_{2,3} e^{-\delta}}{1 + [\rho_s]_{1,2}[\rho_s]_{2,3} e^{-\delta}} \qquad 7.01b$$

In Equation 7.01 δ is a thickness dependent dimensionless attenuation factor, and ρ_p and ρ_s are the Fresnel coefficients for the respective polarizations. The indices 1, 2 and 3 correspond to the ambient, film and substrate respectively. For the i^{th} constituent, the values of the Fresnel coefficient are related to the angle of incidence (ϕ_i) and the complex index of refraction (N_i) by

$$[\rho_p]_{i,j} = \frac{N_j \cos(\phi_i) - N_i \cos(\phi_j)}{N_j \cos(\phi_i) + N_i \cos(\phi_j)} \qquad 7.02a$$

$$[\rho_s]_{i,j} = \frac{N_i \cos(\phi_i) - N_j \cos(\phi_j)}{N_i \cos(\phi_i) + N_j \cos(\phi_j)} \qquad 7.02b$$

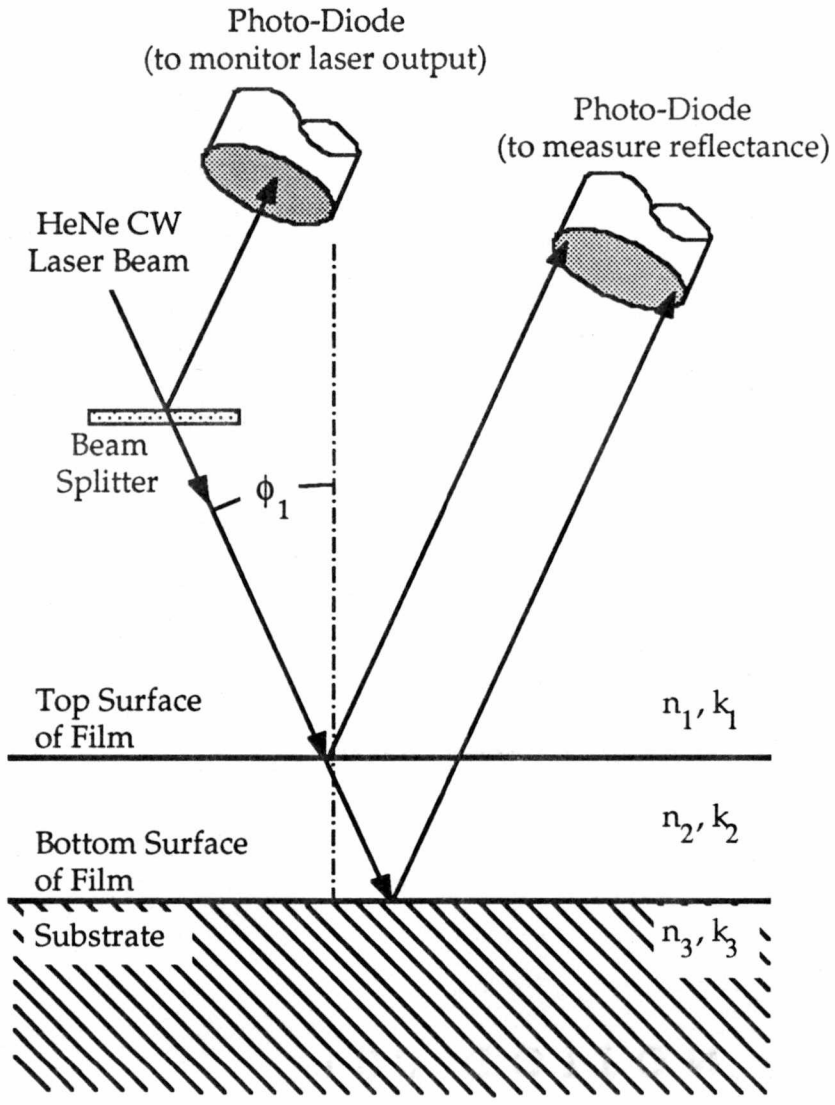

Figure 7-8 Geometry for the reflectance measuring technique

The value of δ is related to ϕ, the wavelength of the probe laser (λ), the film thickness (L), and the optical properties of the material by

$$\delta = \frac{4i\pi L}{\lambda} N_2 \cos(\phi_2) \qquad 7.03$$

Because the light passes through the film twice, the wavelength of the probe beam is chosen so that little attenuation occurs. Since both ZnS and ZnSe are transparent at 633 nm, the light from a HeNe laser was used as the probe. Figure 7-9 (top) shows the calculated normalized reflectivity (R = 1 at L = 0) from a λ = 633 nm probe beam incident at 25° on a ZnS film grown on a GaAs substrate. The real index of refraction (n) and extinction coefficient (k) used in this calculation were the (interpolated) values for bulk ZnS (n = 2.358, k = 0.002; Palik, 1985), and GaAs (n = 3.857, k = 0.1982; Aspnes, 1983). During experiments when the heater assembly was not rotated, the measured reflectivity curve closely matched the calculated curve. Figure 7-9 (bottom) shows the measured reflectivity from such an experiment. It was found that a change in reflectivity of ~ 0.5% of full scale could be resolved easily; in the region between the minima and maxima this corresponds to a change in film thickness of ~ 0.23 nm, which is less than half a unit cell. Similar results (both calculated and experimental) were observed for ZnS films grown on a GaP substrate and for ZnSe films grown on both GaAs and GaP substrates.

Because of the orientation of the heater assembly (i.e., facing the rear main port), the ports located 25° from the main rear port were used as probe laser entry and exit ports in all the experiments. During those experiments in which the single target holder was used to hold the growth target, the probe ports located at 65° also were used. However, at 65° the error in measured reflectivity caused by an error in the angle of incidence ϕ, is larger than at 25°. Consequently the error in the measurement of L is also larger. For example, at the signal midpoint (R ~ 0.7 at ϕ = 65°, R ~0.5 at ϕ = 25°) from a film ~235 nm thick, the error in thickness ($\partial L / \partial \phi$) is 0.97 nm per degree for ϕ = 65°, but only 0.27 nm per degree for ϕ = 25°. Furthermore, no additional physical information was gained using the

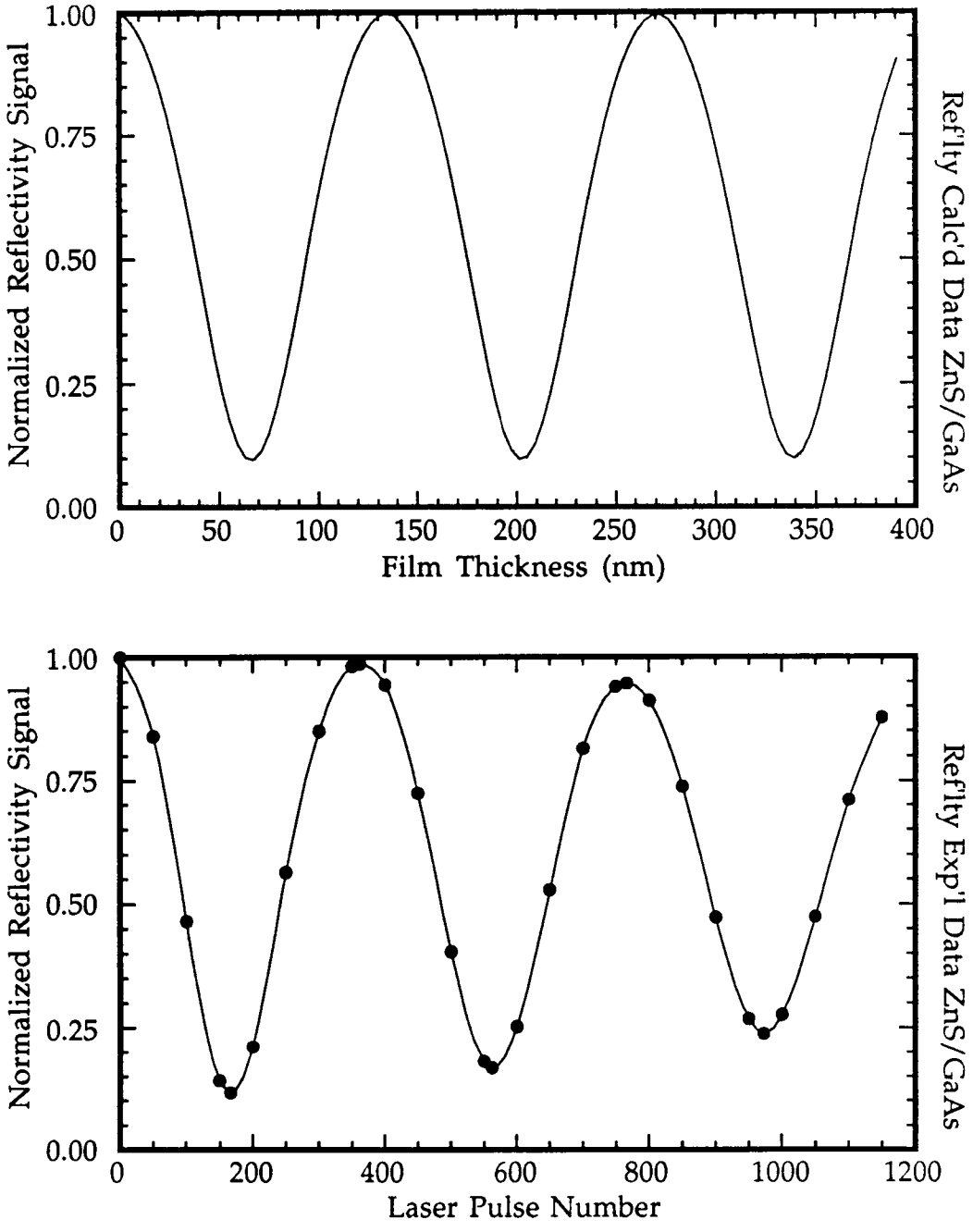

Figure 7-9 Calculated (top) and experimental (bottom) reflectance from ZnS/GaAs without substrate rotation. For clarity selected, representative datum are shown in the measured reflectance.

additional probe laser. Thus, when the multitarget holder made using the 65° ports difficult, they were abandoned.

The face of a substrate mounted on the heater assembly was never precisely perpendicular to the axis of rotation. Thus, when the heater assembly was rotated, the reflected beam did not remain in one location on the photo-diode; this resulted in variations in the signal output. Consequently, during all experiments in which the heater assembly was rotated, the signal modulation consisted of a superimposed fast component (from the rotational effects) and a slow component (from the change in film thickness). Nevertheless, in these experiments, the resolution of this technique, using less than 5 shots, was still better than ~ 1.0 nm, while the resolution, using a few hundred shots was less than 0.1 nm.

Analysis of Film Dimensions and Surface Morphology

The reflectance method also was used *ex situ* to more precisely determine the thickness uniformity of films grown using the offset-rotation geometry. After the sample was removed from the chamber, it was mounted on an x-y translation stage. Using this stage, the sample could be moved in both the x- and y-directions in steps as small as 1.0 μm. The HeNe beam was focussed onto the sample surface using a +5 cm spherical lens at an angle of incidence of 11.2°. The width of the focussed spot limited the x-y spatial resolution to ~50 nm. Because this system was mounted on a high stability optical bench, the resolution was such that a change in thickness as small a 1.0 nm could be measured in a ~250 nm thick sample.

The surface morphology of the films was examined using a JEOL 840 scanning electron microscope. Both the ZnS and ZnSe films appeared smooth and mirrorlike under all deposition conditions, and no surface features or structures were seen at the 50 nm level of resolution. These results are in good agreement with those for the HT_c superconductors. For those materials, scanning tunneling microscopy (STM) is often used to resolve surface structure. However, all the ZnS and ZnSe films were highly resistive, and STM measurements were not possible.

Analysis of Crystal Structure and Quality

The crystal structure and constituent phases of each sample were determined from $\theta/2\theta$ scans using a 2-circle Scintag Pad V x-ray diffraction (XRD) unit. The x-ray source was a stationary Cu target with variable exit slits, and a Ni filter was used to reduce the K_β radiation from the Cu source. The detector was a Ge single crystal with variable entrance slits and cooled with liquid nitrogen. Each circle on the goniometer could be operated independently, and this permitted evaluation of the crystal mosaic spread along the direction parallel to the surface normal. Because the goniometer radius was only 22.0 cm long the Cu $K_{\alpha 1}$ x-ray radiation line could not be separated from the $K_{\alpha 2}$ line. The interference between these lines resulted in a large signal-to-noise ratio which did not allow this unit to be used for evaluation of the strained-layer-superlattice sample.

After good quality films had been identified, XRD was also used to find the epitaxial orientation of the film. This was done using a 4-circle XRD unit that had a rotating Cu anode x-ray source. The signal-to-noise ratio for this system was small because the source and detector arms were of sufficient length to permit angular separation and selection of the $K_{\alpha 1}$ radiation, and the detector was a LN-cooled Ge single crystal. Thus, SLS samples were evaluated using this machine.

Another technique used to analyze the structural quality of films was transmission electron microscopy (TEM). This technique also provided direct evidence about the film/substrate interface and the quality of the epitaxy. The TEM images were obtained at the University of Tennessee on a Hitachi 2000 electron microscope. Although good results were obtained for cross sections of the ZnS/GaAs(001) samples, numerous attempts to prepare TEM specimens from the ZnSe/GaAs and superlattice samples failed catastrophically during the ion milling stage of processing. The reason for this is not known, but may be related to large residual strain present in the ZnSe/GaAs and to full relaxation of strain in the (~4% mismatched) ZnS/GaAs samples.

Analysis of Lattice Defect Density and Location

Because the stacking fault energy is small in ZnS and ZnSe stacking faults would be expected to be the dominant lattice defect present in these films. These defects are known to broaden and shift the XRD peaks obtained from powder samples (Paterson, 1952; Warren, 1959). More recently, the effect of stacking faults on the XRD pattern from single crystal cubic ZnS was examined (Sebastian, 1987). It was shown that, for random growth faults (i.e., twins), all the reflections with indices (H, K, L) for which $H - K \neq 3$ are equally broadened and show negligible shift of the peak location. The broadening of the 2θ reflections ($\Delta 2\theta$) due to the stacking fault probability (α) is found from the real part of

$$\Delta 2\theta = \frac{3}{\pi}\cos^{-1}\left[-\frac{z^2-4z+1}{2z}\right] \qquad 7.04$$

Where z is given by

$$z = \sqrt{2\alpha - 1} \qquad 7.05$$

Once the stacking fault probability has been determined, the density of stacking faults (ρ_{sf}) can be found from (Vassamillet, 1961)

$$\rho_{sf} = \frac{2\pi\alpha\gamma}{Gd(\mathbf{b}_1 \bullet \mathbf{b}_2)} \quad , \qquad 7.06$$

where γ is the stacking fault energy (Table 2-1), G is the shear modulus, d is the interplanar spacing of the slip planes, and $\mathbf{b}_1$, $\mathbf{b}_2$ are the Burgers vectors of the two partial dislocations bounding the stacking fault.

The presence of line defects (e.g., misfit dislocations) leads to broadening of the XRD rocking curve. The density of these defects is related to the rocking curve FWHM ($\Delta\omega$) by (Tromson-Carli, 1991)

$$(\Delta\omega)^2 = (\Delta\omega_T)^2 + (\Delta\omega_S)^2 \quad , \qquad 7.07$$

where $\Delta\omega_T$ is the broadening due to a Gaussian distribution of mosaic tilt, and $\Delta\omega_S$ is the broadening due to lattice strain, caused by the presence of the dislocations. These two components are related to the dislocation density (ρ_d, CGS units), the Burger's vector (**b**), and the geometry of the dislocation (with respect to a particular XRD peak reflection) by

$$(\Delta\omega_T)^2 = 4.35(\mathbf{b} \bullet \mathbf{b})\,\rho_d \qquad 7.08a$$

$$(\Delta\omega_S)^2 = 0.28(\mathbf{b} \bullet \mathbf{b}) f\,\rho_d \ln\left(\frac{10^7}{2(\rho_d)^{1/2}}\right)\tan^2(\theta) \quad , \qquad 7.08b$$

where f is a geometrical factor. For dislocations on the {111} planes, with **b** along the (110) and an (00ℓ) reflection, the value for this factor is $f \sim 0.5$.

This approach to interpreting the XRD reflection peak and rocking curve widths must be used with the understanding that there are other factors (e.g., heteroepitaxial by induced strain) that also contribute to the broadening as well. Thus, the values determined by Equations 7.04 - 7.08 are conservative and represent (within experimental error) an upper bound on the defect densities.

In heteroepitaxial films one would expect a nonuniform distribution of the lattice defects, with a larger concentration in the strained material near the interface. Although XRD can be used to quantify the number of stacking faults, the distribution of these defects is not easily determined using this technique. On the other hand, analysis of the film using Rutherford backscattering spectrometry (RBS) can provide information about the spatial distribution of these defects, but not about their concentration. Figure 7-10 illustrates schematically the RBS process. In this technique, the sample is mounted in a vacuum chamber (~10^{-8} Torr), and a well collimated beam of energetic ions impinges on the sample. In this work, a beam of 2.3 MeV, $^4He^+$ ions was used as the probe beam. When the ions are incident on the sample in a high symmetry direction,

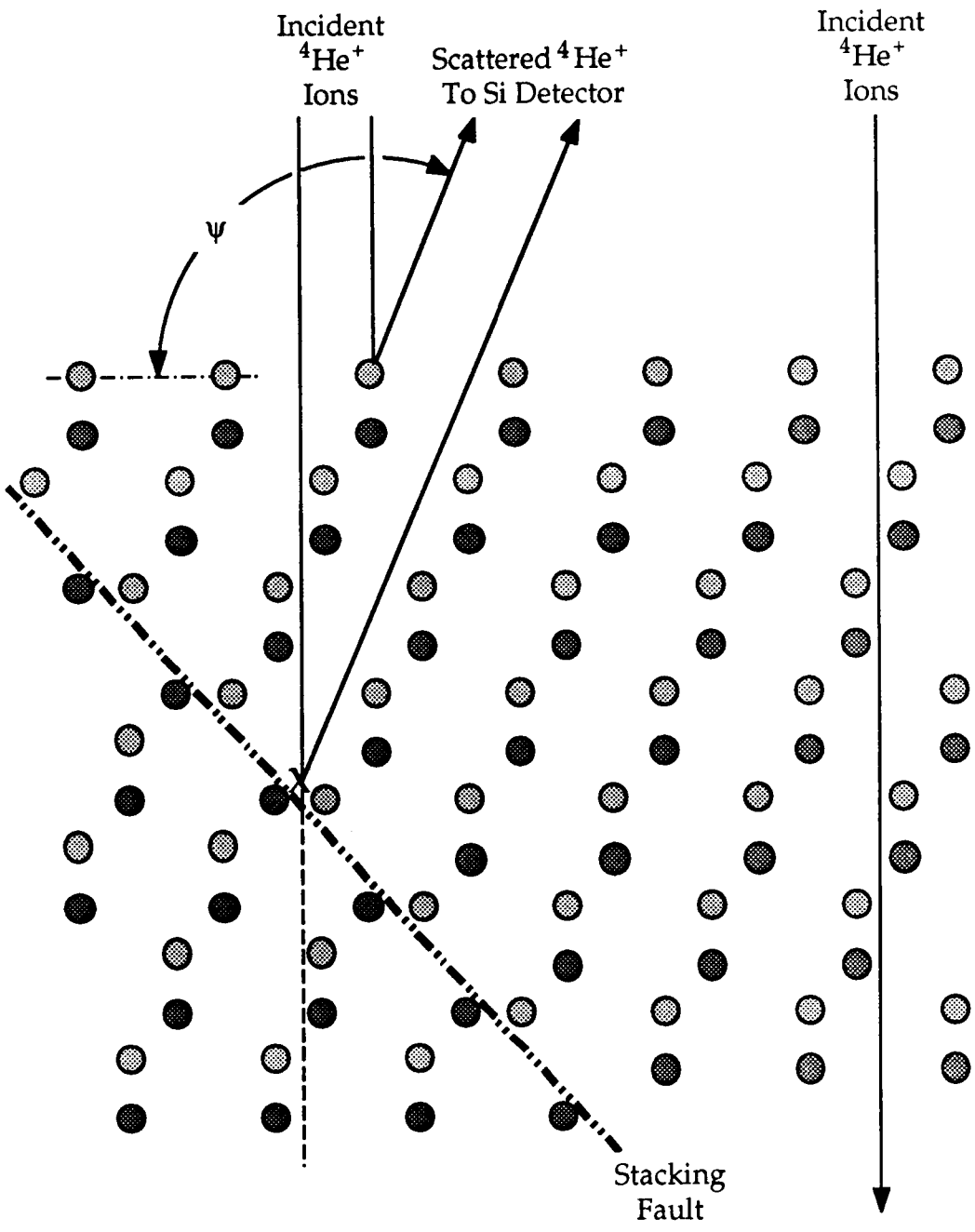

Figure 7-10 Schematic of the RBS geometry and scattering events.

most of the ions travel ("channel") between the lattice planes (as illustrated by the rightmost incident ion in Figure 7-10) until they come to rest within the sample. A small fraction of the incident ions undergo Coulomb scattering as illustrated by the middle incident ion. The number and energy of these scattered ions are detected at an angle ψ; in this work a Si detector mounted at $\psi = 160°$ was used. The scattering is essentially elastic in nature, with the energy loss of the incident ion determined by the stopping cross section. This energy loss allows analysis of the sample as a function of depth. The fraction of incident ions that are scattered is called the minimum yield (χ_{min}) and is used as a measure of the film quality. The χ_{min} is experimentally measured by comparing the number of scattering events observed when the sample is aligned in the high symmetry direction (aligned spectrum), to the number observed when the sample is oriented such that essentially all the ions are scattered (random spectrum). However, even along high symmetry directions in perfect crystals, a small fraction of the ions is always scattered. The χ_{min} in this case can be theoretically determined by (Taguchi, 1982)

$$\chi_{min} \cong \rho_a \pi \delta (2\upsilon^2 + \xi^2) \quad , \qquad 7.09$$

where ρ_a is the atomic density of the compound, δ is the divalent atomic distance, υ is a temperature dependent lattice vibrational term, and ξ is the Thomas-Fermi screening radius. For $N_a = 5 \times 10^{22}$ cm^{-3}, $\upsilon \sim 0.0167$ nm, and $\xi \sim 0.01$ nm, the theoretical $\chi_{min} = 0.032$ for a perfect crystal. If defects are present in the film (illustrated by the stacking fault in Figure 7-10), the lattice symmetry is destroyed. This results in an increase in scattering events (illustrated by the leftmost incident ion) and a corresponding increase in the measured χ_{min}. By measuring the χ_{min} as a function of depth (backscattered ion energy), the spatial distribution of lattice defects and strain can be determined.

The location, width and separation of the peaks in the RBS spectra are factors that influence the depth resolution. The energy loss during the scattering process is related to the mass of the ions and the material being

probed. For a particular atomic species A, the energy (E_s) of the scattered He at the leading edge of the RBS peak from this species is given by

$$E_s = E_o\left[\frac{M_{He}\cos(\psi)+\left(M_A^2 - M_{He}^2\sin^2(\psi)\right)^{1/2}}{M_{He}+M_A}\right]^2 \quad , \qquad 7.10$$

where E_o is the energy of the incident ion, M_{He} is the mass of the He atom, and M_A is the mass of the constituent A. Since the ions also lose energy as they travel deeper, the peak width of the energy spectrum from a particular film constituent (i.e., Zn, S, and Se) is proportional to the film thickness. The energy separation (ΔE) between ions scattered from two different atomic species is given by Equation 7.11 (Taguchi, 1982).

$$\Delta E \cong 2E_o M_{He}(1-\cos(\psi))\frac{M_A - M_B}{M_A M_B} \quad , \qquad 7.11$$

where M_A and M_B are the masses of constituents A and B. For thin films ($L < \sim 3\ \mu m$) the ions probe the substrate as well. Thus, Equation 7.11 also applies to the atomic species of the substrate. For a ZnS film on a Si substrate, there is little or no overlap of the Zn, S, and Si peaks (depending on the film thickness), and the depth resolution is ~ 5 nm. For a ZnS film on GaAs, the position of the S peak is such that the resolution is nearly the same. However, for a ZnSe film, both the Zn and Se peaks overlap the Ga and As peaks, resulting in poor depth resolution. In this last case, only qualitative statements about film quality can be made based on the χ_{min} of RBS.

Analysis of Composition Profile in Multilayers and Superlattices

Since it was not possible using RBS to determine accurately the compositional profile of the alloyed multilayers containing Se grown on GaAs, secondary ion mass spectrometry (SIMS) was utilized for compositional profiling. This technique also involves directing a beam of

ions toward the sample. However, in SIMS the ionic species and energies are chosen such that the sample is sputtered and the sputtered atoms are collected and analyzed in a mass spectrometer. As the sputtered depth increases, a composition versus depth profile is generated. In this work Cs was chosen as the ionic species and the energies and beam currents were chosen to provide a depth resolution of ~ 5 nm.

For the ZnS-ZnSe strained layer superlattices (SLS), the compositional modulation of the SLS also was determined using XRD. XRD is well suited for this investigation because it correlates equivalent atomic positions from period to period, and the nature and thickness of corresponding constituent strained layers can be determined. These periodically spaced layers act as another lattice with a larger lattice constant (the "superlattice constant") and generate periodically spaced diffraction satellite peaks on both sides of the primary diffraction peak. For a superlattice with periodicity along the [001] direction, the superlattice period (L_{SLS}) is related to the separation between (00ℓ) reflections by Bragg's law, such that

$$\sin(\theta_{\ell+n})-\sin(\theta_{\ell}) = \frac{n\lambda}{2L_{SLS}} \quad , \qquad 7.12$$

where λ is the wavelength of the x-ray radiation, and n is the difference in peak indices (i.e., n = 1 for adjacent peaks). By including the solution for the central peak and rearranging 7.12, the index ℓ can be determined using

$$\ell = \frac{\sin(\theta_{\ell})}{\sin(\theta_{\ell+1})-\sin(\theta_{\ell})} \qquad 7.13$$

A more sophisticated kinematic model also was made available at the Oak Ridge National Laboratory (Budai, 1992), and was also used to evaluate the SLS XRD patterns.

Analysis of Optical Properties and Bandstructure

Because many of the uses of ZnS and ZnSe are optical in nature, the investigation of their optical properties is especially important for a complete evaluation of the film quality. Ellipsometry is a powerful and nondestructive method for doing this, and is similar to the reflectance method used to monitor the growth rate. However, in ellipsometry the incident probe laser beam is elliptically polarized and the change in polarization of the reflected light is measured. The results are generally expressed as the ellipsometric angles Δ and ψ. These angles are related to r_s and r_p by

$$\frac{r_p}{r_s} = \tan(\psi)e^{i\Delta} \qquad 7.14$$

Typically, the measurement of ψ and Δ is done using a single-wavelength, nulling ellipsometer. However, since the optical properties of a material and its bandstructure are intimately related, determination of the bandstructure requires that these measurements be taken over an appropriately chosen range of photon energies (i.e., by spectroscopic ellipsometry). This was done using a two-channel spectroscopic polarization modulation ellipsometry (2-C PME). This equipment measures the associated ellipsometric parameters, which are given by (Jellison, 1993)

$$N_m = \cos(2\psi) \qquad 7.15a$$

$$S_m = \sin(2\psi)\sin(\Delta) \qquad 7.15b$$

$$C_m = \sin(2\psi)\cos(\Delta) \qquad 7.15a$$

where the subscript m indicates that these are measured quantities. For a given physical model of the film structure, the effective dielectric function (ε_1, ε_2) can be calculated from these data by (Jellison, 1985)

$$\langle \varepsilon_1 \rangle = \sin^2(\theta_i)\left(1+\tan^2(\theta_i)\frac{N^2-S^2}{(1+C)^2}\right) \qquad 7.16a$$

$$\langle \varepsilon_2 \rangle = \sin^2(\theta_i)\tan^2(\theta_i)\frac{2NS}{(1+C)^2} \qquad 7.16b$$

where θ_i is the angle of incidence of the probe laser beam.

To determine a film's dielectric function by this method it was necessary first to specify its layer–structure. A three-layer model was used, consisting of the substrate, the film, and a roughened film–surface layer. The thicknesses of the film and film–surface layer were determined using a single-term Lorentz approximation for the optical functions of the film below the bandedge, and the Bruggeman effective medium approximation for the surface layer (i.e., it is assumed that the surface consists of 50% voids and 50% film). In determining the layer thicknesses, the biased estimator χ^2 was used as the figure of merit ($\chi^2 >> 1$ indicates a fit not consistent with the data, $\chi^2 \sim 1$ indicates a fit that is consistent with the data). Once the thickness of each layer was determined, the dielectric function was determined accurately across the full spectral range of 1.5-5.0 eV. This range was sufficient to observe the E_0, $E_0 + \Delta_0$, E_1 and the $E_1 + \Delta_1$ transitions in the ZnSe films, and the E_0, and $E_0 + \Delta_0$ transitions in the ZnS films. The spacing between data points was in the range 20-40 meV, depending on the spectral region.

Analysis of Midgap Defects and Impurities

The presence of defects or impurities in the lattice nearly always introduces electronic defect levels in the midgap region (Chapter 2). Their presence (or lack) is perhaps the best indication of the quality of the material, short of electrical transport measurements. Both room temperature and cryogenic photoluminescence (PL) spectroscopy was used in this study to probe the midgap region for defect levels.

The room temperature PL measurement was performed using a Lumonics excimer laser with a KrF gas mixture ($\hbar\nu$ = 5.00 eV) as the

excitation source. The beam path was designed such that the energy density at the sample was ~2.5 x 10^{-3} J·cm^{-2}, which corresponds to ~85 kW·cm^{-2} (τ ~ 30 ns FWHM). The PL emission from the sample was collimated and then introduced into a MacPherson 1.3 m spectrometer. The light transmitted through the spectrometer was measured using a RT photomultiplier (PMT) tube. Figure 7-11 shows the calculated response of this spectrometer-PMT combination; at the bandedges of ZnS and ZnSe, the response is 7% and 9%, respectively. The signal from the PMT was processed by a boxcar integrator. The gate on the boxcar was typically 100 ns wide. Control of the spectrometer and data collection was coordinated using a MacIntosh™ computer equipped with LabView™ software. Measurement error was reduced by taking ~10 readings at every selected wavelength, and then discarding the outlier points; the remaining data was then averaged. Because this data was taken at ~300 K, the near bandedge PL peak widths were such that significant overlap of different peaks occurred.

To decrease the thermal broadening of these peaks, cryogenic PL spectroscopy was performed at Columbia University under the direction of Dr. Irving Herman. The excitation source in this work was a HeCd CW laser (λ = 315 nm, E_ℓ = 3.94 eV). Most of the data was taken at 9 K, with a number of investigations covering the range T = 9-90 K.

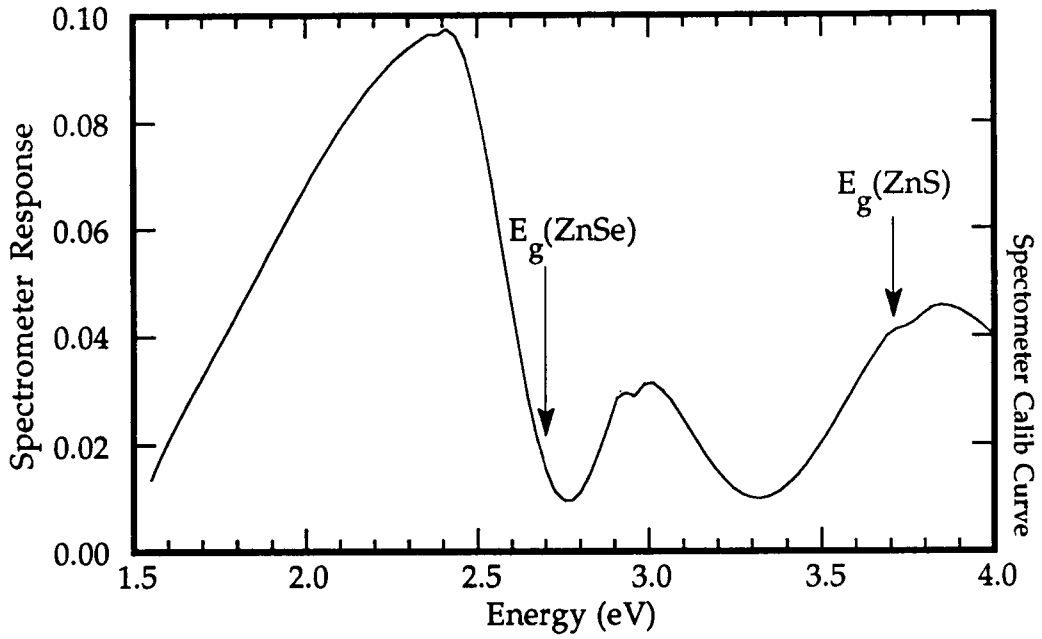

Figure 7-11 Room temperature PL spectrometer and PMT response.

CHAPTER 8

EXPERIMENTAL PROCEDURES AND RESULTS

Research Overview

This work was undertaken to evaluate the PLA process for the growth of wide-bandgap II-VI materials. This was begun by growing ZnS films to determine such operational parameters as the substrate-target separation and range of energy densities within which growth would occur. Different substrates and substrate preparation techniques also were investigated to identify surfaces appropriate for epitaxial growth. Because of the chemical similarity of ZnS and ZnSe, these same parameters were used for the growth of ZnSe.

A series of ZnS and ZnSe films (each ~275 nm thick) were grown at different temperatures and analyzed using $\theta/2\theta$ and rocking curve (ω scan with fixed θ) XRD to determine the optimal growth temperatures. Films grown at the optimal temperature then were evaluated by measuring their structural, optical, and electronic properties, and comparing those results with data found in the literature. Finally, PLA growth was studied in different ambients to determine if doped or alloyed films can be grown using this technique.

Substrate Materials and Preparation Procedures

The first criterion used in selecting substrate materials was that the lattice mismatch between the film and substrate must be small (i.e., $< \sim 4\%$). A second was that the substrate material must be useable in electronic applications (i.e., not intrinsically insulating). These criteria were met by four materials: Si, Ge, GaAs and GaP. Table 8-1 shows the attributes (i.e., doping, crystallographic orientation, etc.) of the materials used in this work. In all cases, ~ 0.6 cm x 0.6 cm squares were scribed and broken from the as-received wafers. These substrate squares were degreased by ultrasonic cleaning in pure solutions of trichloroethylene, acetone, and finally methanol, and then stored in a desiccator until use.

Table 8-1
Substrate Materials

Substrate Material	Doping	ZnS Mismatch	ZnSe Mismatch	Supplier
Si (001) B doped	p-type	- 0.40%	4.2%	Wacker
Si (001) P doped	n-type	- 0.40%	4.2%	Wacker
Ge (001) undoped	intrinsic	- 4.6%	0.18%	Naval Research Laboratory
GaAs (001) Zn doped	n-type	- 4.5%	0.26%	Sumitomo USA
GaAs (001) Cr doped	semi-insulating	- 4.5%	0.26%	Sumitomo USA
GaAs (111) S doped	n-type	- 4.5%	0.26%	Sumitomo USA
GaP (001) Zn doped	p-type	- 0.76%	3.8%	Sumitomo USA

Table 8-2 shows the preparation procedures that were used with these substrate materials. These procedures were carried out immediately before the samples were mounted on the substrate heater and installed in the growth chamber. ZnS films then were deposited on these substrates at various growth temperatures (T_g) and laser energy densities (E_ℓ) to evaluate the effectiveness of the various preparation techniques.

For the Si and Ge substrates, the sulfur passivation step and sample transfer in an N_2 atmosphere were tried following the buffered HF acid etch to prevent regrowth of the oxide on the substrate surface. RBS was used to analyze the crystallinity of the ZnS films deposited at T_g =200°C on one Si(111) substrate and on two Si(001) substrates that were prepared using the $(NH_4)_2S_x$ treatment. These films were deposited on the Si(111) and the first Si(001) sample using an E_ℓ = 0.22 J·cm^{-2}; an E_ℓ = 0.33 J·cm^{-2} was used to deposit the ZnS film on the second Si(001) sample. For all these samples, the RBS showed a χ_{min} = 100% along the surface normals. Further, the $\theta/2\theta$ XRD patterns showed no diffraction from any films (~30 samples) deposited on either the Si or the Ge substrates, regardless of the preparation procedure, and for the full range of deposition temperatures (T_g = 150-450°C) and laser energy densities (E_ℓ = 0.2-1.5 J·cm^{-2}) used. These results indicate that the ZnS films deposited on Si and Ge substrates have an amorphous or randomly oriented polycrystalline structure. This conclusion is consistent with highly oriented growth being prevented by the lack of polar symmetry across the film-substrate interface. Because the surfaces of these substrate materials and their oxides are non-polar, the ZnS nuclei that were initially formed would have random orientations, and growth from these nuclei would result in a polycrystalline film. Since the final film thicknesses were only ~ 250 nm, there was insufficient coherent diffraction for measurement. If the final thickness had been greater (e.g., several μm), it is possible that a preferred growth orientation would have been observed. However, following these results, the growth of ZnS on Si and Ge substrates was discontinued, and no attempts were made to grow epitaxial ZnSe films on either Si or Ge substrates.

The preparation protocols for the GaP and GaAs substrates are also shown in Table 8-2. When the sulfur passivation step (i.e., $(NH_4)_2S_x$

Table 8-2
GaAs and GaP Substrate Preparation Procedures

Substrate Material	Oxide Removal	Acid Wash	Rinse	Passivation	Final
Si	BHF 10 s				N_2 blow dry
Si	BHF 10 s			$(NH_4)_2S_x$ 90 s	N_2 blow dry
Ge	CP6S 10 s				DIW rinse N_2 blow dry
Ge	CP6S 10 s			$(NH_4)_2S_x$ 90 s	N_2 blow dry
GaP	Br_2:MeOH (1:99) 10 s	HNO_3:HCl (1:2) 10 s			DIW rinse N_2 blow dry
GaP	Br_2:MeOH (1:99) 10 s	HNO_3:HCl (1:2) 10 s	DIW rinse N_2 blow dry	$(NH_4)_2S_x$ 90 s	N_2 blow dry
GaAs	H_2SO_4 (conc.) 10 s				DIW rinse N_2 blow dry
GaAs	H_2SO_4 (conc.) 10 s		DIW rinse N_2 blow dry	$(NH_4)_2S_x$ 90 s	N_2 blow dry

BHF: Buffered HF acid; CP6S: commercial acid etch for Ge; DIW: distilled and deionized water; MeOH: methanol

treatment) was not used, the GaAs and GaP substrates were heated immediately prior to growth at either 585°C or 685°C in vacuum for ~ 10 minutes to remove any oxide present, and then cooled to the T_g. While this annealing treatment is known to remove the oxide layer on the GaAs surface (Eres, 1991), it also has been reported that the final GaAs surface is not stoichiometric and that the surface reconstruction is dependent on the arsenic coverage (Massies, 1980). The $\theta/2\theta$ XRD patterns showed only (111) and (333) reflections from ZnS films grown on the GaAs(001) substrates that had undergone this treatment. This clearly indicated that the growth was not epitaxial.

When the $(NH_4)_2S_x$ passivation step was included during preparation, the substrates were heated at 420°C for three minutes, and then cooled to the T_g. It has been reported in MOMBE growth experiments that this passivation-preheat treatment results in a (2 x 1) reconstruction of the GaAs surface, a reduction of the surface-state density, and allows two-dimensional (2D) nucleation to occur from the beginning of growth (Kawakami, 1991). To determine the effectiveness of this protocol in PLA growth, ZnS films were grown on untreated GaAs(001) and GaP(001), and on $(NH_4)_2S_x$ treated GaAs(001) and GaP(001) substrates. Because the heater face and area of uniform film growth were large compared to the substrate size, all four samples were grown during the same growth run. The pregrowth anneal was 420°C and the growth conditions were E_ℓ = 0.25 $J \cdot cm^{-2}$, T_g = 300°C, with a substrate-target separation (D_{st}) was 5.7 cm. The $\theta/2\theta$ XRD showed no significant difference in the quality of the films grown on the passivated and non-passivated GaAs surfaces. All films showed (00ℓ) reflections at the expected $\theta/2\theta$ positions. No ($\ell\ell\ell$) peaks were observed in the pattern. Both the Cu $K_{\alpha 1}$ and $K_{\alpha 2}$ peaks were resolved for the (004) reflection from the films grown on the GaAs(001) substrates. These same reflections from the ZnS films grown on the GaP substrates showed substantially less peak intensity and the broadening was such that the $K_{\alpha 1}$ and $K_{\alpha 1}$ peaks could not be deconvoluted. Thus, RBS analysis was used to quantify the crystalline quality of the ZnS films grown on the GaP. For the ZnS films grown on the untreated GaP substrate, the χ_{min} = 100% along the surface normal; while for the film grown on the

passivated substrate, χ_{min} = 78%. The sulfur passivation step was included in the preparation protocol for both the GaP and GaAs substrates because of this observed improvement.

Intrinsic, doped (n- and p-type), and semi-insulating substrates were tried (Table 8-1) in all phases of this work. However, no difference was observed in either ZnS or ZnSe film quality that was related to the dopant type or quantity present in the substrate.

Ambient Gas Effects

ZnS films were grown in a He ambient to evaluate the effect an inert gas ambient would have on film quality. The purpose of this was threefold. First, it was observed that during growth in vacuum, significant film deposition occurred on the window the excimer beam passed through; by growing in an ambient of moderate pressure (~few mTorr), it was believed that the rate of deposition on the window could be reduced. Secondly, it is well known that the energy of the ablated species can be as great as several hundred eV (Lowndes, 1992). Such energies are sufficient to produce atomic displacement damage in semiconductor films. By growing in an ambient, the kinetic energy of the ablated species would be reduced, together with damage to the growing film. Finally, before attempting doping or alloying (using a chemically active ambient) it had to be determined if physical entrainment of the ambient would occur to an extent that was structurally detrimental.

To evaluate the effect growth in an inert ambient would have on film quality, ZnS films were grown in 0.0 mTorr, 0.5 mTorr, 2.0 mTorr, and 10.0 mTorr He atmospheres. All the films were grown at E_ℓ = 0.25 J·cm^{-2} and a T_g = 300°C. No significant change in growth rate of the films was observed because the substrate was only 5.7 cm from the ablation target during all these experiments. However, the deposition rate on the laser access window ~45 cm from the target was greatly reduced for growth in the 2 mTorr and 10 mTorr ambients. This result qualitatively indicates that He ambients of as little as 2 mTorr modify the kinetic energy of the ablated species, over distances of tens of centimeters. The effect of these ambients

on the film quality was measured by comparing the rocking curve width (FWHM) from the ZnS(004) $K_{\alpha 1}$ XRD peak. These widths were 0.86°, 0.77°, 0.89° and 0.78° for growth in the 0.0, 0.5, 2.0 and 10.0 mTorr He ambients respectively. The lack of correlation of the rocking curve widths with ambient pressure showed that the presence of the He ambient at these pressures did not measurably affect the mosaic structure of the films along the (00ℓ) direction. Because of these results, an ambient of 2 mTorr He was used during the growth of the ZnS and ZnSe films.

Laser Energy Density (E_ℓ) Effects

The characteristics of the ablated species are strongly dependent on the laser energy density at the target surface. Because of the difference in the vapor pressures of the Zn and the chalcogen species, the E_ℓ necessary for congruent transfer of material must be above the thermal evaporation regime. For ZnSe the evaporation regime lies below $E_\ell \sim 0.13$ J·cm^{-2} (Chapter 5). However, no literature data was found regarding the E_ℓ required for nonthermal ablation of ZnS.

To determine the E_ℓ necessary for epitaxial growth, E_ℓ values in the range 0.15-1.50 J·cm^{-2} were used to grow ZnS films on GaAs(001) and GaP(001) at T_g = 300°C and P(He) = 2 mTorr. For both substrates, the $\theta/2\theta$ XRD from the films grown at D_{st} = 5.7 cm with E_ℓ = 0.15 J·cm^{-2} showed only ($\ell\ell\ell$) peaks; no (00ℓ) reflections were observed under these conditions. For E_ℓ = 0.20 J·cm^{-2}, the XRD patterns from the films grown on the GaAs(001) showed (00ℓ) reflections, while only the ($\ell\ell\ell$) reflections were seen from films grown on GaP(001). For films grown on both substrates using E_ℓ = 0.25 and 0.30 J·cm^{-2}, only the (00ℓ) reflections were observed, while for $E_\ell \geq 0.30$ J·cm^{-2}, no reflections were observed.

The D_{st} then was increased to D_{st} = 10.8 cm and E_ℓ = 0.15-1.50 J·cm^{-2} again were used to grow ZnS films on GaAs(001) and GaP(001) at T_g = 300°C and P(He) = 2 mTorr. As before, the $\theta/2\theta$ XRD patterns showed only ($\ell\ell\ell$) peaks from the films grown using E_ℓ = 0.15 J·cm^{-2}. However, only (00ℓ) reflections were observed for all films grown using $E_\ell \geq 0.25$ J·cm^{-2}.

The similarity of the results seen at E_ℓ = 0.15 and 0.20 J·cm^{-2} for both D_{st} are consistent with non-congruent deposition of ZnS in this E_ℓ range.

This was investigated further using an ion probe to measure the time of flight (TOF) of the ionized species in the ablation plume. This probe was a Cu plate housed 0.2 cm behind a grounded Cu plane. Ions were introduced to the probe through a 0.02 cm^2 aperture in the ground plane. The probe was floated with respect to the chamber and target by biasing it with an isolated and shielded 300 V battery. The bias at the probe was controlled using a potentiometer placed in series with the battery, and the ionized cation flux was measured by applying a negative bias to the probe. The probe was positioned along the surface normal of the target. The distance between the collector and target (D_{ct}) could be changed and this allowed the dynamics of the plume species to be studied. The laser used in this case was a Lambda Physik EMG 210 KrF excimer (λ = 248 nm) having a pulse width (FWHM) of 50 ns. All the TOF data was obtained in a vacuum ambient.

Figure 8-1 shows the TOF spectra of the ions in the ablation plume at a D_{ct} = 3 cm for E_ℓ = 0.20-0.56 $J \cdot cm^{-2}$. The TOF signal obtained by a flux-sensitive probe (i.e., an ion probe) for species whose kinetic energies are distributed thermally can be described by the Maxwell-Boltzmann function (Kelly, 1988)

$$I(t) = \left(\frac{c_1}{t^5}\right) e^{-c_2/t^2} \qquad 8.01$$

For a flux sensitivity detector the effective kinetic energy (T_{eff}) of the translational kinetic motion of the species in the plume also can be determined from the position of the peak of the TOF spectra by (Kelly, 1988):

$$T_{eff} = \frac{m D_{ct}^2}{\eta t^2} \qquad 8.02$$

Where m is the mass of the ion species and η is a constant. When the flux sensitivity detector is used, η = 2.5 (Kelly, 1988). Assuming that the ionized

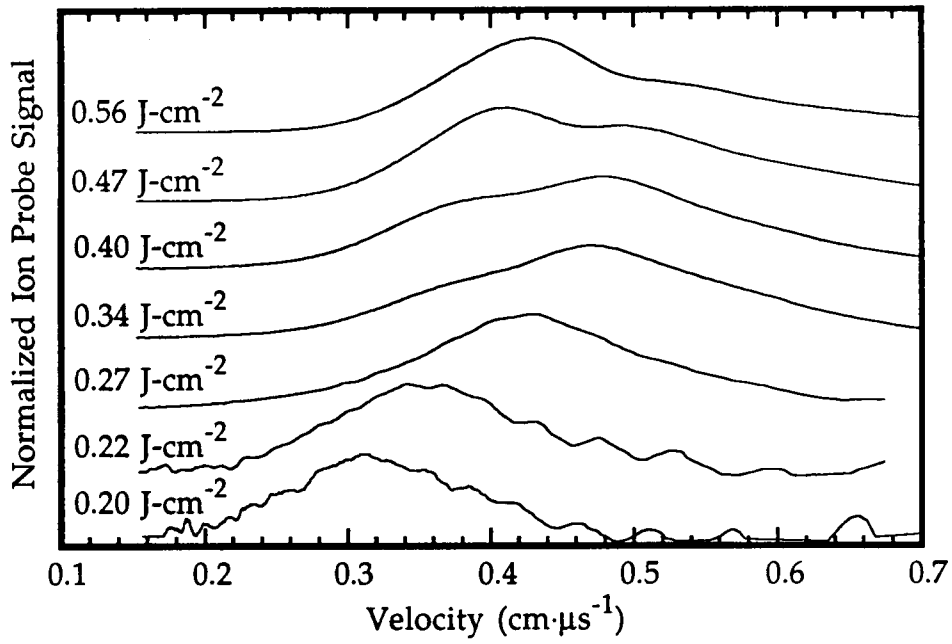

Figure 8-1 Normalized time of flight spectra of ions in the ZnS ablation plume at 3 cm from the target in vacuum at various energy densities. Signal traces have been offset vertically for clarity.

species were Zn ($m = 1.06 \times 10^{-25}$ kg) the T_{eff} obtained using Equation 8.02 were 1.3, 1.7 and 2.4 eV for $E_\ell = 0.20$, 0.22 and 0.27 J·cm^{-2} respectively. The T_{eff} obtained by fitting these TOF spectrum with Equation 8.01 were 1.38, 1.75, and 2.58 eV respectively.

Above $E_\ell = 0.27$ J·cm^{-2} the TOF begins to deviate from the Maxwellian distribution. This becomes obvious for $E_\ell \geq 0.34$ J·cm^{-2}, where a second peak appears. If the mechanism were completely thermal, all the species would be in equilibrium and show a singly peaked Maxwellian distribution. Thus, the presence of a second peak indicates that ablation at these energy densities involves at least one nonthermal process.

Figure 8-2 shows the integrated ion charge in the ablation plume for $E_\ell = 0.15$-1.0 J·cm^{-2} and $D_{ct} = 3$ cm. For $E_\ell = 0.15$-0.35 J·cm^{-2}, the number of ions increases with a $(E_\ell)^{4.8}$ multiphoton dependence, and a threshold energy density $E_{th} \sim 13$ mJ·cm^{-2}. This threshold is in excellent agreement with the value predicted by the relation shown in Figure 5-1 of this work. For $E_\ell > 0.35$ J·cm^{-2} a single-photon dependence was observed, $I \propto (E_\ell)^{1.05}$. The difference in epitaxial growth observed at $D_{st} = 5.7$ cm and $D_{st} = 10.8$ cm for $E_\ell > 0.35$ J·cm^{-2} appears to be related to the nonthermal behavior and increased kinetic energy of the ablated species that were observed at these higher energy densities. Figure 8-3 shows TOF spectra of the ionized plume species for $E_\ell = 0.84$ J·cm^{-2} and $D_{ct} = 3$-10 cm. As the plume expands, the various peaks coalesce. This data is consistent with thermalization of the ionized species due to collisions within the plume. As this occurs, the translational kinetic energies of the plume constituents also decrease, and the distribution becomes Maxwellian with T_{eff} (10 cm)/T_{eff} (7 cm) ~ 0.9. Further, the total energy of all the constituents is reduced because of the free expansion of the plume. Thus, at the higher E_ℓ (i.e., in the nonthermal regime) and for short D_{st}, the growing film is damaged by the energetic species in the plume, and it is this damage that is responsible for the lack of epitaxial growth. At longer D_{st}, the incident species have a lower average translational energy because ofthis free expansion and thermalization process. Consequently, the growing film is not damaged and epitaxial growth can proceed.

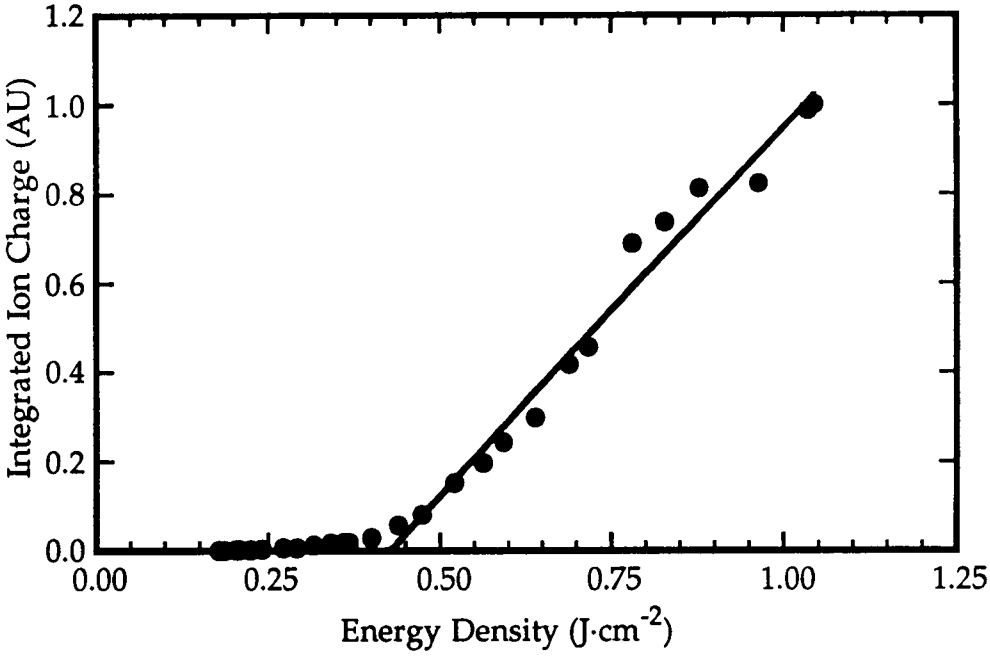

Figure 8-2 Relation between integrated ion signal of ZnS and energy density.

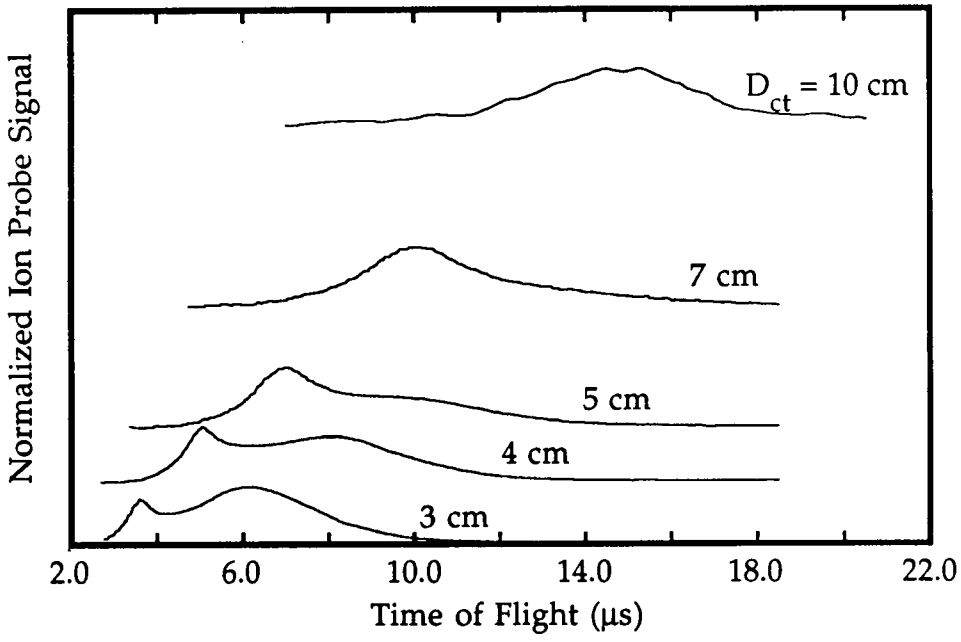

Figure 8-3 Normalized time of flight spectra spectra vs target-collector separation (D_{ct}), for perspective the spectra have been offset vertically by an amount proportional to the D_{ct} of that spectra.

Film Thickness Uniformity

ZnS films were grown on ~ 2 cm x 2 cm Si(001) substrates using 2000 laser pulses at E_ℓ = 0.25 J·cm^{-2}, vacuum ambient, and D_{st} = 5.7 cm to evaluate the growth of uniform thickness films using the rotation-offset geometry (see Chapter 5). Each substrate for these experiments was centered on the rotational axis of the substrate heater. In all cases this resulted in the deposition being circularly symmetric about the center of the substrate. Figure 8-4 shows the variation in thickness, measured along the horizontal centerline (scan direction A, Figure 8-4 inset), for a film grown with an offset of ρ = 0.6 cm. The film thickness also was measured along directions at 45° and 90° to this centerline (scan directions B and C, Figure 8-4 inset). The same variation in thickness was observed for all three measurements because of the symmetry of the deposition about the center of rotation. The average thickness across the entire substrate was 159.75 nm. The maximum deviation from the average thickness was 3% (4.8 nm) over the entire deposition (~3 cm^2), and 1.8% (2.9 nm) across the ~0.7 cm^2 center region. The average change in total thickness, dL/dr, across this central region is 12.6 nm·cm^{-1}, which corresponds to a change in relative thickness of 7.9 %·cm^{-1}. Taking this experimental offset (ρ = 0.6 cm) as being nearly optimal (because of the good uniformity) gives a $(D/\rho)_{opt}$ in the range 9 - 10.

At D_{st} = 10.8 cm, the variation in film thickness was consistently greater than that discussed above. Under these same deposition conditions, the optimal offset distance for this D_{st} would be ρ ~ 1.13 cm, which is greater than was permitted by the target radius and area struck by the laser beam (ρ ~ 1 cm). Nevertheless, a ZnS film was grown on a GaAs(001) substrate using 1650 laser pulses at E_ℓ = 0.25 J·cm^{-2}, D_{st} = 10.8 cm, and an offset ρ ~ 0.7 cm. The average film thickness was 257.1 nm, and theaverage change in total thickness was 30.0 nm·cm, which corresponds to a change in relative thickness of 11.7 %·cm.

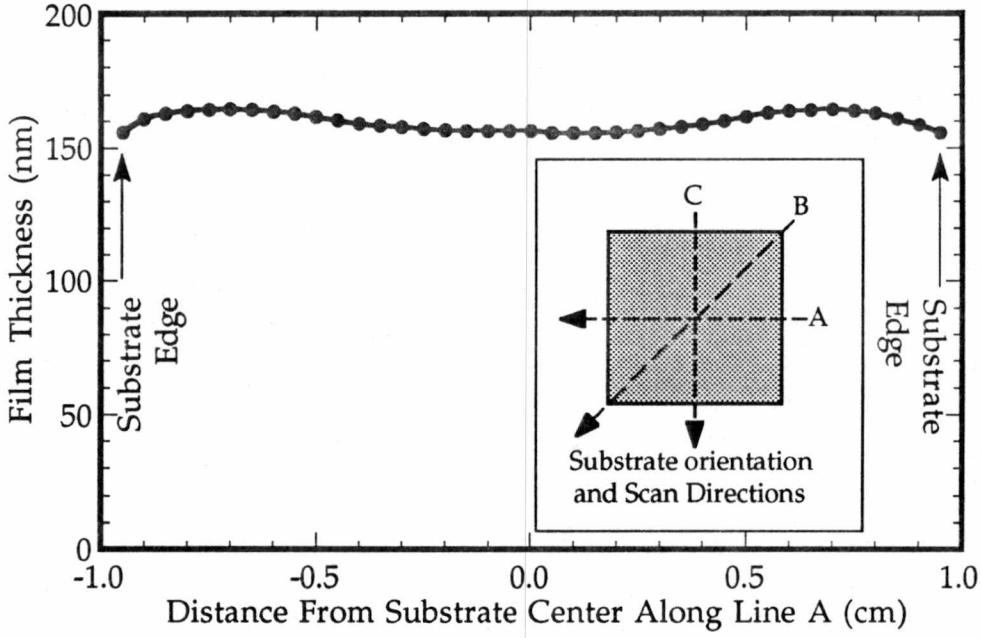

Figure 8-4 Experimental film thickness uniformity using offset-source pulsed-laser ablation.

Crystal Structure and Epitaxial Orientation of ZnS and ZnSe Films

X-ray diffraction data from the deposited films were used for much of the structure determination and characterization. Figure 8-5 shows the typical (and expected) $\theta/2\theta$ XRD patterns obtained using a 2-circle goniometer for ZnS films grown on GaAs(001). Figure 8-6 shows the corresponding data for the ZnSe films. Both figures include the peak locations for both the zinc blende and wurtzite structures of those materials and for the (zinc blende structure) GaAs substrate.

For both ZnS and ZnSe, no wurtzite reflections were present in those XRD patterns that also corresponded to the (00ℓ) reflections of the zinc blende structure. Thus, the zinc blende structure was unambiguously identified when these (00ℓ) reflections were present. Conversely, the use of ($\ell\ell\ell$) reflections in structure determination was ambiguous because this is the stacking direction for both the zinc blende and wurtzite structures. Indeed, the Cu K_α (111) XRD reflection from ZnS for the zinc blende structure and the (00•2) reflection for wurtzite are separated by only 165 arcsec. However, no reflections that could be associated with the wurtzite structure were observed from any films. Thus, films that showed the ($\ell\ell\ell$) reflections also were identified as having the zinc blende structure.

Only (00ℓ) reflections were found in the XRD patterns from ZnS and ZnSe films grown on GaAs(001) and GaP(001) substrates, using $E_\ell \geq 0.25$ J·cm^{-2} and $D_{st} = 10.8$ cm, for all growth temperatures investigated (T_g = 150-450° C for ZnS and T_g = 200-400° C for ZnSe). In addition, only ($\ell\ell\ell$) reflections were observed from films grown on GaAs(111) substrates. In no instances were (00ℓ) reflections observed from films grown on GaAs(111) substrates. As discussed above, ($\ell\ell\ell$) reflections were observed from films grown on (001) substrates only for $E_\ell < 0.25$ J·cm^{-2}, and may indicate that the wurtzite structure is formed for deposition with those energy densities. Taken together, these results show that ZnS and ZnSe films grown on GaAs(001), GaP(001) and GaAs(111) substrates, using $E_\ell \geq 0.25$ J·cm^{-2}, had only the zinc blende structure. These results also

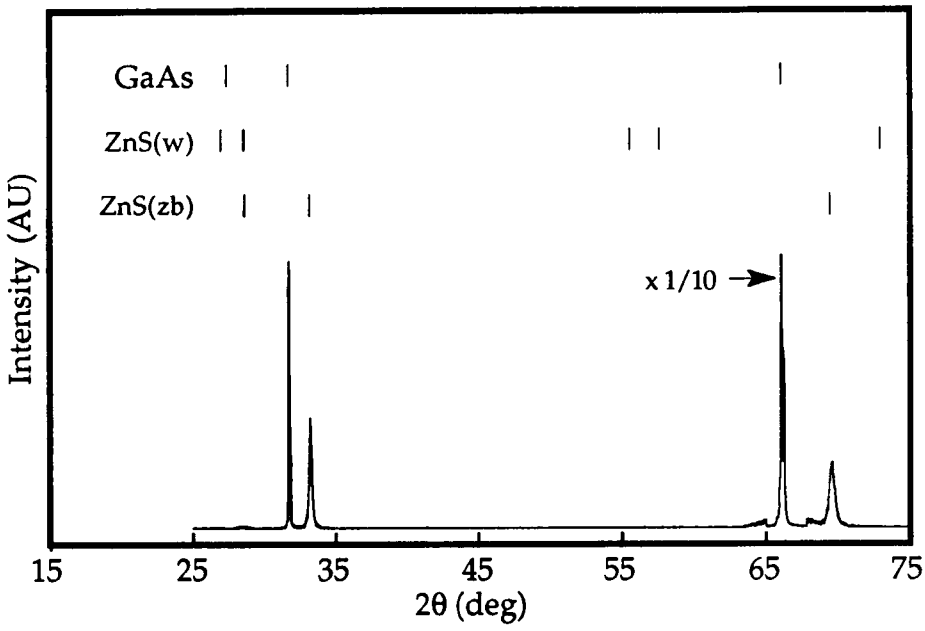

Figure 8-5 Typical x-ray diffraction pattern for ZnS/GaAs(001)

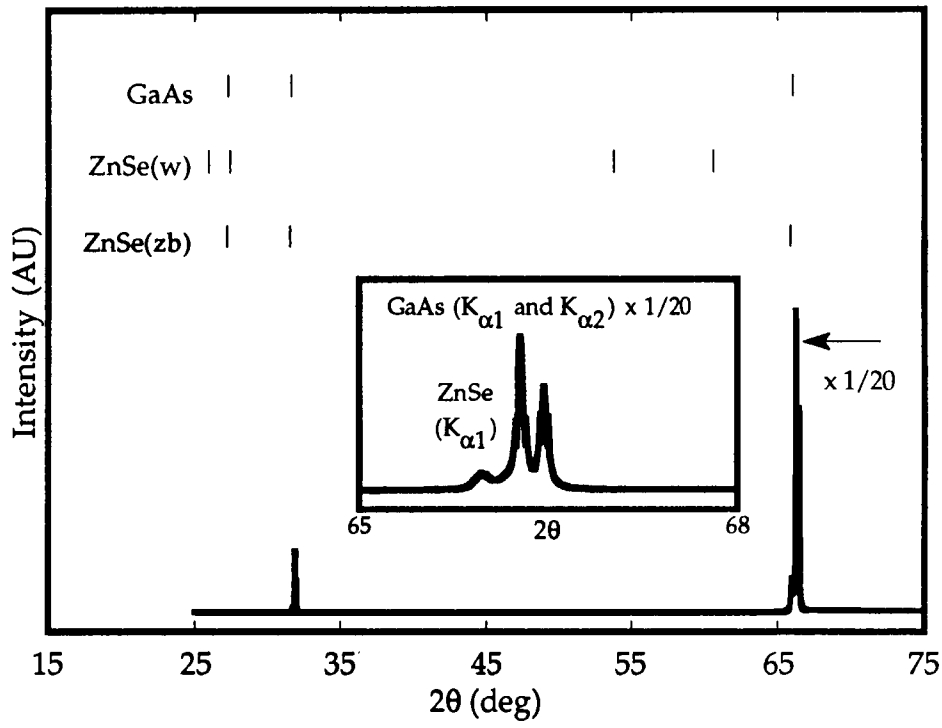

Figure 8-6 Typical x-ray diffraction pattern for ZnSe/GaAs(001)

demonstrate that the out-of-plane (i.e., (00ℓ) or (ℓℓℓ)) directions of the films were aligned with the out-of-plane directions of the underlying substrates.

The in-plane and out-of-plane alignments of the films, with respect to the underlying substrate, were determined more precisely by XRD using a 4-circle goniometer. The XRD pattern from a ZnS film grown on a GaAs(001) substrate showed that the angle between the ZnS(00ℓ) and the GaAs(00ℓ) was less than 0.2°, confirming their alignment along the out-of-plane direction. Figure 8-7 shows the XRD ϕ scan through the ZnS{202} reflections. The sharp peaks located every 90° shows that the in-plane ZnS and GaAs [100] and [010] also were aligned, i.e., there was true three-dimensional epitaxy.

The XRD pattern from a ZnS film grown on a GaAs(111) substrate showed that the angle between the ZnS(ℓℓℓ) and the GaAs(ℓℓℓ) was less than 0.4°, again confirming the alignment along the out-of-plane direction. Figure 8-8 shows the XRD ϕ scan through the ZnS {400} and {220} reflections respectively. The peaks located every 60° show that the in-plane directions of the ZnS and GaAs were aligned in two types of domains. This was confirmed in the ϕ scan through the {440} reflections of this sample. The more populated domain (as indicated by greater peak intensities) was the one expected for three-dimensional epitaxy. The less populated domain was rotated by 60° (i.e., the film $[2\bar{1}\bar{1}]$ was aligned with the substrate $[11\bar{2}]$). A three-fold rotation symmetry is expected for the perfect zinc blende structure, while a six-fold rotation is expected for the wurtzite structure. The presence of the two unequally populated domains, each with a three-fold rotation symmetry, is consistent with a zinc blende structure with a large degree of hexagonal stacking. The relative content of hexagonal material in this film was 62%, and was found by taking the ratio of integrated intensities (e.g., the population of the domains) as the degree of anisotropy (α_{sf}). This result is not surprising, given that the (111) plane of growth is the plane of rotation for stacking faults.

The XRD pattern from the ZnSe film grown on a GaAs(001) substrate showed that the angle between the ZnSe(00ℓ) and the GaAs(00ℓ) was less than 0.04°, confirming alignment along the out-of-plane direction.

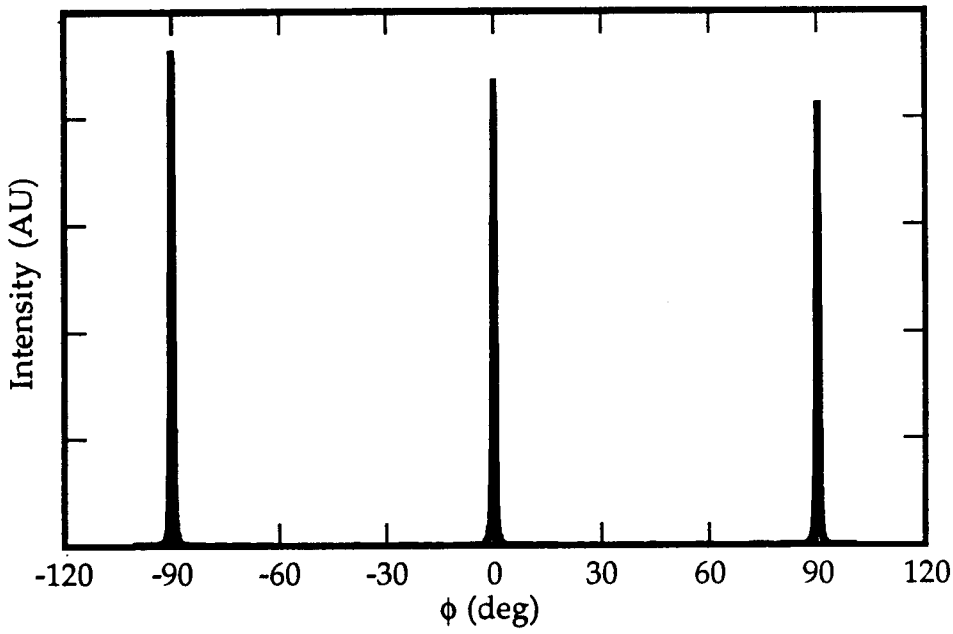

Figure 8-7 X-ray diffraction ϕ scan through the ZnS{202} reflections from ZnS on GaAs(001).

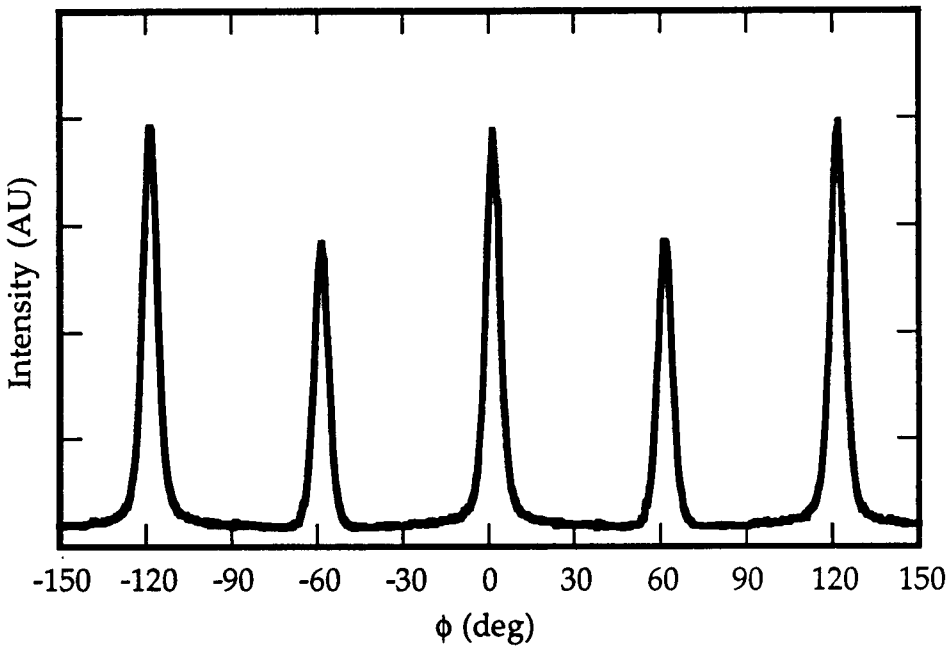

Figure 8-8 X-ray diffraction ϕ scan through the ZnS {220} reflections from ZnS on GaAs(111).

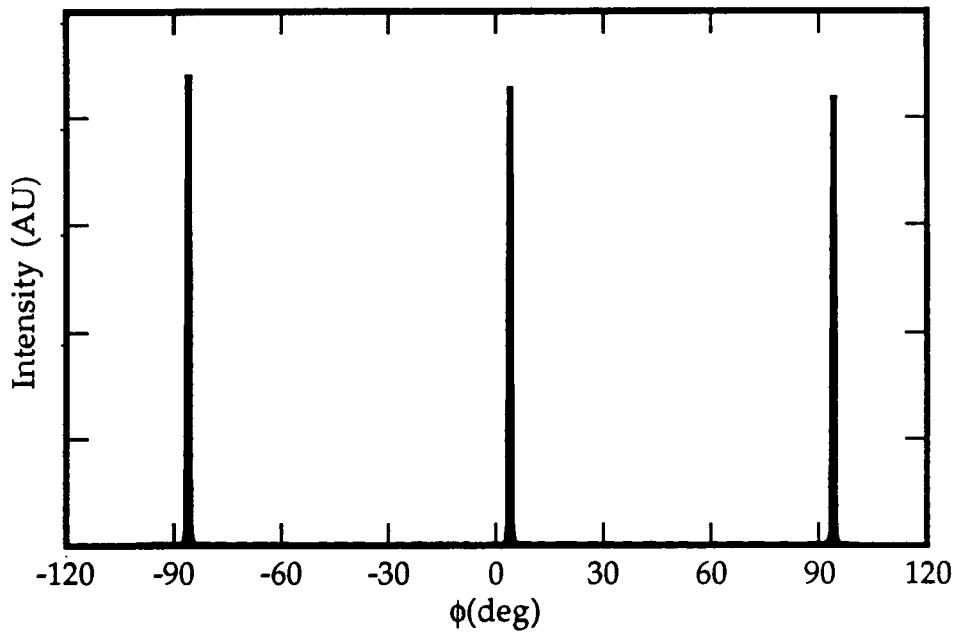

Figure 8-9 X-ray diffraction ϕ scan through the ZnSe{404} reflections from ZnSe on GaAs(001).

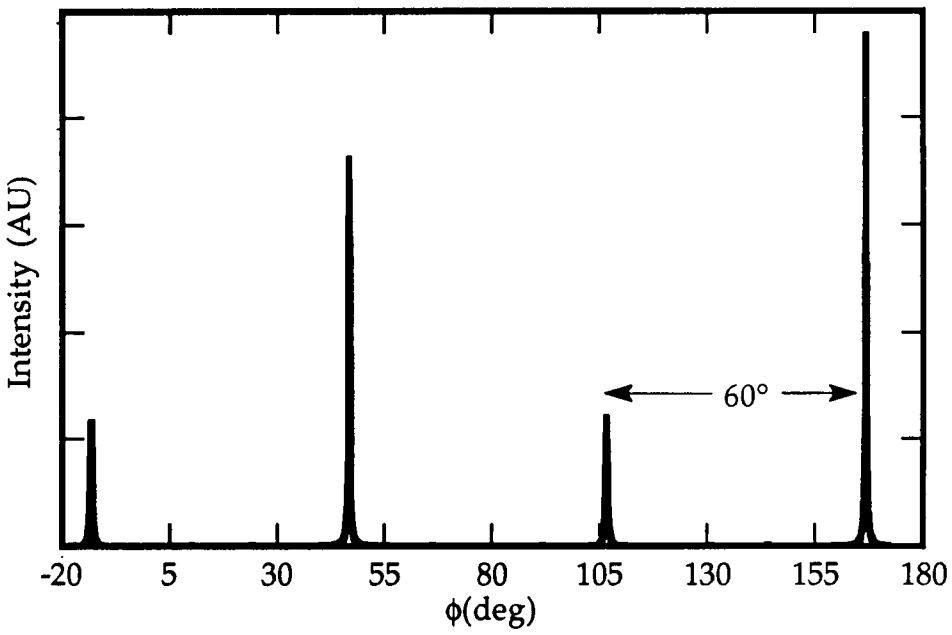

Figure 8-10 X-ray diffraction ϕ scan through the ZnSe {220} reflections from ZnSe on GaAs(111).

Figure 8-9 shows the ϕ scan through the ZnSe{404} reflections. The sharp peaks located every 90° shows that the in-plane ZnSe and GaAs [100] and [010] also were aligned, again indicating true three-dimensional epitaxy.

The XRD pattern from a ZnSe film grown on a GaAs(111) substrate showed that the angle between the ZnSe($\ell\ell\ell$) and the GaAs($\ell\ell\ell$) was less than 0.04°, confirming the alignment along the out-of-plane direction. Figure 8-10 shows the ϕ scan through the ZnSe {220} reflections. The peaks located every 60° indicate that the in-plane directions of the ZnSe and GaAs might have been aligned in two types of domains. These reflections are forbidden in the zinc blende structure; in spite of this, however, these reflections are often observed in real materials. Because of the nearness of the GaAs reflections, we cannot unambiguously that the reflections seen in these XRD patterns are not due to the occurrence of these 'forbidden' peaks from the GaAs substrate. This would make it difficult to distinguish the in-plane ZnSe peaks from the tails of the GaAs peaks. Thus, a definitive statement about the presence (or lack) of domains in the film, and their alignment with respect to the underlying substrate, cannot be made.

Crystalline Quality of ZnS Films Grown on GaAs

To quantify the crystalline quality and determine the optimal growth temperature a series of ZnS films (each ~275 nm thick) were grown at temperatures in the range T_g = 150-450°C and analyzed using rocking curve XRD (ω scan with fixed θ), obtained using the 2-circle goniometer. The resolution of this instrument in this configuration was $\Delta\omega$~288 arcsec as determined by the FWHM of the {004} reflection from the as-received GaAs(001) material. The corrected widths ($\Delta\omega_c$) of the rocking curves obtained from the films were determined by

$$\Delta\omega_c = \left[(\Delta\omega_m)^2 - (\Delta\omega_i)^2\right]^{1/2} , \qquad 8.03$$

where $\Delta\omega_m$ is the measured FWHM of the rocking curve from the film and $\Delta\omega_i$ is the instrumental resolution.

Figure 8-11 (top) show typical rocking curve line profiles for the ZnS(004) $K_{\alpha 1}$ reflections. Two superimposed peaks, one narrow and one much broader, were observed for each orientation. The narrow central peak has a FWHM of $\Delta\omega_c$ = 150-220 arcsec; the width of this peak did not change with growth temperature. However, for films grown on both the GaAs(001) and GaAs(111) substrates, the width of the second, broad peak was temperature dependent. For the ZnS(004) peak, the width of the rocking curve decreased as T_g increased, reaching a minimum of $\Delta\omega_c$ ~ 1400 arcsec at T_g ~325°C, then increased at higher growth temperatures (Figure 8-12). For the ZnS(111) peak, the rocking curve FWHM decreased continuously with increasing growth temperature (Figure 8-12). At T_g = 300°C, the integrated-area intensity ratios of the two peaks, I_{narrow}/I_{broad}, were $I_n/I_b(001)$ ~ 0.06 and $I_n/I_b(111)$ ~ 1.08.

The two peaks seen in the rocking curve line profiles are characteristic of films that contain two distinct types of crystalline material. The broad peak is due to diffraction by strained (or otherwise defective) regions, from which the diffracted amplitude is summed incoherently; the narrow peak originates from regions of coherent addition of the diffracted amplitudes. Consequently, for an epitaxial film, the relative intensities of the narrow and broad peaks provide information about the type of defects present, by the following reasoning. Stacking faults on the (111) planes have little effect on the lattice coherency in the ($\ell\ell\ell$) direction; thus, a narrow rocking curve is obtained. However, lattice planes intersected by stacking faults (e.g., the (00ℓ)) will be offset across the fault by a non-integral multiple of the lattice spacing. This decreases coherency and appears as broadening of the rocking curve. Therefore, the relative diffraction intensities (I_n/I_b) quoted above for the two rocking curve line profiles are consistent with (111)-plane stacking faults being the predominant defects in ZnS films.

The presence of a narrow (00ℓ) peak in the rocking curve profile indicates that a region of near-perfect (coherently diffracting) crystalline material exists. The location of this region of high crystalline quality material, and conversely the location of the poorer quality material, can be determined by RBS channeling. The RBS spectrum from a ~225 nm thick ZnS film grown on GaAs(001) in Figure 8-13 shows that the χ_{min} from the

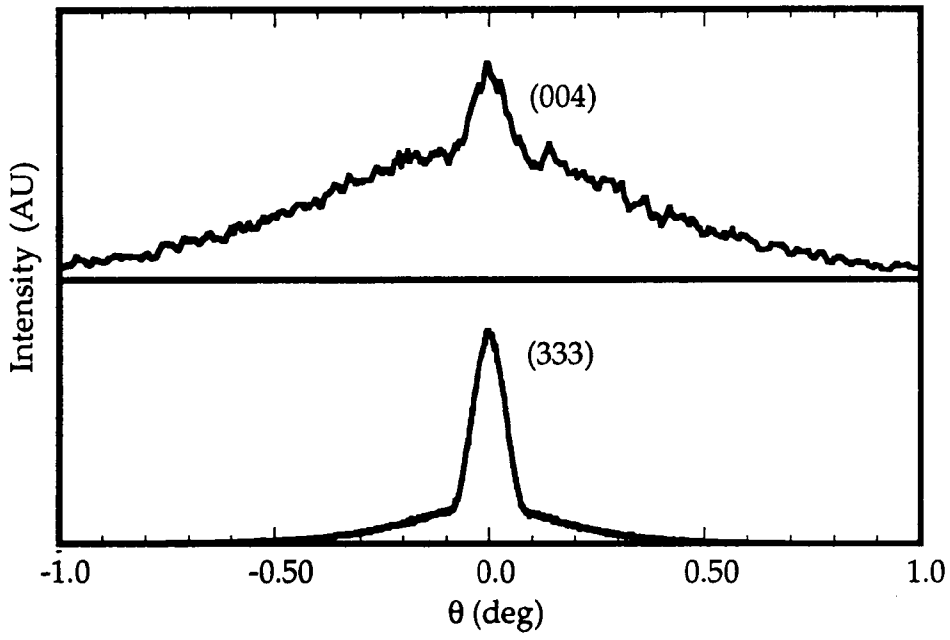

Figure 8-11 X-ray diffraction rocking curve profiles for ZnS(004) and ZnS(111) reflections.

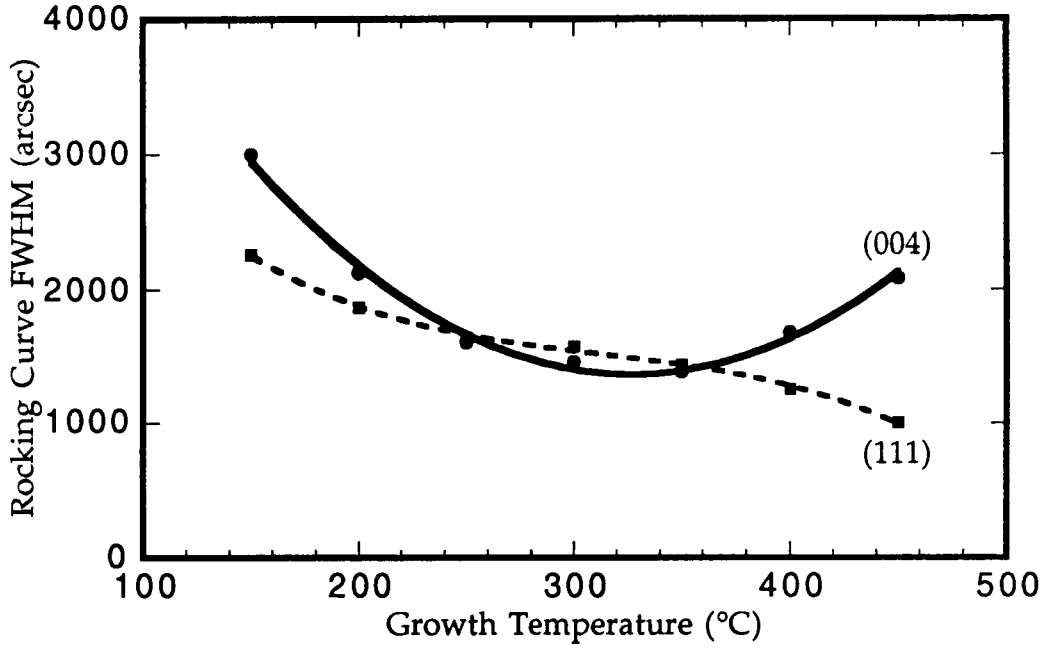

Figure 8-12 X-ray diffraction rocking curve widths of the ZnS(004) reflection from ZnS on GaAs(001) and the ZnS(111) reflection from ZnS on GaAs(111) at various T_g.

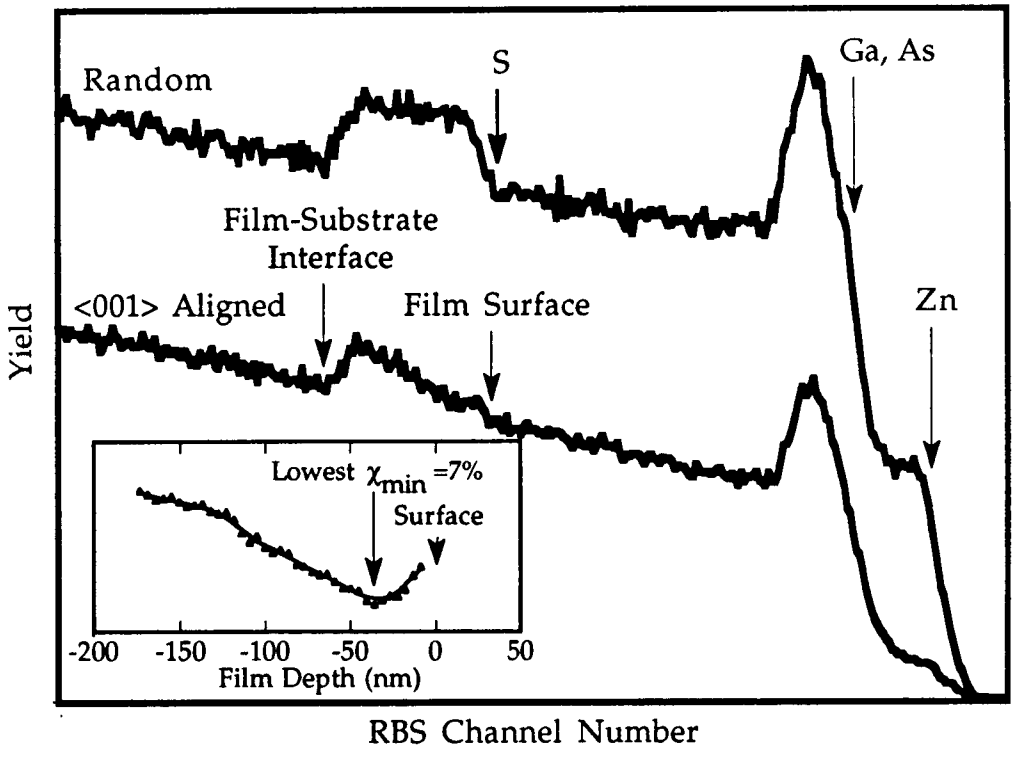

Figure 8-13 Rutherford backscattering spectra for ZnS on GaAs(001).

surface region is much less than from material near the film-substrate interface. (This is most easily seen from the difference in slope of the sulfur peak for the aligned and random spectra.) This indicates that most of the strain and defects are located near the interface, with the uppermost region of the film being near-perfect. The high quality of this near-surface region is evident by the small $\chi_{min} = 7\%$ measured ~40 nm from the film surface. This value compares well with the 3.5% χ_{min} predicted for a perfect and strain-free film (Chapter 7). The difference between these two values is likely due to the strain present in this thin film.

The location of the defective and near-perfect regions, and the hypothesis that stacking faults are the dominant defects, were confirmed directly by [100] cross-sectional TEM of a 275 nm ZnS film grown on GaAs(001). As seen in Figure 8-14 (top), the bottom ~150 nm of this film is highly faulted but the upper ~125 nm is much less defective. While some misfit dislocations are present at the film-substrate interface ("a" in Figure 8-14, bottom), examination of the defective region shows that twins (i.e., stacking faults) are the dominant defects ("b" in Figure 8-14, bottom).

The 3-D nature of the epitaxy is confirmed by the continuity of the lattice plane across the film-substrate interface seen in the cross-sectional TEM (Figure 8-14, bottom). This shows that the crystallographic orientation was preserved across this interface. This was found to be the case for the entire interface region investigated. Further, this continuity also was observed at the twin boundaries. All twins observed showed no change in crystallographic orientation across the twin boundary.

The density of stacking faults (ρ_{sf}) was quantified by measuring the broadening of the 2θ peaks of the (00ℓ) reflections and applying the method of Sebastian (Equation 7.04 and following). Extensive line broadening was observed in the (00ℓ) XRD reflections from the ZnS films grown on GaAs(001). For films grown at $T_g \geq 250°C$, the ZnS(00ℓ) $K_{\alpha 1}$, $K_{\alpha 2}$ peaks were deconvoluted using a Pearson VII function-fitting routine, but for $T_g < 250°C$ these peaks could not be deconvoluted. The $\Delta 2\theta$ values of the ZnS(002) $K_{\alpha 1}$ peak were 0.116°, 0.103° and 0.093° (corrected for instrumental broadening) for T_g's of 300°C, 350°C, and 400°C, respectively. For stacking faults bounded by <112>/6 Shockley partial dislocations, the average broadening observed here corresponds to an upper bound on the stacking fault density of $\rho_{sf} \sim 2.5 \times 10^{10}$ cm·cm^{-3}.

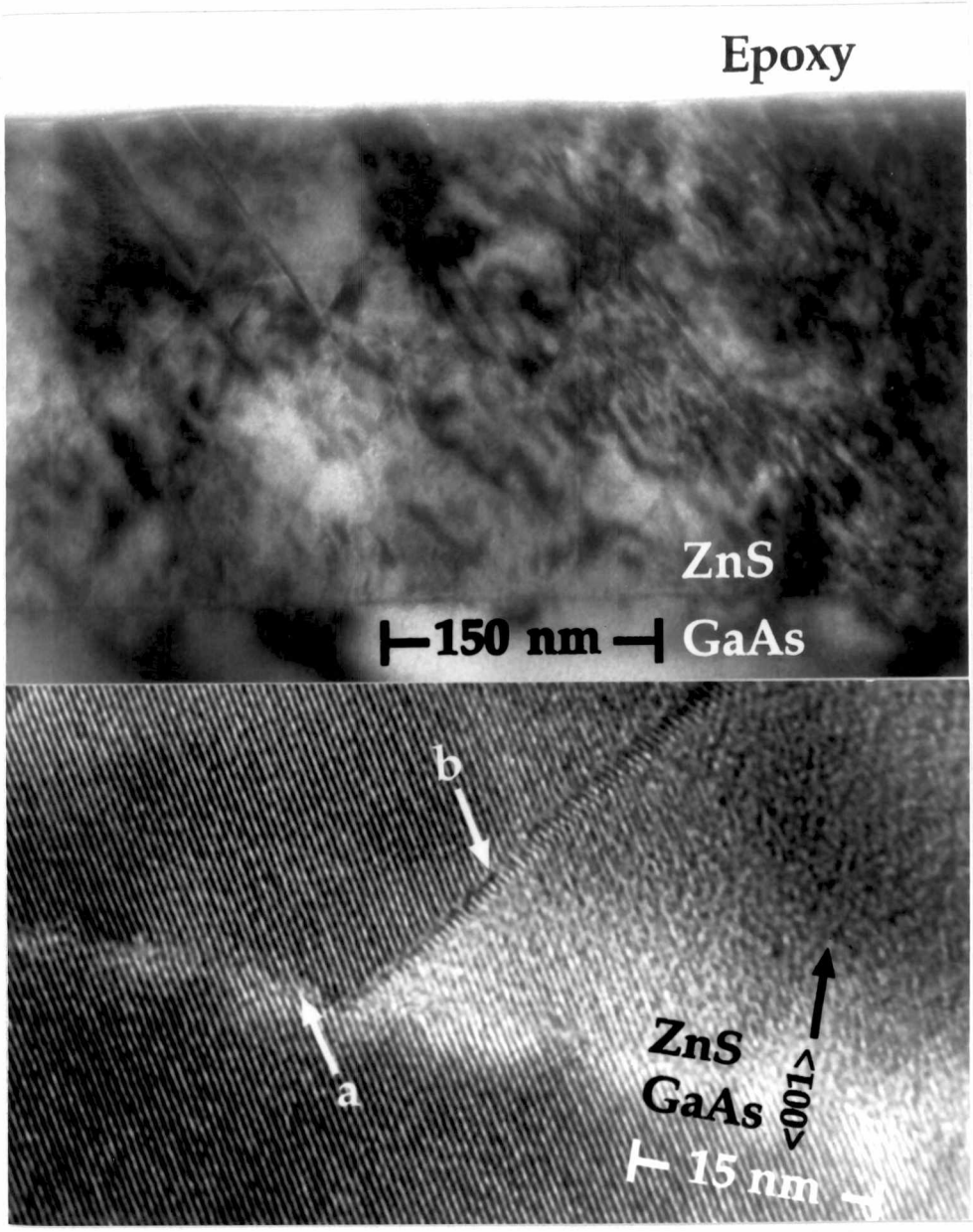

Figure 8-14 Cross-section TEM view of a typical PLA-grown ZnS thin film on GaAs(001).

As noted earlier, the narrow central peak had a width $\Delta\omega_c$ = 150-220 arcsec and originated from the top ~125 nm of the film. Application of the Scherrer equation shows that the intrinsic x-ray line broadening due to the finite thickness of the 125 nm layer is ~140 arcsec. Thus, only ~10-80 arcsec of the narrow central peak's width is due to mosaic spread in this region of the film.

For MBE-grown ZnS films on GaAs(001) the rocking curve widths are ~ 2000 arcsec for films 125-150 nm thick (Benz, 1988). Thus, the rocking curve widths of ~1500 arcsec from the ~150 nm defective region near the film-substrate interface and ~80 arcsec from the near-perfect region in the 125 nm near the film surface, indicate that the structural quality of ZnS films grown by PLA is better than that of MBE-grown material.

The strain present due to the lattice mismatch between the film and substrate was measured by calculating the out-of-plane lattice parameter from the position of the appropriate (00ℓ) or ($\ell\ell\ell$) reflection. This lattice parameter had the bulk value for all the ZnS films grown on GaAs, regardless of the growth temperature or substrate orientation. This was expected since the predicted critical thickness of ZnS on GaAs is 7 nm or less (Chapter 3). The actual critical thickness is much less. As seen in Figure 8-14 (bottom), the misfit dislocations which provide strain relief at the film-substrate interface are ~12 nm apart, which results in strain relief of 45.0 x 10^{-3}. This corresponds to a fully relaxed film, since at T_g ~ 300°C the in-plane (ε_{xx}) misfit strain for ZnS on GaAs is -44.9 x 10^{-3}.

Crystalline Quality of ZnS Films Grown on GaP

ZnS films were grown on GaP(001) during the experimental runs discussed above. Typically the (004) $K_{\alpha 1}$, $K_{\alpha 2}$ peaks from the films could not be deconvoluted using the Pearson VII function-fitting routine. While this was due in part to the close proximity of the GaP (004) reflections, the rocking curve widths shown in Figure 8-15 indicate that the films themselves were of much poorer quality than those grown on GaAs.themselves were of much poorer quality than those grown on GaAs. Although the GaP substrates were included during the growth of ZnSe (for completeness), the use of GaP as a substrate material was not pursued because of these results.

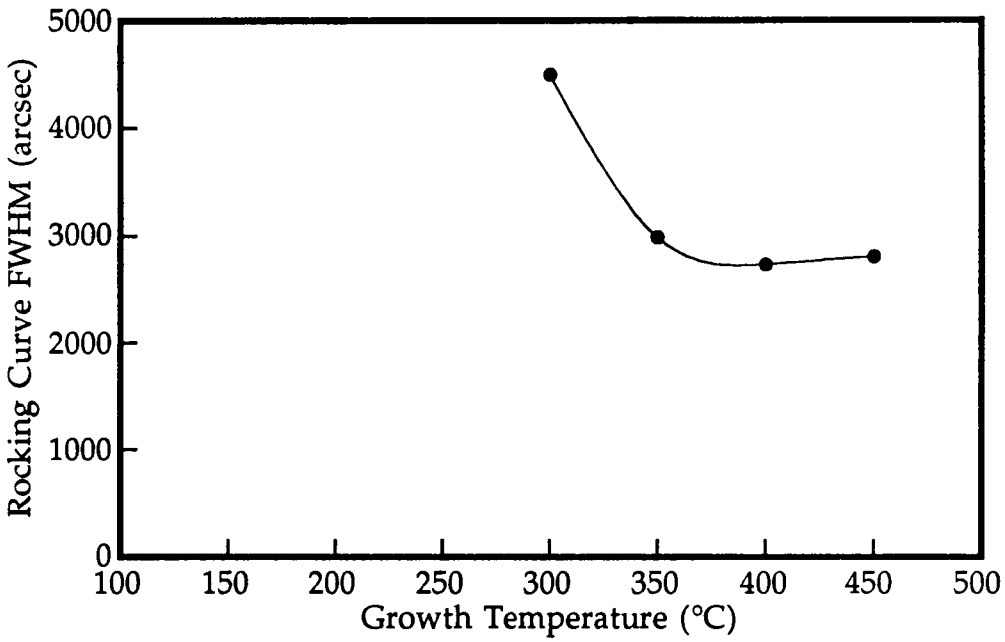

Figure 8-15 X-ray diffraction rocking curve width of the ZnS(004) reflection from ZnS on GaP(001) at various T_g.

Crystalline Quality of the ZnSe Films

In order to quantify the crystalline quality and to determine the optimal growth temperature, a series of ZnSe films (each ~275 nm thick) were grown at temperatures in the range T_g = 200-400°C and analyzed using the same methodology as was used for the ZnS films. For the ~275 nm thick ZnSe films grown on GaAs(001) at T_g > 300°C the rocking curves from the ZnSe(004) reflection showed only a single peak. In contrast, profiles from the ~275 nm thick films grown at T_g = 200 and 250°C had two superimposed peaks. As shown in Figure 8-16, the widths of both peaks were temperature dependent. The minimum width of the narrow peak was found at T_g = 250°C; however, the broad peak also was present in the rocking curve. For the film grown at T_g = 300°C, a single narrow peak was seen in the rocking curve, and the width of this peak was $\Delta\omega_c$ = 298 arcsec. Application of the Scherrer equation shows that the intrinsic x-ray line broadening due the 275 nm film thickness is ~125 arcsec. Thus, only ~175 arcsec of this broadening is due to mosaic spread in the film. This was the minimum width observed for films which showed only this single peak. The optimal growth temperature for ZnSe on GaAs was determined to be T_g = 300°C, because only a single (narrow) peak was observed with the minimum width at this T_g. On the other hand, a single, resolution-limited peak was seen in the rocking curve profiles of the (111) and (333) reflections from ZnSe films grown on GaAs(111), for all T_g.

The mass differences between Zn, Se, Ga and As are small, and the separation of the peaks in the RBS spectra depends on these differences. Thus, while the RBS data in Figure 8-17 showed that the near-surface region was of high crystalline quality (smallest χ_{min} = 6%), it was not possible to use RBS to locate definitively regions of poorer quality, or highly strained, material. Therefore, the existence of such a region could be confirmed only by growing thinner films. Indeed, the two superimposed peaks discussed above were only observed in the rocking curve profile for a film grown to a thickness of ~100 nm on GaAs(001) at T_g = 325°C. In this case, the integrated-area intensity ratio was $I_n/I_b(001)$ ~ 0.77. Based on this data, it is estimated that the region of poorer film quality is confined to the ~25-50 nm nearest the film-substrate interface.

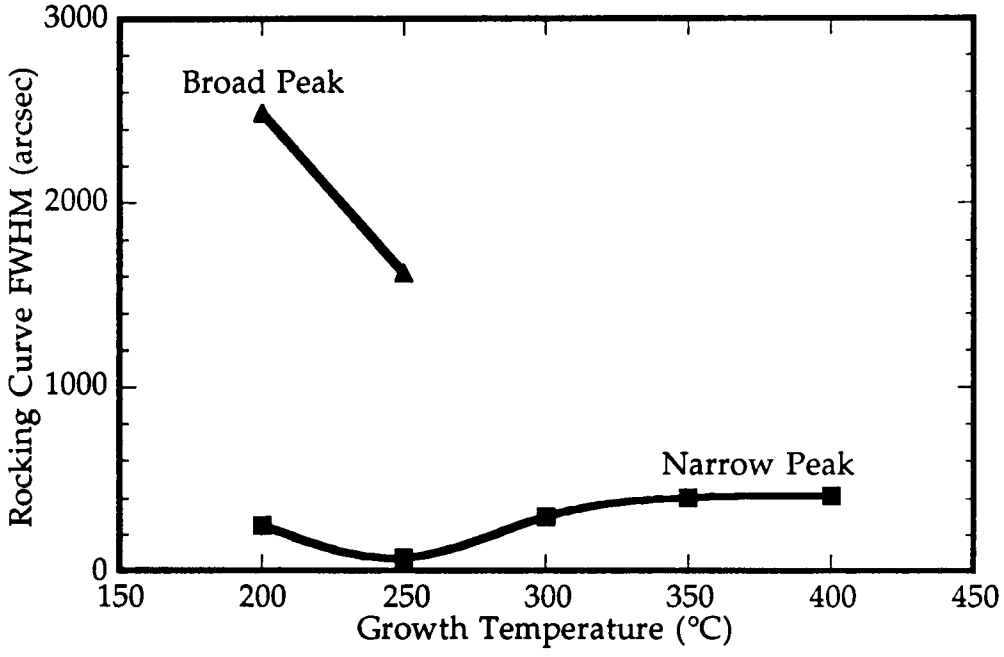

Figure 8-16 X-ray diffraction rocking curve width of the ZnSe(004) reflection from ZnSe on GaAs(001) at various T_g.

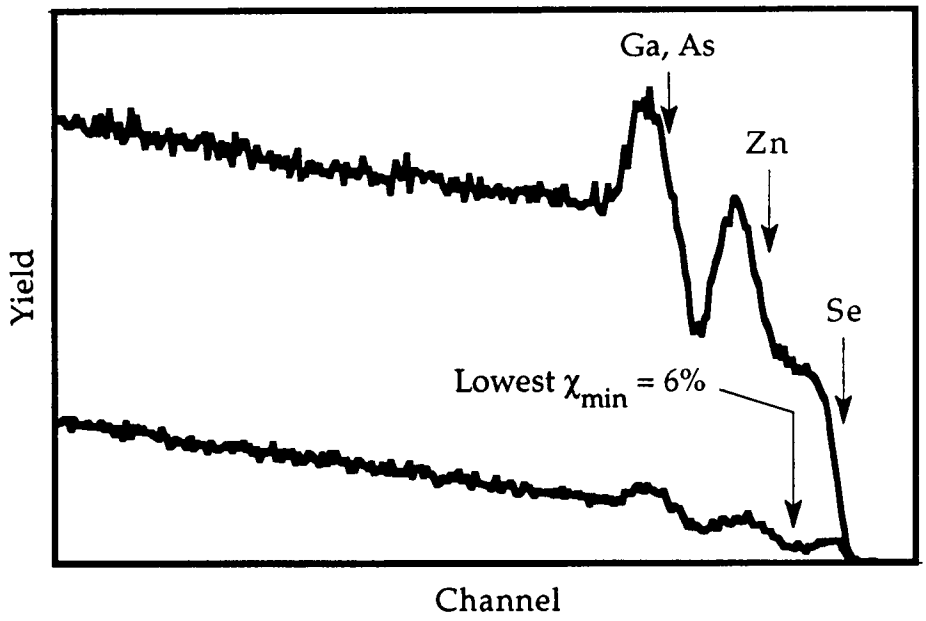

Figure 8-17 Rutherford backscattering spectra from ZnSe on GaAs(001).

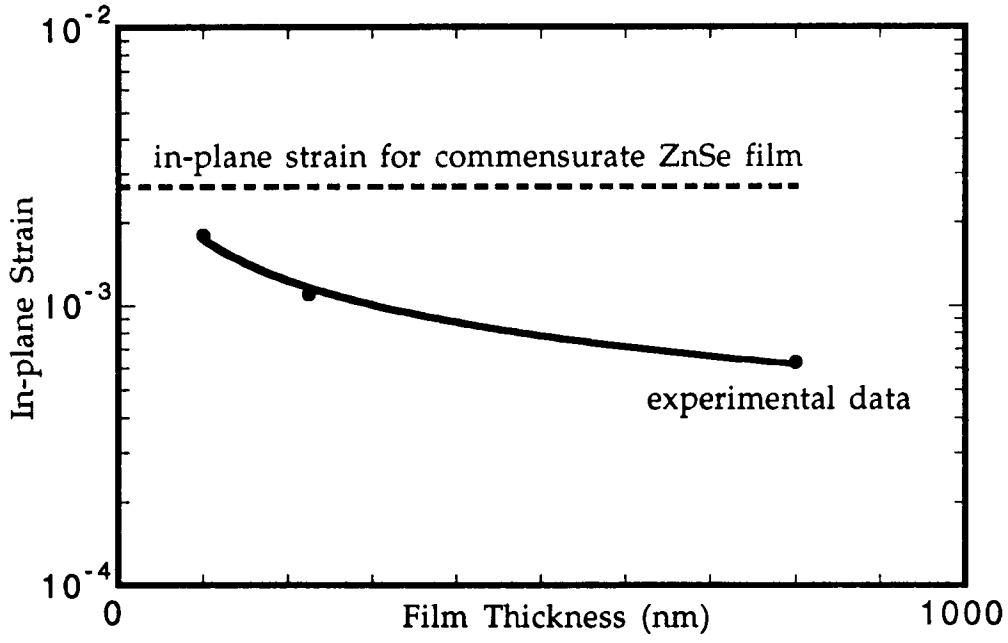

Figure 8-18 In-plane strain of ZnSe on GaAs(001) substrate for various film thicknesses. The line through the experimental data is a least squares fit to a power function ($\varepsilon = cL^n$).

The strain present due to the lattice mismatch between the ZnSe film and GaAs substrate was determined from the position of the $K\alpha_1$ (004) reflection. The in-plane strain ($\varepsilon_{xx}, \varepsilon_{yy}$) was 1.8×10^{-3}, 1.1×10^{-3} and 0.63×10^{-3} for film thicknesses of 100, 225 and 800 nm respectively. These strains correspond to 32%, 58% and 76% relaxation of the strain found in a fully pseudomorphic film. Extrapolation of this data using a power law fit (Figure 8-18) indicates that the film would be completely commensurate at thicknesses less than ~43 nm. This thickness coincides closely with the thickness of the region of film having poorer crystalline quality, and indicates that the presence of the broad peak in the rocking curve is due to strain in the commensurate region of film. This value (43 nm) is taken as the critical thickness (L_c) for ZnSe films grown under these conditions. Although this is less than the predicted and observed critical thickness of ~170 nm (Chapter 3), the rate of strain relaxation as the film thickness was increased is less than that observed by Olego (1988) for MBE growth of ZnSe on GaAs(001) at $T_g = 350°C$. In that work, the ZnSe films retained less than 4% strain at a thickness of 800 nm.

Stacking faults are not thought to be the predominant defect type in these ZnSe films because the presence of a broad peak in the rocking curve is related to the pseudomorphic strain. Misfit dislocations are generated to relieve strain, when films are grown to a thickness greater than L_c. The presence of line defects (e.g., misfit dislocations) broadens the XRD rocking curve. An upper bound on the density of these defects (ρ_d) was determined by applying the method of Tromson-Carli to the measured width of the rocking curve (Equation 7.07). The rocking curve width of 298 arcsec from the ZnSe(004) reflection, for a 225 nm thick film grown at the optimal T_g corresponds to a dislocation density within the film of $\rho_d = 1.6 \times 10^{14}$ cm^{-3}.

Band Structure of the ZnS and ZnSe Films

The band structures of the ZnS and ZnSe films grown on GaAs(001) were investigated by inspecting the dielectric function ($\varepsilon_1, \varepsilon_2$) of films grown at the appropriate optimal temperature. The dielectric function was measured in the 1.5-5.3 eV region using spectroscopic two-channel

polarization modulation ellipsometry (Chapter 7). To determine a film's dielectric function by this method it is necessary first to specify its layer–structure. A three-layer model was used, consisting of the GaAs substrate, the film, and a roughened film–surface layer. The thicknesses of the film and surface layer were determined using a single-term Lorentz approximation for the optical functions below the bandedge. The thickness of the surface layer was obtained by modeling that layer with the Bruggeman effective medium approximation, (i.e., it is assumed that the surface consists of 50% voids and 50% film). The thickness of this layer was typically ~2% of the total film thickness. Once the thickness of each layer was determined, the dielectric function was determined accurately across the full spectral range. Finally, the data was corrected for depolarization effects caused by a distribution in the film thickness uniformity (Jellison and McCamy, 1992).

Figures 8-19 and 8-20 show the spectral dependence of the dielectric function for ZnS and ZnSe films, respectively. The numerical values for the dielectric function are included in Appendices 2 and 3. The optical functions n and k were determined by

$$\langle n \rangle = \left[\frac{1}{2} \varepsilon_1 + \frac{1}{2} \left((\varepsilon_1)^2 + (\varepsilon_2)^2 \right)^{1/2} \right]^{1/2} \qquad 8.04$$

$$\langle k \rangle = \left[-\frac{1}{2} \varepsilon_1 + \frac{1}{2} \left((\varepsilon_1)^2 + (\varepsilon_2)^2 \right)^{1/2} \right]^{1/2} \qquad 8.05$$

and also are included in these Appendices. It can be seen that for both films ε_2 approaches zero below the bandedge, while spectral features are seen clearly just above the bandedges. The transparency ($\varepsilon_2 \sim 0$) of these films below the bandedge indicates that both the ZnS and ZnSe films are of high optical quality.

For the zinc blende structure of ZnS and ZnSe, the fundamental optical absorption edge corresponds to a direct transition (E_0) at the Γ-point in reciprocal space. Splitting of the valence band occurs by spin-orbit

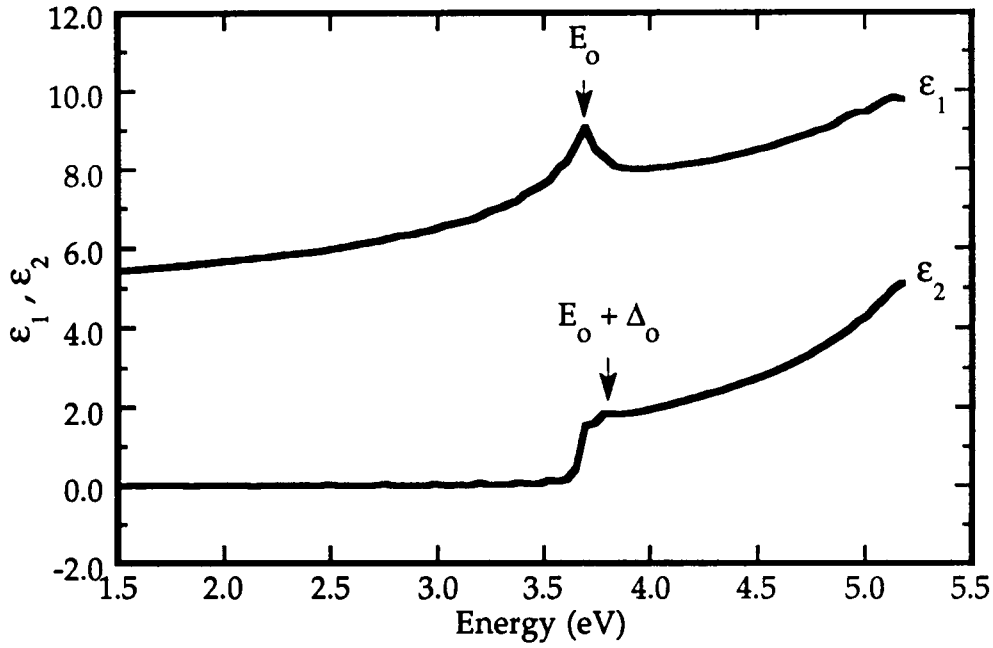

Figure 8-19 Spectral dependence of the dielectric function for ZnS grown on GaAs(001)

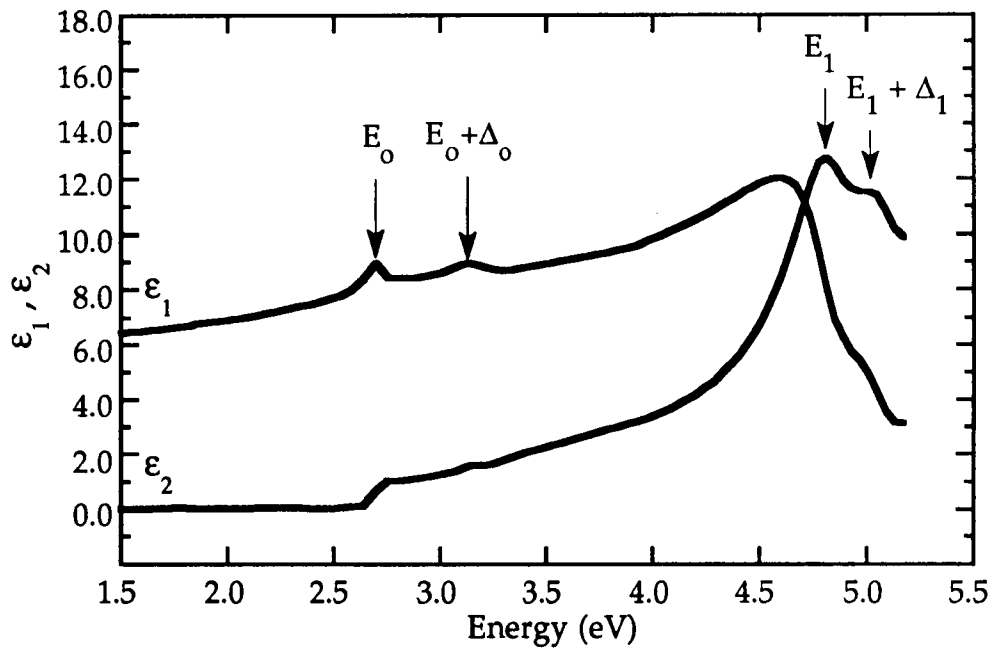

Figure 8-20 Spectral dependence of the dielectric function for ZnSe grown on GaAs(001)

Table 8-3
Experimental optical transitions, determined in this work and from the literature (references in brackets).

	E_0 (eV) $(\Gamma_8^v \rightarrow \Gamma_6^c)$	$E_0+\Delta_0$ (eV) $(\Gamma_7^v \rightarrow \Gamma_6^c)$	E_1 (eV) $(L_{4,5}^v \rightarrow L_6^c)$	$E_1+\Delta_1$ (eV) $(L_6^v \rightarrow L_6^c)$
ZnS	3.68 (3.68 [a])	3.76 (3.75 [b])	(> 5.5 [c])	(> 5.5 [c])
ZnSe	2.68 (2.68[d])	3.13 (3.10 [d])	4.80 (4.75 [d])	5.03 (5.05 [d])

[a] Bertho, D., Boiron, D., Simon, A., Jouanin, C., Priester, C., *Phys. Rev. B* **44**, 6118 (1991).

[b] Wu, Y., Ichino, K., Kawakami, Y., Fujita, S. Fujita, S., *Jpn. J. Appl. Phys.***31**, 1737 (1992).

[c] Walter, J. P., Cohen, M. L., *Phys. Rev.* **183**, 763 (1969)

[d] Adachi, S., Taguchi, T., *Phys. Rev. B* **43**, 9569 (1991).

interaction, with the splitting energy represented by Δ_0. A direct transition (E_1) is also present at the L-point in reciprocal space, with a corresponding spin-orbit splitting of the valence band (Δ_1). The E_0 and $E_0+\Delta_0$ transitions are clearly seen in the dielectric function spectrum of ZnS, while the E_1 and $E_1+\Delta_1$ transitions were not seen because they occur above the upper limit of investigation. The E_0, $E_0+\Delta_0$, E_1, and $E_1+\Delta_1$ transitions are all clearly seen in the dielectric function spectrum of the ZnSe films. Table 8-3 shows the location of transitions determined from this data and the corresponding literature values. There is excellent agreement with previously published values, indicating that the electronic band structure in these PLA-grown materials corresponds closely to that in materials grown by other methods.

Midgap Structure and Defect States in the ZnS Films

The midgap structure and electronic defect states in the bandgap were investigated by photoluminescence (PL) spectroscopy at temperatures in the range T = 9-298K. The peak assignments in these spectra are based on literature values and are considered tentative because a systematic doping study was not undertaken in this work.

Figure 8-21 shows a PL spectrum from an undoped 800 nm thick ZnS sample grown on GaAs(001) at T_g = 325°C. The excitation source for the PL was a CW He-Cd laser (E_x = 3.815 eV) and the spectrum was measured at T = 9 K. The deep emissions at 2.650 eV and 2.838 eV correspond to the SA (self-activated) and DE peaks observed by Yamaga (1988). Although Yamaga's spectrum was from an undoped sample grown by MOCVD, the sample was grown in an apparatus in which Cl and Al doping was being investigated. The SA peak clearly was associated with Al deep levels, but the origin of the DE was not determined. In our work, Al was present in the chamber construction and Cl doping had previously been attempted. It is possible that either of these impurities entered the film from the chamber. Thus, in this work the SA peak is attributed to an Al deep level and the DE peak to either Al or Cl deep levels. In either case, the presence of the SA peak is associated with zinc vacancy-donor complex (V_{Zn}-D).

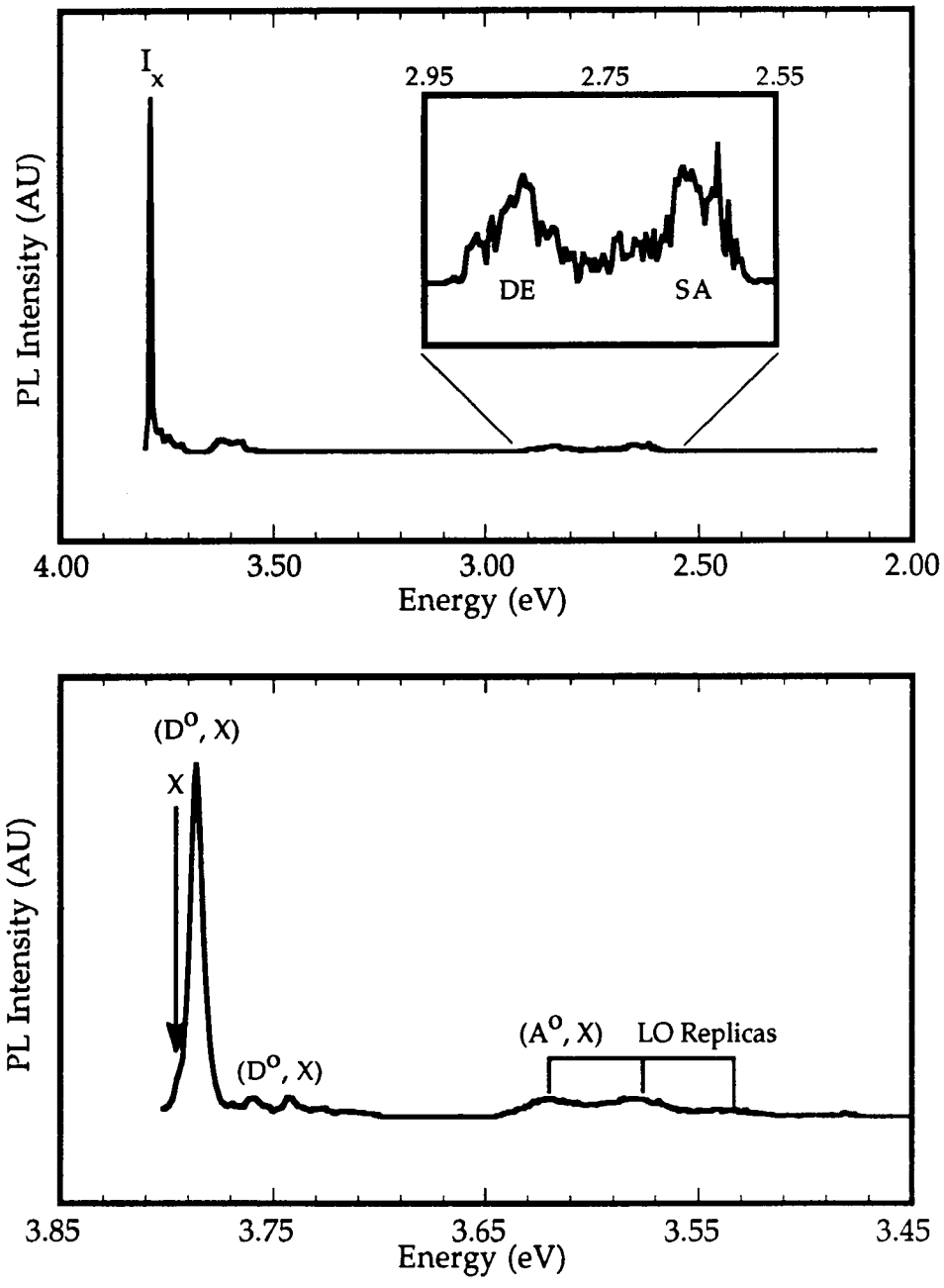

Figure 8-21 Photoluminescence spectrum from ZnS grown on GaAs(001).

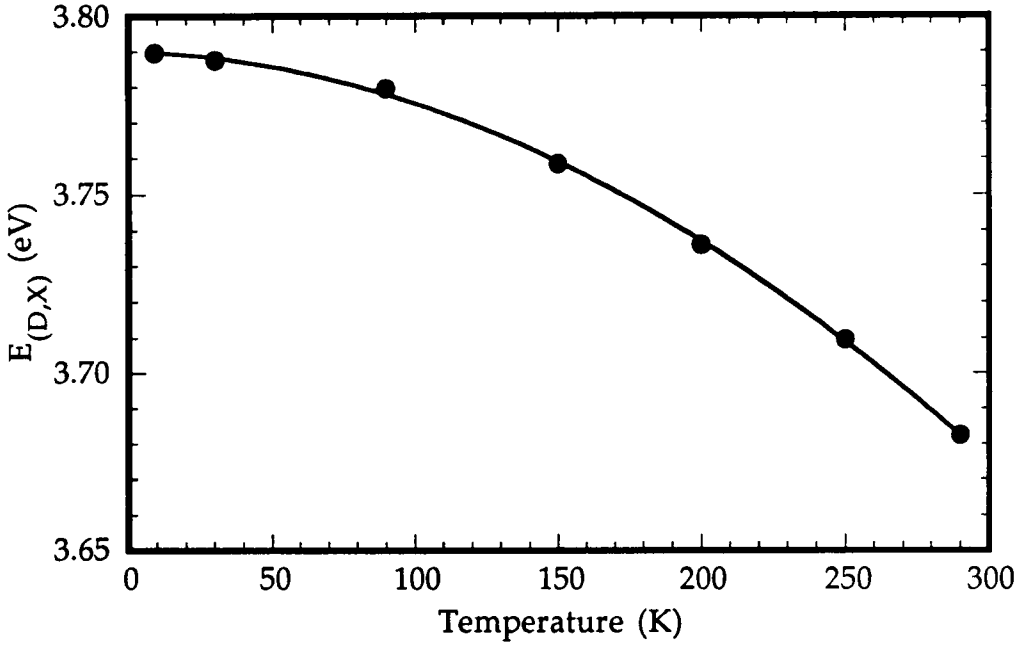

Figure 8-22 Temperature response of the 3.795 eV photoluminescence emission from ZnS grown on GaAs(001).

The peak seen at 3.618 eV is tentatively identified as being associated with an acceptor bound exciton (Kim, 1992). The associated LO phonon replicas were assigned based on a LO phonon energy of 45 meV (Chapter 2). Kanehisa (1988) has identified the peak located at 3.741 eV as due to emission from a shallow donor bound exciton. However, because of the presence of the peak at 3.795 eV in this work, his report that the peak at 3.786 eV is due to free exciton emission cannot be correct. Figure 8-22 shows the shift in position of the 3.786 eV peak at temperatures in the range T = 9 - 298 K. This shift is in good agreement with the corresponding change in Eg with temperature, so it is clear that this peak is due to emission from a bound exciton. Thus, it is likely that the peak at 3.795 eV is the free exciton, while the 3.786 eV peak is due to a donor bound exciton.

Although a number of deep and shallow levels are seen within the bandgap, the presence of the free exciton peak confirms the good quality of this film. However, all the undoped films were found to be semi-insulating, and this also was the case for homoepitaxial growth of ZnS by MBE (Kitagawa, 1989).

Midgap Structure and Defect States in the ZnSe Films

The midgap structure and electronic defect states in the ZnSe bandgap were investigated using the same methodology as was used for ZnS. Similarly, the peak assignments in these spectra are based on literature values and are considered tentative because a systematic doping study was not undertaken.

Figure 8-23 shows the PL spectrum from an undoped 230 nm thick ZnSe sample grown on GaAs(001) at T_g = 300°C. The broad, deep emission centered at ~2.24 eV is indicative of SA emission. The impurity source for this level is not known, but is possibly related to the presence of Cu impurity (Bylsma, 1987) from the target (0.08 ppm, Table 7-3). The peak seen at 2.608 eV is the Yo peak which is associated with the presence of misfit dislocations (Myhajlenko, 1984). The LO replicas were identified based on the phonon energy of ZnSe (E_{LO} ~ 35 meV; Chapter 2).

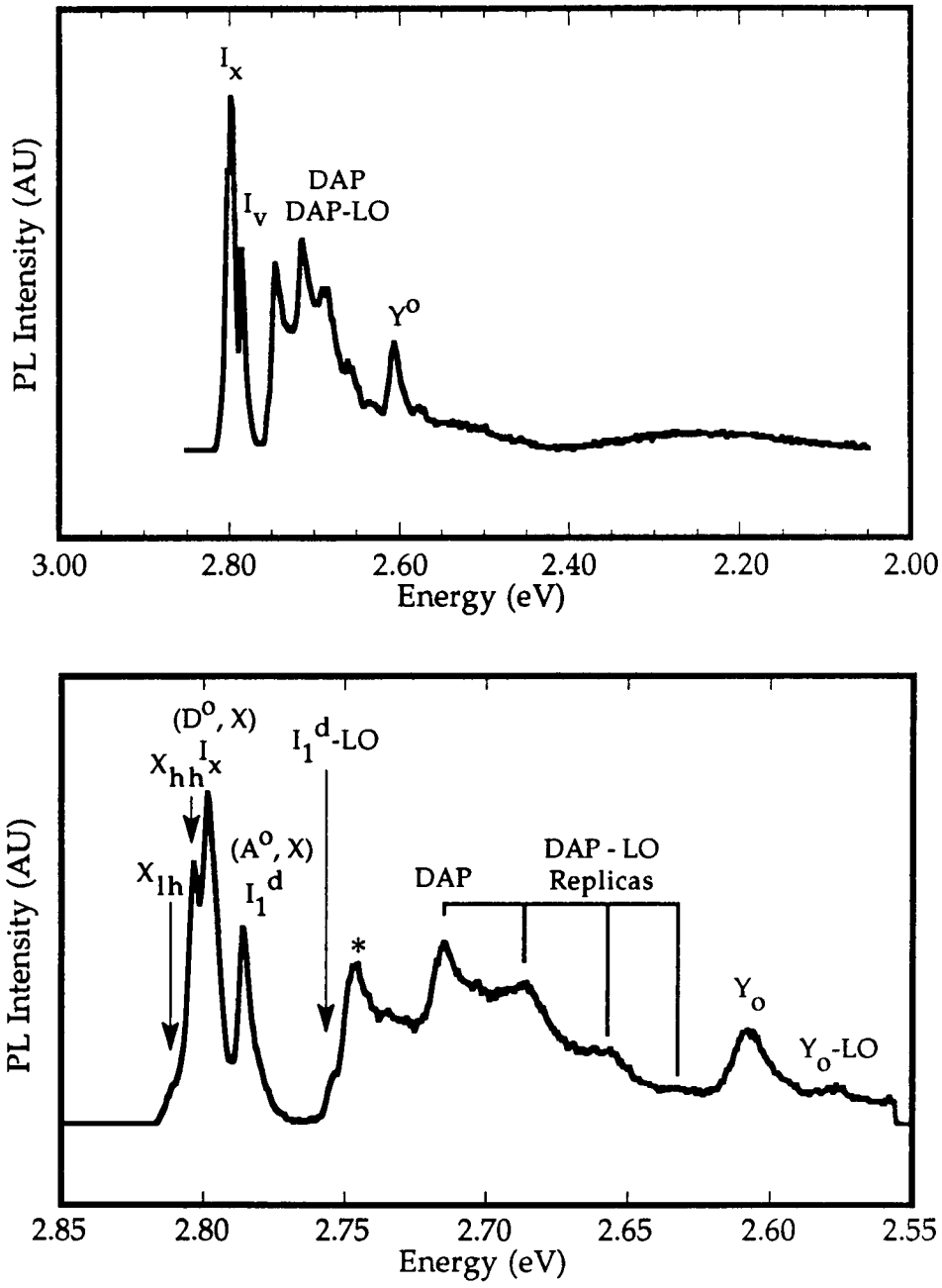

Figure 8-23 Photoluminescence spectrum from ZnSe grown on GaAs(001).

The emission at 2.715 eV (and the associated LO replicas at 2.687, 2.658, and 2.633 eV) is due to the presence of a DAP complex. The donor portion is associated with Ga which has diffused from the substrate. This DAP emission is often seen in thin ZnSe films grown by MBE but is usually not seen in films thicker than ~ 500 nm (Taguchi, 1992).

The peak (designated with a *) found at 2.746 eV (LO replica at 2.736 eV) could not be identified from the literature. The peak at 2.786 eV (LO replica at 2.754 eV) has no exact match in the literature either. However, the 2.786 eV emission is located near both the I_1 peak (2.784 eV; Gutowski, 1990), which is attributed to the V_{Zn} (acceptor) bound exciton, and near an unidentified shallow accepter bound exciton (2.7887 eV; Yao, 1986). Thus, this peak is tentatively identified as being associated with a neutral-acceptor bound exciton (A^o, X) of unknown origin. The strong emission at 2.798 eV is identified as a neutral-donor bound exciton (Yao, 1986).

The peaks at 2.8036 eV and 2.8112 eV are associated with the emissions from the heavy- (X_{hh}) and light-hole (X_{lh}) free excitons. The difference in the peak positions of these two emissions is due to the strain present in the films. The light-hole emission is on the high energy side because the strain is compressive. The strain can be determined from the splitting of these peaks (see Equation 3.05). The splitting observed here was caused by a strain of 1.6×10^{-3} (62% of fully commensurate) at 9K, which corresponds to a strain of 1.9×10^{-3} (74%) at 298 K. This value for the strain is in excellent agreement with that measured in the same manner for a comparable MBE-grown ZnSe film (Figure 2 of Olego, 1988).

ZnS-ZnSe Superlattice Structure

To determine if high quality superlattices of Zn-based II-VI wide bandgap materials can be fabricated using PLA, a structure of the form $(ZnSe)_m$-$(ZnS)_n$ was grown. This was grown at T_g = 325°C and consisted of a 65-period $(ZnSe)_6$-$(ZnS)_3$ superlattice grown on a 370 nm thick ZnSe buffer layer. The growth rate (measured *in situ*) was 0.167 nm per shot throughout this experimental run. Thus, to achieve a period of 5 nm the ZnSe target was ablated for 20 shots followed by 10 shots on the ZnS target.

The targets were changed *in situ* using the multitarget holder described in Chapter 7. A schematic representation of this structure is shown in Figure 8-24.

Figure 8-25 shows the $\theta/2\theta$ XRD pattern in the vicinity of the (004) reflection from this structure. Superlattice satellite peaks are easily seen. The period (L_{SLS}) of the SLS can be determined from the separation of adjacent superlattice peaks by Equation 7.12, such that

$$\sin(\theta_{\ell+1}) - \sin(\theta_{\ell}) = \frac{\lambda}{2\,L_{SLS}} \quad , \qquad 8.05$$

The separation between the peaks here corresponds to a compositional modulation period of L = 4.8 nm, which compares well (only 4% difference) with the desired value. The expected lattice constant parallel to the surface normal for a superlattice with this structure, calculated using Equation 3.07, is 0.556 nm ($2\theta = 67.3°$), in good agreement with the zeroth peak assignment ($2\theta = 67.54°$.) The other peak assignments shown in Figure 8-25 were made by approximating the superlattice as a $(ZnSe)_6$-$(ZnS)_3$ structure and calculating the diffraction peak positions using kinematical XRD theory (Budai, 1992).

The presence of several orders of satellite peaks indicates that this $(ZnSe)_6$-$(ZnS)_3$ superlattice structure has sharp compositional interfaces, and is structurally comparable to superlattices of other materials grown by PLA and to superlattices grown by other techniques. However, the thickness of this superlattice (312 nm) is ten times the critical thickness of a $(ZnSe)_n$-$(ZnS)_{2n}$ multilayer grown on a relaxed ZnSe buffer layer (~ 31 nm, Figure 3-1). Furthermore, based on the results above for ZnS films grown on GaAs(001), it is expected that the ZnS layers in this superlattice are faulted. Thus, the strain in the superlattice will be significantly relaxed and the defective layers will result in broadening of the superlattice peaks. The width of the satellite peaks in Figure 8-25 is ~ 2700 arcsec. The estimated width for a perfect 65 period SLS with this structure is ~ 60 arcsec (Lockwood, 1989). The excess broadening observed most likely is due to the effects discussed here.

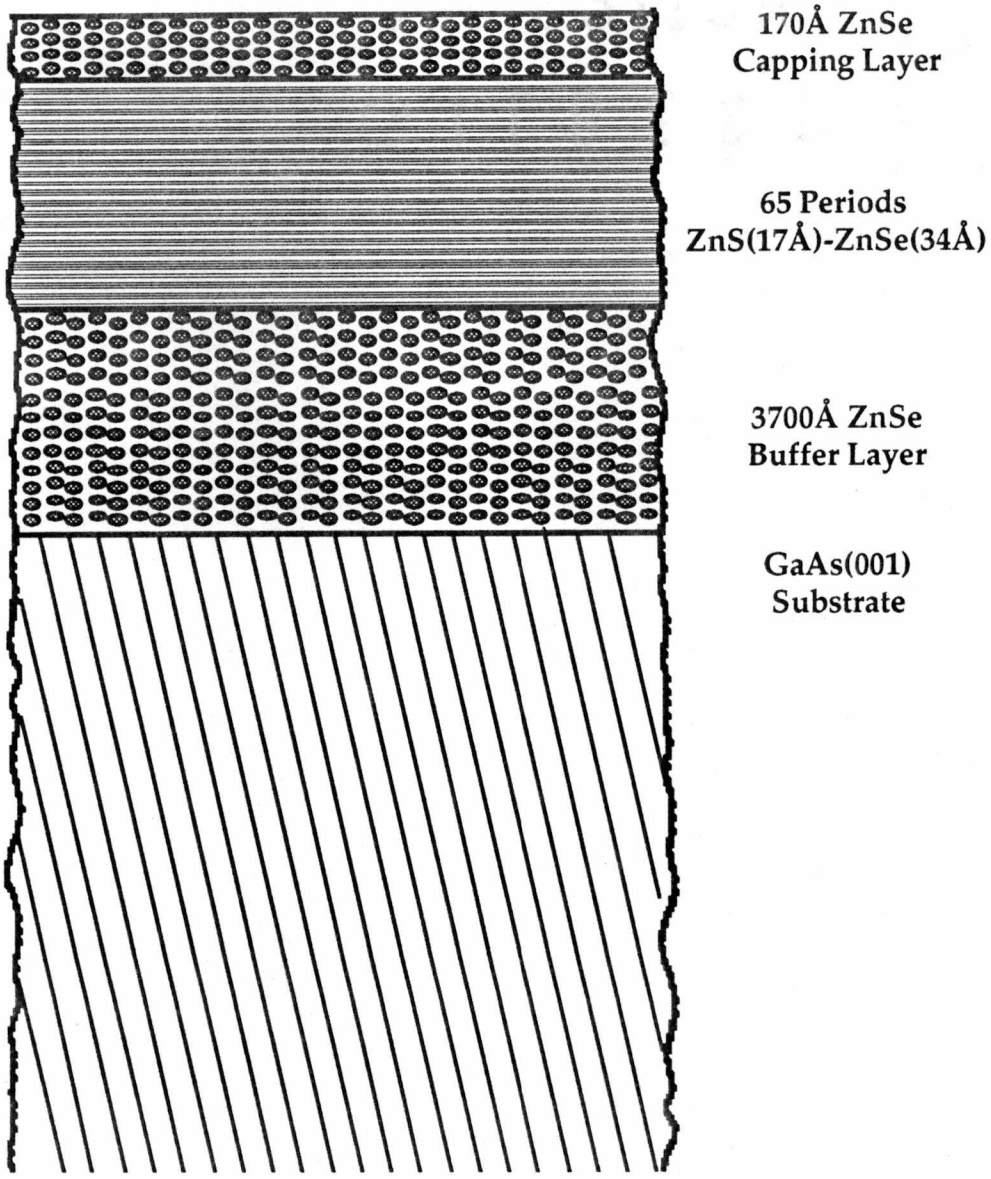

Figure 8-24 Schematic of the ZnS-ZnSe superlattice structure.

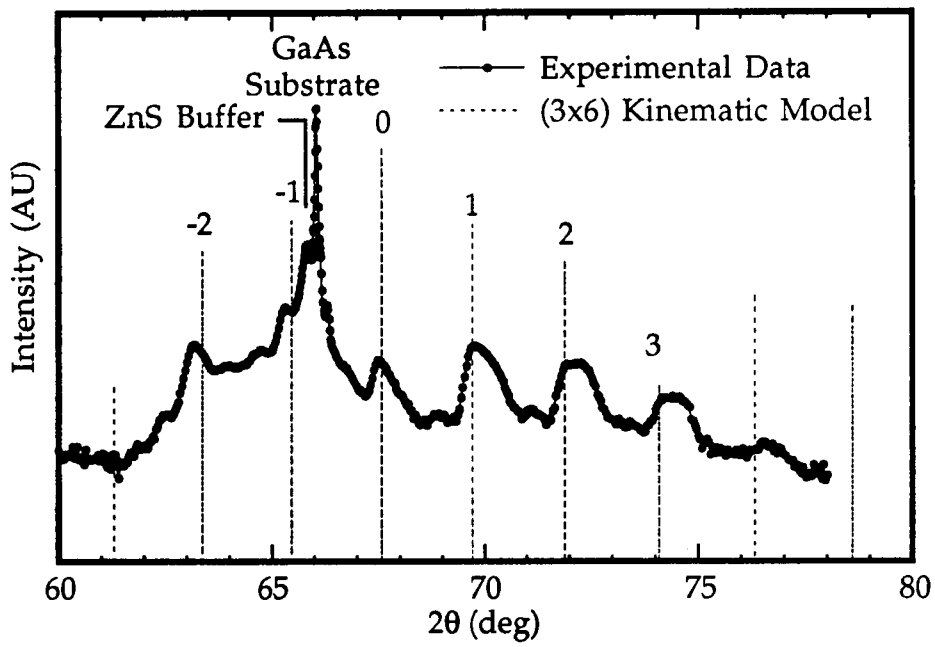

Figure 8-25 ZnS-ZnSe superlattice x-ray diffraction pattern near the (004) reflection.

Growth of $ZnSe_{1-x}S_x$ Alloy Films and Multilayer Structures

As discussed in Chapter 3, $ZnSe_{1-x}S_x$ alloys are required for fabrication of SLS to prevent the formation of defects associated with the strain relaxation that was observed in the ZnSe-ZnS structure. A new technique that utilized ablation of ZnSe into a low-pressure H_2S gas ambient was developed to fabricate $ZnSe_{1-x}S_x$ alloy thin films. This technique is based on either of the following reactions

$$MA + \zeta H_2B \leftrightarrows MA_{1-\gamma}B_\gamma + (\zeta - \gamma)H_2B + \frac{\gamma}{\xi}A_\xi + \gamma H_2 \qquad 8.06a$$

$$MA + \zeta H_2B \leftrightarrows MA_{1-\gamma}B_\gamma + (\zeta - \gamma)H_2B + \gamma H_2A \qquad 8.06b$$

Here M is the metal constituent and A and B are the chalcogen constituents. In this instance the B chalcogen hydride is in gas form and the prefix ζ is an arbitrary number representing the quantity of this hydride present; of this amount, γ is reacted to form the alloy. This results in an equal amount of chalcogen A being released from the metal. The final form of this chalcogen depends on its relative reactivities in the reactions

$$\gamma A \leftrightarrows \frac{\gamma}{\xi}A_\xi \qquad 8.07a$$

$$\gamma A + \gamma H_2 \leftrightarrows \gamma H_2A \qquad 8.07b$$

In Equation 8.07a, ξ is an integer and is determined by the resulting monoatomic molecular species (i.e., $\xi = 2$ for dimers, $\xi = 3$ for trimers, etc.).

A series of films were grown on GaAs(001) and GaAs(111) substrates by ablating a ZnSe polycrystalline target in an ambient of H_2S. The partial pressure of H_2S was varied by controlling the absolute pressure and adding He as a buffer gas. The data reported here were obtained using an energy density $E_\ell = 0.35\ J{\cdot}cm^{-2}$, $T_g = 325°C$, and a $D_{st} = 10.8$ cm. X-ray diffraction and room temperature PL measurements were used to determine the

lattice constant and the bandgap variation of these alloy films. The alloy composition was determined from the XRD measurements assuming Vegard's law. For the $ZnSe_{1-x}S_x$ alloy system this is

$$a_{ZnSeS} = (1-x)a_{ZnSe} + xa_{ZnS} \qquad 8.08$$

A number of films were grown in various H_2S partial pressures. Like the ZnS and ZnSe films, the XRD patterns from these alloy films grown on GaAs(001) showed only the (00ℓ) reflections, and ($\ell\ell\ell$) reflections from films grown on GaAs(111). Figure 8-26 shows the variation of sulfur content (x) with H_2S partial pressure. The three films at $P(H_2S)$ = 11.1 mTorr, 22.2 mTorr and 44.4 mTorr were grown first. These four data points (including $P(H_2S) = 0$) were found to be well fit by

$$x = A[P(H_2S)]^B \qquad 8.09$$

where A = 0.0278 and B = 0.493 ($\chi^2 = 4 \times 10^{-6}$) for the films grown on the GaAs(001). The ability to grow films having predetermined compositions was evaluated by using this relation to determine the H_2S partial pressure needed to grow an (001) oriented alloy film having x = 0.075. (The composition needed for exact lattice matching was avoided since success would be impossible to demonstrate by XRD measurement.) This film was grown using an energy density of $E_\ell = 0.35$ J·cm^{-2}, $T_g = 325$°C, and a $P(H_2S)$ = 7.48 mTorr. XRD of the (006) reflection showed that the resulting sulfur content for this $ZnSe_{1-x}S_x$ (001) film was x = 0.06, indicating that good compositional control is provided by the hydride partial pressure. Including this last data, the best fit of Equation 8.09 gives A = 0.020, B = 0.5905 ($\chi^2 = 7 \times 10^{-5}$) for the (001) films and A = 0.407, B = 0.515 ($\chi^2 = 4 \times 10^{-4}$) for the (111) films.

Since the composition could be controlled by the H_2S partial pressure, the composition of the film could be varied along the growth direction. An abrupt change in composition could be achieved by blocking the laser beam to stop growth, changing the H_2S pressure and then initiating growth again. The thickness of each layer is controlled by the number of laser

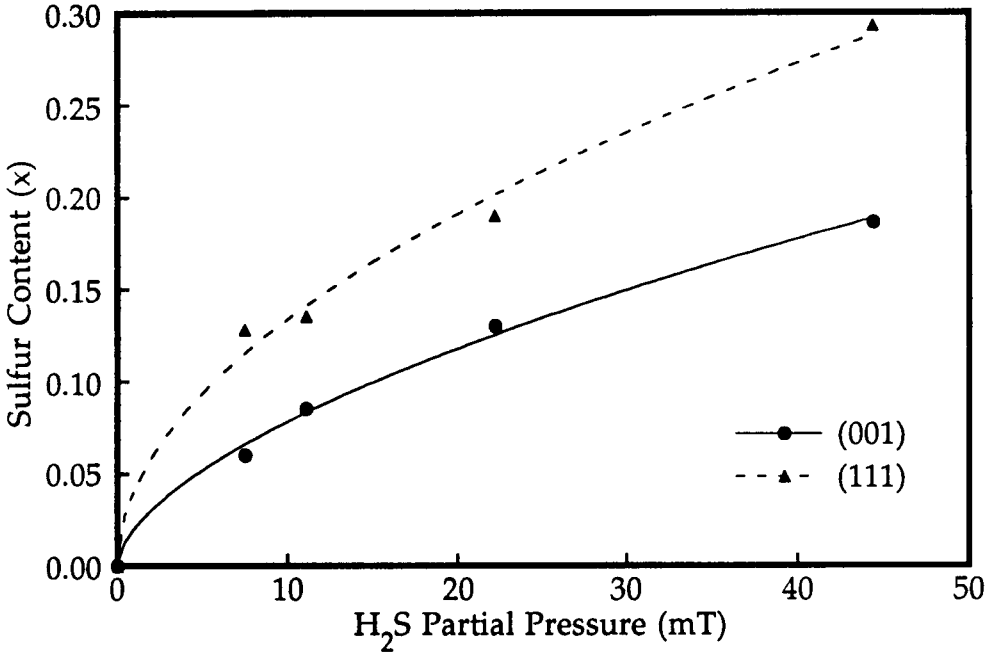

Figure 8-26 Sulfur content of PLA-grown films as a function of the ambient H_2S partial pressure. The lines through the data are least squares best fits of the form $x = A[P(H_2S)]^B$ (Equation 8.09 in the text).

shots, while each layer's composition is determined by the ambient H_2S partial pressure. By changing the pressure gradually without stopping growth, a layer having a continuously graded composition could be grown. To evaluate this spatial control over film composition, a $ZnSe_{1-x}S_x$ multilayer was fabricated that simultaneously incorporated both continuously graded and successive abrupt, periodic compositional changes. This structure is shown schematically in Figure 8-27 and was grown as follows. First, a $ZnSe_{0.94}S_{0.06}$ buffer layer was grown, in order to match lattice constants with the GaAs(001) substrate. The sulfur content then was increased to x = 0.18 and was held constant from 0 nm (top of the buffer layer) to 165 nm, but with a square-wave compositional modulation superimposed. Next, the average sulfur content was ramped down from x = 0.18 (at 165 nm) to x = 0.06 (at 600 nm). Finally, a pure ZnSe cap layer was grown. The resulting structure consists of 35 distinct epitaxial layers (including the buffer and cap layers), with 16 ½ modulation periods of 36 nm each. Figure 8-28 shows the idealized and measured sulfur profile of this structure. The sulfur (S^{32}) content was measured by SIMS (100 pA Cs^+) at the Oak Ridge National Laboratory. Because the depth resolution of the SIMS is only ~5-10 nm, the compositional modulation actually achieved is more abrupt than that shown in Figure 8-28.

Figure 8-29 shows the room temperature PL spectra from (001) $ZnSe_{1-x}S_x$ films grown with differing H_2S partial pressures. The PL peaks broadened and shifted to higher energy with increasing sulfur content ('x' as determined by XRD). The shift in peak position is consistent with sulfur entering the lattice on the selenium sites, while the broadening is consistent with random (disordered) sulfur incorporation. If the shapes of the bandstructures are similar for the two alloy constituents (e.g., ZnS and ZnSe), so that the location of the energy gap within the Brillion zone does not change, then the compositional dependence of the bandgap is described by the bowing parameter, b. For the ZnSe-ZnS system, b = 0.63 at 300 K (Mach, 1982). Alternatively, the bandgap-composition relation (Equation 2.09) can be inverted and the known variation of bandgap can be used to infer the sulfur content from the PL data. The sulfur fractions determined independently from the XRD and PL (the maxima in Figure 8-29)

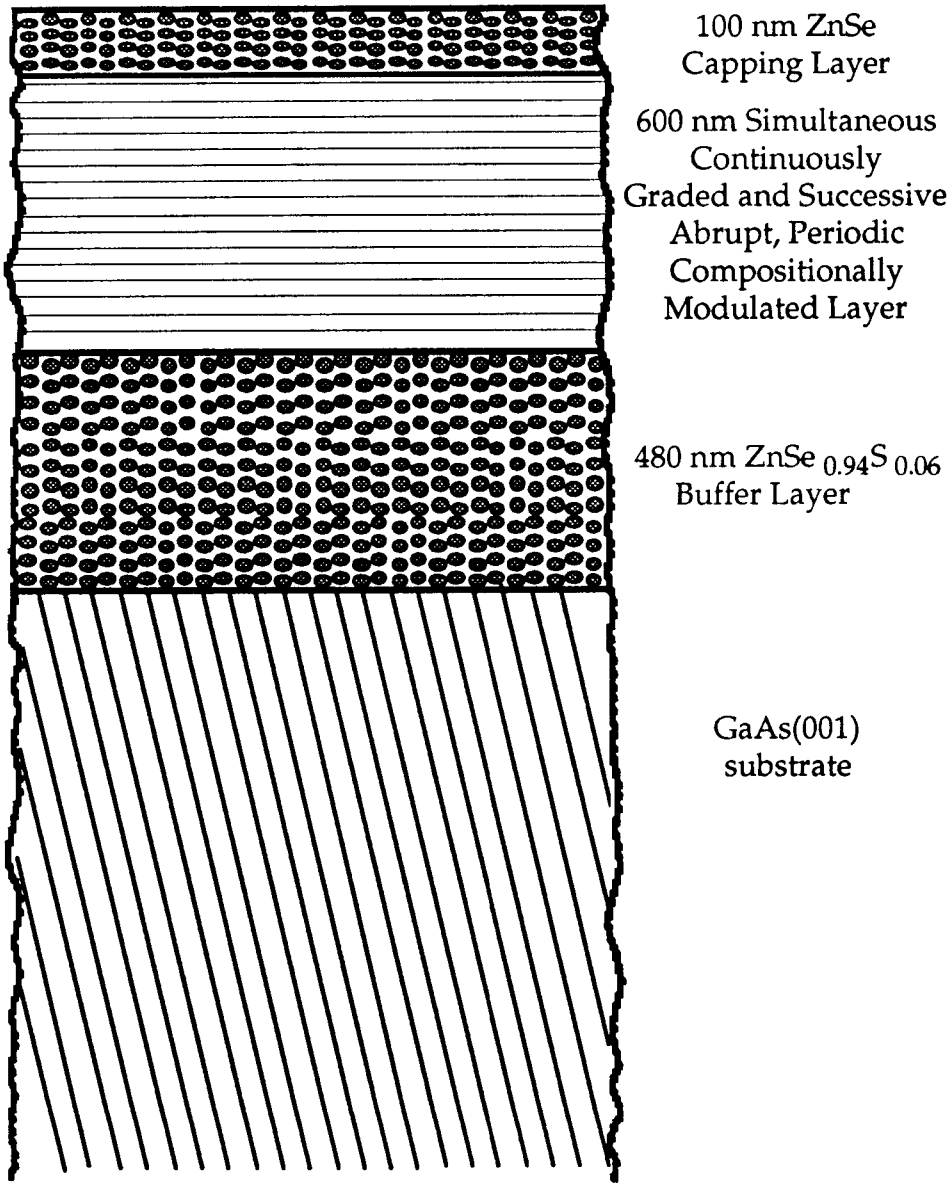

Figure 8-27 Schematic of the compositionally modulated PLA-grown structure.

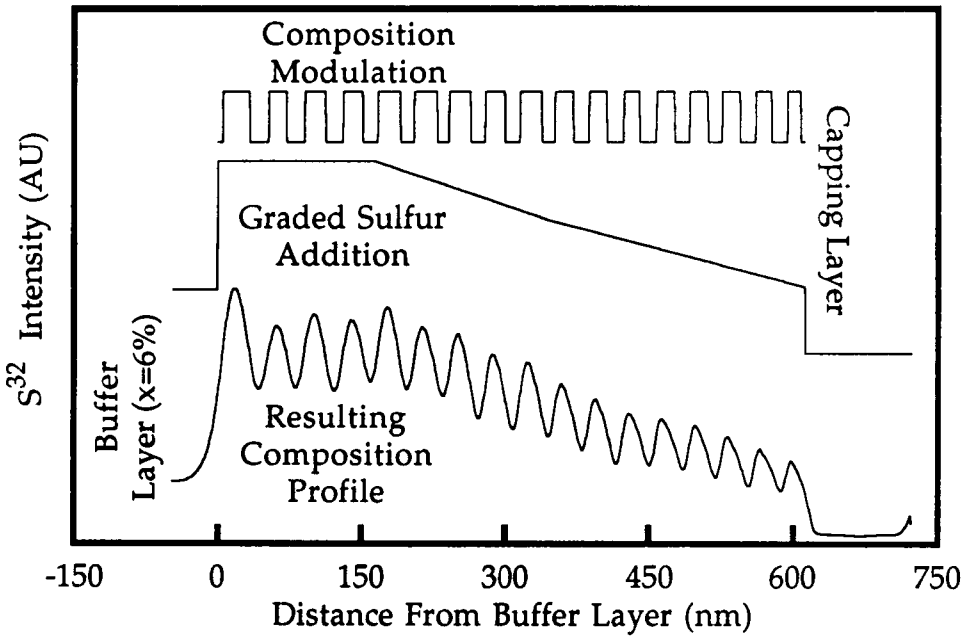

Figure 8-28 Secondary ion mass spectrometry profile of S^{32} content in PLA-grown compositionally modulated structure.

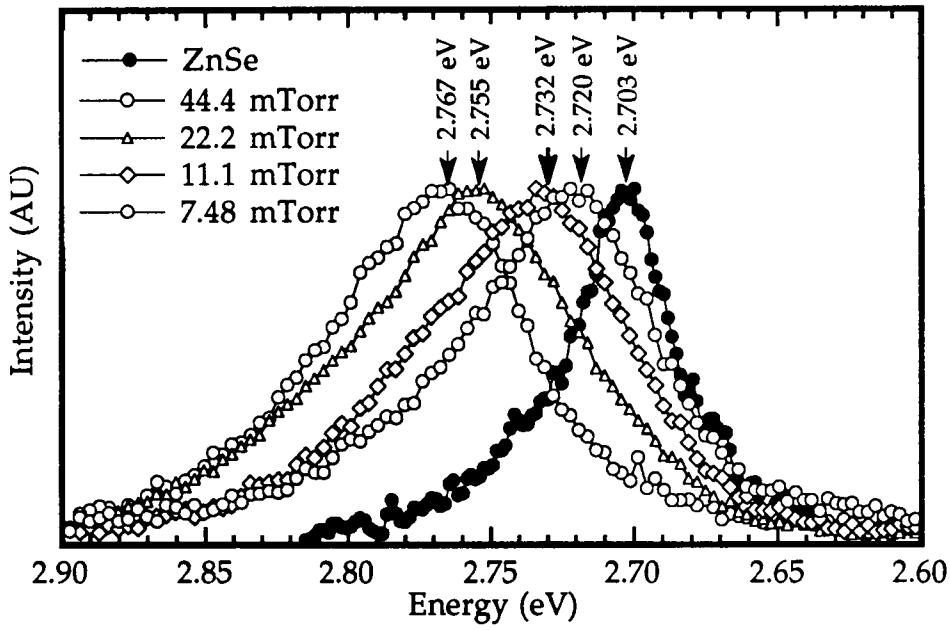

Figure 8-29 Room temperature photoluminescence spectra from PLA-grown $ZnSe_{1-x}S_x$ alloys at various H_2S partial pressures.

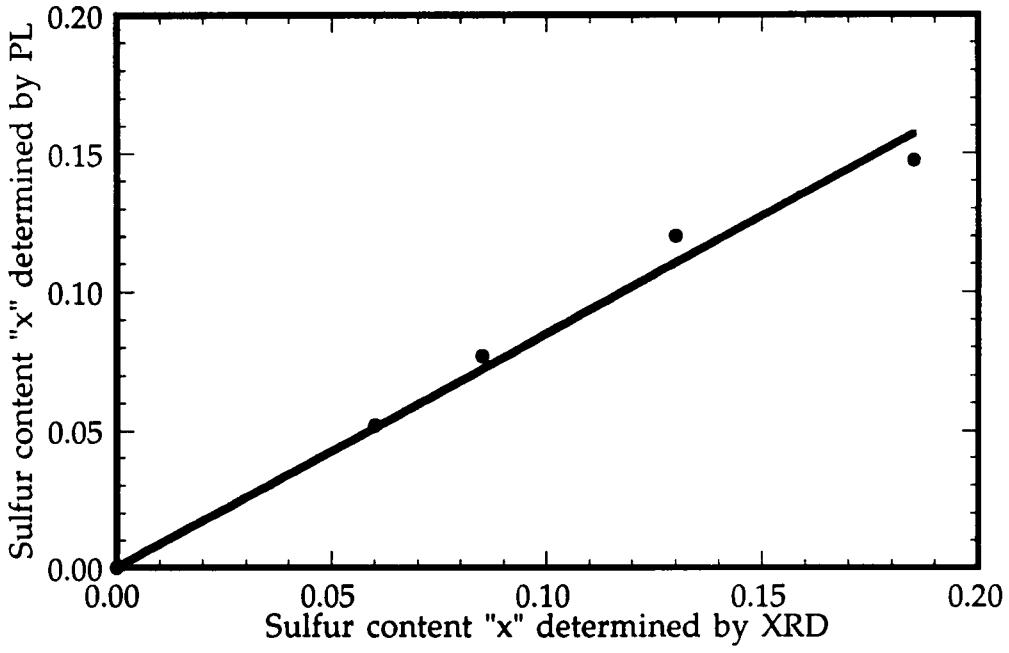

Figure 8-30 Sulfur fraction "x" derived from the photoluminescence spectra and x-ray diffraction data.

measurements are plotted against each other in Figure 8-30. The use of Equation 2.09 assumes that the emissions associated with the PL maxima originate from transitions through levels near the bandedge. Although the PL peaks may be due to DAP complexes (Figure 8-23), the near-linear PL behavior indicates that the near-bandedge structure probably is being maintained.

Dopant Incorporation in PLA Grown ZnS Films

This same technique of PLA growth in a low pressure gas ambient also was evaluated to determine if it can be used to grow doped semiconductor films. A general technique for producing n-type doped semiconductors is to add impurities that lie to the right of the of the anion in the periodic table. Within the group VIIB elements, which (ideally) are substituted onto the chalcogen site, Cl is the best choice for doping since there can be no p-d interaction to form deep levels if zinc vacancies (V_{Zn}) are not present. Thus, PLA of ZnS in low pressure ambients containing Cl was used to determine if Cl could be incorporated into the film. ZnS films were grown on GaAs(001) substrates by ablating a ZnS polycrystalline target in an ambient of 2 mTorr total pressure using an energy density of $E_\ell = 0.35\ J \cdot cm^{-2}$, $T_g = 325°C$, and a target-substrate separation of 10.8 cm. The Cl content of the ambient gas was varied by combining HCl (3.5% HCl in 96.5% He) and He buffer gas streams. By varying the relative flowrates of the two streams, the HCl partial pressure could be varied from zero to 0.07 mTorr. Figure 8-31 shows the room temperature photoluminescence spectrum of a ZnS:Cl film grown in a 0.1% (~ 2 μTorr) HCl ambient. The broad emission between 2 and 3 eV is due to transitions through deep levels associated with Cl complexes, demonstrating that Cl was incorporated into the ZnS structure. The other constituent of these complexes is most likely zinc vacancies. Increasing the HCl partial pressure by a factor of ten produced an asymmetric increase in the PL intensity of these emission peaks. This behavior demonstrated that incorporation of the Cl is controlled via the HCl partial pressure.

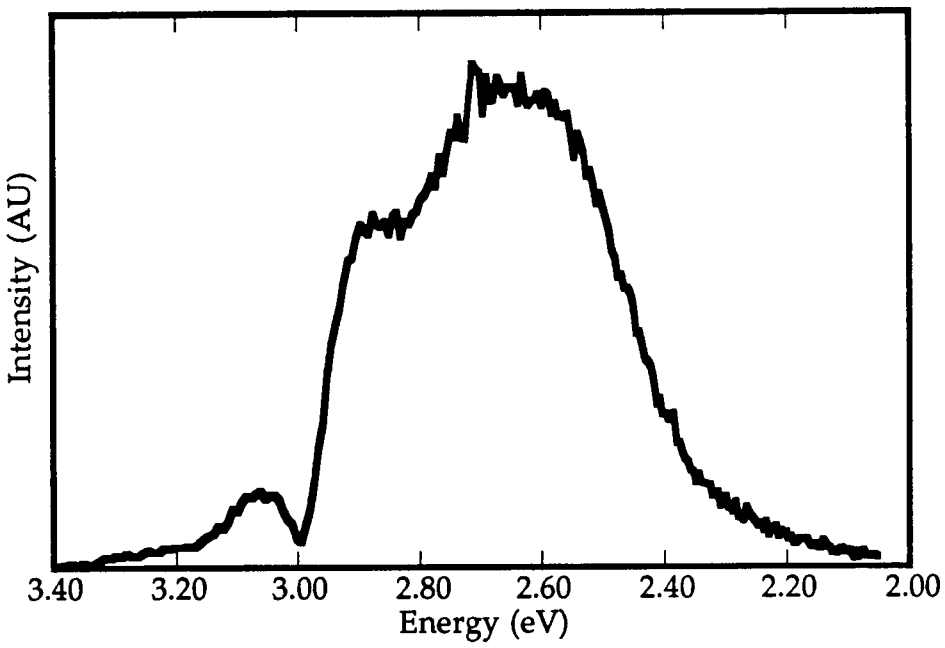

Figure 8-31 Room temperature photoluminescence spectrum from a PLA-grown ZnS:Cl film on GaAs(001).

Processes Involved in PLA Growth of ZnS and ZnSe

An investigation of the processes involved in PLA growth was not included in the initial goals of this work. However, the data obtained from the films grown on the GaAs(001), GaP(001) and GaAs(111) substrates provide some insight into the orientation dependence of this growth. The variation in growth rate (measured *in situ*, Chapter 7) was found to be small in any particular run for growth of both ZnS and ZnSe. Since the radial distance of the HeNe probe laser beam from the rotational centerline varied from run to run, absolute growth rates in different runs were not directly comparable. However, because this distance was fixed during each run, a direct determination of relative growth rates for different pairs of substrate materials, or for substrate surfaces of different crystallographic orientation, could be made during each growth run. For both ZnS and ZnSe it was found that the growth rate was the same on GaAs(001) and GaP(001) at all T_g. However, for both ZnS and ZnSe, the growth rate on GaAs(111) was consistently equal to or less than the growth rate on GaAs(001) at all T_g. The growth rate ratio ($GR_{(111)}/GR_{(001)}$) decreased with increasing temperature. For ZnS this ratio decreased from 1 at T_g = 250°C to 0.85 at T_g = 400°C, while for ZnSe this ratio decreased from 1 at T_g = 200°C to 0.90 at T_g = 350°C.

The growth rate is the sum of the net incident flux ($\vec{J_I}$) and the desorption flux ($\vec{J_D}$). In the case where a flux directed towards the substrate is positive, the growth rate can be described by

$$GR = \vec{J_I} + \vec{J_D} \qquad 8.10$$

During growth using conventional growth techniques (i.e., MBE and MOCVD) the two fluxes occur concurrently. The net incident flux term is dependent on the fluxes of the growth constituents and their respective absorption kinetics; in the case of PLA growth of ZnS and ZnSe the functional form of $\vec{J_I}$ cannot be determined because the precursor

(incident) species and absorption kinetics are not known. Further, during PLA growth the two fluxes do not occur concurrently nor are they present for the same length of time. Thus, interactions between the absorbing and desorbing species (that are present during growth using conventional techniques) are absent. Given these uncertainties, the simplest assumption that will allow us to go further is that the net incident fluxes are the same on the (001) and (111) surfaces. Thus, the difference in growth rates on these two surfaces is due to the differences in their desorption fluxes. The decrease in the relative growth rate as the temperature is increased corresponds to an increase in desorption on the (111) surface, relative to the desorption from the (001) surface.

Equation 8.11 shows the magnitude of the desorption flux from a ZnX surface with a Zn coverage (Θ_{Zn}) and chalcogen coverage (Θ_X).

$$J_D = N\Theta_{Zn}D^{Zn}_{ZnX} + N\Theta_X D^{X}_{ZnX} \qquad 8.11$$

Here N is the concentration of surface lattice sites and D^{Zn}_{ZnX} and D^{X}_{ZnX} are the desorption rate constants for Zn and the chalcogen respectively. For unreconstructed surfaces, the ratio ($N_{(111)}/N_{(001)}$) of the number of surface sites for the two different surfaces is 1.16. The activation energy of the desorption rate constants depends on the number of bonds that bind the desorbing species to the surface. On an unreconstructed {001} surface the atoms will be bound by two bonds (see Figure 2-1), while on an unreconstructed {111} surface, the atoms will be bound by either one or three bonds. Assuming that the Zn-X single bond energy is the same in all cases, the increased desorption rate on the {111} surface at increasing temperatures suggests that the species desorbing from this surface is bound by a single bond. For the ZnX zinc blende structure, the singly-bonded atoms are either S atoms on the (111) surface or Zn atoms on the $(\bar{1}\bar{1}\bar{1})$ surface. A complete picture requires more detailed information regarding the orientation dependence of the desorption rate constants. However, no literature data was found regarding this dependence. Finally, note that our

simplifying assumption following Equation 8.10 ignore a possible orientation dependence of the absorption rates.

Aspects of the Processes Involved in PLA Growth of $ZnSe_{1-x}S_x$

Implicit in the discussion of the alloy growth technique above (e.g., Equation 8.09) was the assumption that the sulfur content was determined by the H_2S partial pressure, independent of total pressure. This was demonstrated during alloy growth with $P(H_2S) = 11$ mTorr. During this run, the total pressure was maintained at 22 mTorr by adding He buffer gas (i.e., $P(H_2S) = \frac{1}{2} P(\text{total})$). In contrast, no buffer gas was added during growth of the other alloys (e.g., $P(H_2S) = 7.48$ mTorr, 22.2 mTorr and 44.4 mTorr). The sulfur content with $P(H_2S) = 11$ mTorr agreed well with that predicted from interpolation of the other data. This confirmed that the alloy mechanism depends only on the H_2S partial pressure and not the total pressure when an inert buffer gas (such as He) is used.

Since Se atoms are incorporated within the deposited film, the concentration of sulfur on the surface of the deposited film is greater than the measured sulfur content by a factor of GR/a_0. Figure 8-32 shows the sulfur surface concentration determined from the measured sulfur content and corrected for the growth rate of the alloy films. Assuming that the sulfur concentration and absorption coverage (Θ) are proportional, the data was found to be well fit by the low pressure form of the Freundlich adsorption isotherm

$$\Theta = c P^{1/n} \qquad 8.12$$

While there is no requirement that n be an integer, the curves shown were well fit ($\chi^2 = 10^{-4}$) for n = 2.

This isotherm often is found to hold in situations for which the adsorbed species is molecular in nature (Zeldowitsh, 1935). This would be true for absorption of the diatomic chalcogen molecule (Equation 8.13b) formed via the H_2S decomposition reaction (Equation 8.13a).

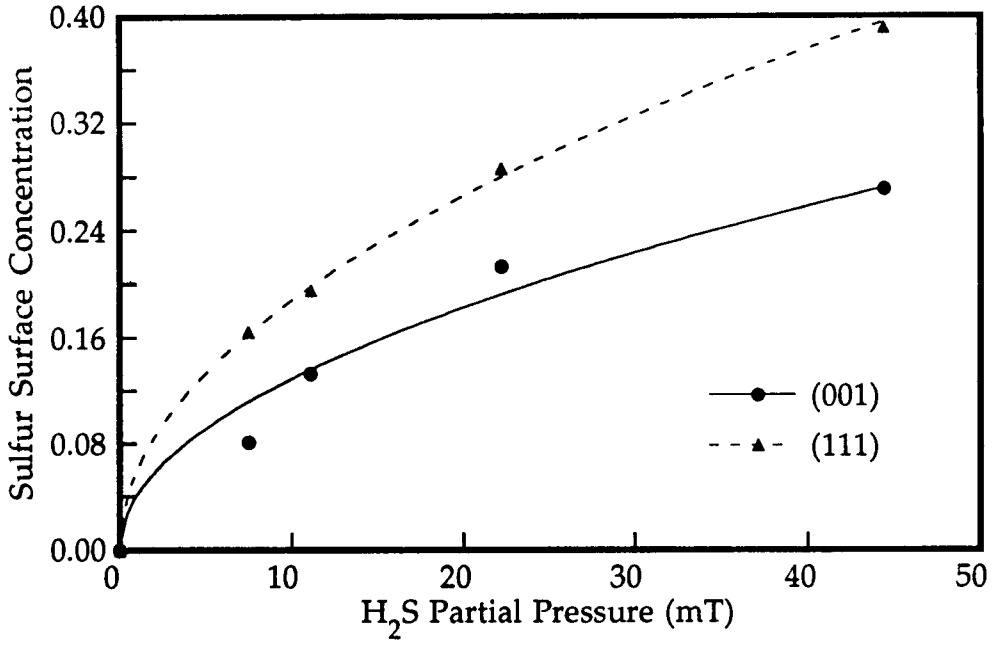

Figure 8-32 Sulfur surface concentration determined from the measured sulfur incorporation and corrected for the growth rate of the alloy films as a function of the ambient H_2S partial pressure. The lines through the data are least squares best fits to functions of the form $x = A[P(H_2S)]^B$ with $B = ½$.

$$H_2S(g) \leftrightarrows H_2(g) + \frac{1}{2}S_2(g) \qquad 8.13a$$

$$ZnSe(s) + \frac{1}{2}S_2(g) \leftrightarrows ZnS(s) + \frac{1}{2}Se_2(g) \qquad 8.13b$$

For these reactions, it would be expected that the alloy composition depends on the partial pressure of the sulfur dimer. Equation 8.14 describes this pressure by the reaction constant K_p for the hydride decomposition reaction (8.13a).

$$K_p = \frac{[P_{H_2}]\,[P_{S_2}]^{1/2}}{[P_{H_2S}]} \qquad 8.14$$

A rate constant of $\log_{10}(K_p) = -5.1$ at $T = 600$ K (Gamelin Handbook of Inorganic Chemistry, 1983) was used to determine the S_2 partial pressure for the various H_2S partial pressures used. Figure 8-33 shows the sulfur coverage plotted against $P(S_2)$. The linear relation indicates that the alloy composition is controlled by the dissociation of H_2S via the reaction 8-13a.

In the discussion to this point it has been implicitly assumed that the rate-limiting step occurs at the growth surface. However, the rate-limiting step can be either a volume (i.e., gas-phase) or surface process. If it is a surface process, then the S-to-Se ratio, x/(1-x), is expected to scale as the ratio of adsorption-to-desorption rates, $(k/d)_S$ / $(k/d)_{Se}$, for S and Se, and to depend on substrate temperature through this ratio (Samuelson, 1982). To further assist in identifying the rate-limiting step, $ZnSe_{1-x}S_x$ films were grown in a $P(H_2S) = 22$ mTorr ambient at a GR ~ 0.05 nm per laser shot, at various T_g. If the rate-limiting step (i) involves the competition between S and Se filling sites on the chalcogen sublattice, or (ii) if S and Se have different desorption rates, then the temperature dependence of x/(1-x) should have an exponentially activated (Arrhenius) form with an activation energy determined by the ratio of their desorption rates (Samuelson, 1982). Thus, in this work the activation energy for x/(1-x) should be related to the different strengths of the Zn-S and Zn-Se bonds.

Figure 8-34 shows the relationship between x/(1-x) and reciprocal thermal energy (kT). For PLA $ZnSe_{1-x}S_x$ alloys grown on GaAs(001), the relative sulfur content increases with increasing T_g. The slope of the line for the (001) oriented alloy data gives an activation energy of 0.23 eV. This is in good agreement with the 0.24 eV difference between the calculated Zn-S and Zn-Se single-bond energies of 0.98 eV and 0.74 eV, respectively (Dryburgh, 1988).

This PLA result is opposite to the behavior found in recent VPE experiments (Zhang, 1992). This suggests that the PLA and VPE growth processes differ significantly. In the VPE experiments, the *decrease* of sulfur content with increasing substrate temperature was thought to result from the sulfur desorption rate increasing more rapidly with temperature than the selenium desorption rate. Thus, the *increase* in sulfur content with increasing temperature, that was observed in our work, is consistent with the rate-limiting step being the replacement of the selenium with sulfur by adsorption. We note that this is not inconsistent with the process described for PLA growth of ZnS and ZnSe films (above). Under those conditions, no ambient exists that supplies continuously either chalcogen constituent. In that case then, the net growth rate is determined by a digital (or stepwise) deposition flux, followed by a long period of desorption. In the case of the growth of the alloy film, however, a second chalcogen constituent is being continuously supplied from the ambient to the growth surface during this desorption period.

Using this technique then, the final sulfur content will depend on, (i) the ambient S_2 concentration, (ii) the reaction rate (i.e., time dependence), and (iii) the selenium available for replacement. Since the selenium embedded in the deposited film is not available for replacement (at these timescales and temperatures), then once all the selenium atoms on the surface have been replaced by sulfur the alloy composition will remain constant, independent of T_g. The time required for the alloy to reach this limiting composition depends on the replacement rate, which depends on the ambient and substrate temperature. The constant alloy composition seen for the (111) oriented films (Figure 8-34) is consistent with the selenium atoms on the surface being quickly replaced with sulfur under

these conditions. The orientational dependence of this behavior (Figure 8-34) is due to only one bond holding the chalcogen atoms to the (111) surface, while both the Zn and chalcogen atoms are held by two bonds on the (001) surface (we neglect consideration of corner sites).

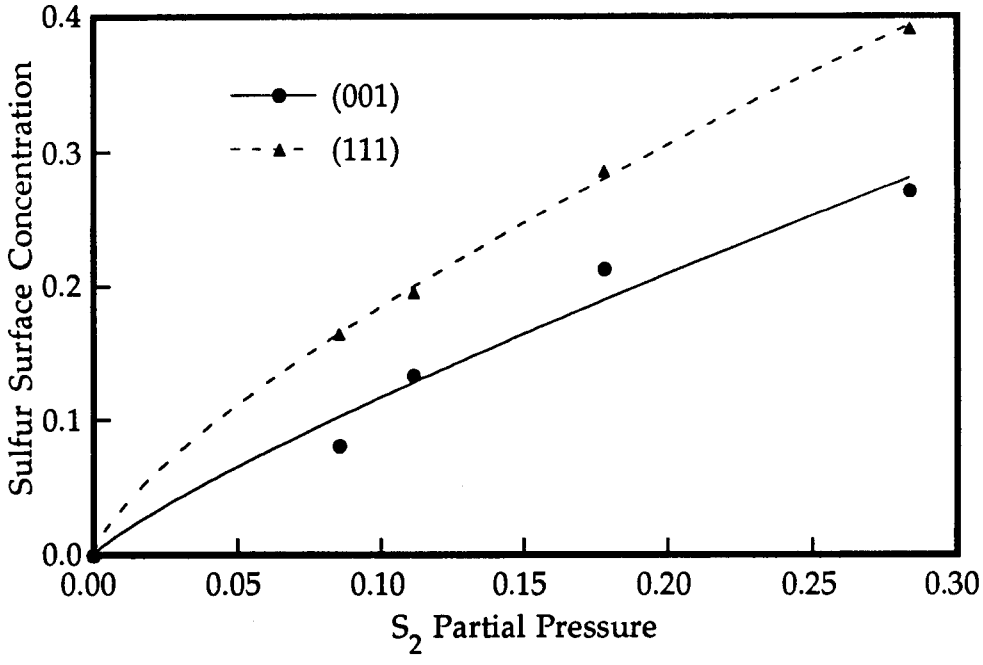

Figure 8-33 Sulfur surface concentration determined from the measured sulfur content and corrected for the growth rate of the alloy films, as a function of the calculated S_2 partial pressure. The lines through the data are least squares best fits to functions of the form $x = A[P(S_2)]^B$, with the variable $B \sim 0.8$ giving the best fit for the (001) oriented films and $B \sim 0.7$ for the (111) oriented films.

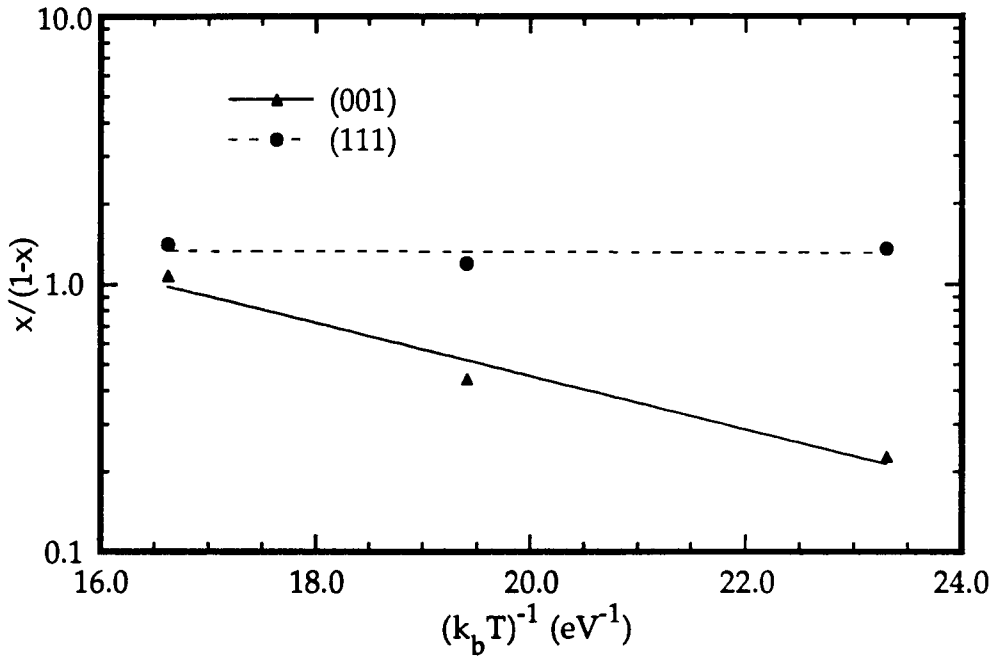

Figure 8-34 Relative content of S to Se ('x/(1-x)', corrected for growth rate) in PLA-grown alloy films on GaAs(001) and GaAs(111) for various T_g.

CHAPTER 9

SUMMARY, CONCLUSIONS, AND FUTURE DIRECTIONS

This work was undertaken to evaluate the Pulsed-Laser Ablation (PLA) process for the growth of wide-bandgap II-VI materials. PLA can be considered a competitive process for the growth of semiconductors if the structural, electrical, and optical properties of PLA-grown materials are equivalent or superior to the properties of material grown by other methods. As is discussed in more detail below, all these criteria were met or exceeded, with the exception of the electrical properties.

Crystal Structure and Epitaxial Orientation of ZnS and ZnSe Films

X-ray diffraction patterns from both ZnS and ZnSe grown on GaAs and GaP (001)-oriented substrates using $E_\ell \geq 0.25$ J·cm^{-2}, $D_{st} = 10.8$ cm, and for all growth temperatures investigated ($T_g = 150$-450°C for ZnS and $T_g = 200$-400°C for ZnSe), showed only the (00ℓ) reflections associated with the zinc blende structure. For films grown under the same conditions on (111)-oriented substrates only, $(\ell\ell\ell)$ reflections were observed. In no case were reflections observed which could be associated exclusively with the wurtzite structure. Thus, all the films grown under these conditions were identified as having the zinc blende structure.

The in-plane and out-of-plane alignments of the films with respect to the underlying substrate were determined by XRD using a 4-circle goniometer. For both ZnS and ZnSe grown on GaAs(001), the [100] and [010] in-plane axes of the film and GaAs were aligned (i.e., true three-dimensional epitaxy). For ZnS grown on GaAs(111), XRD showed that the in-plane directions of the ZnS were aligned in two types of domains with respect to the underlying GaAs substrate. The more populated domain was the one expected for three-dimensional epitaxy. The less populated domain is rotated by 60° (i.e., the film $[2\bar{1}\bar{1}]$ was aligned with the substrate $[11\bar{2}]$). This observation is consistent with a zinc blende structure with a large degree of hexagonal stacking. From the integrated

areas of the XRD rocking curve profiles, the content of hexagonal material in this film was found to be 62%. The XRD pattern from the ZnSe film grown on GaAs(111) indicated that the in-plane directions of the ZnSe also might have been aligned in two types of domains with respect to the GaAs substrate. However, the possibility of 'forbidden' high intensity GaAs {220} substrate peaks located near the ZnSe made it impossible to unambiguously determine if the observed reflections were from in-plane ZnSe peaks or the tails of the GaAs peaks. Thus, a definitive statement about the presence (or lack) of domains in the ZnSe film grown on GaAs(001) and their alignment with respect to the underlying substrate could not be made.

Optimal Growth Temperature of PLA-Grown ZnS and ZnSe Films

The optimal growth temperature was determined from the rocking curve FWHM of the (004) XRD peak. For ZnS the minimum FWHM was found at $T_g = 325°C$; thus, we conclude that the optimal temperature for PLA-growth of ZnS is $T_g = 325°C$. Although this minimum was found at $T_g = 250°C$ for ZnSe, a second, broader peak, superimposed on the first, also was observed. This second peak was not seen at $T_g = 300°C$. Thus, we conclude that the optimal temperature for PLA-growth of ZnSe is $T_g = 300°C$.

Effect of Substrate Preparation on Film Crystalline Quality

Various substrate preparation techniques were investigated to identify surfaces appropriate for epitaxial growth. The number and distribution of defects in the films grown on these substrates was found to be sensitive to the preparation technique applied prior to growth. When only an annealing preparation was used, the $\theta/2\theta$ XRD patterns showed only (111) and (333) reflections from ZnS films grown on GaAs(001) substrates that had undergone this treatment. This clearly indicated that the growth was not epitaxial. However, when a $(NH_4)_2S_x$ passivation step was included during preparation, all the films showed (00ℓ) reflections at the expected $\theta/2\theta$ positions, and no ($\ell\ell\ell$) peaks were observed in the pattern. RBS

analysis of ZnS films grown on GaP(001) clearly showed that films grown on $(NH_4)_2S_x$-passivated substrates were of higher crystalline quality than films grown on unpassivated substrates. The sulfur passivation step was included in the preparation protocol for both the GaP and GaAs substrates because of this improvement.

Structural Defects in PLA-Grown ZnS and ZnSe Films

For both ZnS and ZnSe the thickness of all the films grown for XRD analysis was ~275 nm. Broadening of the rocking curves profiles was observed. This was particularly evident in the ZnS films; but, for both ZnS and ZnSe was found to be due primarily to the defects present near the film-substrate interface. For the ZnSe films, this was investigated by XRD of films having various thicknesses. The extent of boadening increased as the thickness of the film decreased, confirming that the location of the poorer quality (i.e., less coherently diffracting) material was near the film-substrate interface, with the uppermost region of the film being near-perfect. Similar results were obtained for the ZnS films using RBS data. These results for the ZnS films were confirmed by high-resolution TEM analysis.

Stacking faults were found to be the dominant defects present in the ZnS films. The average broadening observed in the $\theta/2\theta$ XRD peaks of ZnS films grown on GaAs(001), corresponds to an upper bound on the stacking fault density of $\rho_{sf} \sim 2.5 \times 10^{10}$ cm·cm^{-3}. This stacking fault density is less than that in ZnS films grown by conventional techniques (e.g., MOCVD). Furthermore, the widths of the rocking curves of the PLA-grown ZnS films were less than for MBE-grown ZnS films of comparable thickness.

Misfit dislocations are believed to be the dominant defects present in the PLA-grown ZnSe films on GaAs(001). The rocking curve width from the ZnSe(004) reflection, for a 225 nm thick film grown at the optimal T_g, implied a dislocation density within the film of $\rho_d = 1.6 \times 10^{14}$ cm^{-3}. No data was found in the literature for dislocation densities in films so thin.

The literature does suggest that ZnSe grown by conventional methods (e.g., MOCVD or MBE) requires a buffer layer to reduce the dislocation density. Thus, large dislocation densities in ZnSe films grown on GaAs appear to be an inherent problem, due to the lattice constant mismatch. A better comparison of the defect density would be obtained with thicker films (i.e., ~several μm); this would remove the influence of the strain due to the lattice constant mismatch, and permit observation of the effects due only to the differences between the growth methods.

Film Surface Morphology

The surface morphology of the films was examined using a JEOL 840 scanning electron microscope. Both the ZnS and ZnSe films appeared smooth and mirrorlike under all deposition conditions, and no surface features or structure were seen at the 50 nm level of resolution.

Epitaxy and Growth Mode

Although not conclusive evidence, the lack of more than one domain visible in the 4-circle XRD pattern and the lack of a change in orientation across the twin boundary seen in TEM, indicate that islanding does not occur during the growth of ZnS films on GaAs(001) substrates. This conclusion is supported by the presence of multiple satellite peaks in the XRD pattern from the ZnS-ZnSe SLS structure. During growth, islands are incomplete layers of two or more monolayers thickness on the growth surface. The presence of islands having minimum height (i.e., two monolayers) would represent fluctuations of more than 20% in the interface, in the SLS structure fabricated in this work. Clearly this would destroy the coherency required to generate the satellite peaks observed. Thus, we conclude that, for PLA-grown ZnS on GaAs(001), the growth mode is Frank-van der Merwe (i.e. layer-by-layer). This conclusion is consistent with the rod structures observed in RHEED data for the growth of CdTe by PLA (Dubowski, 1989, 1990).

Band Structure of the ZnS and ZnSe Films

The band structures of the ZnS and ZnSe films grown on GaAs(001) were investigated by inspecting the dielectric function (ε_1, ε_2) of films grown at the respective optimal temperatures. The dielectric function was measured in the 1.5-5.3 eV region using spectroscopic two-channel polarization modulation ellipsometry. For both the ZnS and ZnSe films ε_2 approached zero below the bandedge, while spectral features are seen clearly just above the bandedges. The transparency ($\varepsilon_2 \sim 0$) of these films below the bandedge indicates that both the PLA-grown ZnS and ZnSe films were of high optical quality.

The E_o and $E_o+\Delta_o$ transitions were clearly seen in the dielectric function spectrum of ZnS, while the E_1 and $E_1+\Delta_1$ transitions were not seen because they occur above the upper limit of investigation. The E_o, $E_o+\Delta_o$, E_1, and $E_1+\Delta_1$ transitions all were seen clearly in the dielectric function spectrum of the ZnSe films. There was excellent agreement with published values, indicating that the electronic band structure in these PLA-grown materials corresponds closely to that in materials grown by other methods.

Midgap Structure and Defect States in the ZnS and ZnSe Films

The midgap structure and electronic defect states in the bandgap were investigated by photoluminescence (PL) spectroscopy at temperatures in the range T = 9-298K. Deep emissions were observed in the PLA-grown ZnS film at 2.650 eV and 2.838 eV; these emissions correspond with the SA (self-activated) and DE peaks observed by Yamaga (1988). In this work the SA peak is attributed to an Al deep level and the DE peak to either Al or Cl deep levels. The presence of the SA peak is associated with a zinc vacancy-donor complex (V_{Zn}-D). Acceptor and donor bound exciton peaks were identified in this same sample at 3.618 eV and 3.741 eV, respectively. In contrast with the findings of Kanehisa (1988), a peak located at 3.786 eV was clearly identified as being due to emission from a bound exciton. Finally, an emission peak at 3.795 eV was identified as being due to

emission from the free exciton. The presence of this free exciton peak confirms the good quality of this film.

The SA emission (at ~2.24 eV) also was observed in a PLA-grown ZnSe film on GaAs(001). The impurity source for this level is not known, but possibly is related to the presence of Cu impurity from the target (0.08 ppm). Once again, the presence of the SA peak is associated with a zinc vacancy-donor complex (V_{Zn}-D). The Y_o peak, associated with misfit dislocations, was observed at 2.608 eV. The corresponding LO-phonon replicas of this defect level also were observed. This is further evidence that misfit dislocations are the dominant defects in these films. A donor-acceptor-pair (DAP) emission was observed at 2.715 eV; the associated LO replicas were observed at 2.687, 2.658, and 2.633 eV. The donor portion is associated with Ga which has diffused from the substrate. A number of acceptor- and donor-bound exciton emission peaks also were identified in the near-bandedge region, while the heavy- (X_{hh}) and light-hole (X_{lh}) emissions of the free exciton were seen at 2.8036 eV and 2.8112 eV, respectively. The splitting of the free exciton observed here corresponds to a strain of 1.6×10^{-3}. This value for the strain is in excellent agreement with that measured in the same manner for a comparable MBE-grown ZnSe film (Olego, 1988).

ZnS-ZnSe Superlattice Structure

To determine if high quality superlattices of Zn-based II-VI wide bandgap materials can be fabricated using PLA, a structure of the form $(ZnSe)_m$-$(ZnS)_n$ was grown. This structure consisted of a 65-period $(ZnSe)_6$-$(ZnS)_3$ superlattice grown on a 370 nm thick ZnSe buffer layer. The expected lattice constant parallel to the surface normal for a superlattice with this structure was 0.556 nm ($2\theta = 67.3°$). The $\theta/2\theta$ XRD pattern in the vicinity of the (004) reflection from this structure showed several orders of superlattice satellite peaks, while the position of the observed zeroth peak ($2\theta = 67.54°$) in the XRD was in good agreement with the calculated lattice constant. The compositional modulation period of the SLS, determined from the separation of adjacent superlattice peaks, was L = 4.8 nm. This

period compares well (only 4% difference) with the desired value. The presence of several orders of satellite peaks indicates that this $(ZnSe)_6$-$(ZnS)_3$ superlattice structure has sharp compositional interfaces, and is structurally comparable to superlattices of other materials grown by PLA, and to superlattices grown by other techniques.

Growth of $ZnSe_{1-x}S_x$ Alloy Films and Multilayer Structures

A new technique that utilized ablation of ZnSe into a low-pressure H_2S gas ambient was developed to permit fabrication of $ZnSe_{1-x}S_x$ alloy films. A number of films were grown in various H_2S partial pressures to investigate the incorporation of sulfur into these films. The variation of sulfur content (x) with H_2S partial pressure was found to follow the relation $x = A[P(H_2S)]^B$, with $B \sim ½$. The ability to grow films having predetermined compositions was evaluated by using this relation to determine the H_2S partial pressure needed to grow an (001)-oriented alloy film having $x = 0.075$. XRD of the (006) reflection showed that the resulting sulfur content for this $ZnSe_{1-x}S_x$ (001) film was $x = 0.06$. This showed that the composition can be precisely determined prior to growth, even by interpolation between well separated data points.

Since composition could be controlled by the H_2S partial pressure, the film composition can be varied along the growth direction. To evaluate this spatial control over film composition, a $ZnSe_{1-x}S_x$ multilayered epitaxial structure was fabricated which simultaneously incorporated both continuously graded and successive abrupt, periodic compositional changes.

The bandgap structure of the (001) $ZnSe_{1-x}S_x$ films was investigated using room temperature photoluminescence. The PL peaks broadened and shifted to higher energy with increasing sulfur content. The shift in peak position is consistent with sulfur entering the lattice on the selenium sites, while the broadening is consistent with random (disordered) sulfur incorporation. An implied sulfur content for each alloy film was obtained from the position of the PL peak maximum and the known variation of

bandgap (i.e., the bowing parameter). The sulfur fractions determined independently from the XRD and PL showed a near-liner behavior and indicates that the near-bandedge structure probably is being maintained.

Dopant Incorporation in PLA Grown ZnS Films

This same technique also was applied to grow doped semiconductor films. ZnS films were grown by PLA in low pressure HCl ambients to determine if Cl could be incorporated into the film. Room temperature photoluminescence of a ZnS:Cl film grown in a 0.1% (~ 2 μTorr) HCl ambient showed a broad emission between 2 and 3 eV. This emission was identified as being due to transitions through deep levels associated with Cl complexes, demonstrating that Cl was incorporated into the ZnS structure. Increasing the HCl partial pressure by a factor of ten produced an asymmetric increase in the PL intensity of these emission peaks. This behavior demonstrated that incorporation of the Cl is controlled via the HCl partial pressure.

Processes Involved in PLA Growth of ZnS and ZnSe

For both ZnS and ZnSe, the growth rate on GaAs(111) was consistently equal to or less than the growth rate on GaAs(001) at all T_g, and the growth rate ratio ($GR_{(111)}/GR_{(001)}$) decreased with increasing temperature. For ZnS this ratio decreased from unity at T_g = 250°C to 0.85 at T_g = 400°C, while for ZnSe this ratio decreased from unity at T_g = 200°C to 0.90 at T_g = 350°C. This difference in growth rates probably is due to differences in desorption rates on these two surfaces. This difference in the rates is likely related to the difference in: (i) the site densities of the two surfaces, and (ii) the activation energies of the desorption rate constant. As a result, the decrease in the relative growth rate as the temperature is increased corresponds to an increase in desorption on the (111) surface, relative to the desorption from the (001) surface.

Processes Involved in PLA Growth of $ZnSe_{1-x}S_x$ Alloys

Growth of the $ZnSe_{1-x}S_x$ alloys in ambients with and without He buffer gas showed that the alloy-formation mechanism depends only on the H_2S partial pressure and not the total ambient pressure. Further, the relation, $[P(H_2S)]^{1/n}$ with $n \sim 2$, is the low pressure form of the Freundlich adsorption isotherm. This isotherm often is found to hold in situations for which the adsorbed species is molecular in nature. Thus, we conclude that the sulfur incorporation depends on the absorption of the diatomic chalcogen molecule. This molecule (S_2) is formed in the gas phase via decomposition of the H_2S molecule. The equilibrium S_2 partial pressures ($P(S_2)$) at the various growth temperatures and H_2S partial pressures were determined for this reaction. The linear relation observed between sulfur surface concentration and $P(S_2)$ showed that the alloy composition is indeed controlled by the formation of the diatomic chalcogen molecule via dissociation of H_2S and the absorption of this molecule on the growth surface.

To further assist in identifying the rate-limiting step, $ZnSe_{1-x}S_x$ films were grown in a $P(H_2S) = 22$ mTorr ambient at a GR ~ 0.05 nm per laser shot, at various T_g. For the (001)-oriented alloys, the sulfur content was found to increase with increasing temperature, while the (111)-oriented alloys showed a constant sulfur content at all T_g under these growth conditions. This PLA result for the (001)-oriented alloy films is opposite to the behavior found in recent VPE experiments, and suggests that the PLA and VPE growth processes differ significantly. The slope of the line for the (001)-oriented alloy data gave an activation energy of 0.23 eV. This is in good agreement with the 0.24 eV difference between the calculated Zn-S and Zn-Se single-bond energies. These data are consistent with the rate-limiting step being the replacement of the selenium with sulfur by adsorption.

We note that this model is not inconsistent with the process described for PLA growth of ZnS and ZnSe films (above). Under those conditions, no ambient exists that supplies continuously either chalcogen constituent. In that case then, the net growth rate is determined by a digital (or stepwise)

deposition flux, followed by a long period of desorption. For the PLA growth of an alloy film, however, a second chalcogen constituent is being continuously supplied from the ambient to the growth surface during this desorption period.

These conclusions emphasize the importance of *in situ* studies of (i) the precursor species present, (ii) the surfaces on which growth occurs, as well as (iii) the behavior of the deposited species during the growth and desorption phases of growth, in order to obtain a detailed understanding of PLA growth mechanisms. Such an understanding is necessary to fully develop the PLA process.

Summary

In summary, comparison of the properties of PLA-grown ZnS, ZnSe and $ZnSe_{1-x}S_x$ alloy thin films, with those grown by other techniques (MBE and MOCVD), shows that the PLA-process can be regarded as competitive in this field. For almost all the properties evaluated in this work, the PLA-grown materials properties met or exceeded those found in the literature for films grown by MBE and MOCVD. The exception was the electrical conductivity. All the films grown in this work were insulating. This is likely primarily due to two causes. The first is that these films were very thin (~250 nm), and the lattice constant mismatch between the films and substrates resulted in large numbers of dislocations. The deep level defects associated with these dislocations trap the carriers, so that the film is insulating. The second problem is that zinc vacancies are present in the films. The deep levels associated with vacancy complexes also trap carriers.

The first of these problems can be solved either by growing on a buffer layer which is lattice-matched to the film, or by growing a film that is thick enough to have a substantial volume that is free of defects. The second problem can be solved by growing in an ambient overpressure containing Zn or by co-ablation of a Zn-containing target.

A new technique for growing compound semiconductor alloy films with continuously variable composition also was developed. This technique is entirely general; it is expected that it can be used with other

alloy systems as well. The alloy composition can be easily and precisely controlled by varying the ambient gas pressure and gas composition during ablation. The ease of alloy growth by this technique is an advantage not shared by the MBE growth technique. This further illustrates the competitiveness of the PLA growth technique and its continuing evolution.

BIBLIOGRAPHY

BIBLIOGRAPHY

Adachi, S., Taguchi, T., *Phys. Rev. B*, **43**, 9569 (1991)

Adachi, S., Taguchi, T., *Phys. Rev. B*, **44**, 10633 (1991)

Arlinghaus, H.F., Calaway, W.F., Young, C.E., Pellin, M.J., Gruen, D.M., Chase, L.L., *J. Appl. Phys.*, **65**, 281 (1989)

Aspnes, D.E., Studina, A.A., *Phys. Rev. B*, **27**, 985 (1983)

Aydinli, A., Compaan, A.D., *Adv. Matl. Optics Elect.*, **2**, 79 (1993)

Ball, C.A.B., van der Merwe, J.H., "The Growth of Dislocation-Free Layers" in *Dislocations in Solids*, F.R.N. Nabarro, ed., North-Holland, New York, 1983

Ban, V.S., Kramer, D.A., *J. Mater. Sci.*, **5**, 978 (1970)

Baru, V. G., Petrov, V. A., Sandomirskii, V. B., *Sov. Phys. Semicond.*, **9**, 1344 (1976)

Benz, R.G., Huang, P.C., Stock, S.R., Summers, C.J., *J. Cryst. Growth* **86**, 303 (1988)

Bertho, D., Boiron, D., Simon, A., Jouanin, C., Priester, C., *Phys. Rev. B*, **44**, 6118 (1991)

Bertho, D., Jouanin, C., *Phys. Rev. B*, **47**, 2184 (1993)

Blacha, A., Presting, H., Cardona, M., *Phys. Stat. Sol. (b)*, **126**, 11 (1984)

Böer, K.W., *Survey of Semiconductor Physics, Electrons and Other Particles in Bulk Semiconductors*, Van Nostrand Reinhold, New York, 1990

Brandt, S., Jaszczyn-Kopec, P., *J. Lum.*, **11**, 381 (1976)

Budai, J., Research Staff Member, Oak Ridge National Laboratory, private communication, 1992

Bylsma, R.B., Kossut, J., Becker, W.M., Kolodziejski, L.A., Gunshor, R.L., Frohne, R., *J. Appl. Phys.*, **61**, 3011 (1987)

Chemla, D.S., Miller, D.A.B., "Nonlinear Optical Properties of Semiconductor Quantum Wells" in *Optical Nonlinearities and Instabilities in Semiconductors*, Hartmut Haug, ed., Academic Press, New York, 1988

Cheung, J.T., Madden, J., *J. Vac. Sci. Tech.*, **B5**, 705 (1987)

Cheung, J.T., Sankur, H., *CRC Critical Rev. Solid State Matl. Sci.*, **15**, 63 (1988)

Cheung, J.T., Sankur, H., "The Unique Applications of Pulsed Laser Deposition To the Epitaxial Growth of Semiconductor Films", in *Laser Ablation of Electronic Materials, Basic Mechanisms and Applications*, E. Fogarassy and S. Lazare, eds., Elsevier Science Publishers BV, 1992

Cockayne, B., Wright, P.J., Skolnick, M.S., Pitt, A.D., Williams, J.O., Ng, T.L., *J. Crys. Gwth.*, **72**, 17 (1985)

Dabbicco, M., Cingolani, R., Ferrara, M., Suemune, I., Kuroda, Y., *J. Appl. Phys.*, **72**, 4969 (1992)

Dietsch, R., Mai, H., Pompe, W., Völlmar, S., *Adv. Matr. Opt. Elect.*, **2**, 19 (1993)

Ding, J., Jeon, H., Ishihara, T., Hagerott, M., Nurmikko, A.V., *Phys. Rev. Lett.*, **69**, 1707 (1992)

Dow, J. D., "Localized Perturbations in Semiconductors" in *Highlights of Condensed-Matter Theory (Proceedings of the International School of Physics "Enrico Fermi"; course 89)*, F. Bassani, F. Fumi and M. P. Tosi (eds), North-Holland, New York, 1985

Dryburgh, P.M., *J. Cryst. Growth* **87**, 397 (1988)

Dubkov, V.M., *Sov. J. Opt. Technol.*, **49**, 168 (1982)

Dubowski, J.J., Bhat, P.K., Williams, D.F., Becla, P., *J. Vac. Sci. Tech.*, **A4**, 1879 (1986)

Dubowski, J.J., *Chemtronics*, **3**, 66 (1988)

Dubowski, J.J., Williams, D.F., Wrobel, J.M., Sewell, P.B., LeGeyt, J., Halpin, C., Todd, D., *Can. J. Phys.*, **67**, 343 (1989)

Dubowski, J.J., Thompson, J.R., Rolfe, S.J., McCaffrey, J.P., "Laser Induced Growth of $Cd_{1-x}Mn_xTe$ and CdTe-$Cd_{1-x}Mn_xTe$ Superlattices", presented at the Fifth International Conference on Superlattices and Microstructures, Berlin, August 13-16, 1990

Ebina, A., Fukunaga, E., Takahashi, T., *Phys. Rev. B*, **10**, 2495 (1974)

Eres, G., Research Staff Member, Oak Ridge National Laboratory, private communication (1991)

Fedrov, D.L., *J. Lum.*, **52**, 233 (1992)

Fujita, Sz., Takeuchi, F.Y., Fujita, Sg., *Jpn. J. Appl. Phys.*, **27**, L2019 (1988)

Fuke, S., Araki, H., Kuwahara, K., Imai, T., *J. Appl. Phys.*, **59**, 1761 (1986)

Fukuda, Y., Kohama, Y., Ohmachi, Y., *Jpn. J. Appl. Phys.*, **29**, L20 (1990)

Gaines, J.M., Ponzoni, C.A.,*J. Vac. Sci. Tech.*, **B10**, 918 (1992)

Gamelin Handbook of Inorganic Chemistry, S Sulfur, Supplement Volume 4a/b, Hubert Bitterer ed in chief, Springer-Verlag, New York, 1983

Gaponov, S.V., Luskin, B.M., Salashchenko, N.N., *Sov. Phys. Semicond.*, **14**, 873 (1980)

Giapis, K. P., Jensen, K. F., Potts, J. E., Pachuta, S. J., *J. Elect. Mater.* **19**, 453 (1990).

Gossard, A.C., "Solid-Solid Interfaces and Superlattices" in *Solvay Conference on Surface Science,*, F.W., de Wette, ed., Springer-Verlag, Berlin, 1988

Guha, S., Munekata, H., LeGoues, F. K., Chang, L. L., *Appl. Phys. Lett.*, **60**, 3220 (1992)

Guha, S., Munekata, H., Chang, L.L.,*J. Appl. Phys.*, **73**, 2294 (1993)

Gutowski, J., Presser, N., Kudler, G., *Phys. Stat. Sol. (a)*, **120**, 11 (1990)

Haase, M. A., Qiu, J., DePuydt, J. M., Cheng, H., *Appl. Phys. Lett.*, **59**, 1272 (1991)

Harris, S.E., *Phys. Rev. Lett.*, **62**, 1033 (1989)

Hauksson, I. S., Simpson, J., Wang, S. Y., Prior, K. A., Cavenett, B. C., *Appl. Phys. Lett.*, **61**, 2208 (1992)

Herman, M.A., *Semiconductor Superlattices*, Akademie-Verlag, Berlin, 1986

Hermans, J., Wagner, V., Geurts, J., Woltok, J., Söllner, J., Heuken, M., Heime, K., *J. Vac. Sci. Tech.*, **B10**, 2062 (1992)

Hingerl, K., Sitter, H., Lilja, J., Kuusisto, E., Imai, K., Pessa, M., Kudiek, G., Gutowski, J., *Semicond. Sci. Tech.*, **6**, A72 (1991)

Hua, G. C., Otsuka, N., Xie, W., Grillo, D. C., Kobayashi, M., Gunshor, R. L., "Growth and Characterization of ZnSe/ZnCdSe Diode Structures on (In,Ga)As Buffer Layers" in *Wide Band Gap Semiconductors, Materials Research Society Symposium Proceedings; vol. 242*, T. D. Moustaka, J. I. Pankove, and Y. Hamakawa eds, Materials Research Society, Pittsburgh, 1992

Ichige, K., Matsumoto, Y., Namiki, A., *Nucl. Instr. Meth.* , **B33**, 820 (1988)

Irvine, S.J.C., *CRC Critical Reviews in Solid State and Materials Sciences*, **13**, 279 (1987)

Isshiki, M., Masumoto, K., *J. Phys. C: Solid State Phys.*, **21**, 2771 (1988)

Jansen, R. W., Sankey, O. F., *Phys. Rev. B*, **39**, 3192 (1989)

Jellison, G.E., Lowndes, D.H., *Appl. Phys. Lett.*, **47**, 718 (1985)

Jellison, G.E., McCamy, J.W., *Appl. Phys. Lett.* **60**, 512 (1992)

Jeon, D., Gislason, H. P., Watkins, G. D., "ODMR-MCD Study of the Zinc Vacancy and Related Complexes in ZnSe" in *Defects in Semiconductors, Materials Science Forum Volumes 10-12*, H. J. Bardeleben, ed., Trans Tech Publications, Ltd., Switzerland, 1986

Jeon, H., Ding, J., Patterson, W., Nurmikko, A.V., Xie, W., Grillo, D.C., Kobayashi, M., Gunshor, R.L., *Appl. Phys. Lett.*, **59**, 3619 (1991)

Jeon, H., Ding, J., Nurmikko, A. V., Xie, W., Grillo, D. C., Kobayashi, M., Gunshor, R. L., Hua, G. C., Otsuka, N., *Appl. Phys. Lett.*, **60**, 2045 (1992)

Kamata, A., Uemoto, T., Okajima, M., Hirahara, K., Kawachi, M., Beppu, T., *J. Crys. Gwth.*, **86**, 285 (1988)

Kanehisa, O., Shiiki, M., Migita, M., Yamamoto, H., *J. Cryst. Growth* **86**, 367 (1988)

Kawakami, Toyoda, Y., T., Wu, Y., Fujita, S., Fujita, S., *J. Cryst. Growth* **107**, 1072 (1991)

Kawakami, Y., Taguchi, T., Hiraki, A., *J. Vac. Sci. Tech.*, **B5**, 1171 (1987)

Kawakami, Y., Toyoda, T., Wu, Y., Fujita, Sz., Fujita, Sh., *Jpn. J. Appl. Phys.*, **29**, 2440 (1990)

Kawakami, Y., Toyoda, T., Wu, Y., Fujita, Sz., Fujita, Sh., *J. Crys. Gwth.*, **107**, 1072 (1991)

Kawakyu, Y., Sasaki, M., Uemoto, T., Beepu, T., in *Extended Abstracts of the 19th International Conference on Solid State Devices and Materials*, Japan Society of Applied Physics, 1987

Kawazu, Z., Kawakami, Y., Taguchi, T., Hiraki, A., *Materials Science Forum*, **38-41**, 555 (1989)

Kelly, R., Dreyfus, R.W., *Surf. Sci.*, **198**, 263 (1988)

Kelly, R., Dreyfus, R.W., *Nucl. Instr. Meth.* , **B32**, 341 (1988)

Kelly, R., *SPIE Vol. 1056, Photochemistry in Thin Films*, 258 (1989)

Kim, S., Research Assistant, Columbia University, New York, NY, private communication

Kitagawa, M., Tomomura, Y., Suzuki, A., Nakajima, S., *J. Crys. Gwth.*, **95**, 509 (1989)

Konagai, M., *J. Cryst. Growth* **120**, 261 (1992)

Koukitu, A., Saegusa, A., Kitho, M., Ikeda, H., Seki, H., *Jpn. J. Appl. Phys.*, **29**, 2165 (1990)

Koukitu, A., Saegusa, A., Kitho, M., Ikeda, H., Seki, H., *Jpn. J. Appl. Phys.*, **29**, L2165 (1990)

Koukitu, A., Miyazawa, T., Kitho, M., Ikeda, H., Seki, H., *J. Cryst. Growth* **123**, 95 (1992)

Kukimoto, H., *J. Cryst. Growth* **107**, 637 (1991)

Kukimoto, H., *Semicond. Sci. Tech.*, **6**, A14 (1991)

Kukimoto, H., Professor, Tokyo Institute of Technology, private communication (1992)

Kuroda, Y., Suemune, I., Fujimoto, M., Fujii, Y., Otsuka, N., Nakamura, Y., *J. Appl. Phys.*, **72**, 3029 (1992)

Kuwabara, H., Fujiyasu, H., Shimizu, H., Sasaki, A., Yamada, S., *J. Cryst. Growth*, **72**, 299 (1985)

Laks, D. B., Van de Walle, C. G., Neumark, G. F., Pantelides, S. T., *Phys. Rev. Lett*, **66**, 648 (1991)

Laks, D. B., Van de Walle, C. G., "Self-Compensation and Doping Problems in ZnSe" in *Wide Band Gap Semiconductors, Materials Research Society Symposium Proceedings; vol. 242*, T. D. Moustaka, J. I. Pankove, and Y. Hamakawa eds, Materials Research Society, Pittsburgh, 1992

Lilley, P., *J. Crys. Gwth.*, **44**, 446 (1978)

Lockwood, D.J., Baribeau, J.-M., Timbrell, P.Y., *Can. J. Phys.*, **67**, 351 (1989)

Lowndes, Douglas H., Norton, David P., Budai, J.D., Pennycook, S.J., Christen, D. K., Feenstra, R., Hua, "Superconductivity in Nonsymmetric Epitaxial $YBa_2Cu_3O_{7-d}$ Superlattices Grown by Pulsed Laser Ablation" in *Laser Ablation for Materials Synthesis, Materials Research Society Symposium Proceedings; vol. 191*, David C. Paine, John C. Bravman eds, Materials Research Society, Pittsburgh, 1990

Lowndes, Douglas H., "Growth of Epitaxial Thin Films by Pulsed Laser Ablation", in *Eighth International Summer School on Crystal Growth*, invited lecture and book chapter, *Amer. Inst. of Physics Conf. Proc.*, in press, 1993

Mach, R., Flögel, P., Suslina, L.G., Areshkin, A.G., Maege, J., Voigt, G., *Phys. Stat. Sol. (b)*, **109**, 607 (1982)

Mandel, G., *Phys. Rev. A*, **4**, 1073 (1964)

Maslov, A.Y., Suslina, L.G., *Sov. Phys. Solid State*, **24**, 1928 (1982)

Massies, J., Etienne, P., Dezaly, F., Linh, N.T., *Surf. Sci.*, **99**, 121 (1980)

Matsumura, N., Ishikawa, K., Saraie, J., Yodogawa, Y., *J. Cryst. Growth* **72**, 41 (1985)

Matsumura, N., Mitsutaka, T., Saraie, J., *J. Crys. Gwth.*, **95**, 525 (1989)

Matthews, J.W., Blakeslee, A.E., *J. Crys. Gwth.*, **27**, 118 (1974)

Matthews, J.W., "Coherent Interfaces and Misfit Dislocations" in *Epitaxial Growth*, J.W. Matthews, ed., Academic Press, New York, 1975

McCamy, J.W., Lowndes, Douglas H., Budai, J.D., Chakoumakos, B.C., Zuhr, R.A., "Growth of Epitaxial ZnS and ZnSe Thin Films by Pulsed Laser Ablation", in *Wide Band Gap Semiconductors, Materials Research Society Symposium Proceedings; vol. 242*, T. D. Moustaka, J. I. Pankove, and Y. Hamakawa eds, Materials Research Society, Pittsburgh, 1992

Mitsuishi, I., Shibatani, J., Kao, M-H., Yamamoto, M., Yoshino, J., Kukimoto, H., *Jpn. J. Appl. Phys.*, **29**, L733 (1990)

Mohammed, K., Cammack, D.A., Dalby, R., Newbury, P., Greenburg, B.L., Petruzzello, J., Bhargava, R.N., *Appl. Phys. Lett.*, **50**, 37 (1987)

Muramatsu, S., Kitamura, M., *J. Appl. Phys.*, **73**, 4270(1993)

Muranoi, T., Fujita, Y., Watanabe, T., Ishii, N., Moto, Y., Furukoshi, M., *Jpn. J. Appl. Phys.*, **29**, L1959 (1990)

Muranoi, T., Kurosawa, K., Yammoto, K., Miyokawa, T., Shimizu, M., Furukoshi, M., *Jpn. J. Appl. Phys.*, **29**, 2820 (1990)

Myhajlenko, S., Batstone, J. L., Hutchinson, H. J., Steeds, J. W., *J. Phys. C: Solid State Phys.*, **17**, 6477 (1984)

Nakao, T., Uenoyama, T., in *Extended Abstracts of the 1992 International Conference on Solid State Devices and Materials*, Japan Society of Applied Physics, 1992

Namiki, A., Kawai, T., Ichige, K., *Surf. Sci.*, **166**, 129 (1986)

Namiki, A., Cho, S., Ichige, K., *Jpn. J. Appl. Phys.*, **26**, 39 (1987)

Nelkowski, S., and Gumlich, T.T., in *Landbolt-Börnstein, Numerical Data and Functional Relationships in Science and Technology, Volume 17b*, K.-H. Hellwege, O. Madelung, eds., Springer-Varlag, New York, 1982

NoorBatcha, I., Lucchese, R.R., Zeiri, Y., *J. Chem. Phys.*, **10**, 5816 (1987)

NoorBatcha, I., Lucchese, R.R., Zeiri, Y., *Surf. Sci.*, **200**, 113 (1988)

Norton, SLS paper (1991)

Nurmikko, A.V., Gunshor, R.L., *Phys. Stat. Sol. (b)*, **173**, 291 (1992)

Ohkawa, KTsujimura, A., Hayashi, S., Yoshii, S., Mitsuyu, T., in *Extended Abstracts of the 1992 International Conference on Solid State Devices and Materials*, Japan Society of Applied Physics, Tokyo, 1992

Ohno, T., Taguchi, T., *J. Crys. Gwth.*, **107**, 649 (1991)

Okuyama, H., Nakono, K., Miyajima, T., Akimoto, K., *J. Crys. Gwth.*, **117**, 139 (1992)

Olego, D.J., *J. Vac. Sci. Tech.*, **B6**, 1193 (1988)

Osip'yan, Y. A., Petrenko, V. F., Zaretski, A. V., Whitworth, R. W., *Adv. in Physics*, **35**, 115 (1986)

Palik, Edward D., Addamiano, A., "Zinc Sulfide (ZnS)" in *Handbook of Optical Constants of Solids*, Edward D. Palik, ed., Academic Press, New York, 1985

Parbrook, P.J., Kamata, A., Uemoto, T., in *Extended Abstracts of the 1992 International Conference on Solid State Devices and Materials*, Japan Society of Applied Physics, Tokyo, 1992

Paterson, M.S., *J. Appl. Phys.*, **23**, 805 (1952)

Pelekanos, N.T., Ding, J., Hargerott, M., Nurmikko, A.V., Luo, H., Samarth, N., Furdyna, J.K., *Phys. Rev. B* **45**, 6037 (1992).

People, R., Bean, J.C., *Appl. Phys. Lett.*, **47**, 322 (1985)

People, R., Bean, J.C., Erratum, *Appl. Phys. Lett.*, **49**, 229 (1986)

People, R., Sputz, S.K., *Phys. Rev. B*, **41**, 8431 (1990)

Petruzzello, J., Greenberg, B.L., Cammack, D.A., Dalby, R.,*J. Appl. Phys.*, **63**, 2299 (1988)

Petruzzello, J., Gaines, J., van der Sluis, P., Olego, D., Ponzoni, C., *Appl. Phys. Lett.*, **62**, 1496 (1993)

Pikus, G.E., Bir, G.L., *Sov. Phys.-Solid State*, **1**, 136 (1959)

Ren, J., Bowers, K.A., Sneed, B., Reed, F.E., Cook, Jr., J.W., Schetzina, J.F., *J. Cryst. Growth* **111**, 829 (1991)

Reynolds, D. C., Collins, T. C., in *Excitons, Their Properties and Uses*, Academic Press, New York, 1981

Roth, W. L., "Crystallography" in *Physics and Chemistry of II-VI Compounds*, M. Aven and J. S. Prener (eds), North-Holland, Amsterdam, 1967 though the wurtzite form of ZnSe has been reported at growth temperatures as low as 480°C (Roth, 1967).

Saenger, K.L., *J. Appl. Phys.*, **70**, 5629 (1991)

Saitoh, T., Yokogawa, T., Narusawa, T., *Jpn. J. Appl. Phys.*, **30**, 667 (1991)

Samuelson, L., Omling, P., Titze, H., Grimmeiss, H.G., *J. de Physique* , **C5**, 323 (1982)

Schmitt-Rank, S., Chemla, D.S., Miller, D.A.B., *Adv. in Phys.*, **38**, 89 (1989)

Sebastian, M.T., Krishina, P., *Prog. Crystal Growth Charact.*, **14**, 103 (1987)

Shahzad, K., Olego, D.J., Van de Walle, C.G., *Phys. Rev. B*, **38**, 1417 (1988)

Shahzad, K., Olego, D.J., Van de Walle, C.G., Cammack, D.A., *J. Lum.*, **46**, 109 (1990)

Simpson, J., Williams, J.O., *J. Appl. Phys.*, **70**, 2001 (1991)

Smith, H.W., Turner, A.F., *Appl. Opt.*, **4**, 417 (1965)

Stutius, W., *J. Electron. Mater.*, **10**, 95 (1981)

Stutius, W., *J. Appl. Phys.*, **53**, 284 (1982)

Suemune, I., Masato, H., Nakanishi, K., Yamada, K., Kan, Y., Yamanishi, M., *J. Cryst. Growth* **101**, 754 (1990)

Taguchi, T., Palmer, D.W., *Phys. Stat. Sol. (a)*, **69**, K55 (1982)

Taguchi, T., Professor Osaka University, Osaka, Japan, private communication, 1992

Taguchi, T., Endoh, Y., Ohno, T., Nozue, Y., *J. Lum.*, **52**, 123 (1992)

Talas, J. J. A., Allen, J. W., *Semicond. Sci. Tech.*, **6**, A138 (1991)

Tomomura, Y., Kitagawa, M., Suzuki, A., Nakajima, S., *J. Cryst. Growth* **99**, 451 (1990)

Tromson-Carli, A., Svob, L., Marfaing, Y., Druilhe, R., Desjonqueres, F., Triboulet, R., *J. Matl. Sci.*, **2**, 187 (1991)

Van de Walle, C. G., Laks, D. B., *J. Lum.*, **52**, 1 (1992)

van der Merwe, J.H., *Surf. Sci.*, **31**, 198 (1972)

Vassamillet, L.F., *J. Appl. Phys.*, **32**, 778 (1961)

Ward, L., "Zinc Selenide (ZnSe) Zinc Telluride (ZnTe)" in *Handbook of Optical Constants of Solids II*, Edward D. Palik, ed., Academic Press, New York, 1991

Warren, B.E., *Progr. in Metal Phys.*, **8**, 147 (1959)

Watkins, G. D., "Lattice Defects in II-VI Semiconductors" in *International Conference on Radiation Effects in Semiconductors, Dubrovnik, 1976, Institute of Physics, Conference Series; No. 31*, The Institute of Physics, New York, 1977

Wei, S.-H., Zunger, A., *Phys. Rev. B*, **37**, 8958 (1988)

Weisbuch, C., Dingle, R., Gossard, A.C., Wiegmann, W., *Solid State Commun.*, **38**, 709 (1981)

Wilkinson, M., Yang, F., Austin, E.J., O'Donnell, K.P., *J. Phys.: Cond. Matter*, **4**, 8863 (1992)

Williams, J.O., Ng, T.L., Wright, A.C., Cockayne, B., Wright, P.J., *J. Crys. Gwth.*, **68**, 237 (1984)

Wright, P.J., Parbrook, P.J., Cockayne, B., Jones, A.C., Orrell, E.D., O'Donnell, K.P., Henderson, B., *J. Cryst. Growth* **94**, 441 (1989)

Wu, Y., Toyoda, T., Fujita, Sz., Fujita, Sh., *Jpn. J. Appl. Phys.*, **29**, L144 (1990)

Yahata, A., Mitsuhashi, H., Hirahara, K., Beppu, T., *Jpn. J. Appl. Phys.*, **29**, L4 (1990)

Yamada, Y., Taguchi, T., *J. Crys. Gwth.*, **99**, 408 (1990)

Yamaga, S., Yoshikawa, A., Kasai, H., *J. Cryst. Growth* **86**, 252 (1988)

Yang, Z., Bowers, K.A., Ren, J., Lansari, Y., Cook Jr., J.W., Schetzina, *Appl. Phys. Lett.*, **61**, 2671 (1992)

Yao, T., Maekawa, S., *J. Cryst. Growth* **53**, 423 (1981)

Yao, T., "MBE Growth of II-VI Compounds" in *The Technology and Physics of Molecular Beam Epitaxy*, E.H.C. Parker, ed., Plenum Press, New York, 1985

Yao, T., *Jpn. J. App. Phys.*, **25**, L544 (1986)

Yasuda, T., Kara, K., Kukimoto, H., *J. Crys. Gwth.*, **77**, 485 (1986)

Yokogawa, T., Fujita, T., Ogura, M., Kajiwara, T., *J. Crys. Gwth.*, **93**, 708 (1988)

Yoshikawa, A., Muto, S., Yamaga, S., Kasai, H., *Jpn. J. Appl. Phys.*, **27**, 992 (1988)

Zalm, P.C., Marée, P.M.J., Olthof, R.I.J., *Appl. Phys. Lett.*, **46**, 597 (1985)

Zeldowitsh, J., *Acta Physicochimica U.R.S.S.*, **1**, 9 (1935)

Zhang, J.H., Fan, X.W., *J. Cryst. Growth* **121**, 769 (1992)

Zheng, J. Z., Allen, J. W., *J. Appl. Phys.*, **67**, 2060 (1990)

Zheng, J. Z., Allen, J. W., Spence, D. E., Sleat, W. E., Sibbett, W., *Appl. Phys. Lett.*, **62**, 63 (1992)

Zhu, Z., Nomura, T., Miyao, M. Hagino, M., *J. Cryst. Growth* **95**, 529 (1989)

Zhu, Z., Hagino, M., Uesugi, K., Kamiyama, S., Fujimoto, M., Yao, T., *J. Cryst. Growth* **99**, 441 (1990)

Zhu, Z., Mori, H., Yao, T., *Appl. Phys. Lett.*, **61**, 2811 (1992)

APPENDICES

APPENDIX 1

Film Thickness Uniformity: Simulation of Pulsed-Laser Deposition Using the Offset-Source Geometry

Figure A1-1 shows the offset-source geometry. The substrate and target planes are parallel, separated by a distance D, and their rotational centerlines are coincident. This rotational axis intersects the target plane at the point O. The laser is focussed onto the point S, which is offset from the rotational centerline by a distance ρ. The motion of the point S, relative to the position of the substrate, is achieved either by rotating the substrate or by scanning the laser beam in a circle of radius ρ on the target surface. (The center of this circle is the rotational centerline of the substrate.) The relation for the thickness of the deposit is obtained at an arbitrary point P on the substrate. P is located along the surface normal from a point on the target defined by a radial distance R from the centerline and the angle ϕ from S. θ is the angle between the surface normal at S and the line $\vec{SP}$.

Dupkov has shown (Dubkov, V.M., *Sov. J. Opt. Technol.*, **49**, 168 (1982)) that if more than six sources are equally spaced about a circle of radius ρ, this geometry can be treated as an annular, ring-like source. Thus, this geometry is applicable to PLA when this criterion is met.

From simple geometric construction, the relations between the various angles and displacement vectors (Figure A1.1) can be written

$$r^2 = R^2 + \rho^2 - 2R\rho\cos(\phi) \qquad \text{A1.01}$$

$$\tan(\theta) = \frac{r}{D} \qquad \text{A1.02}$$

so that

$$\theta = \tan^{-1}\left[D^{-1}\left(R^2 + \rho^2 - 2R\rho\cos\{\phi\}\right)^{1/2}\right] \qquad \text{A1.03}$$

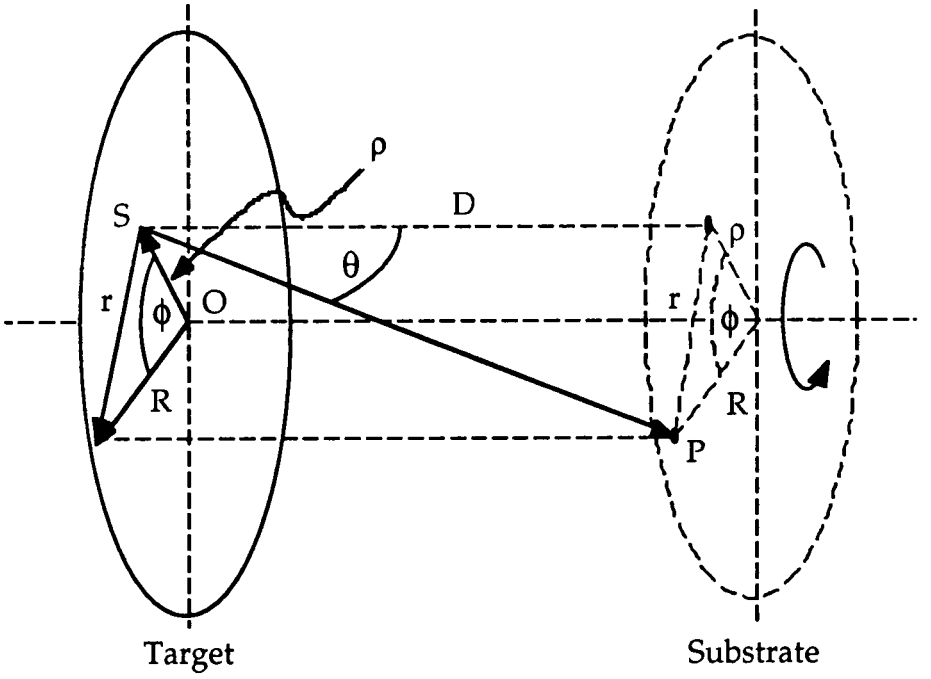

Figure A1-1 Offset-source geometry for pulsed-laser ablation.

The distribution of the flux (J) of a species rapidly desorbing from a surface can be written as (see Chapter 5)

$$J(\theta) = J_0 \cos^n(\theta) \qquad \text{A1.04}$$

where J_0 is the flux along the $\theta = 0$ direction and n typically is in the range $5 \leq n \leq 25$. For an annular ring source the resulting thickness (L) deposited is

$$L = 2\left(\int_0^{\pi} J[\theta]\, d\phi\right) \quad . \qquad \text{A1.05}$$

Substituting for the flux (A1.04), and the relations (A1.01-A1.03), then

$$L = 2\int_0^{\pi}\left[J_0 \cos^n\left\{\tan^{-1}\left(\left[\frac{R^2+\rho^2}{D^2} - \frac{2R\rho}{D^2}\cos\{\phi\}\right]^{1/2}\right)\right\}\right] d\phi \qquad \text{A1.06}$$

For ease of manipulation, C_i is defined such that

$$C_1 = \frac{R^2+\rho^2}{D^2} \qquad \text{A1.07a}$$

$$C_2 = \frac{2R\rho}{D^2} \qquad \text{A1.07b}$$

and the following relations can be written

$$\tan(\Phi) = (C_1 - C_2\cos[\phi])^{1/2} \qquad \text{A1.08a}$$

$$\cos(\Phi) = (1 + C_1 - C_2\cos[\phi])^{-1/2} \qquad \text{A1.08b}$$

Making appropriate rearrangements of A1.08, the cosine term in Equation A1.06 can be simplified using the trigonometric relation

$$\cos\left(\tan^{-1}\left[\{C_1 - C_2\cos(\phi)\}^{1/2}\right]\right) = (1 + C_1 - C_2\cos[\phi])^{-1/2} \qquad \text{A1.09}$$

with the following result for the thickness

$$L = 2\left(\int_0^{\pi}\left[J_0\{1 + C_1 - C_2\cos(\phi)\}^{-n/2}\right]d\phi\right) \quad . \qquad \text{A1.10}$$

As illustrated in Figures A1.2 and A1.3, by controlling ρ, the thickness can be varied from a central peak at R = 0 (ρ less than optimal, Figure A1.2) to a local minimum (ρ greater than optimal, Figure A1.3). At the optimal offset (ρ_{opt}), an area of uniform film thickness is obtained (Figure A1.4). The optimal offset was found by evaluating the normalized thickness (i.e., $L(x,y,\rho)/L(0,0,\rho = 0)$) over the interval $x,y \in [0,\rho-\delta]$. Here δ is a small value and, in this work, assumed to be $\delta \leq 1/3\rho$. The relative thickness was calculated at a number of equally spaced points (0,y) on the interval $y \in [0,2/3\rho]$, and, at ρ_{opt}, the average of these relative thickness data is 1.

The optimal offset was determined for various target-substrate separations with a fixed n value. For a given n, it was found that the ratio

$$m = \left(\frac{D}{\rho}\right)_{opt} \qquad \text{A1.11}$$

was a constant value for all D. However, the value of this ratio was found to depend on n. The relation between this optimal offset ratio and n is shown in Figure A1.5, where the curve through the data points is the least squares fit of the equation

$$m = 0.658\, n^{0.509} \qquad \text{A1.12}$$

Thus, for example, if n = 15 and D = 10 cm, then m~2.6 and $\rho_{opt} = D/m \sim 4$ cm. Thus, a target diameter of ~4 inches may be required, which suggests using an annular ring target rather than a disk, in order to minimize the amount of target material used.

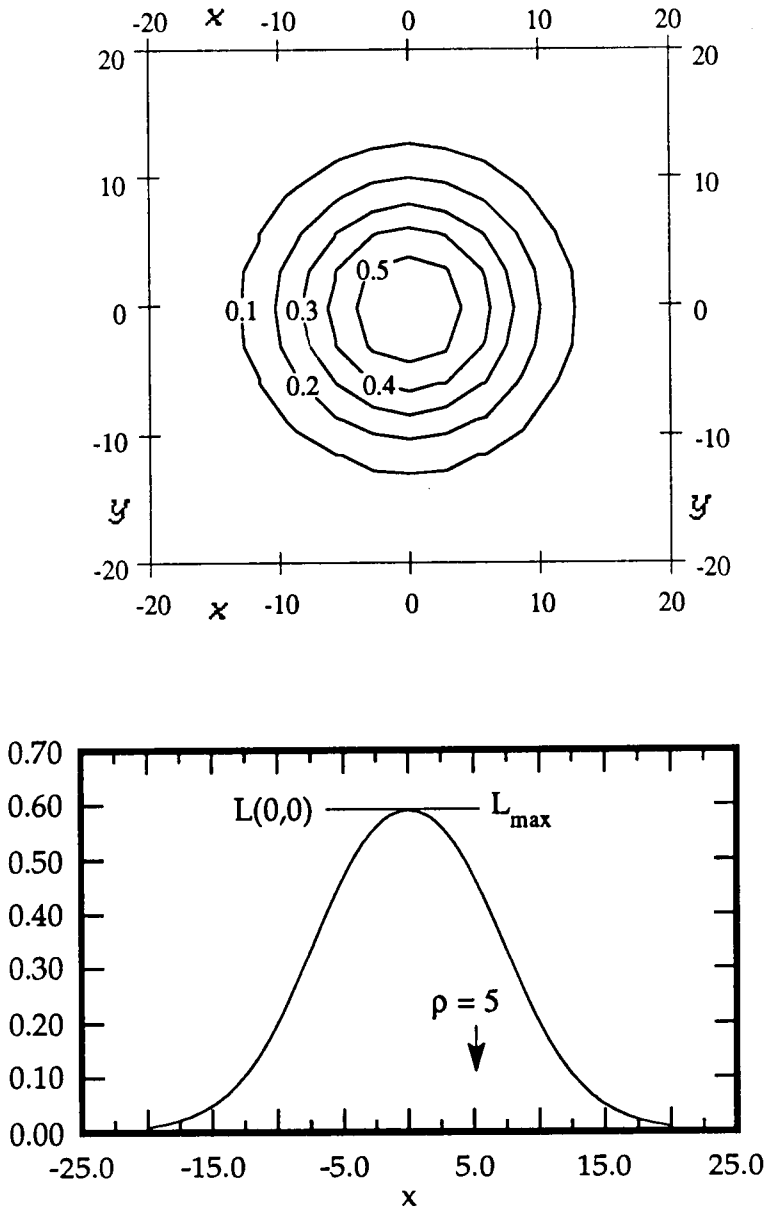

Figure A1.2 Thickness contour (top), and thickness cross-section at y = 0 (bottom), for n = 10, D = 15, ρ = 5 (ρ_{opt} = 7.06). Ordinates (x,y) have the same units as D and ρ.

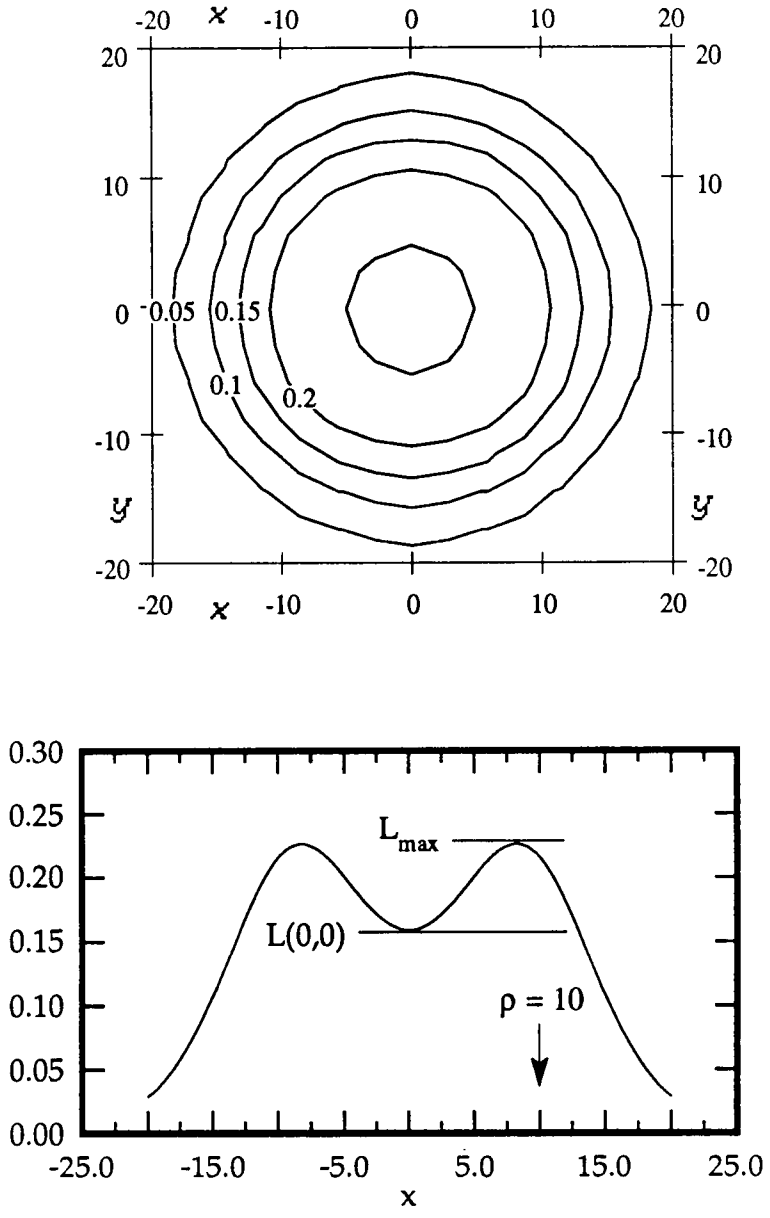

Figure A1.3 Thickness contour (top), and thickness cross-section at y = 0 (bottom), for n = 10, D = 15, ρ = 10 (ρ_{opt} = 7.06). Ordinates (x,y) have the same units as D and ρ.

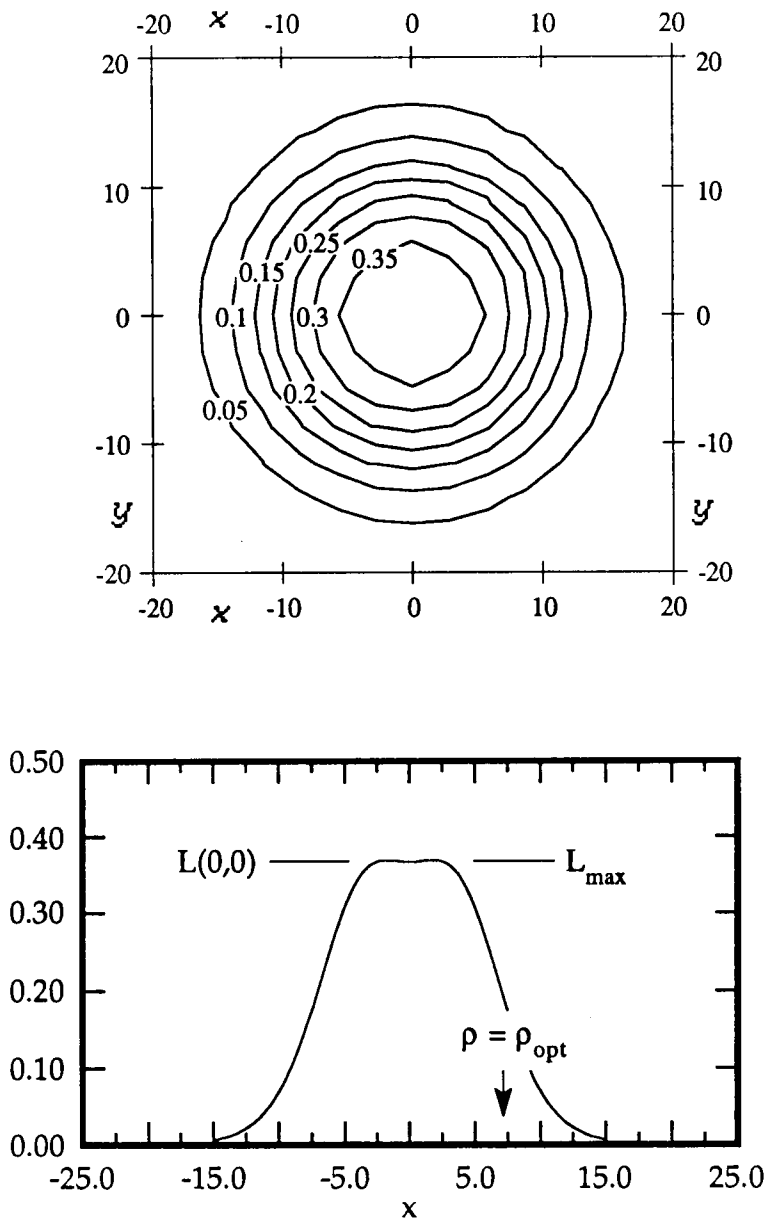

Figure A1.4 Thickness contour (top), and thickness cross-section at y = 0 (bottom), for n = 10, D = 15, $\rho = \rho_{opt}$ (ρ_{opt} = 7.06). Ordinates (x,y) have the same units as D and ρ.

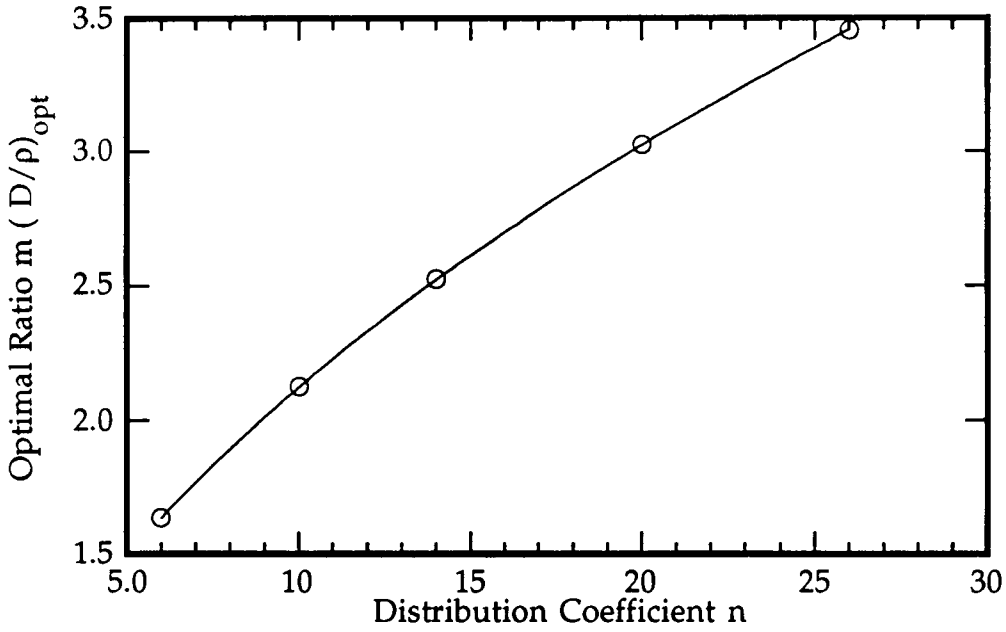

Figure A1.5 Relation between the optimal offset ratio $(D/\rho)_{opt}$ and the distribution coefficient (n) of the ablation plume (i.e., $J=J_o\cos^n(\theta)$)..

APPENDIX 2

Table A2 ZnS/GaAs Optical Data

Wavelength (nm)	Photon Energy (eV)	n	k	ε_1	ε_2
240	5.175	3.224	0.795	9.762	5.126
242	5.132	3.226	0.769	9.816	4.962
244	5.090	3.204	0.736	9.724	4.716
246	5.049	3.177	0.714	9.584	4.537
248	5.008	3.147	0.680	9.441	4.280
250	4.968	3.142	0.661	9.435	4.154
252	4.928	3.125	0.635	9.362	3.969
254	4.890	3.103	0.615	9.250	3.817
256	4.851	3.076	0.601	9.101	3.697
258	4.814	3.057	0.580	9.009	3.546
260	4.777	3.048	0.565	8.971	3.444
262	4.740	3.029	0.547	8.876	3.314
264	4.704	3.019	0.536	8.827	3.236
266	4.669	3.007	0.522	8.770	3.139
268	4.634	2.995	0.510	8.710	3.055
270	4.599	2.982	0.497	8.645	2.964
272	4.566	2.967	0.485	8.568	2.878
274	4.532	2.959	0.476	8.529	2.817
276	4.499	2.950	0.465	8.486	2.743
278	4.467	2.941	0.455	8.442	2.676
280	4.435	2.930	0.448	8.384	2.625
282	4.403	2.923	0.437	8.353	2.555
284	4.372	2.916	0.430	8.318	2.508
286	4.342	2.908	0.420	8.280	2.443
288	4.312	2.901	0.413	8.245	2.396
290	4.282	2.894	0.406	8.210	2.350
292	4.252	2.889	0.400	8.186	2.311
294	4.223	2.883	0.391	8.159	2.255

Table A2 (continued)

Wavelength (nm)	Photon Energy (eV)	n	k	ε_1	ε_2
296	4.195	2.878	0.385	8.135	2.216
298	4.167	2.874	0.378	8.117	2.173
300	4.139	2.870	0.372	8.099	2.135
304	4.084	2.862	0.360	8.061	2.061
308	4.031	2.855	0.348	8.030	1.987
312	3.979	2.850	0.337	8.009	1.921
316	3.929	2.849	0.327	8.010	1.863
320	3.880	2.849	0.322	8.013	1.835
324	3.832	2.858	0.322	8.064	1.841
328	3.785	2.899	0.320	8.302	1.855
332	3.739	2.930	0.272	8.511	1.594
336	3.695	3.021	0.253	9.062	1.529
340	3.651	2.935	0.075	8.609	0.440
344	3.609	2.863	0.030	8.196	0.172
348	3.567	2.831	0.019	8.014	0.108
352	3.527	2.778	0.028	7.717	0.156
356	3.487	2.754	0.012	7.584	0.066
360	3.448	2.733	0.009	7.469	0.049
364	3.410	2.713	0.011	7.360	0.060
368	3.373	2.681	0.016	7.188	0.086
372	3.337	2.668	0.007	7.118	0.037
376	3.301	2.652	0.006	7.033	0.032
380	3.267	2.641	0.006	6.975	0.032
384	3.233	2.627	0.007	6.901	0.037
388	3.199	2.608	0.015	6.801	0.078
392	3.166	2.596	0.005	6.739	0.026
396	3.134	2.587	0.004	6.693	0.021
400	3.103	2.580	0.005	6.656	0.026
404	3.072	2.572	0.004	6.615	0.021
408	3.042	2.565	0.004	6.579	0.021

Table A2 (continued)

Wavelength (nm)	Photon Energy (eV)	n	k	ε_1	ε_2
412	3.013	2.557	0.007	6.538	0.036
416	2.984	2.544	0.011	6.472	0.056
420	2.955	2.537	0.004	6.436	0.020
425	2.920	2.531	0.002	6.406	0.010
430	2.886	2.521	0.004	6.355	0.020
435	2.853	2.516	0.004	6.330	0.020
440	2.821	2.512	0.003	6.310	0.015
445	2.789	2.505	0.003	6.275	0.015
450	2.758	2.496	0.008	6.230	0.040
455	2.728	2.488	0.005	6.190	0.025
460	2.698	2.482	0.002	6.160	0.010
465	2.669	2.476	0.003	6.131	0.015
470	2.641	2.472	0.003	6.111	0.015
475	2.613	2.466	0.004	6.081	0.020
480	2.585	2.460	0.004	6.052	0.020
485	2.559	2.455	0.003	6.027	0.015
490	2.533	2.450	0.004	6.002	0.020
495	2.507	2.446	0.006	5.983	0.029
500	2.482	2.440	0.007	5.954	0.034
505	2.457	2.435	0.004	5.929	0.019
510	2.433	2.432	0.003	5.915	0.015
515	2.410	2.429	0.003	5.900	0.015
520	2.386	2.426	0.003	5.885	0.015
525	2.364	2.424	0.003	5.876	0.015
530	2.341	2.422	0.003	5.866	0.015
535	2.319	2.419	0.003	5.852	0.015
540	2.298	2.417	0.003	5.842	0.015
545	2.277	2.415	0.003	5.832	0.014
550	2.256	2.412	0.003	5.818	0.014
555	2.236	2.409	0.003	5.803	0.014

Table A2 (continued)

Wavelength (nm)	Photon Energy (eV)	n	k	ε_1	ε_2
560	2.216	2.405	0.004	5.784	0.019
565	2.196	2.402	0.004	5.770	0.019
570	2.177	2.400	0.003	5.760	0.014
575	2.158	2.399	0.001	5.755	0.005
580	2.139	2.396	0.001	5.741	0.005
585	2.121	2.393	0.001	5.726	0.005
590	2.103	2.391	0.002	5.717	0.010
595	2.085	2.390	0.002	5.712	0.010
600	2.068	2.388	0.002	5.703	0.010
605	2.051	2.386	0.002	5.693	0.010
610	2.034	2.384	0.002	5.683	0.010
615	2.018	2.382	0.002	5.674	0.010
620	2.001	2.381	0.002	5.669	0.010
625	1.985	2.380	0.002	5.664	0.010
630	1.970	2.375	0.002	5.641	0.010
635	1.954	2.375	0.002	5.641	0.010
640	1.939	2.373	0.002	5.631	0.009
645	1.924	2.372	0.002	5.626	0.009
650	1.909	2.370	0.002	5.617	0.009
655	1.894	2.368	0.002	5.607	0.009
660	1.880	2.367	0.002	5.603	0.009
665	1.866	2.365	0.001	5.593	0.005
670	1.852	2.364	0.001	5.588	0.005
675	1.838	2.360	0.001	5.570	0.005
680	1.825	2.359	0.001	5.565	0.005
685	1.811	2.358	0.002	5.560	0.009
690	1.798	2.357	0.002	5.555	0.009
695	1.785	2.356	0.002	5.551	0.009
700	1.772	2.355	0.002	5.546	0.009
705	1.760	2.354	0.002	5.541	0.009

Table A2 (continued)

Wavelength (nm)	Photon Energy (eV)	n	k	ε_1	ε_2
710	1.747	2.353	0.002	5.537	0.009
715	1.735	2.350	0.002	5.522	0.009
720	1.723	2.349	0.002	5.518	0.009
725	1.711	2.349	0.002	5.518	0.009
730	1.700	2.348	0.002	5.513	0.009
735	1.688	2.348	0.002	5.513	0.009
740	1.677	2.347	0.002	5.508	0.009
745	1.665	2.346	0.002	5.504	0.009
750	1.654	2.345	0.002	5.499	0.009
755	1.643	2.344	0.002	5.494	0.009
760	1.632	2.343	0.002	5.490	0.009
765	1.622	2.341	0.002	5.480	0.009
770	1.611	2.340	0.001	5.476	0.005
775	1.601	2.339	0.001	5.471	0.005
780	1.591	2.338	0.002	5.466	0.009
785	1.580	2.337	0.002	5.462	0.009
790	1.570	2.336	0.002	5.457	0.009
795	1.561	2.336	0.002	5.457	0.009
800	1.551	2.335	0.001	5.452	0.005
805	1.541	2.334	0.001	5.448	0.005
810	1.532	2.334	0.001	5.448	0.005
815	1.522	2.334	0.001	5.448	0.005
820	1.513	2.332	0.001	5.438	0.005
825	1.504	2.332	0.001	5.438	0.005
830	1.495	2.332	0.001	5.438	0.005
835	1.486	2.332	0.001	5.438	0.005
840	1.477	2.332	0.000	5.438	0.000

APPENDIX 3

Table A3 ZnSe/GaAs Optical Data

Wavelength (nm)	Photon Energy (eV)	n	k	ε_1	ε_2
240	5.180	2.596	1.900	3.129	9.865
242	5.132	2.632	1.937	3.175	10.196
244	5.090	2.735	1.979	3.564	10.825
246	5.049	2.870	1.984	4.301	11.388
248	5.008	2.960	1.948	4.967	11.532
250	4.968	3.017	1.909	5.458	11.519
252	4.928	3.063	1.902	5.764	11.652
254	4.890	3.146	1.896	6.302	11.930
256	4.851	3.258	1.912	6.959	12.459
258	4.814	3.403	1.875	8.065	12.761
260	4.777	3.540	1.773	9.388	12.553
262	4.740	3.632	1.634	10.521	11.869
264	4.704	3.673	1.496	11.253	10.990
266	4.669	3.690	1.362	11.761	10.052
268	4.634	3.676	1.253	11.943	9.212
270	4.599	3.655	1.157	12.020	8.458
272	4.566	3.627	1.078	11.993	7.820
274	4.532	3.597	1.005	11.928	7.230
276	4.499	3.566	0.941	11.831	6.711
278	4.467	3.535	0.894	11.697	6.321
280	4.435	3.503	0.845	11.557	5.920
282	4.403	3.472	0.806	11.405	5.597
284	4.372	3.444	0.773	11.264	5.324
286	4.342	3.418	0.746	11.126	5.100
288	4.312	3.390	0.713	10.984	4.834
290	4.282	3.365	0.689	10.849	4.637
292	4.252	3.341	0.669	10.715	4.470
294	4.223	3.320	0.649	10.601	4.309

Table A3 (continued)

Wavelength (nm)	Photon Energy (eV)	n	k	ε_1	ε_2
296	4.195	3.302	0.628	10.509	4.147
298	4.167	3.281	0.614	10.388	4.029
300	4.139	3.263	0.597	10.291	3.896
304	4.084	3.229	0.567	10.105	3.662
308	4.031	3.196	0.546	9.916	3.490
312	3.979	3.169	0.523	9.769	3.315
316	3.929	3.139	0.509	9.594	3.196
320	3.880	3.121	0.497	9.494	3.102
324	3.832	3.105	0.480	9.411	2.981
328	3.785	3.089	0.469	9.322	2.897
332	3.739	3.077	0.453	9.263	2.788
336	3.695	3.066	0.437	9.209	2.680
340	3.651	3.055	0.424	9.153	2.591
344	3.609	3.042	0.410	9.086	2.494
348	3.567	3.031	0.397	9.029	2.407
352	3.527	3.019	0.384	8.967	2.319
356	3.487	3.008	0.371	8.910	2.232
360	3.448	2.997	0.359	8.853	2.152
364	3.410	2.987	0.348	8.801	2.079
368	3.373	2.977	0.335	8.750	1.995
372	3.337	2.969	0.320	8.713	1.900
376	3.301	2.965	0.302	8.700	1.791
380	3.267	2.966	0.285	8.716	1.691
384	3.233	2.972	0.275	8.757	1.635
388	3.199	2.986	0.270	8.843	1.612
392	3.166	2.998	0.270	8.915	1.619
396	3.134	3.003	0.261	8.950	1.568
400	3.103	2.995	0.246	8.910	1.474
404	3.072	2.977	0.234	8.808	1.393
408	3.042	2.959	0.224	8.706	1.326

Table A3 (continued)

Wavelength (nm)	Photon Energy (eV)	n	k	ε_1	ε_2
412	3.013	2.945	0.217	8.626	1.278
416	2.984	2.934	0.210	8.564	1.232
420	2.955	2.926	0.203	8.520	1.188
430	2.886	2.910	0.190	8.432	1.106
440	2.821	2.906	0.180	8.412	1.046
450	2.758	2.907	0.179	8.419	1.041
460	2.698	2.996	0.111	8.964	0.665
470	2.641	2.894	0.022	8.375	0.127
480	2.585	2.828	0.016	7.997	0.090
490	2.533	2.789	0.009	7.778	0.050
500	2.482	2.768	0.007	7.662	0.039
510	2.433	2.748	0.007	7.551	0.038
520	2.386	2.732	0.007	7.464	0.038
530	2.341	2.720	0.008	7.398	0.044
540	2.298	2.708	0.009	7.333	0.049
550	2.256	2.695	0.009	7.263	0.049
560	2.216	2.681	0.010	7.188	0.054
570	2.177	2.671	0.009	7.134	0.048
580	2.139	2.660	0.008	7.076	0.043
590	2.103	2.650	0.007	7.022	0.037
600	2.068	2.642	0.006	6.980	0.032
610	2.034	2.634	0.006	6.938	0.032
620	2.001	2.628	0.005	6.906	0.026
630	1.970	2.622	0.004	6.875	0.021
640	1.939	2.618	0.004	6.854	0.021
650	1.909	2.612	0.004	6.823	0.021
660	1.880	2.607	0.004	6.796	0.021
670	1.852	2.602	0.005	6.770	0.026
680	1.825	2.590	0.007	6.708	0.036
690	1.798	2.585	0.008	6.682	0.041

Table A3 (continued)

Wavelength (nm)	Photon Energy (eV)	n	k	ε_1	ε_2
700	1.772	2.580	0.008	6.656	0.041
710	1.747	2.575	0.008	6.631	0.041
720	1.723	2.570	0.006	6.605	0.031
730	1.700	2.567	0.005	6.589	0.026
740	1.677	2.563	0.004	6.569	0.021
750	1.654	2.559	0.004	6.548	0.020
760	1.632	2.556	0.002	6.533	0.010
770	1.611	2.550	0.001	6.502	0.005
780	1.591	2.547	0.001	6.487	0.005
790	1.570	2.545	0.003	6.477	0.015
800	1.551	2.546	0.003	6.482	0.015
810	1.532	2.541	0.002	6.457	0.010
820	1.513	2.539	0.000	6.447	0.000
830	1.495	2.539	-0.001	6.447	-0.005
840	1.477	2.536	-0.001	6.431	-0.005

VITA

James McCamy was born in Florence, Alabama on February 10, 1959. He attended elementary school in that city and was graduated from Mars Hill Bible School in June 1977. He entered Auburn University in September of that year, and in June 1982 received a Bachelor of Chemical Engineering degree from that institution.

After two years as an engineer with Amoco Production Company, he and his bride moved to Knoxville, Tennessee where he entered the Graduate School of the University of Tennessee as a part-time student in September of 1984. In June of 1985 he accepted a teaching assistantship and began full-time pursuit of a Master of Science degree in Metallurgical Engineering. This degree was conferred in December 1987.

In April 1987, Mr. McCamy accepted an appointment from the Oak Ridge Associated Universities program to pursue a Doctor of Philosophy degree in Metallurgical Engineering. This degree was conferred in December 1993.

In October 1993, Mr. McCamy accepted a postdoctoral appointment with the Division of Applied Physics at Harvard University. In that capacity, he will continue to study the pulsed-laser ablation process, with particular emphasis on the fundamental growth aspects of this technique.